

Sea-ice dynamics along West Antarctic  
continental shelves  
from the last deglacial to the Holocene

A multi-proxy biomarker approach

---

Kumulative Dissertation

zur Erlangung des akademischen Grades  
eines Doktors der Naturwissenschaften

Dr. rer. nat.

am Fachbereich Geowissenschaften  
der Universität Bremen


vorgelegt von  
Nele Steinberg  
Bremen, 2024

Gutachter der Dissertation:  
Dr. Juliane Müller  
Prof. Dr. Matthias Forwick

Datum des Promotionskolloquiums: 03. Mai 2024

## Versicherung an Eides Statt / Affirmation in lieu of an oath

gem. § 5 Abs. 5 der Promotionsordnung vom 28.04.2021 / according to § 5 (5) of the Doctoral Degree Rules and Regulations of 28 April, 2021

Ich / I, Nele Steinberg, 

versichere an Eides Statt durch meine Unterschrift, dass ich die vorliegende Dissertation selbstständig und ohne fremde Hilfe angefertigt und alle Stellen, die ich wörtlich dem Sinne nach aus Veröffentlichungen entnommen habe, als solche kenntlich gemacht habe, mich auch keiner anderen als der angegebenen Literatur oder sonstiger Hilfsmittel bedient habe und die zu Prüfungszwecken beigelegte elektronische Version (PDF) der Dissertation mit der abgegebenen gedruckten Version identisch ist. / *With my signature I affirm in lieu of an oath that I prepared the submitted dissertation independently and without illicit assistance from third parties, that I appropriately referenced any text or content from other sources, that I used only literature and resources listed in the dissertation, and that the electronic (PDF) and printed versions of the dissertation are identical.*

Ich versichere an Eides Statt, dass ich die vorgenannten Angaben nach bestem Wissen und Gewissen gemacht habe und dass die Angaben der Wahrheit entsprechen und ich nichts verschwiegen habe. / *I affirm in lieu of an oath that the information provided herein to the best of my knowledge is true and complete.*

Die Strafbarkeit einer falschen eidesstattlichen Versicherung ist mir bekannt, namentlich die Strafandrohung gemäß § 156 StGB bis zu drei Jahren Freiheitsstrafe oder Geldstrafe bei vorsätzlicher Begehung der Tat bzw. gemäß § 161 Abs. 1 StGB bis zu einem Jahr Freiheitsstrafe oder Geldstrafe bei fahrlässiger Begehung. / *I am aware that a false affidavit is a criminal offence which is punishable by law in accordance with § 156 of the German Criminal Code (StGB) with up to three years imprisonment or a fine in case of intention, or in accordance with § 161 (1) of the German Criminal Code with up to one year imprisonment or a fine in case of negligence.*



Größe besteht nicht darin, was man hat,  
sondern darin, was man gibt.

- für Ötti -



## Abstract

After experiencing three record-breaking low sea-ice summers in a course of seven years, Antarctic sea ice prompts a gaining interest among climate researchers. It is now more important than ever to get the best possible understanding of past Antarctic sea-ice behavior and its response to long- and short-term atmospheric and oceanographic changes on regional and pan-Antarctic scales. The knowledge as well as newly collected data will improve model simulations that aim to predict the future development of this climate-sensitive feature. Therefore, the need for tools that allow consistent and reliable paleo-reconstructions of Southern Ocean sea ice is high. The recently introduced organic sea-ice biomarker proxy IPSO<sub>25</sub> has the potential to fulfill this need, however, thorough assessments of its applicability hitherto are sparse. A suite of sediment samples from West Antarctic continental shelves, which are affected most by strongly negative sea-ice trends, were investigated within this thesis to evaluate the proxy's potential to display the recent and past sea-ice coverage in the study areas.

A study on seafloor surface sediments from the West Antarctic Peninsula, the Amundsen and Weddell seas demonstrated that the IPSO<sub>25</sub> concentrations within the sediments do not adequately reflect the recent sea-ice conditions derived from satellite and numerical model data. For a semi-quantitative estimation of the sea-ice cover, IPSO<sub>25</sub> was combined with a phytoplankton marker, resulting in the sea-ice index PIPSO<sub>25</sub> (analogous to the sea-ice index IP<sub>25</sub> for the Arctic), that allows a more realistic estimate of sea-ice coverage and hence seems to be a more suitable tool for paleo sea-ice reconstructions. To gather more information on ocean temperature, measurements of isoprenoidal glycerol dialkyl glycerol tetraethers were carried out and compared to instrument measurements of sea surface and subsurface temperatures, revealing the general capability of the proxy to mirror ocean temperatures.

In a further study, the applicability of IPSO<sub>25</sub> alongside phytoplankton biomarkers, the sea-ice index PIPSO<sub>25</sub>, sedimentological parameters and physical properties was further investigated by means of a high-resolution sediment core located in the direct vicinity of the Pine Island Glacier in the eastern Amundsen Sea Embayment. Here, the multi-proxy dataset revealed the evolution from a polynya setting towards a more sea-ice dominated regime during the early Holocene and a following build-up of a heavy sea-

ice cover. Potential interconnections between the regional sea-ice conditions and the inflow of Circumpolar Deep Water onto the continental shelf were drawn and discussed.

For the third study as part of this thesis, IPSO<sub>25</sub>, phytoplankton biomarkers, the sea-ice index PIPSO<sub>25</sub> and sedimentological proxies were used for sea-ice reconstructions in the western Amundsen Sea and compared to winter sea ice-estimates based on diatom assemblages. The multi-proxy dataset documents the waxing and waning of the Getz Ice Shelf since the last deglaciation. The first break-up of the Getz Ice Shelf around 13 cal. ka BP and the establishment of a sea-ice cover was followed by a phase of significantly reduced sea-ice cover at around 12.7 cal. ka BP until a re-expansion of sea ice occurred throughout the Holocene. These developments were linked to interhemispheric climate patterns.

Regarding the new findings collected within this thesis, IPSO<sub>25</sub> and the PIPSO<sub>25</sub> approach can be considered a promising tool for (paleo) sea-ice reconstructions on the continental shelves off West Antarctica when interpreted carefully and alongside other paleoenvironmental parameters.



## Zusammenfassung

Nach drei Sommern mit rekordverdächtig niedrigen Meereisausdehnungen innerhalb von sieben Jahren, weckt das antarktische Meereis zunehmend das Interesse der Klimaforscher. Heute ist es wichtiger denn je, das Verhalten des antarktischen Meereises in der Vergangenheit und seine Reaktion auf lang- und kurzfristige atmosphärische und ozeanografische Veränderungen auf regionaler und pan-antarktischer Ebene so gut wie möglich zu verstehen. Das Wissen, sowie neu erhobene Daten werden gebraucht um Modellsimulationen zu verbessern, mit denen die künftige Entwicklung dieses klimasensiblen Elements vorhergesagt werden soll. Daher besteht ein großer Bedarf an Indikatoren, die zuverlässige Paläorekonstruktionen des Meereises im Südlichen Ozean ermöglichen. Der vor kurzem eingeführte organische Meereis-Biomarker IPSO<sub>25</sub> hat das Potenzial, diesen Bedarf zu decken, allerdings liegen bisher nur wenige Bewertungen seiner Anwendbarkeit vor. Eine Reihe von Sedimentproben von westantarktischen Kontinentalschelfen, die am stärksten von stark negativen Meereis-Trends betroffen sind, wurden im Rahmen dieser Arbeit untersucht, um das Potenzial des Proxys zur Darstellung der aktuellen und vergangenen Meereisbedeckung in den Untersuchungsgebieten zu bewerten.

Eine Studie an Oberflächensedimenten des Meeresbodens der Westantarktischen Halbinsel, des Amundsen- und des Weddellmeeres zeigte, dass die IPSO<sub>25</sub>-Konzentrationen in den Sedimenten die aus Satelliten- und numerischen Modelldaten abgeleiteten aktuellen Meereisbedingungen nicht sehr gut wiedergeben. Für eine semiquantitative Einschätzung der Meereisverteilung wurde IPSO<sub>25</sub> mit einem Phytoplankton-Biomarker kombiniert, woraus sich der Meereis-Index PIPSO<sub>25</sub> (analog zum Meereis-Index PIP<sub>25</sub> für die Arktis) ergibt, der eine realistischere Abschätzung der Meereisbedingungen erlaubt und somit ein geeigneter Proxy zur Rekonstruktion vergangener Meereisbedingungen ist. Um Informationen über die Ozeantemperaturen zu erhalten, wurden Isoprenoid-Glycerol-Dialkyl-Glycerol-Tetraether untersucht und mit instrumentellen Messungen der Meeresoberflächentemperaturen und Subsurface-Temperaturen verglichen, was auf eine generelle Fähigkeit dieses Proxys, die Ozeantemperaturen widerzuspiegeln, hindeutet.

In einer weiteren Studie wurde die Anwendbarkeit von IPSO<sub>25</sub> zusammen mit Phytoplankton-Biomarkern, sedimentologischen Parametern und physikalischen

Eigenschaften anhand eines hochauflösenden Sedimentkerns in unmittelbarer Nähe des Pine-Island-Gletschers im östlichen Amundsenmeer untersucht. Der Multi-Proxy-Datensatz zeigte die Entwicklung von einer Polynya hin zu einem Meereis-dominierten Regime während des frühen Holozäns und den darauffolgenden Aufbau einer starken Meereisdecke. Mögliche Zusammenhänge zwischen den regionalen Meereisbedingungen und dem Zufluss von zirkumpolarem Tiefenwasser auf den Kontinentalschelf wurden aufgezeigt und diskutiert.

Für die dritte Studie im Rahmen dieser Arbeit wurden IPSO<sub>25</sub>, Phytoplankton-Biomarker, der Meereis-Index PIPSO<sub>25</sub> und sedimentologische Proxies für Meereis-Rekonstruktionen im westlichen Amundsenmeer verwendet und mit Winter-Meereis-Abschätzungen auf Grundlage von Diatomeen verglichen. Der Multi-Proxy-Datensatz dokumentiert das Wachsen und Schwinden des Getz-Schelfeises seit des letzten Deglazials. Auf das erste Aufbrechen des Getz-Schelfeises um 13000 Jahren vor heute und die Entstehung einer Meereisdecke folgte eine Phase mit deutlich reduzierter Meereisbedeckung um 12700 Jahren vor heute, bis es im Laufe des Holozäns zu einer erneuten Ausdehnung des Meereises kam. Diese Entwicklungen wurden mit interhemisphärischen Klimamustern in Verbindung gebracht.

In Anbetracht der neuen Erkenntnisse, die im Rahmen dieser Arbeit gesammelt wurden, können IPSO<sub>25</sub> und der PIPSO<sub>25</sub>-Index als vielversprechende Indikatoren für (Paläo-) Meereisrekonstruktionen auf den Kontinentalschelfen vor der Westantarktis betrachtet werden, wenn sie sorgfältig und zusammen mit anderen Paläoumweltparametern interpretiert werden.

## Danksagung

Liebe Jule, dir gilt mein größter Dank! Nicht nur dafür, dass du es mir ermöglicht hast diese Doktorarbeit zu schreiben und mein Arbeitsgebiet, das ewige Eis der Antarktis, mit eigenen Augen zu sehen, sondern auch für deine unsagbare Unterstützung. Du hast mir so viele Freiheiten gewährt, mich in schweren Zeiten unterstützt und mit deinen aufbauenden Worten immer und immer und immer wieder motiviert weiterzumachen.

Außerdem möchte ich Prof. Dr. Matthias Forwick für die Annahme der Zweitbegutachtung meinen Dank aussprechen.

Ganz besonders bedanken möchte ich mich außerdem bei den PALICE-Mädels, Maria-Elena Vorrath, Denise Dieckstall, Mandy Kuck und Gema Martínez-Méndez, und auch bei Julia Hagemann, Kevin Küssner und Nicole Syring. Ihr habt mir die Zeit am AWI mit viel Freude, Vertrauen, offene Ohren, aber auch mal mit Themen abseits der Wissenschaft, versüßt.

Kirsten Fahl danke ich von Herzen für die stundenlange Fehlersuche an unserer Zicke, aber auch für dein Mitgefühl, deine liebevolle und vor allem lockere Art – du bringst ganz viel Sonne in die Irrenanstalt.

Walter Luttmer, Susanne Wiebe, Valea Schumacher und Nicoletta Ruggieri danke ich für die Einführung in sämtliche Labormethoden, für Reisetipps, Strick-Hilfe, Lebensweisheiten und hier und da einen netten Plausch.

Außerdem möchte ich mich herzlich bei Shuzhuang Wu, Weng-si Chao, Henriette Kolling, Anne Kremer, Jakob Belter, Henrik Sadatzki, Thomas Ronge, Michelle van der Does, Ling Liu, Junjie Wu, Jeetendra Saini und Defang You für die gemeinsame Zeit am AWI bedanken.

Meinen Eltern, Schwiegereltern und meinem Bruder danke ich für ihre endlose Unterstützung, auch wenn ihr keine Ahnung habt, was ich hier eigentlich mache – ihr habt meine Entscheidungen nie hinterfragt und mir immer den Rücken gestärkt. Auch wenn du, Ötti, diese Zeilen nicht mehr lesen wirst – leider werde ich nicht zu Dr. Lamping, aber Dr. Steinberg klingt doch auch nicht schlecht.

Jan, seit fast 16 Jahren bist du an meiner Seite, hast meine gesamte Geo-Laufbahn mit all ihren Höhen und Tiefen miterlebt. Ich bin dir unglaublich dankbar, dass du mich gelehrt hast, was im Leben wirklich zählt, mich in allem unterstützt, was ich mir in meinen Kopf setze, und immer bedingungslos für mich da bist.



# Content

|  |     |
|--|-----|
| Abstract   | I   |
| Zusammenfassung  | III |
| Danksagung   | V   |
| 1 Introduction   | 1   |
| 1.1 Polar regions in a warming world   | 1   |
| 1.2 Southern Ocean sea ice   | 2   |
| 1.3 West Antarctica  | 7   |
| 1.3.1 Modern oceanographic setting   | 7   |
| 1.3.2 Key areas of ice loss  | 9   |
| 1.4 Assessing past sea-ice conditions  | 10  |
| 1.4.1 Common sea-ice proxies   | 10  |
| 1.4.2 Biomarkers for environmental reconstructions   | 12  |
| 2 Objectives and concept of this thesis  | 16  |
| 2.1 Declaration of author's contribution   | 17  |
| 3 Materials and methods  | 20  |
| 3.1 Material   | 20  |
| 3.2 Organic geochemical analysis   | 22  |
| 3.2.1 Organic bulk parameter analysis  | 22  |
| 3.2.2 Biomarker analysis   | 22  |
| 3.3 Additional data sets   | 26  |
| 4 Study No. 1: Evaluation of lipid biomarkers as proxies for sea ice and ocean temperatures along the Antarctic continental margin | 29  |
| 4.1 Introduction   | 30  |
| 4.2 Regional setting   | 34  |
| 4.3 Material and methods   | 36  |
| 4.3.1 Sediment samples   | 36  |
| 4.3.2 Bulk sediment and organic geochemical analyses   | 36  |
| 4.3.3 Numerical model  | 39  |
| 4.3.4 Satellite SIC and SSTs   | 40  |
| 4.4 Results and discussion   | 41  |
| 4.4.1 TOC content, HBIs and sterols in Antarctic surface sediments   | 41  |
| 4.4.2 Combining individual biomarker records: the PIPSO <sub>25</sub> index  | 45  |
| 4.4.3 Biomarker-based sea ice estimates vs. satellite and model data   | 47  |
| 4.4.4 TEX <sub>86</sub> <sup>L</sup> - and RI-OH <sup>P</sup> -derived ocean temperatures  | 49  |
| 4.5 Caveats and recommendations for future research  | 54  |
| 4.5.1 Age control  | 54  |

|       |  |     |
|-------|--|-----|
| 4.5.2 | Production and preservation of biomarkers  | 55  |
| 4.5.3 | The role of platelet ice for the production of IPSO <sub>25</sub>  | 57  |
| 4.6   | Conclusions  | 59  |
| 4.7   | Supplements  | 61  |
| 5     | Study No. 2: High-resolution reconstruction of early Holocene sea-ice and productivity fluctuations in the eastern Amundsen Sea Embayment: from a polynya to a sea-ice dominated setting     | 72  |
| 5.1   | Introduction   | 73  |
| 5.2   | Regional setting   | 75  |
| 5.3   | Material and methods   | 77  |
| 5.3.1 | Sediment samples and radiocarbon chronology  | 77  |
| 5.3.2 | Bulk sediment and lipid biomarker analyses   | 77  |
| 5.4   | Results  | 79  |
| 5.4.1 | Lithological succession  | 79  |
| 5.4.2 | Biomarker data   | 83  |
| 5.5   | Paleoenvironmental reconstructions   | 85  |
| 5.5.1 | Unit I – polynya dynamics  | 85  |
| 5.5.2 | Unit II – increased sea-ice cover  | 86  |
| 5.5.3 | Unit III – maximum sea-ice cover   | 87  |
| 5.6   | Conclusions  | 88  |
| 6     | Study No. 3: Highly branched isoprenoids reveal onset of deglaciation followed by dynamic sea-ice conditions in the western Amundsen Sea, Antarctica   | 89  |
| 6.1   | Introduction   | 90  |
| 6.2   | Regional setting   | 93  |
| 6.3   | Material and methods   | 95  |
| 6.3.1 | Material   | 95  |
| 6.3.2 | Bulk sediment and biomarker analyses   | 96  |
| 6.3.3 | Diatom transfer function derived winter sea-ice concentrations   | 97  |
| 6.4   | Results and discussion   | 98  |
| 6.4.1 | Reconstruction of the paleoenvironment from proxies  | 98  |
| 6.5   | Applicability of the combined open-water phytoplankton biomarker and IPSO <sub>25</sub> approach   | 111 |
| 6.6   | Summary and conclusions  | 113 |
| 6.7   | Supplements  | 114 |
| 6.8   | Corrigendum to “Highly branched isoprenoids reveal onset of deglaciation followed by dynamic sea-ice conditions in the western Amundsen Sea, Antarctica” [Quat. Sci. Rev. 228 (2020) 106103] | 116 |
| 7     | Conclusions and outlook  | 119 |
| 8     | References   | 122 |

# 1 Introduction

## 1.1 Polar regions in a warming world

Climate changes - over time. Though, never has climate changed at such a rapid pace, a pace that is undoubtedly attributable to human activities. Since the industrialization in the 18<sup>th</sup> century, mankind and its polluting industries were (and still are) dependent on fossil fuels for transport, agriculture, heat supply... depleting natural resources irreversibly and unsustainably, leading us to the climate situation we are facing right now. Climate change is perceptible all over the world, while some countries are suffering from recurring heat waves and bushfires, others are afflicted by hurricanes and floods.

Polar regions react more amplified to climatic changes than any other region on Earth, i.e., Arctic temperatures – in places – quadrupled when compared to the global average (Intergovernmental Panel on Climate Change, 2023; Rantanen et al., 2022) and Arctic sea-ice extent has declined by about 4 % per decade annually (Vaughan et al., 2013). These alarming numbers have not only become an issue of public concern during the last decade, but also a central matter of climate research.

Due to the generally weaker polar amplification in Antarctica compared to the Arctic, changes in the Southern Hemisphere have not been in the focus of research for a long time. Indeed, since the beginning of satellite observations ~50 years ago, Antarctic sea-ice extent has shown an overall increase (e.g.; Vaughan et al., 2013), before it steadily started to diminish since 2017 to an historic low in Austral winter 2022/2023 (Parkinson, 2019; Purich & Doddridge, 2023; Zhang & Li, 2023). Future Antarctic sea-ice demise will likely be amplified by increasing atmospheric greenhouse gas concentrations (Collins et al., 2013). The loss of the circum-Antarctic sea-ice cover may lead to increasing disintegration of its fringing ice shelves, which in turn results in ice flow acceleration and grounding line retreat of Antarctica's hinterland ice sheets. It is estimated that this process may add as much as one meter to the global sea level by the end of this century (DeConto & Pollard, 2016). Studying Southern Ocean sea ice and improving our understanding of its interaction with the ocean, the atmosphere and the Antarctic ice sheet will lead to more precise simulations of Antarctica's response under future warmer-than-present conditions (e.g., Turner & Comiso, 2017). Owing to its geographical

location and difficult accessibility due to extensive sea-ice cover and extremely harsh environmental conditions, scientific research in Antarctica, however, lags behind that of other regions. Missing proxy-based data hamper the progress of model simulations in resolving sea-ice changes – predicting the future behavior of Antarctica’s sea ice and ice sheets and their role in our climate is hence difficult but essential.

## 1.2 Southern Ocean sea ice

Antarctica is Earth’s southernmost continent and covered by an up to 4 km-thick ice sheet that is surrounded by the most prominently changing feature on Earth – the Antarctic sea ice belt (Thomas, 2017). The pronounced seasonal variability of incoming solar radiation in high latitudes causes sea-ice to melt during the Austral summer. Vice versa, cold temperatures and strong winds favor the formation of a slushy sea surface layer known as frazil ice (Thomas, 2017), which precedes strong circum-Antarctic sea-ice growth during the winter season. After further consolidation, first-year ice is formed, the most common constituent of Southern Ocean sea ice, with thicknesses of 0.5 – 0.6 m (Wadhams, 2000). The sea-ice extent, therefore, undergoes a strong natural interannual variability, usually reaching its maximum extent during September and minimum extent during February (Fig. 1.1).

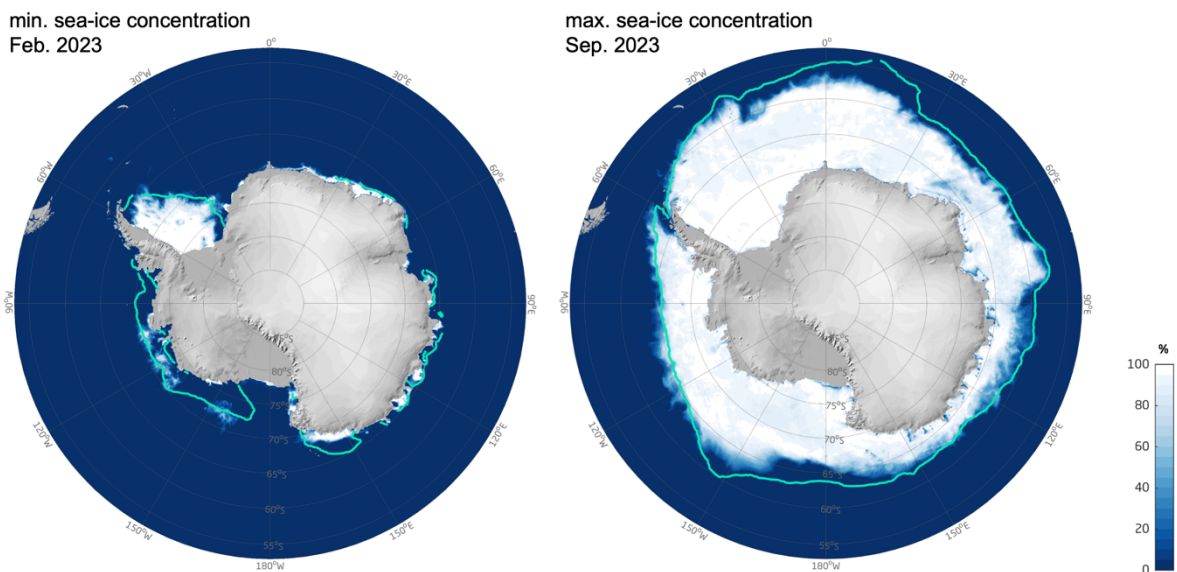


Fig. 1.1: Minimum and maximum sea-ice concentrations (in %) around Antarctica in February (left) and September 2023 (right), respectively. Turquoise lines show average sea-ice extent from 1981-2010 (obtained from NSIDC). Average sea-ice extent in February 2023: 2.15 Mio. km<sup>2</sup> and in September 2023: 16.92 Mio. km<sup>2</sup>. Data derived from NASA’s AMSR2 satellite instruments and downloaded from [www.meereisportal.de](http://www.meereisportal.de) (Spreen et al., 2008; last accessed: Dec. 27, 2023).



The pattern of total Antarctic sea-ice growth and decay is highly asymmetric, with a slow build-up and rapid decay nearly twice as fast (Fig 1.2; Eayrs et al., 2020; Gordon, 1981). The long-term trend of sea-ice coverage is recorded by regular satellite passive microwave observations since its advent in 1978. The  $\sim 45$ -year satellite record exhibits an increasing trend in total annual mean Antarctic sea-ice extent of about 1.5 % per decade, a trend that seems counter-intuitive to what is expected in a warming world. This gradual but uneven sea-ice increase was observed until a record high was reached in 2014, followed by a precipitous decline in the following years and reaching successive February minimum extents of 2.049 Mio. km<sup>2</sup> in 2017, 1.965 Mio. km<sup>2</sup> in 2022 (Raphael & Handcock, 2022) and 1.02 Mio. km<sup>2</sup> in 2023 (Purich & Doddridge, 2023).

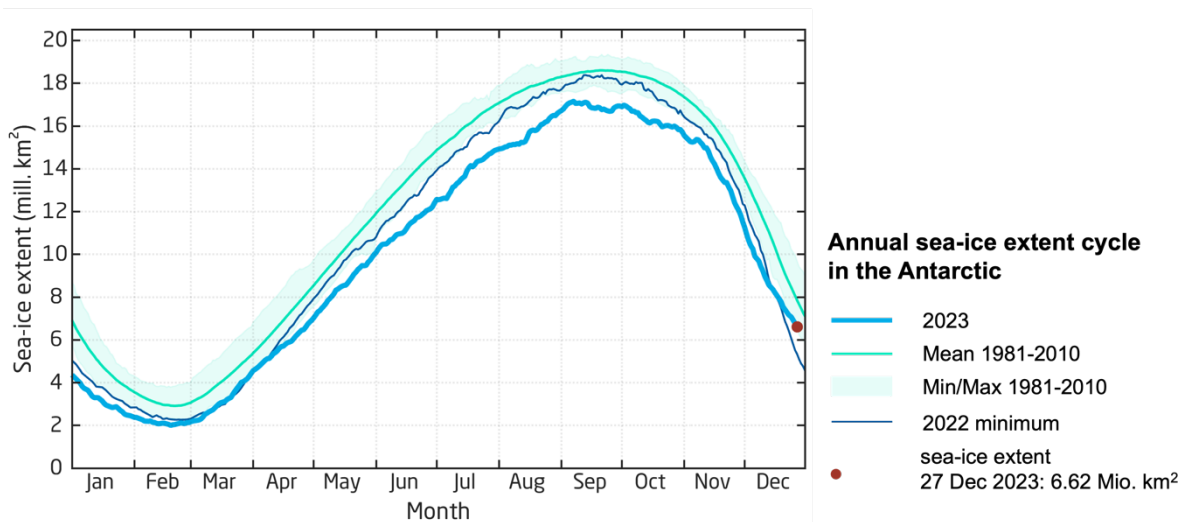


Fig. 1.2: Annual cycle of sea-ice extent in the Antarctic (in Mio. km<sup>2</sup>). 2023 sets a new pronounced record minimum since the beginning of recording in 1981.

Still, the overall trend in total averaged sea-ice extent is positive, although well reduced from the 2014-2023 values (Parkinson, 2019; Purich & Doddridge, 2023; Raphael & Handcock, 2022), yet veils stark regional contrasts. The Southern Ocean sea-ice regime can be divided into areas of sea-ice growth and sea-ice loss in direct adjacency (Massom et al., 2013; Schemm, 2018). While the small, but statistically significant sea-ice increases characterize most of the East Antarctic waters, such as the Weddell Sea, the Indian Ocean, the Western Pacific Ocean and the Ross Sea, the Bellingshausen and Amundsen Seas in West Antarctica exhibit a strong downward trend in yearly ice extents of  $-2.5\% \pm 1.2$  in the 40-year record (Fig. 1.3; Parkinson, 2019).

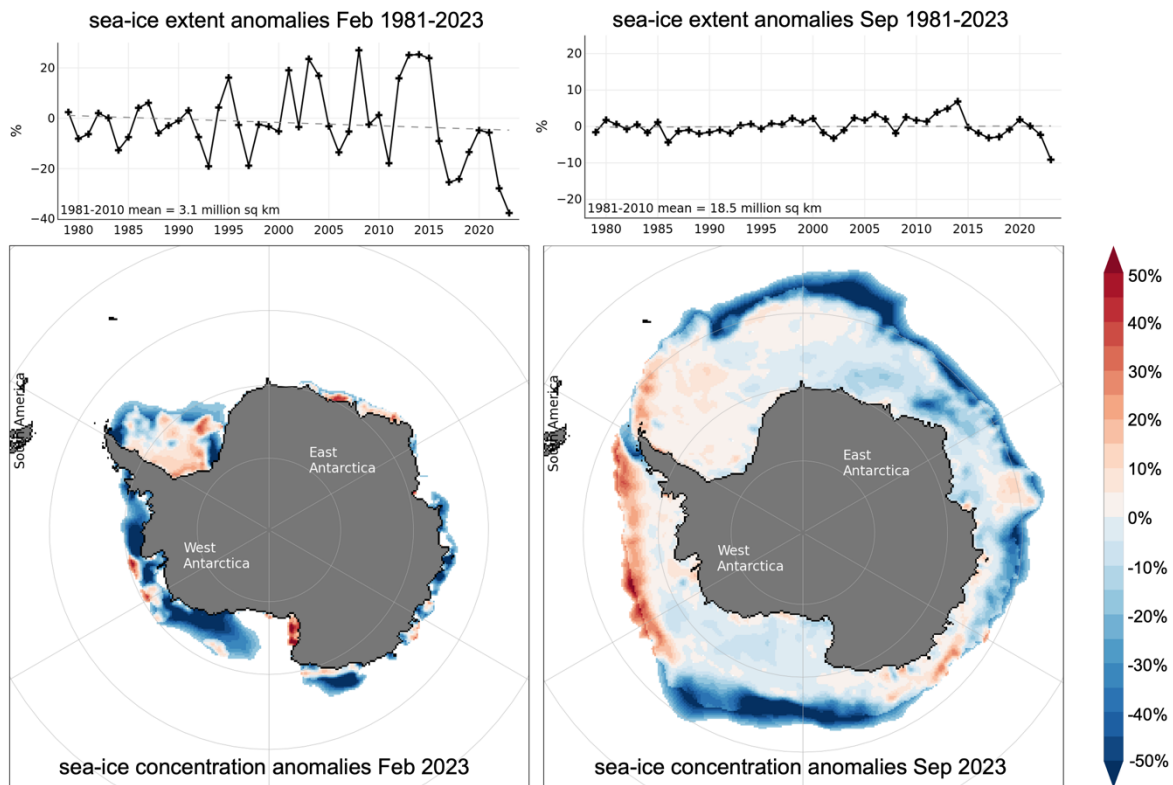


Fig. 1.3: Sea-ice concentration anomalies for Feb 2023 (lower left) and Sep 2023 (lower right) and mean sea-ice extent anomalies for Feb 1981-2023 (upper left) and Sep 1981-2023 (upper right). Graphs and maps downloaded from NSIDC (last accessed: 28 Dec 2023).

Which primary mechanisms control these stark regional differences of Antarctic sea-ice distribution is still debated, but a variety of suggested explanations have been proposed, all of them linked to the atmosphere-ocean-ice system of the Southern Ocean. Atmospheric forcings, such as changes in the Southern Annular Mode or the Amundsen Sea Low, are regarded as main drivers of sea-ice variability and trends in the Southern Ocean (Hobbs et al., 2016). Meridional winds, directed by these drivers, advect moist and warm air from lower latitudes or dry and cold air from the continent, influencing sea-ice motion, formation and melt (Hobbs et al., 2016). Another key component of sea-ice variability is oceanic forcing, such as freshening from West Antarctic Ice Sheet (WAIS) melt and ocean warming (Hobbs et al., 2016).

Southern Ocean sea ice is not only affected by regional climate change, but also affects Earth's climate by interacting with the ocean and atmosphere as a physical barrier between the two (Fig. 1.4; Wadhams, 2000), i.e., limiting gas, heat and moisture exchange and thereby reducing evaporation and hampering wind-induced mixing of surface waters (Dieckmann & Hellmer, 2009). Hence, sea ice may not only control regional atmospheric

circulation patterns, but its high albedo (50-90 %; Curry et al., 1995; Key et al., 2001; Zhou et al., 2019) also reduces solar heat uptake of the ocean, thereby regulating its energy budget (Curry et al., 1995; Hall, 2004). In a warmer climate with retreating sea ice, ocean surfaces which are much less reflective are exposed, initiating a positive feedback mechanism (Hall, 2004). Moreover, the formation of sea ice is one of the driving processes for the production of Antarctic Bottom Water (AABW). Brine rejection associated with sea-ice formation affects local vertical water mass movement leading to the densification and downward convection of shelf waters contributing to AABW. Through this deep-water formation process, sea ice influences the global thermohaline circulation (Nicholls et al., 2009). The broad shelves of the Weddell and Ross Seas are regarded as the main locations where waters are formed that are sufficiently

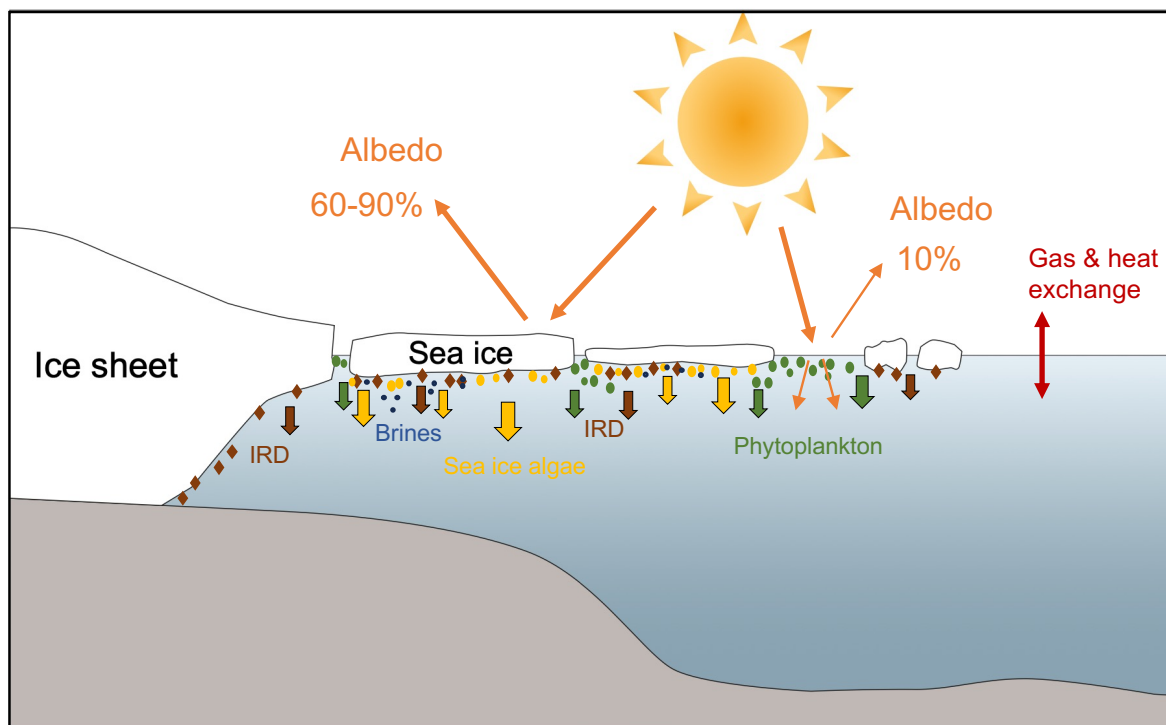


Fig. 1.4: Feedback mechanisms associated with the presence or absence of sea ice. Modified after Stein (2019).

dense to contribute to AABW production. Due to their higher density, brines that are released into the water column also build local barriers that hamper incursions of relatively warmer modified Circumpolar Deep Water (CDW) masses from entering sub-ice shelf cavities. Consequently, basal melting of ice shelves is minimized in regions of active sea-ice formation (Hellmer et al., 2012). Sea ice may therefore indirectly protect ice shelves, which in turn buttress the WAIS. Since the WAIS is currently Antarctica's

main contributor to global sea-level rise, with  $\sim 4.5$  cm per century, the presence or absence of Southern Ocean sea ice plays a critical role in the WAIS' future ice loss and thus global sea-level rise.

Furthermore, Southern Ocean sea ice represents one of the largest and most dynamic ecosystems on Earth by providing a habitat for some specialized (sympagic) algae living within or at the bottom of the ice (e.g., Arrigo et al., 1997). The melting of sea ice in spring releases 1) fresh water that supports the stratification of the ocean and 2) nutrients that initiate algae growth. In the brine filled channels at the bottom of the melting sea ice, ice algae (mainly composed of diatoms) grow and form a bottom ice algae layer. Such ice algae blooms rely on the increase of sunlight during spring and the light penetration is dependent on the thickness of the sea ice and its snow cover. The ice algae not only contribute to the primary production of the Southern Ocean but also form the basis for the marine food web (Arrigo & Thomas, 2004), contributing to the algal biomass and the biological carbon pump, driving the long-term sequestration of  $\text{CO}_2$  in the Southern Ocean (Falkowski et al., 1998). The cold Southern Ocean is hence an important sink for anthropogenic carbon (Frölicher et al., 2015; Orsi et al., 1999). Most of the uptake occurs north of the sea-ice zone, but in the south, sea ice regulates the rate of deep-water upwelling, and hence limits  $\text{CO}_2$  outgassing (Frölicher et al., 2015).

### 1.3 West Antarctica

#### 1.3.1 Modern oceanographic setting

The Southern Ocean is characterized by the Antarctic Circumpolar Current (ACC) – with up to  $136 \pm 7.8$  Sv (Cunningham et al., 2003) world’s largest current system circulating the globe. A strong wind-driven eastward flow connects all major ocean basins. The northern boundary of the ACC, the Subtropical Front (STF), reaches – in places – as far north as  $35^\circ\text{S}$ . It encircles Antarctica on its  $\sim 24\,000$  km-long path, with depths varying between 2000 – 4000 m (Whitworth III, 1988). The narrowest constriction of the ACC is the permanently ice-free Drake Passage, located between the southern tip of South America and the Antarctic Peninsula.

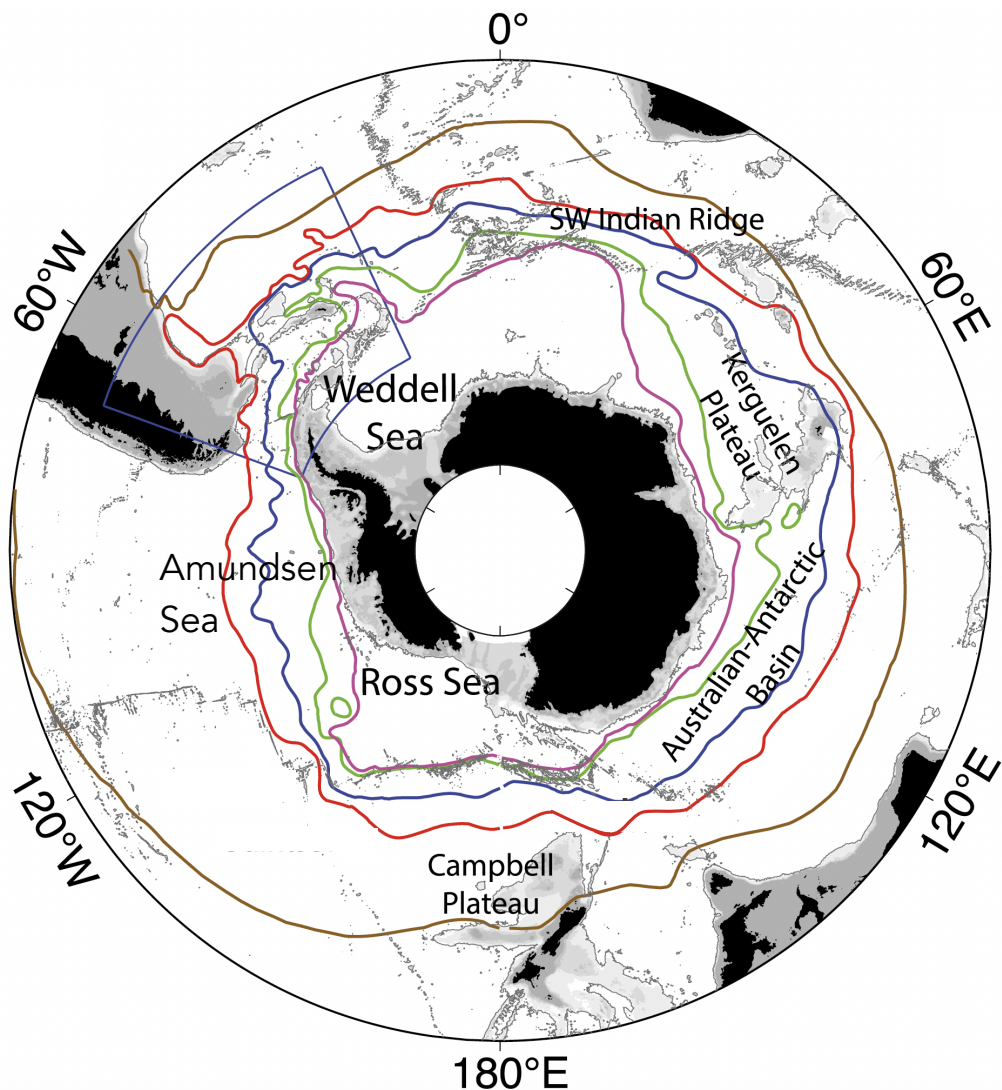


Fig. 1.5: Zones and fronts in the Southern Ocean; colored lines are locations from Orsi et al. (1995). Subtropical front (STF; tan), SAF (red), PF (blue), sACCf (green) and SBdy (magenta); frontal zones are separated by these fronts. Modified after Kim and Orsi (2014).

The ACC acts like an insulation between the warm subtropics and the cold South Polar region characterized by three major frontal systems, i.e., the STF, the Subantarctic Zone (SAZ), the Subantarctic Front (SAF), the Polar Frontal Zone (PFZ), the Polar Front (PF), the Antarctic Zone, the southern ACC Front (sACCf) and the Southern Boundary of the ACC (SBdy) (Fig. 1.5). Those fronts are characterized by prominent and sudden changes in water properties over short distances. The circum-Antarctic extent of the ACC and location of different fronts is visualized in Fig. 1.5. At locations where the ACC is located sufficiently far from the Antarctic Continent, cyclonic cells of recirculating waters develop further poleward, south of the sACCf. Those subpolar cyclonic circulations have been identified in the Weddell and Ross Seas (Fig. 1.5), known as the Weddell and Ross gyres (Orsi et al., 1995). The Weddell Gyre is a large, elongated clockwise circulation and thereby accounts for a significant northward sea-ice drift in the western part of the Weddell Sea along the coast of the East Antarctic Peninsula (Harms et al., 2001). Furthermore, the Weddell Sea represents a major ventilation area of the global ocean since precursors of the coldest and densest bottom water mass, AABW, are formed here (Harms et al., 2001).

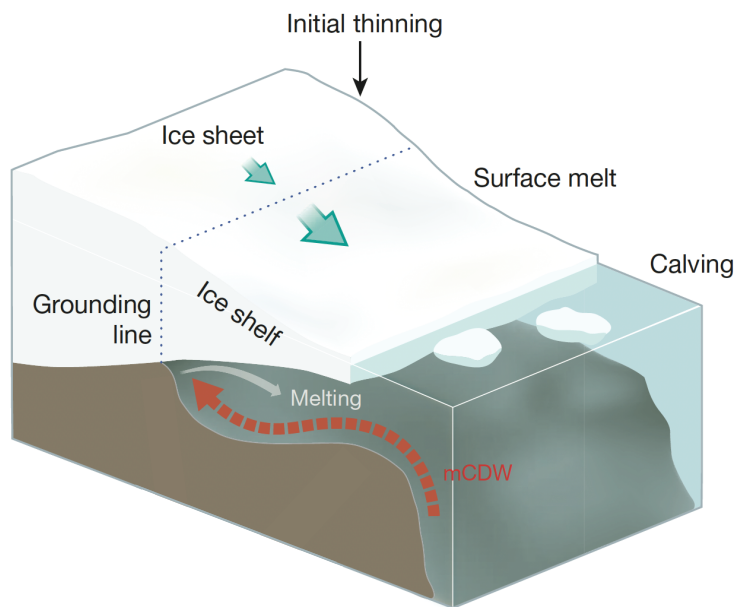


Fig. 1.6: Illustration of the mechanisms occurring during the basal melting at the base of a West Antarctic ice shelf, induced by the inflow of CDW onto the continental shelf. Modified after Hanna et al. (2013).

At locations, where the ACC flows proximal to the continental shelf edge, in the Amundsen Sea, the Bellingshausen Sea and at the West Antarctic Peninsula, relatively warm CDW is branching off and upwelling onto the shelf via subglacially eroded paleo-

ice stream troughs, now exposed on the continental shelf as prominent bathymetric troughs. In locations, where the CDW reaches the ice sheet grounding line, it considerably contributes to the melting of the floating ice shelves from below. This process is regarded as the key driver for the observed elevated melt rates of glaciers in the Amundsen Sea and Bellingshausen Sea (Fig. 1.6; Jacobs et al., 2011; Jenkins & Jacobs, 2008; Klinck et al., 2004).

### 1.3.2 Key areas of ice loss

West Antarctica is widely regarded as the Achilles heel of Antarctic Ice Sheet stability. The Transantarctic Mountains separate the Antarctic Ice Sheet into two distinct parts. While the East Antarctic Ice Sheet (EAIS) mainly sits on continental crust above sea level, much of the grounded ice of the marine-based WAIS lies on a bed many hundreds of meters below sea level. The continental shelves off West Antarctica deepen inland and are hence much more vulnerable to oceanic and atmospheric warming. The floating

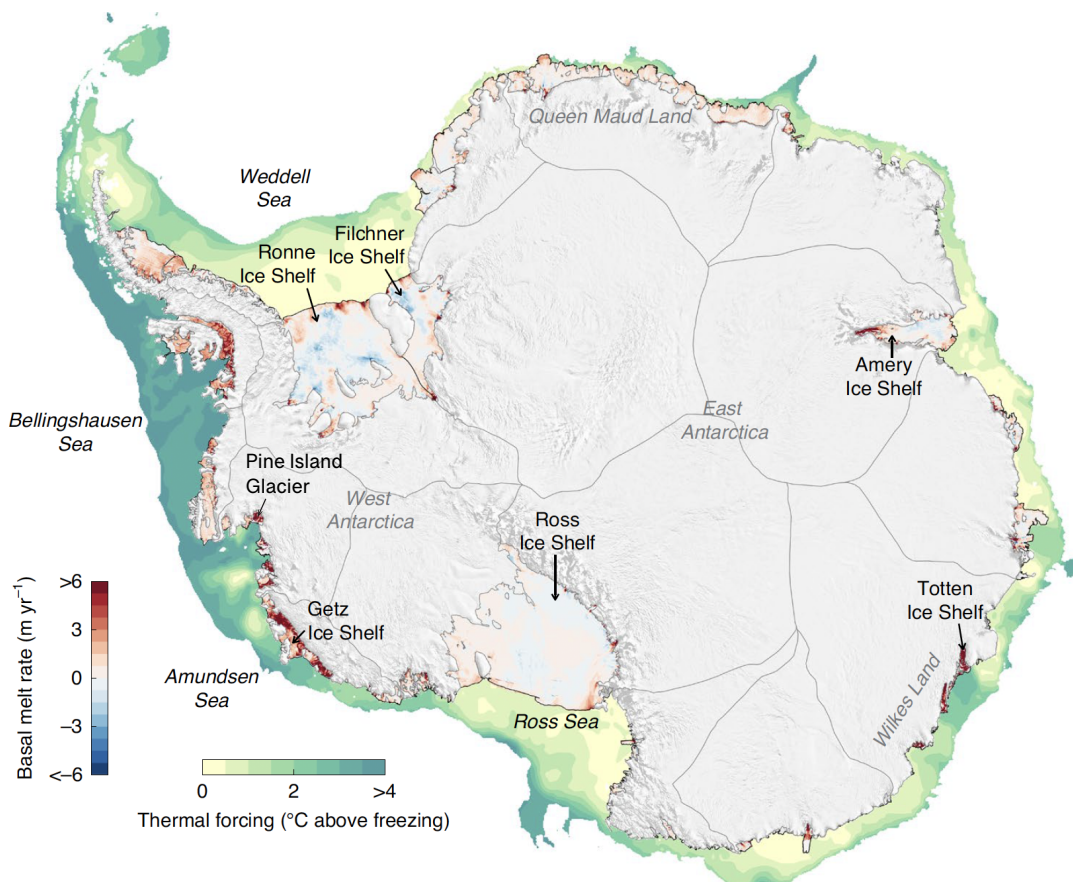


Fig. 1.7: Basal melt rates [m yr<sup>-1</sup>] of Antarctic ice shelves, averaged over 2010-2018, based on estimates from CryoSat-2 altimetry. Modified after Adusumilli et al. (2020).

ice shelves, fed by the inland ice and draining the WAIS, are either losing mass by iceberg calving or by oceanic forcing (Lythe & Vaughan, 2001). Around West Antarctica, basal melt is highest at the Antarctic Peninsula and on the warm-water shelves in the Amundsen and Bellingshausen seas, consistent with the high thermal forcing values above freezing (up to  $> 4$  °C; Fig. 1.7), and reach melt rates up to  $6 \text{ m yr}^{-1}$  (Adusumilli et al., 2020). The inherently unstable WAIS is particularly susceptible to potential collapse. Beside the various atmospheric and anthropogenic forcing parameters, the oceanographic forcing on the stability of the WAIS is one of the key components. One crucial parameter is the presence or absence of sea ice with its several feedback mechanisms described previously. To expand our knowledge about the past, the recent and the future evolution of sea ice and the role it plays, not only in the stability of the WAIS, but also in the global climate system, a wide spectrum of data from several disciplines is required.

#### 1.4 Assessing past sea-ice conditions

Since the beginning of satellite observations in 1979, satellite sea-ice records enable us to accurately assess the variability of Antarctic sea-ice conditions. To gain a longer term understanding of the evolution of Antarctic sea-ice, on centennial to millennial timescales, an array of geochemical, sedimentological and microfossil parameters are common tools used in paleoceanographic studies around Antarctica. These paleo-climate data are pivotal for documenting the natural variability of sea ice, its feedback mechanisms on other climatic components and its drivers. Collecting as many observational data as possible will continuously enhance the performance of numerical climate models, which currently still struggle to evaluate whether observed changes in sea-ice cover undergo natural climate variability or are driven by anthropogenic forcing (Eayrs et al., 2021; Hobbs et al., 2015; Jones et al., 2016).

##### 1.4.1 Common sea-ice proxies

A direct signal for an ice cover is provided by ice rafted detritus (IRD), fine ( $>40 \mu\text{m}$ ) or coarse ( $>500 \mu\text{m}$ ) lithogenic particles, which are frequently used in sedimentological studies and allow, by means of mineralogical analyses of the lithogenic particles, a



provenance assessment. While ice drift pathways can be reconstructed with this proxy, it is limited in its capability of distinguishing between sea ice and iceberg transport, offering only ambiguous signals in this regard (e.g., St. John, 2008 and Darby and Bischof, 2004). Another common proxy for Antarctic sea-ice reconstructions and sea surface temperatures (SSTs) are diatoms preserved in marine sediments. The biogeographic distribution patterns of diatom assemblages are related to surface water temperatures, which, on the one hand, makes them a powerful tool for reconstructing past SSTs (Armand et al., 2017). On the other hand, specific diatom species living at the sea-ice edge or attached to sea ice are useful proxies for sea-ice reconstructions (Allen et al., 2011; Armand and Leventer, 2003; Crosta et al., 1998; Esper and Gersonde, 2014a; Gersonde and Zielinski, 2000; Leventer, 1998). However, a critical drawback of these fragile and only lightly silicified diatoms is their limited preservation ability. Dissolution effects on biogenic silica ( $\text{SiO}_2$ ) within the water column or after deposition may alter the assemblage record, leading to erroneous reconstructions (Fig. 1.8; Leventer, 1998; Zielinski et al., 1998).

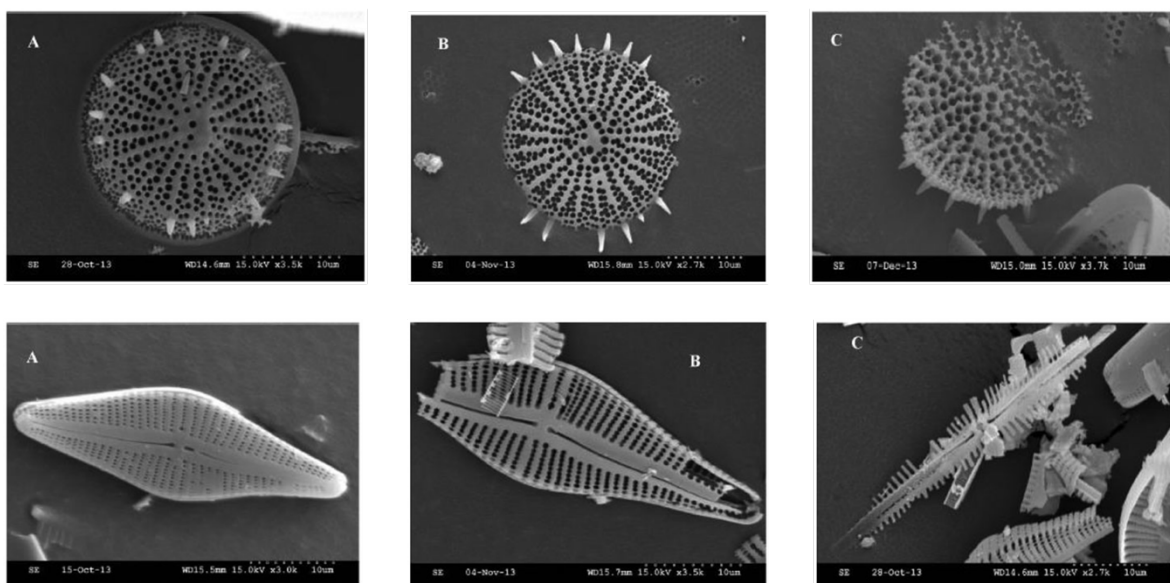


Fig. 1.8: Dissolution effects on diatom frustules with good preservation to the left and major dissolution on the right. Upper panel: *Stephanodiscus formosus* var. *minor*, lower panel: *Gomphocymbella* spp. Modified from Smith et al. (2016).

Other microfossils, such as sea-ice associated foraminifers (and their  $\delta^{18}\text{O}$  signal), which may represent ideal direct ice markers for sea-ice presence, may succumb carbonate dissolution effects and hence face the same limitations than diatom assemblages. Bulk proxies, such as  $\text{CaCO}_3$  and TOC, work as an indirect indicator of

past sea-ice occurrences. High sedimentary contents of these proxies may point to ice free conditions, while low contents may indicate a high sea-ice coverage, regarding the favorable growth environment of the producing phytoplankton, which usually thrives under ice-free conditions at the sea surface. Another way of estimating past sea-ice conditions is by evaluating chemical tracers incorporated in Antarctic ice cores. Particularly useful for sea-ice reconstructions are the aerosols sea salt sodium, methane sulfonic acid, bromine and iodine. For each proxy applies, the prevailing sea-ice conditions influence the region's atmosphere, which is reflected in the composition of snow subsequently archived in the ice core (Crosta et al., 2022).

#### 1.4.2 Biomarkers for environmental reconstructions

##### *Reconstructing (paleo-) sea-ice conditions - the sea-ice biomarker IPSO<sub>25</sub>*

A rather recently identified tool for past sea-ice reconstructions are organic molecules that belong to the group of highly branched isoprenoids (HBIs), which are omnipresent in marine sediments and mainly biosynthesized by diatoms (Belt et al., 2000; Rowland & Robson, 1990). The number of double bonds (the degree of unsaturation) in HBI alkenes is supposed to be dependent on the growth temperature, with higher unsaturated HBIs being produced at relatively high temperatures (up to 25 °C) and HBIs with less double bonds being biosynthesized at relatively lower temperatures (0-5 °C; Rowland et al., 2001). In 2007, Belt et al. (2007) introduced a highly branched, mono-unsaturated C<sub>25</sub> isoprenoid alkene as the new sea-ice proxy IP<sub>25</sub> (Fig. 1.9; **I**ce **P**roxy with **25** carbon atoms) for the Arctic. Next to its single double bond, various indicators pointed to an ice-related origin, such as the absence of IP<sub>25</sub> in open-water phytoplankton samples as well as its isotopic <sup>13</sup>C signature determined in sediment and sea-ice samples (Belt et al., 2008; Brown, 2011). In 2014, the Arctic sympagic diatoms *Haslea crucigeroides/spicula* and *Pleurosigma stuxbergii var. rhomboides* were identified as source organisms of IP<sub>25</sub> (Brown et al., 2014). In 2011, Massé et al. proposed that the structurally closely related HBI C<sub>25:2</sub> diene could serve as Antarctic counterpart for sea-ice reconstructions but the source organism remained unidentified until 2016, when Belt et al. documented the sympagic diatom *Berkeleya adeliensis* as the source of the HBI C<sub>25:2</sub> diene. *Berkeleya adeliensis* lives in platelet, landfast and bottom ice in the coastal regions of Antarctica (Riaux-Gobin & Poulin, 2004). In analogy to the sea-ice proxy IP<sub>25</sub> for the Arctic, the term IPSO<sub>25</sub> (**I**ce

Proxy of the Southern Ocean with 25 carbon atoms) was given for the southern sea-ice proxy (Belt et al., 2016).

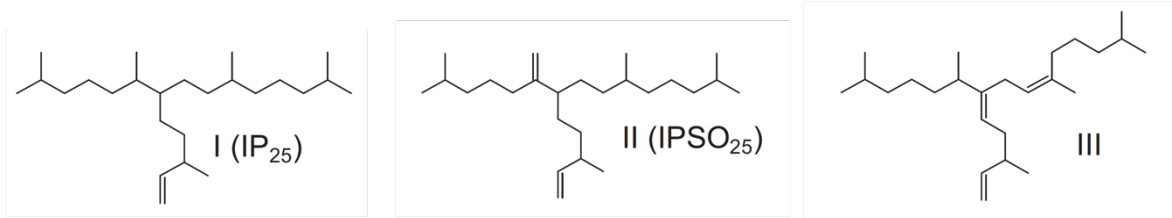


Fig. 1.9: Chemical structures of the highly branched isoprenoids mono-unsaturated IP<sub>25</sub>, di-unsaturated IPSO<sub>25</sub>, and tri-unsaturated HBI III (triene).

So far, only a limited number of studies were performed to investigate the spatial distribution and the applicability of the novel sea-ice proxy for the Southern Ocean (Belt et al., 2018; Massé et al., 2011; Smik et al., 2016b; Vorrath et al., 2019; Vorrath et al., 2020) but it presents a promising approach for (paleo-) sea-ice reconstructions. A critical factor that needs consideration when applying IPSO<sub>25</sub>, is the absence of the sea-ice biomarker in a sediment sample, which may result from either ice-free conditions or a heavy perennial sea-ice and/or ice shelf cover. Both scenarios inhibit ice algae productivity due to a lack of light availability for the photosynthesizing organisms. To circumvent any misinterpretations, tri-unsaturated C<sub>25</sub>-HBI alkenes (*Z*-Trienes and/or *E*-Trienes), which are mostly biosynthesized by open ocean diatoms such as *Rhizosolenia* spp. (Belt et al., 2017), are considered alongside the sea-ice proxy for a semi-quantitative approach. Following the PIP<sub>25</sub> approach for the Arctic introduced by Müller et al. (2011), the ratio of IPSO<sub>25</sub> to the sum of IPSO<sub>25</sub> and an open-water phytoplankton biomarker has recently been proposed as the PIPSO<sub>25</sub>-index by Vorrath et al. (2019):

$$\text{PIPSO}_{25} = \text{IPSO}_{25} / (\text{IPSO}_{25} + (\text{phytoplankton marker} \times c)),$$

with *c* (*c* = mean IPSO<sub>25</sub> concentration/mean phytoplankton marker concentration) being a balance factor to compensate for concentration differences between IPSO<sub>25</sub> and the phytoplankton marker.

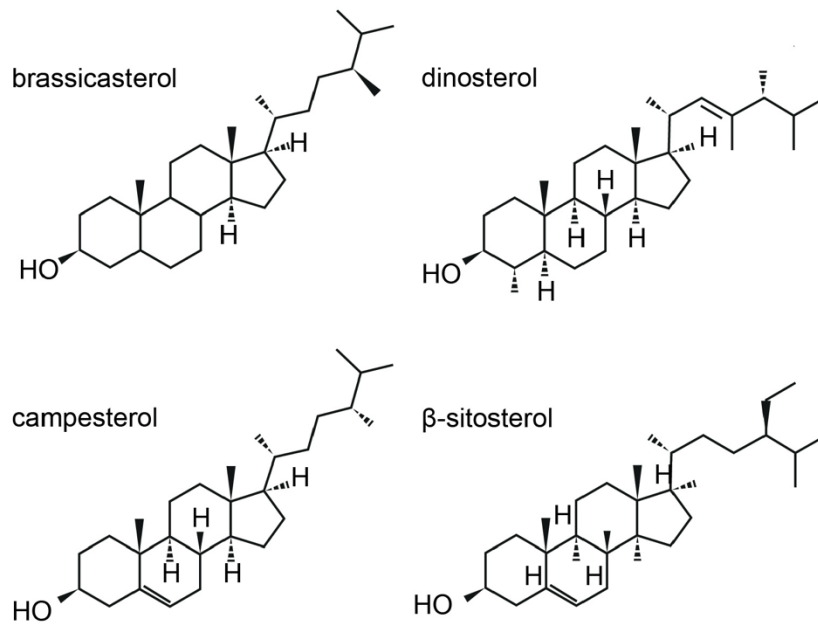


Fig. 1.10: Chemical structures of brassicasterol, dinosterol, campesterol and  $\beta$ -sitosterol.

For the calculation of the PIPSO<sub>25</sub>-index, not only HBI trienes can be used as open-water phytoplankton marker. The phytosterols brassicasterol (i.e., P<sub>B</sub>IPSO<sub>25</sub>; Fig. 1.10) and dinosterol (i.e., P<sub>D</sub>IPSO<sub>25</sub>; Fig. 1.10) provide an additional option, although their source is not as specific as of HBI-trienes, since they are produced by a variety of organisms, such as dinoflagellates, haptophytes and diatoms (Boon et al., 1979; Volkman et al., 1998). Hence, the sedimentary signal of the sterols may reflect variable environmental conditions, which may pose uncertainties when interpreting the resulting PIPSO<sub>25</sub>-indices.

### *Reconstructing (paleo-) SST*

Biomarker-based SST reconstructions in tropical and temperate regions are commonly carried out by using the isoprenoidal GDGT (glycerol dialkyl glycerol tetraether) – based TEX<sub>86</sub> index (Schouten et al., 2002). However, isoGDGTs tend to inaccurate results when influenced by colder water masses (Huguet et al., 2008; Kim et al., 2008; Schouten et al., 2013). Kim et al. (2010) have hence developed a modified TEX<sup>L</sup><sub>86</sub>-index explicitly designed for reconstructing colder SSTs below 15 °C, which applies a different GDGT combination:

$$\text{TEX}_{86}^L = \text{LOG} \frac{[\text{GDGT-2}]}{[\text{GDGT-1}] + [\text{GDGT-2}] + [\text{GDGT-3}]}$$

$$\text{SOT}^{\text{TEX}} [^{\circ}\text{C}] = 50.8 * \text{TEX}_{86}^L + 36.1.$$

A few years later, Liu et al. (2012) discovered that archaea adapt their membrane in cold waters by changing the number of rings and by adding hydroxyl groups. The number of their cyclopentane rings and the relative abundance of individual OH-GDGTs vary with their growth temperature (Fietz et al., 2013). Considering the OH-GDGTs, Lü et al. (2015) presented an SST proxy for the polar environment, the RI-OH':

$$\text{RI} - \text{OH}' = \frac{[\text{OH-GDGT-1}] + 2 * [\text{OH-GDGT-2}]}{[\text{OH-GDGT-0}] + [\text{OH-GDGT-1}] + [\text{OH-GDGT-2}]}$$

$$\text{SST}^{\text{OH}} [^{\circ}\text{C}] = (\text{RI} - \text{OH}' - 0.1) / 0.0382.$$

Park et al. (2019) and Varma et al. (2023) have further tested and evaluated the applicability of OH-GDGT based calibrations, supporting their capability of reconstructing temperatures in cold regions with temperatures below 15 °C and advocate the use of regional calibrations rather than a single global  $\text{TEX}_{86}^L$  calibration in these regions.

## 2 Objectives and concept of this thesis

The significance of sea ice for regional and global climate processes has increasingly gained attention among the climate research community. Reconstructions of its paleo-variability and its connection to specific climate conditions are attempted from different angles of various research areas. As described in chapter 1, the presence and distribution of Southern Ocean sea ice, especially on western Antarctic continental shelves, are critical determinants for the stability of Antarctic ice shelves. While experiencing natural variations, West Antarctica's sea-ice cover declined at an unforeseen rate during the last years, elevating the importance of a profound understanding of its interactions coupled to such changes. The novel sea-ice biomarker IPSO<sub>25</sub> constitutes the potential to identify and trace (paleo) sea-ice coverage in the Southern Ocean. To test whether IPSO<sub>25</sub> can be considered as a similar promising tool for sea-ice reconstructions than its counterpart IP<sub>25</sub> for the Arctic, the proxy needs thorough evaluation on its applicability, its function as paleo sea-ice tracer, but also on its limitations and caveats to be considered when applying the proxy. The West Antarctic continental shelves, and especially the Amundsen Sea continental shelf, serve as ideal study areas to test the proxy's accuracy since these regions experience the most severe sea-ice decline compared to any other region around Antarctica. Accordingly, the studies on IPSO<sub>25</sub> presented in this thesis serve as an evaluation of the sea-ice proxy and provide new insights into its specific applicability for paleo-environmental reconstructions in the Southern Ocean.

The overarching objectives of the three studies within this thesis were:

*Study No 1:* The evaluation of the applicability of IPSO<sub>25</sub> as sea-ice proxy and of GDGTs as temperature proxies on West Antarctic continental shelves.

For this purpose, seafloor surface sediments from the eastern and western Antarctic Peninsula, the Amundsen and Weddell seas were analyzed to find answers to the questions:

- Does IPSO<sub>25</sub> depict recent sea-ice conditions in the study areas?
- Can GDGTs serve as temperature indicators?
- Is the PIPSO<sub>25</sub> approach a suitable tool for semi-quantitative sea-ice reconstructions?

- Is it possible to give a statement about the source organisms of IPSO<sub>25</sub> and their habitat?

*Study No. 2:* The first biomarker-based reconstruction of paleo sea-ice evolution in the eastern Amundsen Sea using the PIPSO<sub>25</sub> approach.

A high-resolution sediment core from the eastern Amundsen Sea Embayment (ASE) was analyzed to further apply the PIPSO<sub>25</sub> approach in a multiproxy study to find answers to the questions:

- Is it possible to use the PIPSO<sub>25</sub> approach for Holocene sea-ice reconstructions in the Amundsen Sea?
- Are there feedbacks between sea-ice cover and ice sheet activity?
- Can we draw conclusions about oceanic forcings on sea ice and depict ice-free conditions?

*Study No. 3:* The first biomarker-based paleo sea-ice reconstructions in the western Amundsen Sea using the PIPSO<sub>25</sub> approach

The continued application of the PIPSO<sub>25</sub> approach on a sediment core from the western Amundsen Sea provided further insights into the suitability of the sea-ice proxy and helped address the following questions:

- How did the sea-ice cover change since the last deglaciation?
- How well do biomarker-based sea-ice reconstructions align with diatom-based sea ice-reconstructions?
- Are sea-ice changes connected to interhemispheric processes?

## 2.1 Declaration of author's contribution

This cumulative dissertation is based on two manuscripts that are published in peer reviewed journals under my maiden name (Lamping) and one manuscript that will be published in an appropriate scientific journal. Here, the author's contributions to the different studies are outlined.

*Study No. 1* Evaluation of lipid biomarkers as proxies for sea ice and ocean temperatures along the Antarctic continental margin

Authors: Nele Steinberg (Lamping), Juliane Müller, Jens Hefter, Gesine Mollenhauer, Christian Haas, Xiaoxu Shi, Maria-Elena Vorrath, Gerrit Lohmann, and Claus-Dieter Hillenbrand

Publication status: Published in the journal “Climate of the Past” as part of the special issue “Reconstructing Southern Ocean sea-ice dynamics on glacial-to-historical timescales” on 29 October 2021.

N. Steinberg (Lamping) and J. Müller conceived the experiment and designed the study. N. Steinberg (Lamping) carried out the TOC and biomarker analyses (HBIs, sterols, GDGTs). <sup>14</sup>C radiocarbon dating was performed in the MICADAS laboratory at AWI. N. Steinberg (Lamping) prepared the samples for radiocarbon dating. J. Müller performed quality control of the HBI and sterol data, J. Hefter performed quality control of GDGT data. C. Haas provided satellite sea-ice data. X. Shi and G. Lohmann provided numerical model data. M.-E. Vorrath provided PS111 surface sediment samples. In close cooperation with J. Müller, N. Steinberg (Lamping) interpreted the data and prepared the first version of the manuscript. J. Müller and C.-D. Hillenbrand improved the manuscript. All co-authors reviewed the final version of the manuscript and supported N. Steinberg (Lamping) during the peer-review process.

*Study No. 2* High-resolution reconstruction of early Holocene sea-ice and productivity fluctuations in the eastern Amundsen Sea Embayment: from a polynya to a sea-ice dominated setting

Authors: Nele Steinberg, Juliane Müller, Johann Philipp Klages, Claus-Dieter Hillenbrand

Publication status: in preparation for submission to a peer reviewed scientific journal.

N. Steinberg and J. Müller conceived the experiment and designed the study. N. Steinberg carried out the laboratory analyses on biomarkers (HBIs and sterols), TOC and CNS. <sup>14</sup>C radiocarbon dating was performed in the MICADAS laboratory at AWI. N. Steinberg prepared the samples for radiocarbon dating. J. Müller performed quality



control of the HBI and sterol data. In close cooperation with J. Müller, N. Steinberg interpreted the data and outlined the findings in a first draft of the manuscript. J. Müller, J. Klages and C.-D. Hillenbrand improved the manuscript. The final version of the manuscript will soon be prepared for submission to a peer reviewed scientific journal.

*Study No. 3* Highly branched isoprenoids reveal onset of deglaciation followed by dynamic sea-ice conditions in the western Amundsen Sea, Antarctica

Authors: Nele Steinberg (Lamping), Juliane Müller, Oliver Esper, Claus-Dieter Hillenbrand, James A. Smith, Gerhard Kuhn

Publication status: published in the journal “Quaternary Science Reviews” on 15 January 2020.

N. Steinberg (Lamping) and J. Müller set up the experimental design and formulated the concept of the study. N. Steinberg (Lamping) performed the laboratory analyses on HBIs and sterols, TOC and CNS. J. Müller carried out the quality control of the HBI and sterol data. Oliver Esper provided sea-ice concentration data based on diatom transfer functions. In collaboration with J. Müller, N. Steinberg (Lamping) interpreted the results and prepared the first version of the manuscript. J. Müller and C.-D. Hillenbrand improved the manuscript. All co-authors reviewed the final version of the manuscript and assisted N. Steinberg (Lamping) during the peer-review process.

### 3 Materials and methods

#### 3.1 Material

##### *Study No. 1: Surface sediment samples*

In total, 41 surface sediment samples (0-1 cm sub-bottom depth; Table 3.1), collected during several cruises of RV *Polarstern* to Antarctic continental shelves over the past 17 years, were investigated. The samples were retrieved using multicorer or giant box corers from the Amundsen Sea continental shelf (n=16; PS ANT-XXIII/4; PS104; Gohl, 2007, 2017) and from the southeastern and southwestern Weddell Sea continental shelf (n=25; PS111; PS118; Dorschel, 2019; Schröder, 2018). Previously published data by Vorrath et al. (2019) collected from the Bransfield Strait and the West Antarctic Peninsula (WAP) were used to complement the herein established dataset. Due to different sedimentation rates and possible bioturbation activity at the core sites, no precise age constrain could be provided for the investigated surface sediment samples - the samples could hence easily span decades to millennia. AMS  $^{14}\text{C}$  dating of calcareous microfossils and  $^{210}\text{Pb}$  dating of surface sediment samples from adjacent locations, however, document recent ages for most sites (for a more detailed description, see chapter 4.5.1).

Table 3.1: Station list of surface sediment samples investigated in Study No. 1. Station numbers in italic represent samples retrieved via a giant box corer, all other samples were retrieved using a multicorer.

| Station Nr.       | Long<br>[°E] | Lat<br>[°N] | Water Depth<br>[m] | Station Nr. | Long<br>[°E] | Lat<br>[°N] | Water Depth<br>[m] |
|-------------------|--------------|-------------|--------------------|-------------|--------------|-------------|--------------------|
| <i>PS69/255-3</i> | -104,36      | -71,80      | 640                | PS111_40-2  | -54,24       | -76,00      | 513                |
| <i>PS69/269-1</i> | -115,58      | -73,22      | 822                | PS111_42-1  | -53,36       | -76,14      | 493                |
| <i>PS69/272-3</i> | -118,48      | -73,89      | 1529               | PS111_47-2  | -60,00       | -74,98      | 660                |
| <i>PS69/275-2</i> | -117,55      | -73,89      | 1472               | PS111_53-3  | -54,12       | -76,03      | 497                |
| <i>PS69/283-5</i> | -115,38      | -72,76      | 588                | PS111_60-3  | -45,41       | -77,02      | 332                |
| <i>PS69/284-2</i> | -115,40      | -73,02      | 736                | PS111_70-2  | -33,65       | -76,11      | 794                |
| <i>PS69/288-3</i> | -102,99      | -74,42      | 742                | PS111_80-3  | -35,43       | -76,64      | 932                |
| <i>PS69/292-3</i> | -105,19      | -74,68      | 1113               | PS111_98-3  | -40,45       | -77,80      | 928                |
| <i>PS69/297-1</i> | -103,67      | -74,08      | 460                | PS111_114-3 | -33,93       | -76,38      | 839                |
| <i>PS69/299-1</i> | -103,65      | -73,44      | 685                | PS111_131-2 | -36,94       | -74,61      | 387                |
| <i>PS69/302-3</i> | -105,65      | -71,13      | 544                | PS111_139-2 | -25,28       | -74,82      | 663                |
| PS104_12-4        | -101,62      | -74,68      | 358                | PS118_5-3   | -57,75       | -64,98      | 428                |
| PS104_14-2        | -102,59      | -74,55      | 600                | PS118_8-4   | -55,90       | -63,98      | 414                |
| PS104_17-2        | -104,75      | -74,36      | 1395               | PS118_10-3  | -55,98       | -64,00      | 414                |
| <i>PS104_22-3</i> | -107,09      | -72,77      | 733                | PS118_12-2  | -55,74       | -63,81      | 455                |
| <i>PS104_43-3</i> | -112,33      | -73,30      | 482                | PS118_24-2  | -51,43       | -62,26      | 3289               |
| PS111_13-2        | -6,85        | -70,09      | 1775               | PS118_38-5  | -54,33       | -63,08      | 415                |
| PS111_15-1        | -15,78       | -71,67      | 1405               | PS118_48-2  | -51,13       | -61,57      | 2908               |
| PS111_16-3        | -17,82       | -72,38      | 1418               | PS118_62-3  | -46,56       | -60,93      | 329                |
| PS111_29-3        | -27,68       | -75,97      | 211                | PS118_75-1  | -49,65       | -60,85      | 2643               |

*Study No. 2: Sediment core PS104\_14-3 - eastern Amundsen Sea*

The investigated sediment core PS104\_14-3 was retrieved from the eastern Pine Island Bay (74.55°S, 102.59°W; 600 m water depth) during RV *Polarstern* expedition PS104 in 2017 (Gohl, 2017). The sediments were collected using a gravity corer with a recovery of 8.24 m. <sup>14</sup>C radiocarbon dating on benthic foraminifera revealed an early Holocene age of the sediments with very high sedimentation rates up to 1700 cm/ka. Due to the possible loss of the core top during the coring process and a lack of a reliable core top age, we assume that it may not reflect modern times. The data are plotted versus core depth, while the determined ages are indicated along the depth-axis. The lithological composition of the sediments allows a distinction of three different units. The oldest unit, Unit I, is characterized by laminated to stratified mud alternating with laminated to stratified gravelly sandy mud. Unit II consists predominantly of laminated mud, while Unit III (the youngest unit) is comprised of bioturbated mud with dispersed sand and gravel grains (IRD).

*Study No. 3: Sediment core PS69/274-1 - western Amundsen Sea*

The investigated sediment core PS69/274-1 was retrieved offshore from the westernmost Getz Ice Shelf from the western Amundsen Sea shelf (73.85°S, 117.78°W; 1452 m water depth) during RV *Polarstern* expedition ANT-XXIII/4 in 2006 (PS69; Gohl, 2007). The sediments were collected using a gravity core with a recovery of 4.51 m. Giant box core PS69/275-2 (73.89°S, 117.55°W; 1472 m water depth), located adjacent to PS69/274-1, provided an undisturbed surface sediment sample. Previously published radiocarbon ages of the acid-insoluble organic fraction (AIO) of the sediments and relative paleomagnetic intensity (RPI) dating revealed an oldest reliable age of 12 681 cal. a BP for the sediment core. Considering the relatively coarse resolution of the age model (based on Hillenbrand et al. (2010); for further details, see chapter 6.3.1), the data are plotted versus depth and the ages are presented as age constraints along the depth-axis. Three distinct units can be deduced with the oldest unit, Unit I, being comprised of bioturbated and stratified mud and silty clay. Unit II consists of bioturbated and stratified diatomaceous ooze and diatomaceous mud, while the youngest unit, Unit III, can be split into two subunits with Unit IIIa consisting of bioturbated mud, sandy mud and muddy sand (with diatoms) and Unit IIIb comprising strongly

laminated to stratified mud, sandy mud and muddy sand barren of diatoms (Hillenbrand et al., 2010).

## 3.2 Organic geochemical analysis

### 3.2.1 Organic bulk parameter analysis

Sediment samples being used for molecular analysis were freeze-dried and homogenized with an agate mortar and kept in glass vials (to avoid contamination) at -20 °C (to prevent degradation processes). The total amounts of carbon (TC) and nitrogen (TN) were analyzed using a Carbon-Nitrogen-Sulfur Analyzer (Elementar Vario EL III). Assuming that calcite is the predominant carbonate (CaCO<sub>3</sub>), the contents were calculated using the following equation:  $\text{CaCO}_3 (\%) = (\text{TC} - \text{TOC}) * 8.333$ , with 8.333 being the stoichiometric calculation factor. Total organic carbon (TOC) contents were determined by means of a carbon-sulfur analyzer (CS 2000; Eltra). Prior to the measurement, inorganic carbon was removed by adding 500 µl 12 N hydrochloric acid. Before the first analysis and after every 10<sup>th</sup> sample (error ± 0.02 %), external standards with a known carbon content were routinely measured for calibration purposes.

### 3.2.2 Biomarker analysis

Lipid biomarker extraction from the freeze-dried and homogenized sediments (between 4-6 g per sample; for exact quantities, see method sections of the different studies; Fig. 3.1) was carried out by means of ultrasonication using dichloromethane:methanol (DCM:MeOH; 2:1 *v/v*) as solvent. For the quantification of HBI (IPSO<sub>25</sub>, HBI E-triene and HBI Z-triene), sterols (brassicasterol, dinosterol, β-sitosterol, campesterols and desmosterol) and GDGTs, 7-hexylnonadecane (7-HND), 5 α-androstan-3-ol and C<sub>46</sub> were added as internal standards prior to extraction (for details on concentrations of the standards, see method sections of the individual studies). The sediment and solvent mixture was put into the ultrasonic bath for 15 min, was then centrifuged for 1 min at 2500 rpm and afterwards decanted. This step was repeated three times.

Open-column chromatography was used for separating the polar from the apolar fraction of the total lipid extract, with SiO<sub>2</sub> as stationary phase. First, the apolar fraction (HBIs) was eluted with 5 ml *n*-hexane and subsequently, the polar fraction (sterols and

GDGTs) was eluted with 5 ml DCM:MeOH (1:1 *v/v*). For further processing, the polar fraction was subsequently split into two fractions (Fig. 3.1, GDGTs and sterols). If needed, the sterol fraction was further purified using ethylacetate:*n*-hexane (20:80 *v/v*) via open-column chromatography and then silylated with 300  $\mu$ l bis-(trimethylsilyl)-trifluoroacetamide (BSTFA; 60 °C, 2 h) prior to analyses. By means of N<sub>2</sub>, the GDGT fraction was dried, redissolved with 120  $\mu$ l *n*-hexane:isopropanol (*v/v* 99:1) and then filtered with a polytetrafluoroethylene (PTFE) filter with a 0.45  $\mu$ m pore size membrane.

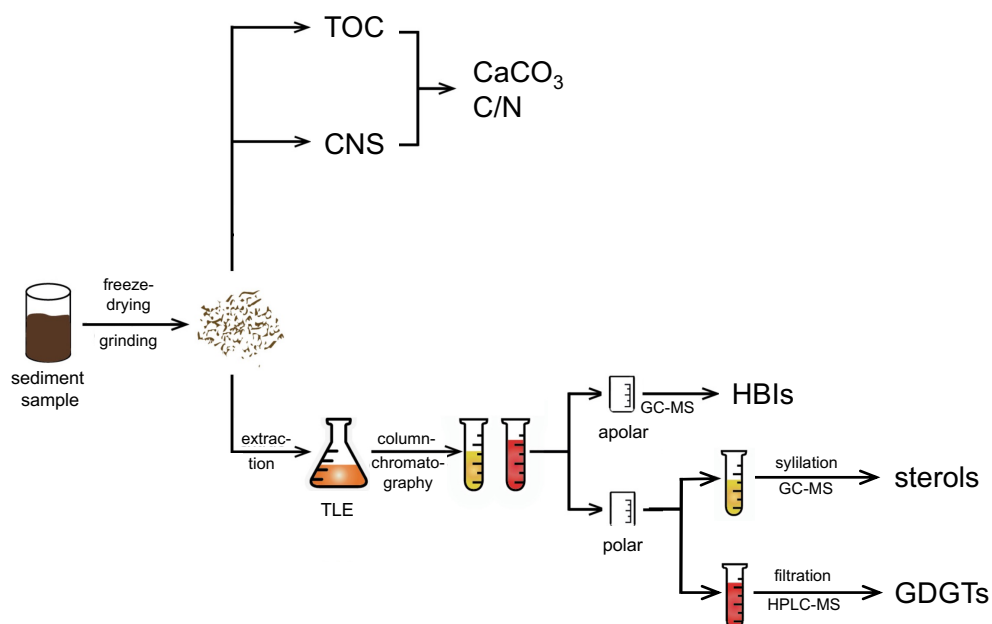


Fig. 3.1: Schematic illustration of the laboratory methods used for bulk parameter and biomarker analyses. TLE: Total Lipid Extract, GC-MS: Gas Chromatograph – Mass Spectrometer, HPLC – MS: High Performance Liquid Chromatograph – Mass Spectrometer. Modified after Kremer (2018).

Compound analysis of HBIs and sterols was carried out via gas chromatography mass spectrometry (GC-MS) using and Agilent Technologies 7890B gas chromatograph (fitted with a 30 m DB 1MS column; 0.25 mm diameter and 0.25  $\mu$ m film thickness) coupled to an Agilent Technologies 5977B mass selective detector (MSD; with 70 eV constant ionization potential, Scan 50-550  $m/z$ , 1 scan/s, ion source temperature of 230 °C). The individual oven temperature program of the GC for the analyses of HBIs was set to 60 °C (3 min), 150 °C (rate: 15 °C min<sup>-1</sup>), 320 °C (rate: 10 °C min<sup>-1</sup>) and 320 °C (15 min isothermal) and for the analyses of sterols was set to 60 °C (2 min), 150 °C (rate: 15 °C min<sup>-1</sup>), 320 °C (rate: 3 °C min<sup>-1</sup>) and 320 °C (20 min isothermal). Carrier gas was helium (1 ml min<sup>-1</sup>, constant flow). Samples were measured in full scan mode and the hydrocarbon fraction were also measured in selected ion monitoring (SIM) mode.

Instrument stability was ensured by measuring external standards and replicate measurements of individual random samples.

HBI and sterol compounds were identified by their individual mass spectral characteristics and their GC retention times (Belt et al., 2000; Belt et al., 2018; Boon et al., 1979). The quantification of each lipid was achieved by setting its individual GC-MS molecular ion response (in SIM mode) in relation to the molecular ion of the respective internal standard and by normalizing the ratios with an instrumental response factor obtained for each target lipid (Belt et al., 2014; Fahl & Stein, 2012).

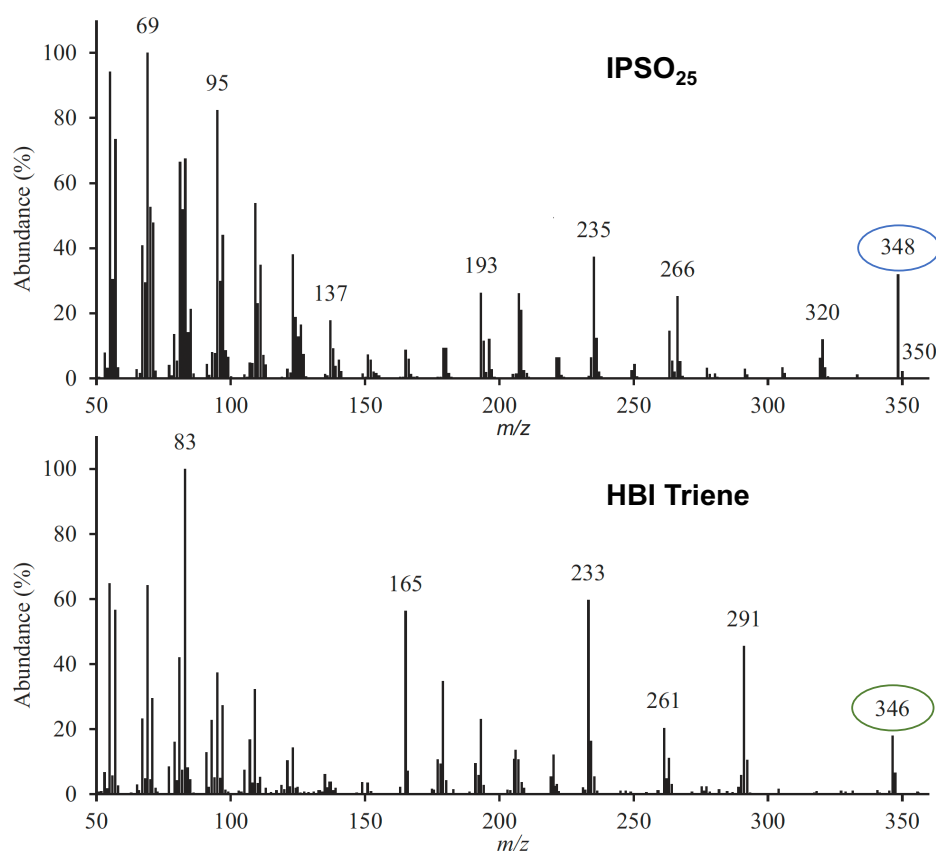


Fig. 3.2: Mass spectra of IPSO<sub>25</sub> and HBI Trienes.

HBI Z-triene ((9Z)-2,6,10,14-Tetramethyl-7-(3-methylpent-4-enyliden)pentadeca-9-ene), HBI E-triene ((9E)-2,6,10,14-Tetramethyl-7-(3-methylpent-4-enyliden)pentadeca-9-ene) and IPSO<sub>25</sub> (2,10,14-Trimethyl-6-enyl-7-(3-methylpent-4-enyl)pentadecane) were quantified by comparing the molecular ion of  $m/z$  346 for HBI-trienes (Fig. 3.2) and  $m/z$  348 for IPSO<sub>25</sub> (Fig. 3.2) to the molecular ion  $m/z$  266 of the internal standard 7-HND (Belt et al., 2018). Sterols were quantified by relating the molecular ion  $m/z$  470 for brassicasterol (24-methylcholesta-5,22E-dien-3 $\beta$ -ol),  $m/z$  500 for dinosterol (4 $\alpha$ ,23,24R-

trimethyl-5 $\alpha$ -cholest-22E-en-3 $\beta$ -ol),  $m/z$  486 for  $\beta$ -sitosterol (24-ethylcholest-5-en-3 $\beta$ -ol),  $m/z$  472 for campesterol (24-methylcholest-5-en-3 $\beta$ -ol) and  $m/z$  456 for desmosterol (cholesta-5,24-dien-3 $\beta$ -ol) with the molecular ion  $m/z$  348 of the internal standard 5  $\alpha$ -androstan-3-ol. By means of the mass of extracted sediment, the masses of the individual lipids derived by the GC-MS were converted to sedimentary concentrations and subsequently normalized to the TOC content of each sample.

Compound analysis of GDGTs on surface sediments for Study No. 1 was carried out via high performance liquid chromatography (HPLC; Agilent 1200 series HPLC system) coupled to an Agilent 6120 mass spectrometer (MS). The HPLC-MS was operated with atmospheric pressure chemical ionization (APCI), the injection volume was 20  $\mu$ L. A Prevail Cyano 3  $\mu$ m column (Grace, 150 mm x 2.1 mm) was kept at 30  $^{\circ}$ C to separate the GDGTs. At a flow rate of 0.2 mL min $^{-1}$ , each sample was eluted isocratically for 5 min with solvent A (hexane/2-propanol/chloroform; 98:1:1). The volume of solvent B (hexane/2-propanol/chloroform; 89:10:1) was increased linearly to 10 % within 20 min and afterwards to 100 % within 10 min. After 7 min and after each sample, the column was back-flushed (for 5 min with a flow rate of 0.6 mL min $^{-1}$ ) and re-equilibrated with solvent A (for 10 min with a flow rate of 0.2 mL min $^{-1}$ ). APCI settings were as follows: N $_2$  drying temperature to 350  $^{\circ}$ C and gas flow at 5 L min $^{-1}$ , vaporizer gas temperature to 350  $^{\circ}$ C, nebulizer pressure to 50 psi, capillary voltage to 4kV and corona current to +5 $\mu$ A. GDGT detection was achieved via selective ion monitoring of [M+H] $^{+}$  ions (dwell time 76 ms).

Quantification of GDGT-0 ( $m/z$  1302), GDGT-1 ( $m/z$  1300), GDGT-2 ( $m/z$  1298), GDGT-3 ( $m/z$  1296) and crenarchaeol ( $m/z$  1292) as well as brGDGT-III ( $m/z$  1050), brGDGT-II ( $m/z$  1036) and brGDGT-I ( $m/z$  1022) was done by comparing their molecular ions to the molecular ion of the internal standard C $_{46}$  ( $m/z$  744). The late eluting hydroxylated GDGTs (OH-GDGT-0, OH-GDGT-1 and OH-GDGT-2 with  $m/z$  1318, 1316 and 1314 respectively) were quantified in the scans ( $m/z$  1300, 1298 and 1296) of their associated GDGTs, as proposed by Fietz et al. (2013).

### 3.3 Additional data sets

#### *Study No. 1*

##### Numerical model description

AWI-ESM2 is a modern coupled climate model developed by Sidorenko et al. (2019). It consists of an atmospheric component ECHAM6 (Stevens et al., 2013) and an ocean-sea-ice component FESOM2 (Danilov et al., 2017). The atmospheric module ECHAM6 is the latest version of the ECHAM model developed at the Max Planck Institute for Meteorology (MPI) in Hamburg. The model is derived from an early version of the European Centre for Medium-Range Weather Forecasts (ECMWF) model (Roeckner et al., 1989). The dynamics of ECHAM6 is based on hydrostatic primitive equations with traditional approximation. We used a T63 Gaussian grid with a spatial resolution of about  $1.9^\circ \times 1.9^\circ$  ( $1.9^\circ$  or 210 km). There are 47 vertical layers in the atmosphere. The momentum transport resulting from boundary effects is calculated using the sub-grid orography scheme described by Lott (1999).

Radiative transfer in ECHAM6 is represented according to the method proposed by Iacono et al. (2008). ECHAM6 also contains a land surface model (JSBACH) that includes 12 plant functional types of dynamic vegetation and 2 types of bare surfaces (Loveland et al., 2000; Raddatz et al., 2007). The ice-ocean module in AWI-ESM2 is based on the finite volume discretization formulated on unstructured meshes. The multi-resolution for the ocean is up to 15 km for polar and coastal regions and 135 km over far-field oceans, with 46 uneven vertical depths. The impact of local dynamics on the global ocean is related to several FESOM-based studies (Danilov et al., 2017). The multi-resolution approach advocated by FESOM makes it possible to study the impact of local processes on the global ocean with only moderate computational effort (Danilov et al., 2017). AWI-ESM2 uses the OASIS3-MCT coupler (Valcke, 2013) with an intermediate regular exchange grid. The mapping between the atmospheric/oceanic grid and the intermediate grid is carried out with bilinear interpolation. The atmospheric component calculates 12 air-sea fluxes based on four surface fields provided by the ocean module FESOM2. AWI-ESM2 was validated under recent climate conditions (Sidorenko et al., 2019) and applied to marine radiocarbon concentrations (Lohmann et al., 2020), the late Holocene (Vorrath et al., 2020) and the Last Interglacial (Otto-Bliesner et al., 2021).



### Numerical model: experimental design

AWI-ESM2 was used to perform a transient experiment in which the boundary conditions, including orbital parameters and greenhouse gases, were applied. The orbital parameters were calculated according to Berger (1978), and the concentrations of greenhouse gases were obtained from ice core records and measurements of recent firn air and atmosphere samples (Köhler et al., 2017). The model was initialized with a 1000-year spin-up run under mid-Holocene (6000 BP) boundary conditions, as described by Otto-Bliesner et al. (2017). In our modeling strategy, we follow Lorenz and Lohmann (2004) and use the climate conditions from the mid-Holocene spin-up run as the initial state for the subsequent transient simulation, which covers the period from 6000 BP to 2014 CE (Common Era). In this study, the seasonal SIC, SST and SOT values in the study areas were derived from a segment of the transient experiment (1950-2014 CE). The topography, including the prescribed ice sheet configuration, was held constant in the transient simulation.

### Satellite SIC and SST data

Satellite sea-ice data were derived from Nimbus-7 Scanning Multichannel Microwave Radiometer (SMMR) and Defence Meteorological Satellite Program (DMSP) Special Sensor Microwave Imager/Sounder (SSM/I-SSMIS) passive microwave data and downloaded from the National Snow and Ice Data Center (NSIDC; Cavalieri et al., 1996). The sea-ice data depict mean monthly SIC values, which range from 0 % to 100 % and are averaged over a time frame from the beginning of satellite observations in 1978 CE to the individual year of sample collection. The monthly mean SIC values were split into seasons: winter (JJA), spring (SON) and summer (DJF), and these data are considered to represent the recent mean state of sea-ice coverage. All satellite data are provided in Table S4.3.

Modern annual mean SSTs and SOTs were derived from the World Ocean Atlas 2013 and represent averaged temperatures for the years 1955–2012 CE (WOA; Locarnini et al., 2013).

*Study No. 3*

## Diatom assemblage data

WSI concentrations were reconstructed using a transfer function (TF) developed by Esper and Gersonde (2014a), which applies the Modern Analog Technique (MAT) (after Hutson, 1980). Statistical details, the background of the method and its performance at different application levels compared to other estimation methods are presented in Esper and Gersonde (2014a). According to standard techniques, quantitative diatom slides were prepared for this purpose (Gersonde & Zielinski, 2000). For diatom counting, a Zeiss Axioplan 2 microscope at 1000x magnification was used and the methods of Schrader and Gersonde (1978) were applied. Diatoms were identified to species or species group level and, where possible, to forma or variety level, with taxonomy mainly following Hasle and Syvertsen (1996), Zielinski and Gersonde (1997) and Armand and Zielinski (2001). Species and species groups used for sea-ice reconstructions show close relationships with environmental variables (Armand et al., 2005; Crosta et al., 2005; Esper & Gersonde, 2014a, 2014b; Esper et al., 2010; Romero et al., 2005; Zielinski & Gersonde, 1997). To estimate WSI concentrations, we used the TF MAT-D274/28/6an, which comprises 274 reference samples from surface sediments in the western Indian, Atlantic and Pacific sectors of the Southern Ocean with 28 diatom taxa and taxa groups and an average of 6 analogs (Esper & Gersonde, 2014a). The WSI estimates refer to September sea-ice concentrations averaged over a time span from 1981 to 2010 at each surface sediment location (National Oceanic and Atmospheric Administration, NOAA; Reynolds et al., 2002; 2007). The reference dataset uses a 1 deg. by 1 deg. grid, which makes it suitable for the approach and gives a higher resolution than previously used data and results in a root mean square error of prediction (RMSEP) of 5.52 % (Esper & Gersonde, 2014a).

#### 4 Study No. 1: Evaluation of lipid biomarkers as proxies for sea ice and ocean temperatures along the Antarctic continental margin

Nele Steinberg (Lamping)<sup>1</sup>, Juliane Müller<sup>1,2,3</sup>, Jens Hefter<sup>1</sup>, Gesine Mollenhauer<sup>1,2,3</sup>, Christian Haas<sup>1</sup>, Xiaoxu Shi<sup>1</sup>, Maria-Elena Vorrath<sup>1</sup>, Gerrit Lohmann<sup>1,3,4</sup>, Claus-Dieter Hillenbrand<sup>5</sup>

<sup>1</sup>Alfred-Wegener-Institut Helmholtz-Zentrum für Polar- und Meeresforschung, Am Alten Hafen 26, 27568, Bremerhaven, Germany

<sup>2</sup>Department of Geosciences, University of Bremen, Klagenfurter Straße, 28359 Bremen, Germany

<sup>3</sup>Marum - Center for Marine Environmental Sciences, Leobener Straße 8, 28359 Bremen, Germany

<sup>4</sup>Department of Environmental Physics, University of Bremen, 28359 Bremen, Germany

<sup>5</sup>British Antarctic Survey, High Cross, Madingley Road, Cambridge CB3 0ET, United Kingdom

Published in the journal “Climate of the Past”, Special Issue “Reconstructing Southern Ocean sea-ice dynamics on glacial-to-historical timescales” in October 2021.

#### Abstract

The importance of Antarctic sea ice and Southern Ocean warming has come into the focus of polar research during the last couple of decades. Especially around West Antarctica, where warm water masses approach the continent and where sea ice has declined, the distribution and evolution of sea ice play a critical role for the stability of nearby ice shelves. Organic geochemical analyses of marine seafloor surface sediments from the Antarctic continental margin allow an evaluation of the applicability of biomarker-based sea ice and ocean temperature reconstructions in these climatically sensitive areas. We analysed highly branched isoprenoids (HBIs), such as the sea-ice proxy IPSO<sub>25</sub> and phytoplankton-derived HBI-trienes, but also phytosterols and isoprenoidal glycerol dialkyl glycerol tetraethers (GDGTs), which are established tools for the assessment of primary productivity and ocean temperatures, respectively. The combination of IPSO<sub>25</sub> with a phytoplankton marker (*i.e.* the PIPSO<sub>25</sub> index) permits semi-quantitative sea-ice reconstructions and avoids misleading over- or underestimations of sea-ice cover. Comparisons of the PIPSO<sub>25</sub>-based sea-ice distribution patterns and TEX<sub>1-86</sub>- and RI-OH'-derived ocean temperatures with (1) sea-

ice concentrations obtained from satellite observations and (2) instrument measurements of sea surface and subsurface temperatures corroborate the general capability of these proxies to determine oceanic key variables properly. This is further supported by model data. We also highlight specific aspects and limitations that need to be taken into account for the interpretation of such biomarker data and discuss the potential of IPSO<sub>25</sub> as an indicator for the former occurrence of platelet ice and/or the export of ice shelf water.

#### 4.1 Introduction

One of the key components of the global climate system, influencing major atmospheric and oceanic processes, is floating on the ocean's surface at high latitudes – sea ice (Thomas, 2017). Southern Ocean sea ice is one of the most strongly changing features of the Earth's surface as it experiences considerable seasonal variabilities with sea-ice extent decreasing from a maximum of  $20 \times 10^6$  km<sup>2</sup> in September to a minimum of  $4 \times 10^6$  km<sup>2</sup> in March (Arrigo et al., 1997; Zwally, 1983). This seasonal waxing and waning of sea ice substantially modifies deep-water formation, influences the ocean-atmosphere exchange of heat and gas and strongly affects surface albedo and radiation budgets (Abernathey et al., 2016; Nicholls et al., 2009; Turner et al., 2017). Moreover, sea ice regulates ocean buoyancy flux, upwelling and primary production (Schofield et al., 2018).

Based on the 40-year satellite record, Southern Ocean sea-ice extent as a whole followed an increasing trend (Comiso et al., 2017; Parkinson and Cavalieri, 2012), experiencing an abrupt reversal from ca. 2015 to 2018 (Parkinson, 2019; Turner et al., 2020; Wang et al., 2019), which has been attributed to a decades-long oceanic warming and increased advection of atmospheric heat (Eayrs et al., 2021). However, the sea-ice extent around major parts of West Antarctica has been decreasing over the last 40 years (Parkinson and Cavalieri, 2012). The Antarctic Peninsula is particularly affected by a significant reduction in sea-ice extent and rapid atmospheric and oceanic warming (Etourneau et al., 2019; Li et al., 2014; Massom et al., 2018; Vaughan et al., 2003). The Larsen A and B ice shelves on the east coast of the Antarctic Peninsula collapsed in 1995 and 2002, respectively. These collapses were triggered by the loss of a sea-ice buffer, which enabled an increased flexure of the ice-shelf margins by ocean swell (Massom et

al., 2018). Along the Pacific margin of West Antarctica, the Amundsen and Bellingshausen seas have also been affected by major sea-ice decline and regional surface ocean warming (Hobbs et al., 2016; Parkinson, 2019). Marine-terminating glaciers draining into the Amundsen and Bellingshausen seas are thinning at an alarming rate, which has been linked to sub-ice shelf melting caused by relatively warm Circumpolar Deep Water (CDW) incursions into sub-ice shelf cavities (*e.g.*, Jacobs et al., 2011; Khazendar et al., 2016; Nakayama et al., 2018; Rignot et al., 2019; Smith et al., 2017). The disintegration of ice shelves reduces the buttressing effect that they exert on ice grounded further upstream, which can lead to partial or total loss of the ice in the catchments of the affected glaciers and, thus, raise global sea level considerably (3.4 to 4.4 m in case of a total West Antarctic Ice Sheet (WAIS) collapse; Fretwell et al., 2013; Jenkins et al., 2018; Pritchard et al., 2012; Vaughan, 2008).

State-of-the-art climate models are not yet fully able to depict sea-ice seasonality and sea-ice cover, which the 5<sup>th</sup> Assessment Report of the Intergovernmental Panel on Climate Change (Stocker et al., 2013) attributes to a lack of validation efforts using proxy-based sea-ice reconstructions. Knowledge about (paleo-)sea-ice conditions and ocean temperatures in the climate sensitive areas around the WAIS is hence considered as crucial for understanding past and future climate evolution.

To date, the most common proxy-based sea-ice reconstructions in the Southern Ocean utilize fossil assemblages of sympagic (*i.e.* living within sea ice) diatoms preserved within the seafloor sediments (Allen et al., 2011; Armand and Leventer, 2003; Crosta et al., 1998; Esper and Gersonde, 2014a; Gersonde and Zielinski, 2000; Leventer, 1998). Dissolution effects within the water column or after deposition, however, determine the preservation of small, lightly silicified diatom taxa and therefore can alter the assemblage record, leading to inaccurate sea-ice reconstructions (Leventer, 1998; Zielinski et al., 1998). Recently, the molecular remains of certain diatom taxa, *i.e.* specific organic geochemical lipids, have emerged as a potential proxy for reconstructing past Antarctic sea-ice cover (Barbara et al., 2013; Collins et al., 2013; Crosta et al., 2021; Denis et al., 2010; Etourneau et al., 2013; Lamping et al., 2020; Massé et al., 2011; Vorrath et al., 2019; 2020). Specifically, a di-unsaturated HBI alkene (HBI diene, C<sub>25:2</sub>) has been detected in both sea-ice diatoms from the Southern Ocean and Antarctic marine sediments (Johns et al., 1999; Massé et al., 2011; Nichols et al., 1988). Recently, the sympagic diatom

*Berkeleleya adeliensis*, which preferably proliferates in platelet ice, has been identified as the producer of these HBI alkene (Belt et al., 2016; Riaux-Gobin and Poulin, 2004). However, *B. adeliensis* seems rather flexible concerning its habitat, since it was also recorded in the bottom ice layer and is apparently well adapted to changes in texture during ice melt (Riaux-Gobin et al., 2013). Belt et al. (2016) introduced the term IPSO<sub>25</sub> (“Ice Proxy of the Southern Ocean with 25 carbon atoms”) by analogy to the counterpart IP<sub>25</sub> in the Arctic. Commonly, for a more detailed assessment of sea-ice conditions, IP<sub>25</sub> in the Arctic Ocean and IPSO<sub>25</sub> in the Southern Ocean have been measured alongside complementary phytoplankton-derived lipids, such as sterols and/or HBI-trienes, which are indicative of open-water conditions (Belt and Müller, 2013; Lamping et al., 2020; Etourneau et al., 2013; Vorrath et al., 2019; 2020). The combination of the sea-ice biomarker and a phytoplankton biomarker, the so-called PIPSO<sub>25</sub> index (Vorrath et al., 2019), allows for a more quantitative differentiation of contrasting sea-ice settings and helps to avoid misinterpretations of the absence of IPSO<sub>25</sub>. An absence of the sea-ice biomarker can result from either a lack of sea-ice cover or a permanent thick sea-ice cover that prevents light penetration and hence limits ice algae growth. These two contrasting scenarios can be distinguished by using the additional phytoplankton biomarker. Recently, Lamping et al. (2020) used the PIPSO<sub>25</sub> index to reconstruct changes in sea-ice conditions during the last deglaciation of the Amundsen Sea shelf, which were likely linked to advance and retreat phases of the Getz Ice Shelf.

Multiple mechanisms exist that can cause ice-shelf instability. As previously mentioned, relatively warm CDW is considered one of the main drivers for ice-shelf thinning in the Amundsen Sea and Bellingshausen Sea sectors of the WAIS (Nakayama et al., 2018; Jenkins and Jacobs, 2008; Rignot et al., 2019). Accordingly, changing ocean temperatures are another crucial factor for the stability of the marine-based ice streams draining most of the WAIS (e.g., Colleoni et al., 2018). As for sea-ice reconstructions, organic geochemical lipid proxies have been employed over the past decades for reconstructing ocean temperatures in high latitudes, since the abundance and preservation of calcareous microfossils commonly used for such reconstructions is very poor in polar marine sediments (e.g., Zamelczyk et al., 2012). In contrast, archaeal isoprenoidal (isoGDGTs), sensitive to temperature change and relatively resistant to degradation processes, are well preserved in all types of marine sediments (Huguet et al.,

2008; Schouten et al., 2013). Schouten et al. (2002) found that the number of rings in sedimentary GDGTs is correlated with surface water temperatures and developed the first archaeal lipid paleothermometer  $\text{TEX}_{86}$ , a ratio of certain GDGTs, as a sea surface temperature (SST) proxy. For polar oceans, Kim et al. (2010) developed a more specific calibration model for temperatures below 15 °C,  $\text{TEX}^{\text{L}}_{86}$ , which employs a different GDGT combination. There is an emerging consensus that GDGTs predominantly reflect subsurface ocean temperatures (SOT) along the Antarctic margin (Kim et al., 2012; Etourneau et al., 2019; Liu et al., 2020). This is supported by observations of elevated archaeal abundances (and GDGTs) in warmer subsurface waters (Liu et al., 2020; Spencer-Jones et al., 2021). Archaea adapt their membrane in cold waters by adding hydroxyl groups and changing the number of rings, OH-GDGTs (Fietz et al., 2020). Huguet et al. (2017) found in molecular dynamic simulations that the additional hydroxyl moieties lead to an increase of the membrane fluidity, which aids trans-membrane transport in cold environments. This explains the higher relative abundance of OH Archaea lipids in cold environments. Taking the OH-GDGTs into account, Lü et al. (2015) proposed an SST-proxy for the polar oceans, the RI-OH'.

The aim of our study is to provide insight into the application of biomarkers in Southern Ocean sediments as sea ice and ocean temperature proxies. Estimates on recent sea-ice coverage and ocean temperatures along the eastern and western Antarctic Peninsula (EAP and WAP) as well as in the Amundsen and Weddell seas are based on the analyses of IPSO<sub>25</sub>, HBI-trienes and phytosterols and GDGTs in seafloor surface sediment samples from these areas. A comparison of biomarker-derived estimates of sea-ice extent and ocean temperature with (1) sea-ice distributions obtained from satellite observations and (2) in-situ ocean temperature measurements allows for an evaluation of the proxy approach. We further consider AWI-ESM2 climate model data to assess the model's performance in depicting recent oceanic key variables and to examine the potential impact of paleoclimate conditions on the biomarker composition of the investigated surface sediments. Taking into account the various factors affecting the use of marine biomarkers as paleoenvironmental proxies, we comment on the limitations of GDGT temperature estimates and the novel PIPSO<sub>25</sub> approach. Furthermore, we discuss the potential connection between IPSO<sub>25</sub> and platelet ice formation under near-coastal fast ice, which is related to the near-surface presence of sub-ice shelf melt water.

## 4.2 Regional setting

The areas investigated in this study include the southern Drake Passage, the continental shelves of the WAP and EAP ( $\sim 60^\circ$  S) and the more southerly located Amundsen and Weddell seas ( $\sim 75^\circ$  S; Fig. 4.1). The different study areas are all connected by the Antarctic Circumpolar Current (ACC), the Antarctic Coastal Current and the Weddell Gyre, respectively (Meredith et al., 2011; Rintoul et al., 2001).

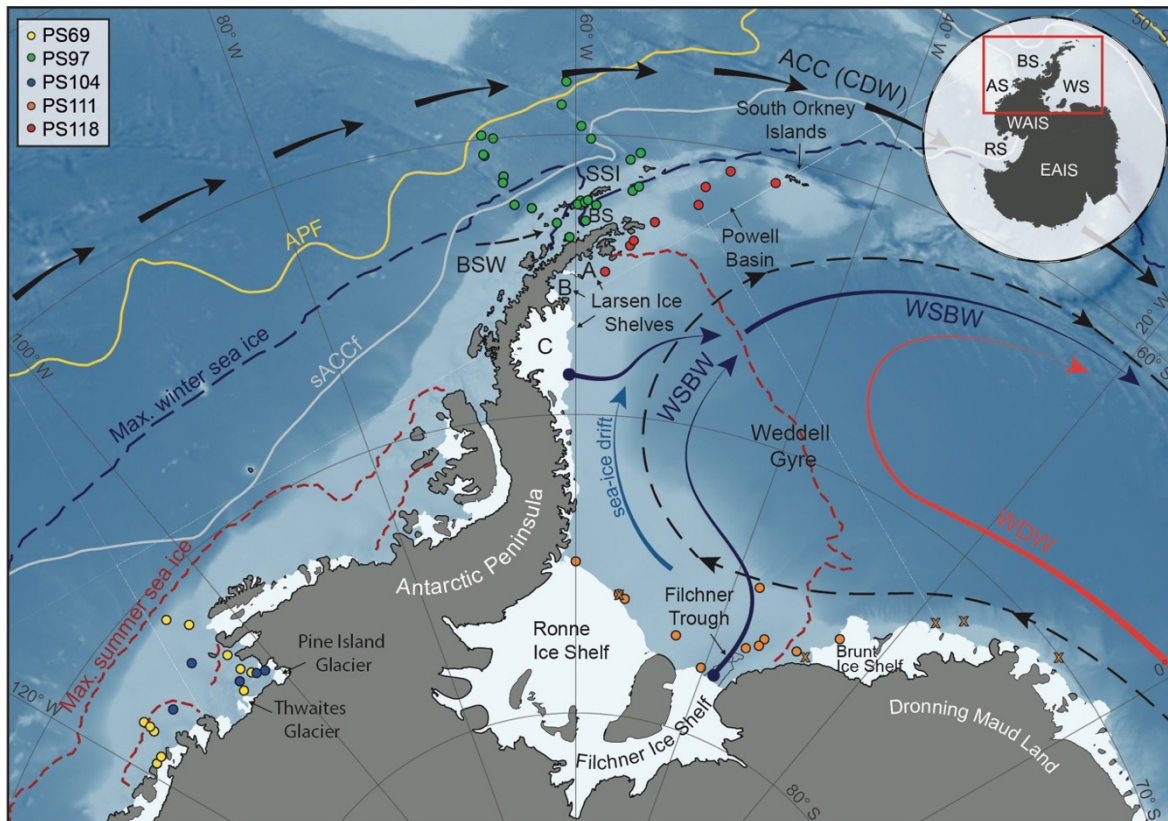


Fig. 4.1: Map of the study area (location indicated by red box in insert map) including all 41 sample locations (see different colored dots for individual RV Polarstern expeditions in the top left corner; for detailed sample information, see Table S4.1) and main oceanographic features. Maximum summer and winter sea-ice boundaries are marked by dashed red and blue line, respectively (Fetterer et al., 2016). The orange crosses in the Weddell Sea indicate samples with low biomarker concentrations close to detection limit, to which we assigned a PIPSO<sub>25</sub> value of 1. ACC: Antarctic Circumpolar Current, APF: Antarctic Polar Front, sACCf: southern Antarctic Circumpolar Current Front, SSI: South Shetland Islands, BS: Bransfield Strait, BSW: Bellingshausen Sea Water, CDW: Circumpolar Deep Water; WDW: Weddell Deep Water, WSBW: Weddell Sea Bottom Water (Mathiot et al., 2011; Orsi et al., 1995). Insert map shows grounded ice (i.e. without ice shelves) in black; WAIS: West Antarctic Ice Sheet, EAIS: East Antarctic Ice Sheet, RS: Ross Sea, BS: Bellingshausen Sea, WS: Weddell Sea. Background bathymetry derived from IBCSO data (Arndt et al., 2013).

The ACC, which is mainly composed of CDW and characterized by strong eastward flow, is the largest current system in the world and has its narrowest constriction in the Drake Passage. In the Amundsen Sea, the Bellingshausen Sea and along the WAP, where the ACC flows close to the continental shelf edge, CDW is upwelling onto the shelf and flows to the coast via bathymetric troughs, contributing to basal melt and retreat of



marine-terminating glaciers and ice shelves (Cook et al., 2016; Jacobs et al., 2011; Jenkins and Jacobs, 2008; Klinck et al., 2004). In the Weddell Sea, the Weddell Gyre, a subpolar cyclonic circulation south of the ACC, deflects part of the ACC's CDW towards the south and turns it into Warm Deep Water (WDW; Fig. 4.1; Hellmer et al., 2016; Vernet et al., 2019). In close vicinity to the Filchner-Ronne and Larsen Ice Shelves, glacial meltwater as well as dense brines released during sea-ice formation contribute to the formation of Weddell Sea Bottom Water (WSBW) - a major precursor of Antarctic Bottom Water (AABW; Hellmer et al., 2016). Along the EAP coast wind and currents force a northward drift of sea ice (Harms et al., 2001), which melts when reaching warmer waters in the North and in Powell Basin (Vernet et al., 2019). At the northern tip of the Antarctic Peninsula, colder and saltier Weddell Sea water masses branch off westwards into the Bransfield Strait, where they encounter the well-stratified, warm, and fresh Bellingshausen Sea Water (BSW; Fig. 4.1), which is entering the Bransfield Strait from the West (Sangrà et al., 2011).

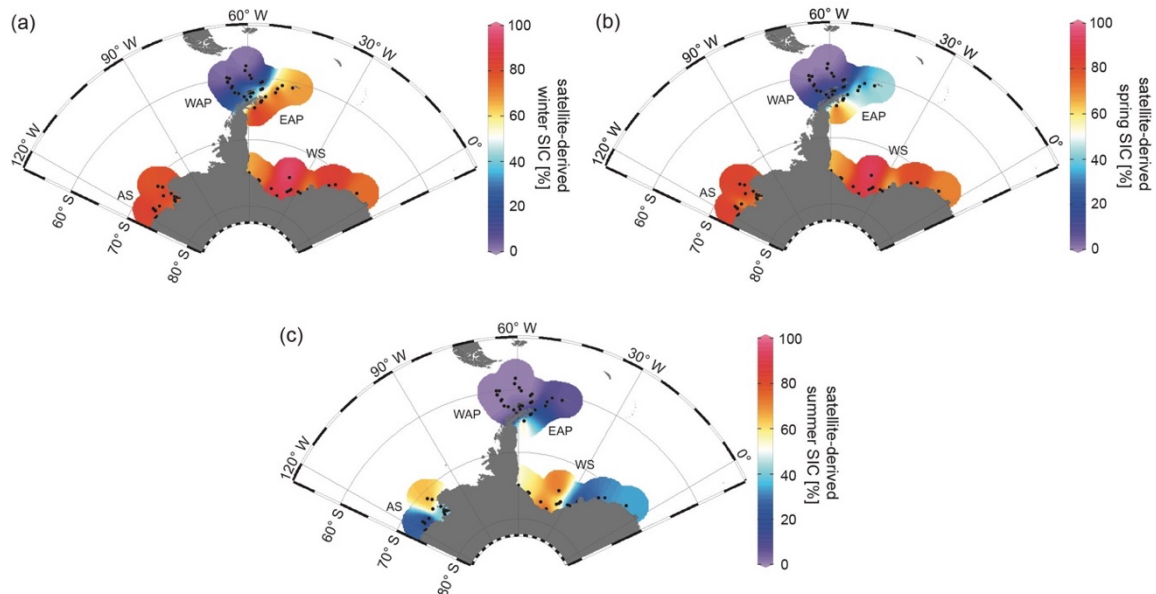


Fig. 4.2: Distribution of mean monthly satellite-derived sea-ice concentrations for (a) winter (JJA), (b) spring (SON) and (c) summer (DJF) in % (downloaded from the National Snow and Ice Data Center, NSIDC; Cavalieri et al., 1996). AS: Amundsen Sea, WAP: West Antarctic Peninsula, EAP: East Antarctic Peninsula, WS: Weddell Sea.

Since 1978, satellite observations show strong seasonal and decadal changes in sea-ice cover around the Antarctic Peninsula, which are less pronounced in the Amundsen and Weddell seas (Vaughan et al., 2003; Parkinson and Cavalieri, 2012). Mean monthly sea-ice concentrations (SIC) for austral winter (JJA), spring (SON) and summer (DJF) reveal a permanently ice-free Drake Passage, while the WAP and EAP shelf areas are

influenced by a changing sea-ice cover throughout the year (Fig. 4.2 a-c). For the Amundsen and Weddell seas, satellite data reveal up to ~90 % sea-ice concentration during winter and spring (Fig. 4.2 a+b), and a minimum concentration of ~30 % during summer (Fig. 4.2 c).

### 4.3 Material and methods

#### 4.3.1 Sediment samples

We analysed a set of 41 surface sediment samples (0-1 cm subbottom depth) from different areas of the Southern Ocean (Fig. 4.1) retrieved by multicorers and giant box corers during RV *Polarstern* expeditions over the past 15 years. Sixteen surface sediment samples from the Amundsen Sea continental shelf were collected during expeditions PS69 in 2006 (Gohl, 2007) and PS104 in 2017 (Gohl, 2017). Twenty-five surface sediment samples from the southeastern and southwestern Weddell Sea continental shelf were collected during expeditions PS111 in 2018 (Schröder, 2018) and PS118 in 2019 (Dorschel, 2019). This new data set was complemented by data from 26 surface sediment samples collected in Bransfield Strait/WAP, which had been previously published by Vorrath et al. (2019).

#### 4.3.2 Bulk sediment and organic geochemical analyses

The sediment material was freeze-dried and homogenized with an agate mortar and stored in glass vials at -20 °C before and after these initial preparation steps to avoid degradation of targeted molecular components. TOC contents were measured on 0.1 g of sediment after removing inorganic carbon (total inorganic carbon, carbonates) with 500 µl 12 N hydrochloric acid. TOC contents were determined with a carbon-sulphur analyzer (CS 2000; Eltra) with standards for calibration being routinely measured before sample analysis and after every tenth sample (error  $\pm$  0.02 %).

Lipid biomarkers were extracted from the sediments (4 g for PS69 and PS104; 6 g for PS111 and PS118) by ultrasonication (3 x 15 min) using DCM:MeOH (3 x 6 ml for PS69 and PS104; 3 x 8 ml for PS111 and PS118; 2:1 *v/v*) as solvent. Prior to this step, the internal standards 7-HND (0.038 µg/sample for PS69 and PS104 and 0.057 µg/sample for PS111 and PS118), 5 $\alpha$ -androstan-3-ol (1.04 µg/sample) and C<sub>46</sub> (0.98 µg/sample)

were added to the sample for quantification of HBIs, sterols and GDGTs, respectively. Via open-column chromatography, with SiO<sub>2</sub> as stationary phase, fractionation of the extract was achieved by eluting the apolar fraction (HBIs) and the polar fraction (sterols and GDGTs) with 5 ml n-hexane and 5 ml DCM/MeOH 1:1, respectively. The polar fraction was subsequently split into two fractions (sterols and GDGTs) for further processing. The sterol fraction was silylated with 300 µl BSTFA (2h at 60 °C). Compound analyses of HBIs and sterols were carried out on an Agilent Technologies 7890B GC (fitted with a 30 m DB 1MS column; 0.25 mm diameter and 0.25 µm film thickness) coupled to an Agilent Technologies 5977B MSD (with 70 eV constant ionization potential, ion source temperature of 230 °C). The GC oven was set to: 60 °C (3 min), 150 °C (rate: 15 °C/min), 320 °C (rate: 10 °C/min), 320 °C (15 min isothermal) for the analysis of hydrocarbons and to: 60 °C (2 min), 150 °C (rate: 15 °C/min), 320 °C (rate: 3 °C/min), 320 °C (20 min isothermal) for the analysis of sterols. Helium was used as carrier gas. The HBI and sterol compounds were identified by their GC retention times and mass spectra (Belt, 2018; Belt et al., 2000; Boon et al., 1979). Lipids were quantified by setting the individual, manually integrated, gas chromatography mass spectrometry (GC-MS) peak area in relation to the peak area of the respective internal standard and normalization to the amount of extracted sediment. IPSO<sub>25</sub> and HBI-trienes were quantified by relating their molecular ions (IPSO<sub>25</sub>:  $m/z$  348 and HBI-trienes:  $m/z$  346) to the fragment ion  $m/z$  266 of the internal standard 7-HND (Belt, 2018). Sterols were quantified by comparing the molecular ion of the individual sterol with the molecular ion  $m/z$  348 of the internal standard 5 $\alpha$ -androstan-3-ol. Instrumental response factors for the target lipids were considered as recommended by Belt et al. (2014) and Fahl and Stein (2012). All biomarker concentrations were subsequently normalized to the TOC content of each sample to account for different depositional settings within the different study areas.

For calculating the phytoplankton-IPSO<sub>25</sub> (PIPSO<sub>25</sub>) index, we used the equation introduced by Vorrath et al. (2019):

$$\text{PIPSO}_{25} = \text{IPSO}_{25} / (\text{IPSO}_{25} + (\text{phytoplankton marker} \times c)) \quad (1)$$

where  $c$  ( $c = \text{mean IPSO}_{25} / \text{mean phytoplankton marker}$ ) is applied as a concentration balance factor to account for high concentration offsets between IPSO<sub>25</sub> and the

phytoplankton biomarker (see Table S4.1 for c-factors of individual PIPSO<sub>25</sub> calculations).

Following the approach by Müller and Stein (2014) and Lamping et al. (2020), a PIPSO<sub>25</sub> value of 1 was assigned to samples with exceptionally low (at detection limit) concentrations of both biomarkers (see chapter 4.4.2). This comprises the five Weddell Sea samples PS111/13-2, /15-1, /16-3, /29-3 and /40-2 (marked as orange x in Fig. 4.1).

The GDGT fraction was dried under N<sub>2</sub>, redissolved with 120 µl hexane:isopropanol (*v/v* 99:1) and then filtered using a polytetrafluoroethylene (PTFE) filter with a 0.45 µm pore sized membrane. GDGTs were measured using HPLC (Agilent 1200 series HPLC system) coupled to an Agilent 6120 MS, operating with APCI. The injection volume was 20 µl. For separating the GDGTs, a Prevail Cyano 3 µm column (Grace, 150 mm \* 2.1 mm) was kept at 30 °C. Each sample was eluted isocratically for 5 min with solvent A = hexane/2-propanol/chloroform; 98:1:1 at a flow rate of 0.2 ml/min, then the volume of solvent B = hexane/2-propanol/chloroform; 89:10:1 was increased linearly to 10 % within 20 min and then to 100 % within 10 min. The column was back-flushed (5 min, flow 0.6 ml/min) after 7 min after each sample and re-equilibrated with solvent A (10 min, flow 0.2 ml/min). The APCI was set to the following: N<sub>2</sub> drying gas flow at 5 l/min and temperature to 350 °C, nebulizer pressure to 50 psi, vaporizer gas temperature to 350 °C, capillary voltage to 4 kV and corona current to +5 µA. Detection of GDGTs was achieved by means of selective ion monitoring (SIM) of [M+H]<sup>+</sup> ions (dwell time 76 ms). GDGT-0 (*m/z* 1302), GDGT-1 (*m/z* 1300), GDGT-2 (*m/z* 1298), GDGT-3 (*m/z* 1296) and crenarchaeol (*m/z* 1292) as well as brGDGT-III (*m/z* 1050), brGDGT-II (*m/z* 1036) and brGDGT-I (*m/z* 1022) were quantified by relating their molecular ions to the molecular ion *m/z* 744 of the internal standard C<sub>46</sub>-GDGT. The late eluting hydroxylated GDGTs (OH-GDGT-0, OH-GDGT-1 and OH-GDGT-2 with *m/z* 1318, 1316 and 1314, respectively) were quantified in the scans (*m/z* 1300, 1298, 1296) of their related GDGTs, as described by Fietz et al. (2013).

TEX<sub>86</sub><sup>L</sup> values and their conversion into SOTs were determined following Kim et al. (2012):

$$\text{TEX}_{86}^L = \text{LOG} \frac{[\text{GDGT-2}]}{[\text{GDGT-1}] + [\text{GDGT-2}] + [\text{GDGT-3}]}, \quad (2)$$

$$\text{SOT}^{\text{TEX}} [\text{°C}] = 50.8 \times \text{TEX}_{86}^L + 36.1. \quad (3)$$

Temperature calculations based on OH-GDGTs were carried out according to Lü et al. (2015):

$$RI - OH' = \frac{[OH-GDGT-1] + 2 \times [OH-GDGT-2]}{[OH-GDGT-0] + [OH-GDGT-1] + [OH-GDGT-2]}, \quad (4)$$

$$SST^{OH} [^{\circ}C] = RI - OH' - 0.1/0.0382 \quad (5)$$

To determine the relative influence of terrestrial organic matter input, the Branched Isoprenoid Tetraether (BIT)-index was calculated following Hopmans et al. (2004):

$$BIT = \frac{[brGDGT-I] + [brGDGT-II] + [brGDGT-III]}{[Chrenarchaeol] + [brGDGT-I] + [brGDGT-II] + [brGDGT-III]} \quad (6)$$

### 4.3.3 Numerical model

#### 4.3.3.1 Model description

AWI-ESM2 is a state-of-the-art coupled climate model developed by Sidorenko et al. (2019) which comprises an atmospheric component ECHAM6 (Stevens et al., 2013) as well as an ocean-sea ice component FESOM2 (Danilov et al., 2017). The atmospheric module ECHAM6 is the most recent version of the ECHAM model developed at the Max Planck Institute for Meteorology (MPI) in Hamburg. The model is branched from an early release of the European Center (EC) for Medium Range Weather Forecasts (ECMWF) model (Roeckner et al., 1989). ECHAM6 dynamics is based on hydrostatic primitive equations with traditional approximation. We used a T63 Gaussian grid with a spatial resolution of about 1.9 x 1.9 degree (1.9 ° or 210 km). There are 47 vertical layers in the atmosphere.

Momentum transport arising from boundary effects is configured using the subgrid orography scheme as described by Lott (1999). Radiative transfer in ECHAM6 is represented by the method described in Iacono et al. (2008). ECHAM6 also contains a Land-Surface Model (JSBACH) which includes 12 functional plant types of dynamic vegetation and 2 bare-surface types (Loveland et al., 2000; Raddatz et al., 2007). The ice-ocean module in AWI-ESM2 is based on the finite volume discretization formulated on unstructured meshes. The multi-resolution for the ocean is up to 15 km over polar and coastal regions, and 135 km for far-field oceans, with 46 uneven vertical depths. The impact of local dynamics on the global ocean is related to a number of FESOM-based studies (Danilov et al., 2017). The multi-resolution approach advocated by FESOM

allows to explore the impact of local processes on the global ocean with moderate computational effort (Danilov et al., 2017). AWI-ESM2 employs the OASIS3-MCT coupler (Valcke, 2013) with an intermediate regular exchange grid. Mapping between the intermediate grid and the atmospheric/oceanic grid is handled with bilinear interpolation. The atmosphere component computes 12 air–sea fluxes based on four surface fields provided by the ocean module FESOM2. AWI-ESM2 has been validated under modern climate conditions (Sidorenko et al., 2019) and has been applied for marine radiocarbon concentrations (Lohmann et al., 2020), the latest Holocene (Vorrath et al., 2020), and the Last Interglacial (Otto-Bliesner et al., 2021).

#### 4.3.3.2 Experimental design

One transient experiment was conducted using AWI-ESM2, which applied the boundary conditions, including orbital parameters and greenhouse gases. Orbital parameters are calculated according to Berger (1978), and the concentrations of greenhouse gases are taken from ice-core records and measurements of recent firn air and atmospheric samples (Köhler et al., 2017). The model was initialized from a 1,000-year spin-up run under mid-Holocene (6,000 before present, BP) boundary conditions as described by Otto-Bliesner et al. (2017). In our modeling strategy, we follow Lorenz and Lohmann (2004) and use the climate condition from the mid-Holocene spin-up run as the initial state for the subsequent transient simulation covering the period from 6,000 BP to 2014 Common Era (CE). In the present study we derived seasonal SIC, SSTs and SOTs in the study areas from a segment of the transient experiment (1950-2014 CE). Topography including prescribed ice sheet configuration was kept constant in our transient simulation. All model data are provided in Table S4.2.

#### 4.3.4 Satellite SIC and SSTs

Satellite sea-ice data were derived from Nimbus-7 SMMR and DMSP SSM/I-SSMIS passive microwave data and downloaded from the National Snow and Ice Data Center (NSIDC; Cavalieri et al., 1996). The sea-ice data represent mean monthly SIC, which are expressed to range from 0 % to 100 % and are averaged over a period of the beginning of satellite observations in 1978 CE to the individual year of sample collection. The monthly mean SIC were then split into different seasons: winter (JJF), spring (SON) and

summer (DJF) (Fig. 4.2 a-c), and these data are considered to represent the recent mean state of sea-ice coverage. All satellite data are provided in Table S4.3.

Modern annual mean SSTs and SOTs were derived from the World Ocean Atlas 2013 and represent averaged values for the years 1955-2012 CE (WOA13; Locarnini et al., 2013).

#### 4.4 Results and discussion

In the following, we first present and discuss the biomarker data generated for this study from North (Antarctic Peninsula) to South (Amundsen and Weddell seas) and draw conclusions about the environmental settings deduced from the data set. In regard to the phytoplankton-derived biomarkers, we focus on the significance of HBI Z-triene and brassicasterol, because the HBI E-triene and dinosterol data, which are presented in the supplementary material (Fig. S4.1), show very similar patterns. All biomarker data are provided in Table S4.1 and are available from the PANGAEA data repository (<https://doi.pangaea.de/10.1594/PANGAEA.932265>). For the discussion of the target environmental variables, i.e. PIPSO<sub>25</sub>-based sea-ice and GDGT-derived ocean temperature estimates, satellite, instrumental and model data are considered. In chapter 4.5, we further address potential caveats in biomarker-based environmental reconstructions that need to be taken into account when applying these proxies.

##### 4.4.1 TOC content, HBIs and sterols in Antarctic surface sediments

TOC contents in marine sediments are often viewed as an indicator for primary productivity in surface waters (Meyers, 1997). However, we are aware that additional factors, such as different water depths and depositional regimes, may exert control on sedimentary TOC as well. The TOC contents of the investigated surface samples are lowest in Drake Passage with values around 0.12-0.54 % and increase from northwest to southeast into Bransfield Strait, where they range from 0.59 to 1.06 % (Fig. 4.3 a; WAP). Along the EAP, higher TOC contents (0.57-0.86 %) prevail around the former Larsen A Ice Shelf and north of James Ross Island but they decrease towards Powell Basin (0.22-0.37 %) and then increase to 0.50 % around the South Orkney Islands, which

may point to elevated productivity or enhanced supply of reworked terrigenous organic matter in this area (Fig. 4.3 a; EAP).

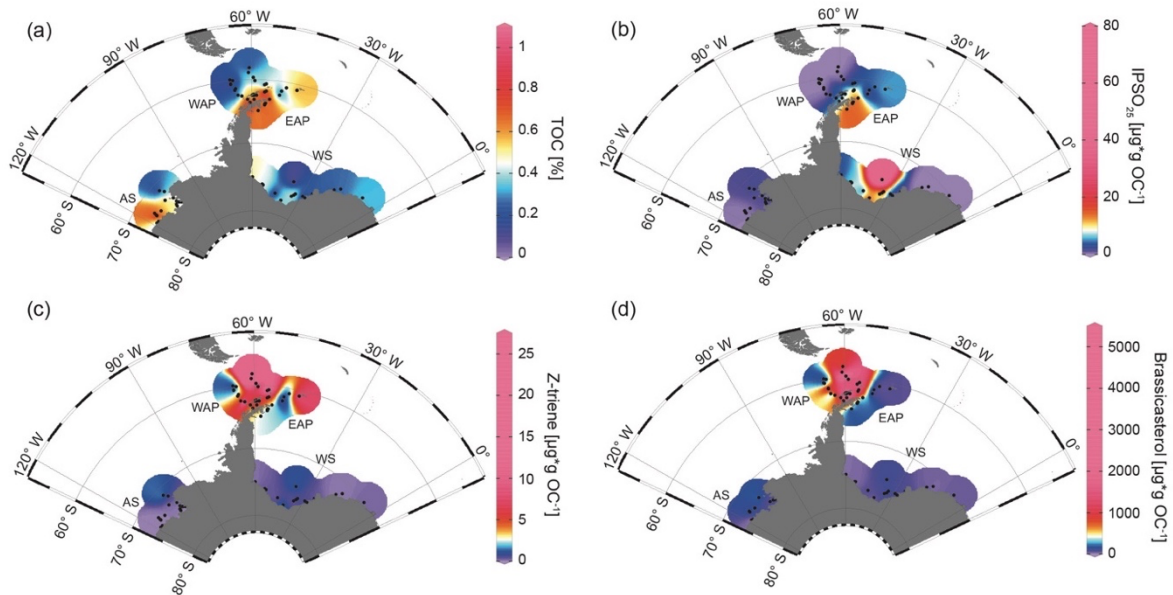


Fig. 4.3: Distribution of (a) TOC [%], (b) IPSO<sub>25</sub>, (c) HBI Z-triene and (d) brassicasterol in surface sediment samples. Sample locations are marked as black dots. Concentrations of biomarkers [ $\mu\text{g} \cdot \text{g} \text{OC}^{-1}$ ] were normalized to the TOC content of each sample. AS: Amundsen Sea, WAP: West Antarctic Peninsula, EAP: East Antarctic Peninsula, WS: Weddell Sea.

At the WAP, concentrations of the sea-ice biomarker IPSO<sub>25</sub> increase from northwest to southeast. IPSO<sub>25</sub> is absent in samples from the permanently ice-free Drake Passage and increases towards the continental slope and the seasonally ice-covered shelf (0.37-17.81  $\mu\text{g} \cdot \text{g} \text{OC}^{-1}$ ; Fig. 4.3 b; Vorrath et al., 2019). Highest IPSO<sub>25</sub> concentrations are observed in samples of the northern Bransfield Strait. Here, the inflow of waters from the Weddell Sea transports sea ice into Bransfield Strait (Vorrath et al., 2019). Elevated IPSO<sub>25</sub> concentrations are also observed at the seasonally sea-ice covered EAP, where relatively high concentrations of the sea-ice biomarker prevail in samples located in the area of the former Larsen A Ice Shelf and north of James Ross Island (12.59-17.74  $\mu\text{g} \cdot \text{g} \text{OC}^{-1}$ ; Fig. 4.3 b). Because these locations are influenced by the northward drift of sea ice within the Weddell Gyre (Fig. 4.1), the elevated IPSO<sub>25</sub> concentrations could also result from sea ice advected from the southern Weddell Sea. We suggest that the decrease of IPSO<sub>25</sub> concentrations towards the Powell Basin and the South Orkney Islands (0.59-5.36  $\mu\text{g} \cdot \text{g} \text{OC}^{-1}$ ; Fig. 4.3 b) is connected to warmer ocean temperatures in the North and reduced sea-ice cover during spring.



Concentrations of the phytoplankton biomarker HBI Z-triene around the Antarctic Peninsula are highest in eastern Drake Passage and along the WAP continental slope (where IPSO<sub>25</sub> is absent) and decrease in Bransfield Strait (0.33-26.86  $\mu\text{g}^*\text{g OC}^{-1}$ ; Fig. 4.3 c; Vorrath et al., 2019). Elevated HBI Z-triene concentrations have, so far, been detected in surface waters along the sea-ice edge (Smik et al., 2016b) and hence were suggested to be a proxy for marginal ice zone conditions (Belt et al., 2015; Collins et al., 2013; Schmidt et al., 2018). Vorrath et al. (2019), however, relate the high concentrations of HBI Z-triene at the northernmost stations in the permanently ice-free eastern Drake Passage to their proximity to the Antarctic Polar Front. Here, productivity of the source diatoms of HBI-trienes (e.g., *Rhizosolenia* spp.; Belt et al., 2017) may be enhanced by meander-induced upwelling leading to increased nutrient flux to surface waters (Moore and Abbott, 2002). Since Cárdenas et al. (2019) document only minor abundances of *Rhizosolenia* spp. in seafloor surface sediments from this area, we assume that HBI-trienes might also be biosynthesized by other diatom taxa. Moderate concentrations along the continental slope of the WAP and in Bransfield Strait were associated with elevated inflow of warm BSW which leads to a retreating sea-ice margin during spring and summer (for more details, see Vorrath et al., 2019; 2020). Samples from the EAP shelf and Powell Basin are characterized by relatively low HBI Z-triene concentrations (Fig. 4.3 c; 0.1-2.37  $\mu\text{g}^*\text{g OC}^{-1}$ ) that decrease from southwest to northeast, whereas the northernmost sample closest to the South Orkney Islands is characterized by an elevated HBI Z-triene concentration of  $\sim 8.49 \mu\text{g}^*\text{g OC}^{-1}$  (Fig. 4.3 c; EAP). This relatively high concentration may be related to an “Island Mass Effect”, coined by Doty and Oguri (1956), which refers to increased primary production around oceanic islands in comparison to surrounding waters. Nolting et al. (1991) found extraordinarily high dissolved iron levels (as high as 50-60 nM) on the South Orkney shelf, while Nielsdóttir et al. (2012) observed enhanced iron and Chl *a* concentrations in the vicinity of the South Orkney Islands. These authors explain the increased dissolved iron levels with input from seasonally retreating sea ice, which is recorded by satellites (Fig. 4.2 a-c) and probably leads to substantial annual phytoplankton blooms, which may also cause the elevated TOC content in the corresponding seafloor sediment sample (Fig. 4.3 a). Alternatively, remobilization of shelf sediments or vertical mixing of iron-rich deep waters, leading to high iron contents in surface waters, may stimulate primary

productivity (Blain et al., 2007; De Jong et al., 2012). However, it remains unclear why the brassicasterol concentration is distinctly low in this sample, and we assume that different environmental preferences of the source organisms may account for this. In Drake Passage and along the EAP, brassicasterol displays a similar pattern as HBI Z-triene, with relatively high concentrations (more than 2 orders of magnitudes) ranging from 1.86 to 5017.44  $\mu\text{g}^*\text{g OC}^{-1}$  (Fig. 4.3 d).

In the Weddell Sea, TOC contents are generally low ( $< 0.4\%$ ), with slightly elevated values in the West (up to 0.50 %) and right in front of the Filchner Ice Shelf (up to 0.52 %; Fig. 4.3 a). The Amundsen Sea is characterized by slightly higher TOC contents, with concentrations of up to 0.91 % in the West and lower values in the East (0.33 %; Fig. 4.3 a; AS).

In the samples from the Amundsen and Weddell seas, that both are dominated by strong winter sea-ice cover lasting until spring (Fig. 4.2 a-c), all three biomarkers are present in low concentrations only. An exception are the samples located in front of the Filchner Ice Shelf with significantly higher concentrations of IPSO<sub>25</sub> (7.09-73.87  $\mu\text{g}^*\text{g OC}^{-1}$ ; Fig. 4.3 b; WS). Concentrations of IPSO<sub>25</sub> on the Amundsen Sea shelf are relatively low (0.04-3.3  $\mu\text{g}^*\text{g OC}^{-1}$ ), with slightly higher values observed in the north-east (Fig. 4.3 b; AS). HBI Z-triene concentrations are also very low, but slightly higher in Filchner Trough (0.04-1  $\mu\text{g}^*\text{g OC}^{-1}$ ) and at more distal locations on the northeastern Amundsen Sea shelf (0.01-1.88  $\mu\text{g}^*\text{g OC}^{-1}$ ; Fig. 4.3 c). Brassicasterol generally shows a similar pattern as HBI Z-triene, with concentrations varying between 1.86 and 220.54  $\mu\text{g}^*\text{g OC}^{-1}$  (Fig. 4.3 d; for HBI E-triene and dinosterol distribution, see Fig. S4.1).

#### 4.4.2 Combining individual biomarker records: the PIPSO<sub>25</sub> index

The PIPSO<sub>25</sub> index combines the relative concentrations of IPSO<sub>25</sub> and a selected phytoplankton biomarker, such as HBI-trienes and sterols, as indicator for an open-ocean environment (Vorrath et al., 2019). The combination of both end members (sea ice vs. open-ocean) prevents misleading interpretations regarding the absence of IPSO<sub>25</sub> in the sediments, which can be the result of two entirely different scenarios. Under heavy/perennial sea-ice coverage, the thickness of sea ice hinders light penetration, thereby limiting the productivity of algae living in basal sea ice (Hancke et al., 2018). This scenario can cause the absence of both phytoplankton and sea-ice biomarkers in the sediment. The other scenario depicts a permanently open ocean, where the sea-ice biomarker is absent as well, but here the phytoplankton biomarkers are present in variable concentrations (Müller et al., 2011). The presence of both biomarkers in the sediment is indicative of seasonal sea-ice coverage and/or the occurrence of stable sea-ice margin conditions, promoting biosynthesis of both biomarkers (Müller et al., 2011). We here distinguish between P<sub>Z</sub>IPSO<sub>25</sub> and P<sub>B</sub>IPSO<sub>25</sub> using HBI Z-triene and brassicasterol as phytoplankton biomarker, respectively (Fig. 4.4 a+b; for PIPSO<sub>25</sub> values based on HBI E-triene and dinosterol see Table S4.1 and Fig. S4.2).

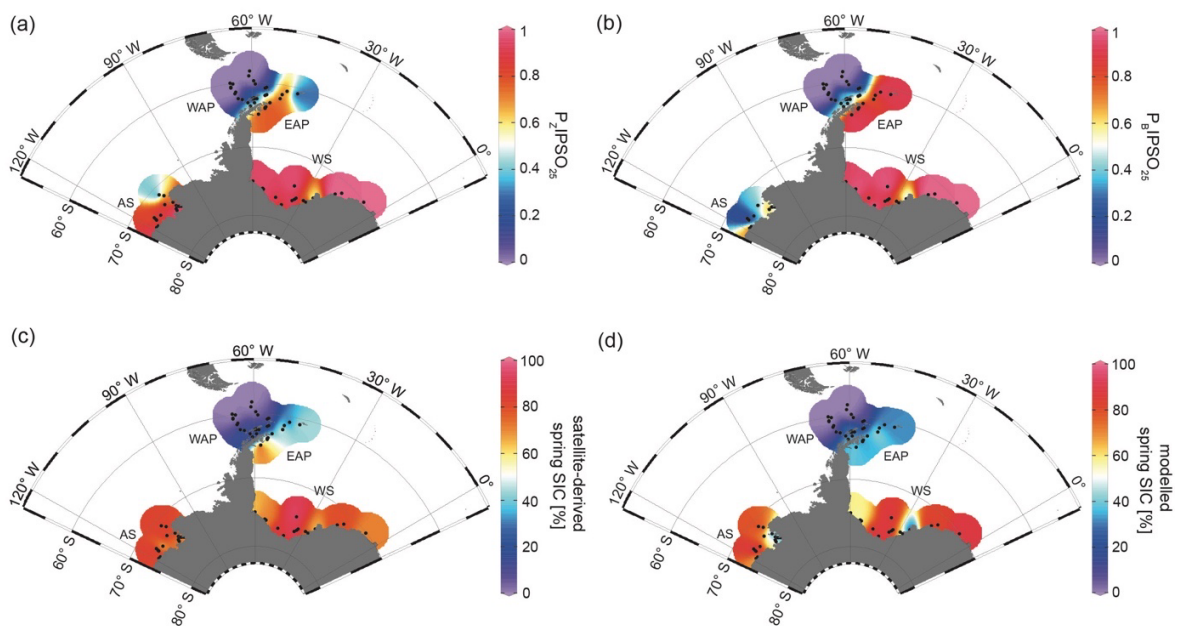


Fig. 4.4: Distribution of the sea-ice index PIPSO<sub>25</sub> in surface sediment samples, with (a) P<sub>Z</sub>IPSO<sub>25</sub> based on HBI Z-triene and (b) P<sub>B</sub>IPSO<sub>25</sub> based on brassicasterol, (c) satellite-derived spring SIC [%] and (d) modelled spring SIC [%]. AS: Amundsen Sea, WAP: West Antarctic Peninsula, EAP: East Antarctic Peninsula, WS: Weddell Sea.

Both PIPSO<sub>25</sub> indices are 0 in the predominantly ice-free Drake Passage and increase towards southeast to intermediate values on the WAP slope and around the South Shetland Islands, reflecting increased influence of marginal sea-ice cover towards the coast (0.02-0.70; Vorrath et al., 2019). At the seasonally sea-ice covered EAP, P<sub>Z</sub>IPSO<sub>25</sub> values reach 0.84, while lower values of around 0.25 are observed close to the South Orkney Islands, which is caused by the elevated HBI Z-triene concentrations at the stations there (Fig. 4.3 c; EAP). The P<sub>B</sub>IPSO<sub>25</sub> index exhibits even higher values of up to 0.98 at the EAP/northwestern Weddell Sea. These elevated PIPSO<sub>25</sub> indices align well with the significant northward sea-ice drift within the Weddell Gyre, which leads to prolonged sea-ice cover along the EAP.

In samples from the southern Weddell Sea, both PIPSO<sub>25</sub> indices show a similar pattern with high values up to 0.9, and slightly lower values in front of the Brunt Ice Shelf (0.6; Fig. 4.4 a+b). Very low concentrations (close to detection limit) of both biomarkers in samples from the continental shelf off Dronning Maud Land (Fig. 4.1) result in low PIPSO<sub>25</sub> values, strongly underestimating the sea-ice cover in this area, where satellite-derived sea-ice data document severe seasonal sea-ice cover (Fig. 4.2). As previously mentioned, we followed the approach by Müller and Stein (2014) and Lamping et al. (2020) by assigning a maximum PIPSO<sub>25</sub> value of 1 to these samples to circumvent misleading interpretations and aid visualization.

The intermediate PIPSO<sub>25</sub> value (~0.51) derived for one sample collected in front of the Brunt Ice Shelf points to a less severe sea-ice cover in that area. A possible explanation for the relatively low PIPSO<sub>25</sub> value is the presence of a coastal polynya that has been reported by Anderson (1993) and which is further supported by Paul et al. (2015). These authors note that the sea-ice area around the Brunt Ice Shelf is the most active in the southern Weddell Sea, with an annual average polynya area of  $3516 \pm 1420$  km<sup>2</sup>. Interestingly, the reduced SIC here is also captured by our model (see chapter 4.4.3).

PIPISO<sub>25</sub> values in the Amundsen Sea point to different scenarios. The P<sub>Z</sub>IPSO<sub>25</sub> index varies around 0.9, with only the easterly, more distal samples having lower values between 0.3 and 0.6 (Fig. 4.4 a). The P<sub>B</sub>IPSO<sub>25</sub> index generally has lower values, ranging from 0.6 in the coastal area to 0.2 in the more distal samples (Fig. 4.4 b). This difference between P<sub>Z</sub>IPSO<sub>25</sub> and P<sub>B</sub>IPSO<sub>25</sub> may be explained by the different source organisms biosynthesizing the individual phytoplankton biomarkers. While the main origin of HBI-

trienes seems to be restricted to diatoms (Belt et al., 2017), brassicasterol is known to be produced by several algal groups that are adapted to a wider range of sea surface conditions (Volkman, 2006; see chapter 4.5.2).

#### 4.4.3 Biomarker-based sea ice estimates vs. satellite and model data

The main ice algae bloom in the Southern Ocean occurs during spring, when solar insolation and air temperatures/SSTs increase and sea ice starts to melt, which results in the release of nutrients and stratification of the water column stimulating the productivity of photosynthesizing organisms (Arrigo, 2017; Belt, 2018). The sea-ice biomarker IPSO<sub>25</sub> is hence commonly interpreted as a spring sea-ice indicator, which is why, in the following, we compare the biomarker-based sea-ice reconstructions to satellite-derived and modelled spring SIC. IPSO<sub>25</sub> concentrations in the surface sediments around the Antarctic Peninsula exhibit similar trends as the satellite-derived and modelled SIC (Figs. 4.3 + 4.4), while they differ significantly in the Amundsen and Weddell seas, where high SIC are recorded by satellites and the model but IPSO<sub>25</sub> is present in low concentrations. The low IPSO<sub>25</sub> concentrations in these areas highlight the uncertainty, when considering IPSO<sub>25</sub> as a sea-ice proxy alone, since such low concentrations are not only observed under open water conditions, but also under severe sea-ice cover. In the Amundsen and Weddell seas, the low IPSO<sub>25</sub> concentrations are the result of the latter, where limited light availability hinders ice algae growth, leading to an underestimation of sea-ice cover. Accordingly, we note a weak correlation between IPSO<sub>25</sub> data and satellite SIC ( $R^2 = 0.19$ ; Fig. 4.5 a). As stated above, the combination of IPSO<sub>25</sub> and a phytoplankton marker may prevent this ambiguity. The higher sea-ice concentrations in the Amundsen and Weddell seas are better reflected by maximum P<sub>Z</sub>IPSO<sub>25</sub> values than by IPSO<sub>25</sub> alone. However, we note that the P<sub>Z</sub>IPSO<sub>25</sub> index apparently does not resolve SICs higher than 50 % (see Fig. S4.3), which may indicate a threshold (here ~50 % SIC) where the growth of the HBI-triene and IPSO<sub>25</sub> producing algae is limited.

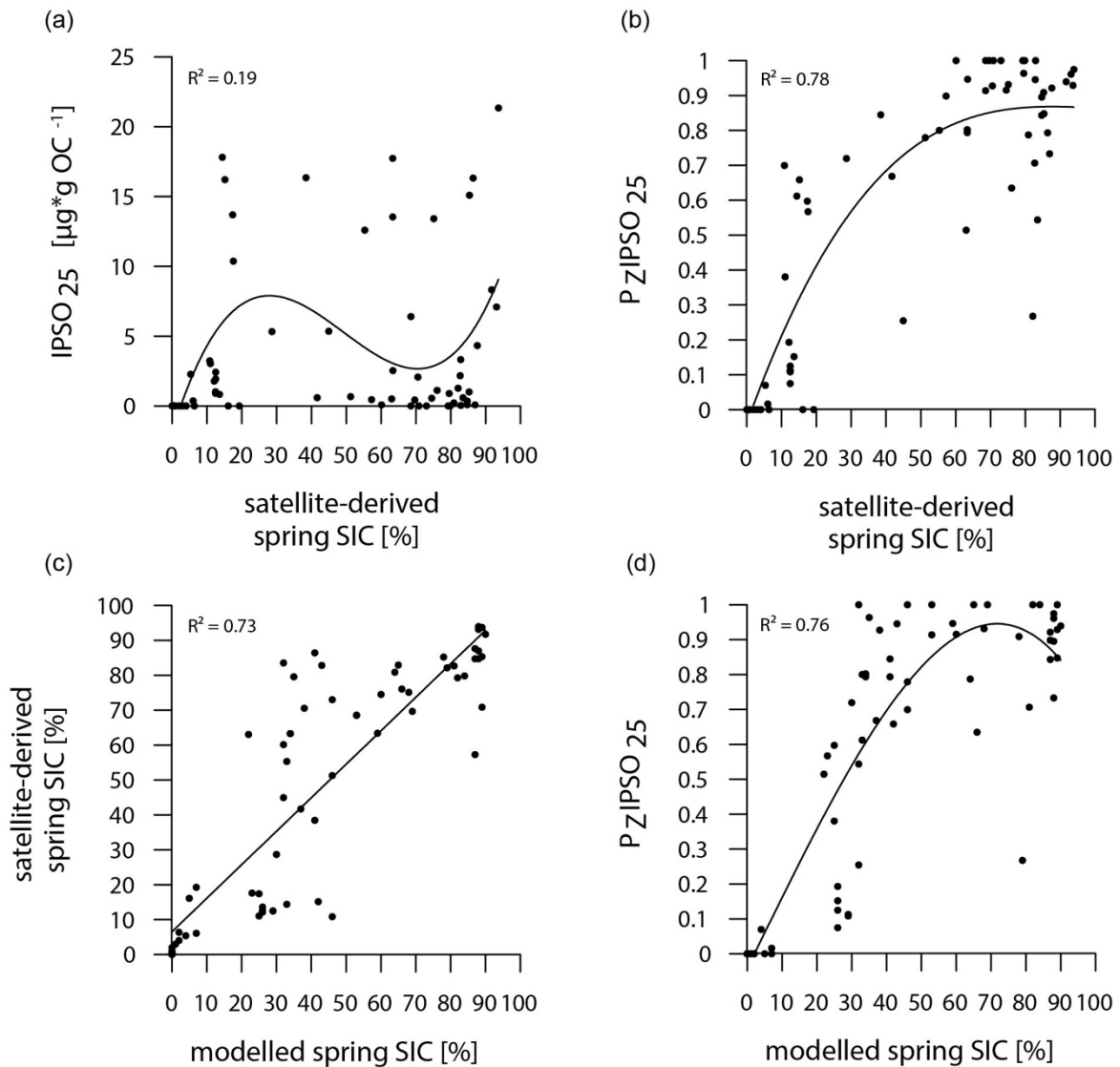


Fig. 4.5: Correlations of (a) IPSO<sub>25</sub> concentrations vs. satellite-derived spring SIC, (b) P<sub>Z</sub>IPSO<sub>25</sub> values vs. satellite-derived spring SIC, (c) satellite-derived spring SIC vs. modelled spring SIC and (d) P<sub>Z</sub>IPSO<sub>25</sub> values vs. modelled spring SIC. Coefficients of determination ( $R^2$ ) are given for the respective regression lines.

In general, however, the P<sub>Z</sub>IPSO<sub>25</sub> values correlate much better with satellite and modelled SIC ( $R^2 = 0.78$  and  $R^2 = 0.76$ , respectively; Fig. 4.5 b+d) than IPSO<sub>25</sub> concentrations. Correlations of satellite and model data with PIPSO<sub>25</sub> calculated using the HBI E-triene, brassicasterol and dinosterol, respectively, are also positive but less significant (Fig. S4.4), and we hence focus the discussion on P<sub>Z</sub>IPSO<sub>25</sub>. The AWI-ESM2-derived spring SICs correctly display the permanently ice-free Drake Passage and the northwest-southeast increase in sea-ice cover from the WAP continental slope towards Bransfield Strait (Fig. 4.4 d). The model, however, significantly underestimates the elevated sea-ice concentrations (up to 70 %) in front of the former Larsen Ice Shelf A

and east of James Ross Island at the EAP observed in satellite data. In the Amundsen and Weddell seas, the model predicts heavy sea-ice cover ( $\sim 90\%$ ), only slightly underestimating the sea-ice cover at the near-coastal sites in front of Pine Island Glacier (PIG) and Ronne Ice Shelf. Interestingly, modelled SIC in front of Brunt Ice Shelf is as low as  $\sim 45\%$  (Fig. 4.4 d+e), corresponding well with the reduced  $P_Z\text{IPSO}_{25}$  value of  $\sim 0.51$ . This may reflect the polynya conditions in that region documented by Anderson (1993) and Paul et al. (2015). Overall, we note that modelled modern SICs correlate well with satellite data ( $R^2 = 0.73$ ; Fig. 4.5 c) and  $P_Z\text{IPSO}_{25}$  values ( $R^2 = 0.76$ ; Fig. 4.5 d), while we observe weaker correlations between modelled paleo-SICs and  $P_Z\text{IPSO}_{25}$  values (Fig. S4.5; see chapter 4.5.1).

#### 4.4.4 $\text{TEX}^{\text{L}_{86}}$ - and RI-OH'-derived ocean temperatures

For a critical appraisal of the applicability and reliability of GDGT indices as temperature proxies in polar latitudes, we here focus on the  $\text{TEX}^{\text{L}_{86}}$  proxy by Kim et al. (2012), which potentially reflects SOTs, and the RI-OH' proxy by Lü et al. (2015), which is assumed to reflect SSTs. The reconstructions are believed to represent annual mean ocean temperatures (for correlations of  $\text{TEX}^{\text{L}_{86}}$ -derived SOTs with WOA spring and winter SOTs, see Fig. S4.6). In all samples, the BIT-index (Eq. 6) is  $< 0.3$ , indicating no significant impact of terrestrial input of organic material on the distribution of GDGTs and hence their reliability as temperature proxy. RI-OH'-derived temperatures and  $\text{TEX}^{\text{L}_{86}}$ -derived SOTs both show a similar pattern, but different temperature ranges between  $-2.62$  to  $+4.67\text{ }^\circ\text{C}$  and  $-2.38$  to  $+8.75\text{ }^\circ\text{C}$ , respectively (Fig. 4.6 a+b). At the WAP, RI-OH'- as well as  $\text{TEX}^{\text{L}_{86}}$ -derived temperatures increase northwestwards across the Antarctic continental slope and into the permanently ice-free Drake Passage, which are influenced by the ACC and relatively warm CDW (Orsi et al., 1995; Rintoul et al., 2001). Temperatures decrease towards Bransfield Strait and the EAP, which are influenced by seasonal sea-ice cover and relatively cold water from the Weddell Sea that branches off the Weddell Gyre (Collares et al., 2018; Thompson et al., 2009). At the EAP, a southwestward decrease is observed, with relatively low temperatures at the former Larsen A Ice Shelf and higher temperatures recorded in Powell Basin and around the South Orkney Islands (Fig. 4.6 a+b).

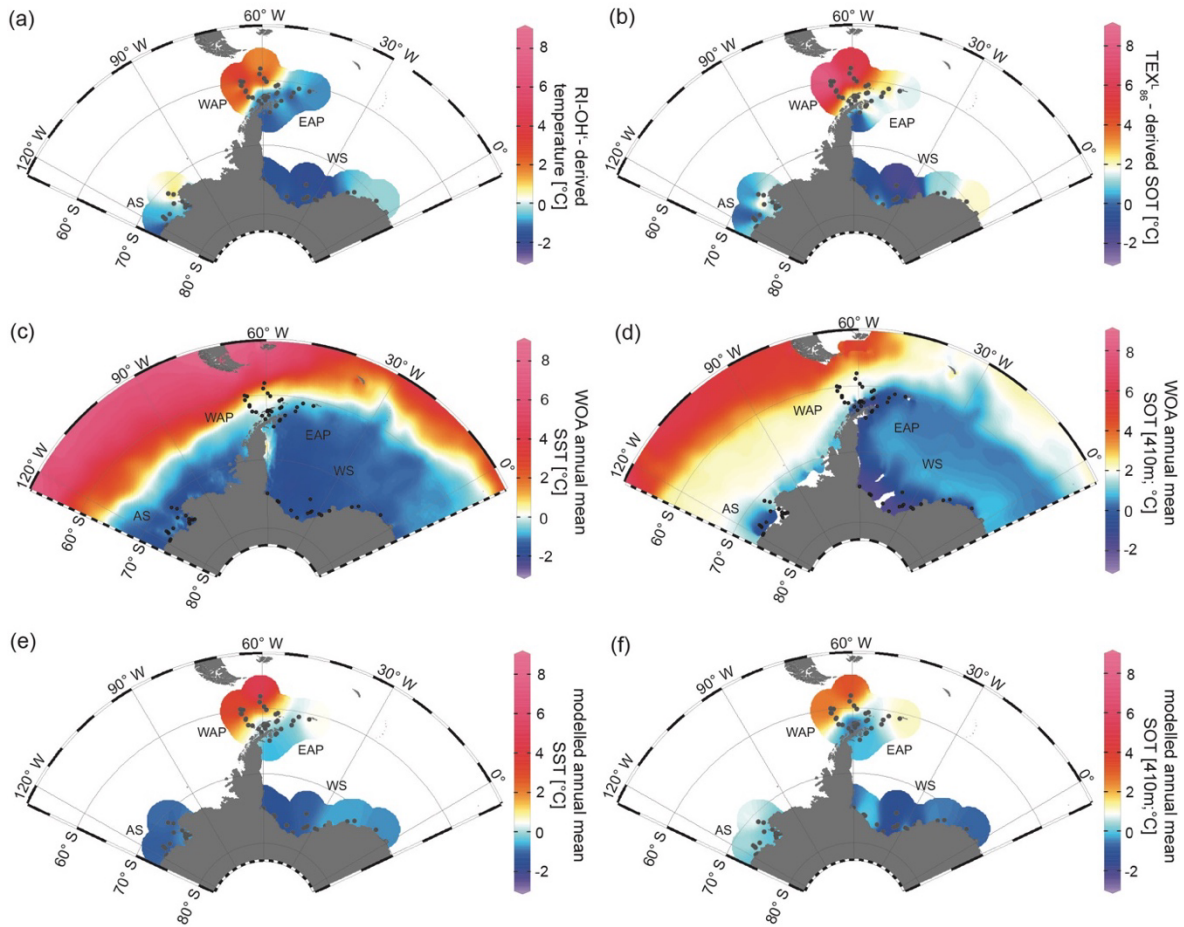


Fig. 4.6: Annual mean temperature distributions with (a) RI-OH'-derived temperature, (b)  $\text{TEX}^{\text{L}}_{86}$ -derived SOT, (c) WOA13 SST (Locarnini et al., 2013), (d) WOA13 SOT (410 m; Locarnini et al., 2013), (e) modelled SST and (f) modelled SOT (410 m) in °C. AS: Amundsen Sea, WAP: West Antarctic Peninsula, EAP: East Antarctic Peninsula, WS: Weddell Sea.

In the Amundsen and Weddell seas further south, reconstructed temperatures are generally lower than around the Antarctic Peninsula. Samples from the Weddell Sea display a temperature decrease from east to west, which may reflect the route of eddies in the northeastern Weddell Gyre. These eddies carry relatively warm, salty CDW westward along the southern limb of the Weddell Gyre, where it becomes WDW (Vernet et al., 2019). Coldest  $\text{TEX}^{\text{L}}_{86}$  and RI-OH' temperatures ( $<0$  °C) at sites along the Filchner-Ronne Ice Shelf front may be further linked to the presence of cold precursor water masses for WSBW.

With regard to ongoing discussions, whether GDGT-based temperature reconstructions represent SSTs or SOTs (Kalanetra et al., 2009; Kim et al., 2012; Park et al., 2019), we here compare our RI-OH' and  $\text{TEX}^{\text{L}}_{86}$ -derived temperatures with surface



and subsurface temperature data obtained by in-situ measurements and modelling (Fig. 4.6 c-f). Comparison of GDGT-derived temperatures with WOA13 temperatures from different water depths reveals the most significant correlation for a water depth of 410 m (for respective correlations, see Fig. S4.7). When discussing instrumental and modelled SOTs, we hence refer to 410 m water depth.

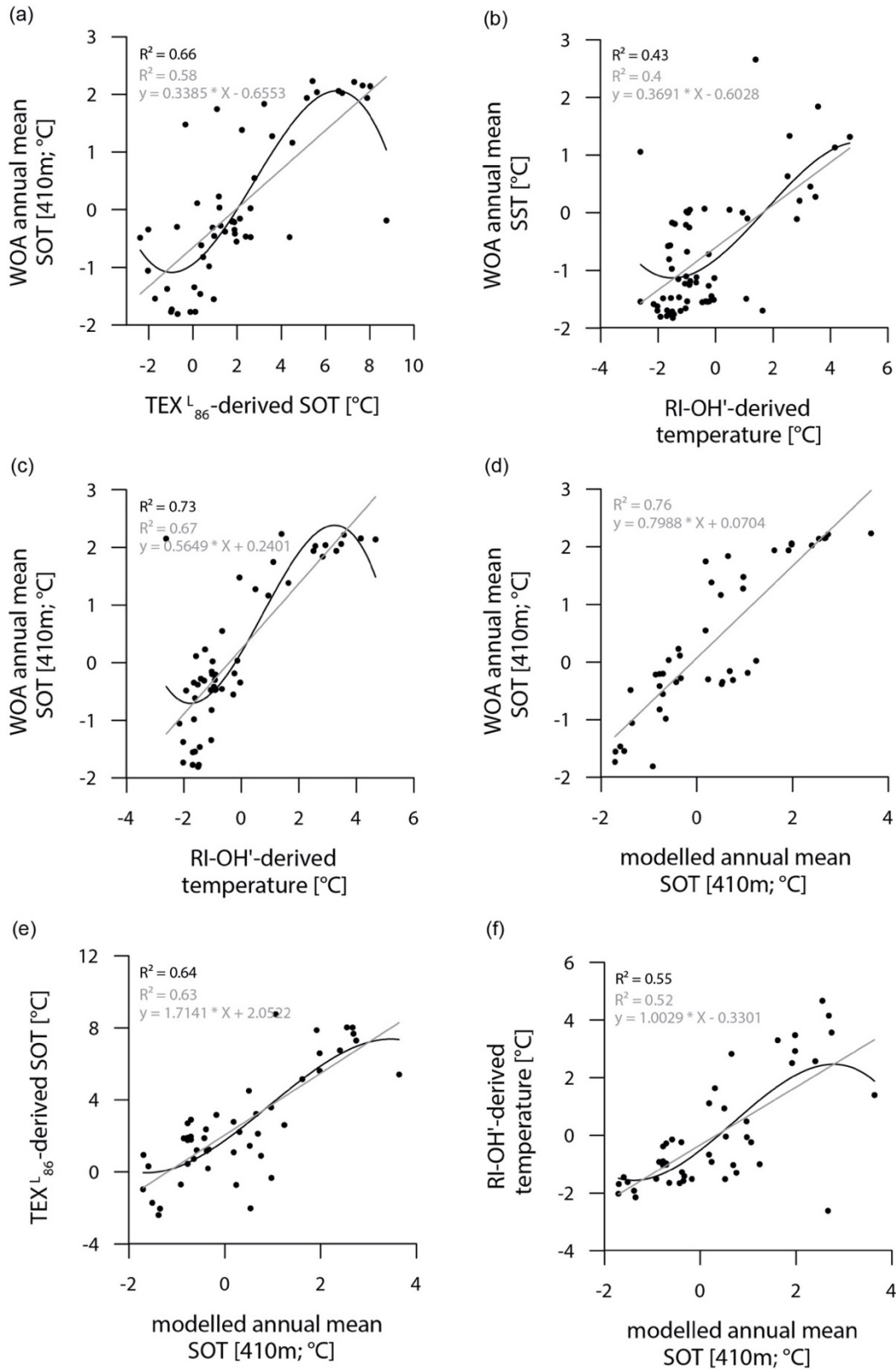


Fig. 4.7: Correlations of (a) WOA annual mean SOT (410 m) vs.  $\text{TEX}^{\text{L}}_{86}$ -derived SOT, (b) WOA annual mean SST vs. RI-OH'-derived temperature, (c) WOA annual mean SOT (410 m) vs. RI-OH'-derived temperature, (d) WOA annual mean SOT (410 m) vs. modelled annual mean SOT (410 m), (e)  $\text{TEX}^{\text{L}}_{86}$ -derived SOT vs. modelled annual mean SOT (410 m), (f) RI-OH'-derived temperature vs. modelled annual mean SOT (410 m) in °C. Coefficients of determination ( $R^2$ ) are given for the respective regression lines.

While the correlation between TEX<sup>L</sup><sub>86</sub>-derived SOTs and instrumental SOTs is reasonably good (Fig. 4.7 a;  $R^2 = 0.66$ ), also supporting a subsurface origin for the TEX<sup>L</sup><sub>86</sub> proxy, we note a significant overestimation of SOTs by up to 6 °C in Drake Passage (Fig. S4.8). This warm-biased TEX<sup>L</sup><sub>86</sub> signal is a known caveat and is, among others, assumed to be connected to GDGTs produced by deep-dwelling Euryarchaeota (Park et al., 2019), which have been reported in CDW (Alonso-Sáez et al., 2011) and in deep waters at the Antarctic Polar Front (López-García et al., 2001). Maximum TEX<sup>L</sup><sub>86</sub>-based SOTs of 5 °C - 8 °C in central Drake Passage (Fig. 4.6 b), however, distinctly exceed the common temperature range of CDW (0-2 °C). Interestingly, TEX<sup>L</sup><sub>86</sub>-derived SOTs in the colder regions of the Amundsen and Weddell seas relate reasonably well to instrumental temperatures and are only slightly warm-biased (Fig. S4.8). Correlations between RI-OH'-derived temperatures and instrumental SSTs are weak ( $R^2 = 0.43$ ; Fig. 4.7 b). Recently, Liu et al. (2020) concluded in their study on surface sediments from Prydz Bay (East Antarctica), that also the RI-OH' index holds promise as a tool to reconstruct SOTs rather than SSTs. When correlating our RI-OH'-derived temperatures with instrumental SOTs, we similarly find a high correlation ( $R^2 = 0.73$ ; Fig. 4.7 c), hence supporting this hypothesis. We further note that the RI-OH' temperature range is much more realistic than the TEX<sup>L</sup><sub>86</sub> range. This suggests that the addition of OH-isoGDGTs in the temperature index is a promising step towards reliable high latitude temperature reconstructions and may improve our understanding of the temperature responses of archaeal membranes in Southern Ocean waters (Fietz et al., 2020; Park et al., 2019). Clearly, more data – ideally obtained from sediment traps, seafloor surface sediment samples and longer sediment cores – and calibration studies will help to further elucidate the applicability of the RI-OH' and TEX<sup>L</sup><sub>86</sub> temperature reconstructions.

Similar to the model-derived sea-ice data, we also evaluate the model's performance in depicting ocean temperatures (Fig. 4.6 e+f). Modelled annual mean SSTs and SOTs are highest (with up to 5 °C and 3 °C, respectively) in the permanently ice-free Drake Passage, which is influenced by the relatively warm ACC. Lower SSTs are predicted for the Antarctic Peninsula continental slope and Bransfield Strait (~0.5 to 1 °C), coinciding with the increase in the duration of seasonal sea-ice cover in that area. At the EAP/northwestern Weddell Sea, modelled SSTs as well as SOTs increase from southwest to northeast towards Powell Basin. In the Amundsen and Weddell seas,

annual mean SSTs are negative, with temperatures ranging from -1 to -0.5 °C, while SOTs are positive in the Amundsen Sea and negative in the Weddell Sea. Overall, we note that modelled SOTs reflect instrumental SOTs reasonably well ( $R^2 = 0.76$ ; Fig. 4.7 d). Interestingly, while RI-OH<sup>2</sup>-derived SOTs relate better to instrumental SOTs (than TEX<sup>L</sup><sub>86</sub>-based SOTs), a better correlation between TEX<sup>L</sup><sub>86</sub>-derived SOTs and modelled SOTs ( $R^2 = 0.64$ ; Fig. 4.7 e) and a weaker correlation with Ri-OH<sup>2</sup>-derived temperatures ( $R^2 = 0.55$ ; Fig. 4.7 f) is found.

#### 4.5 Caveats and recommendations for future research

Marine core top studies evaluating the applicability and reliability of climate proxies are often affected by limitations and uncertainties regarding the age control of the investigated seafloor surface sediments as well as the production, preservation and degradation of target compounds. In the following, we shortly address some of these factors and provide brief recommendations for future investigations.

##### 4.5.1 Age control

Information on the actual age of the surface sediment samples is a major requirement determining their suitability to reflect modern sea surface conditions. When comparing sea-ice conditions or ocean temperatures estimated from biomarker data obtained from 0.5-1 cm thick surface sediment samples (easily spanning decades to millennia, depending on sedimentation rates) with satellite-derived sea-ice data or instrumental records (covering only the past ~40 and 65 years, respectively), the different time periods reflected in the data sets need to be considered when interpreting the results. To address the issue of lacking age constraints for most of the surface sediments investigated here, we also performed paleoclimate simulations providing sea-ice concentration data for three time slices (2 ka, 4 ka and 6 ka BP; see Fig. S4.5) to evaluate if the surface sediments may have recorded significantly older environmental conditions. Correlations of PIPSO<sub>25</sub> values with these paleo sea-ice concentrations are notably weaker (Fig. S4.5) than the correlations with recent (1951-2014 CE) SIC model output, which points to a young to modern age of the majority of the studied sediments. This is further supported by AMS <sup>14</sup>C-dating of calcareous microfossils and <sup>210</sup>Pb-dating of seafloor surface

sediments from the Amundsen Sea shelf documenting recent ages for most sites (Hillenbrand et al., 2010, 2013, 2017; Smith et al., 2011, 2014, 2017; Witus et al., 2014) as well as modern  $^{210}\text{Pb}$ -dates obtained for three multicores collected in Bransfield Strait (PS97/56, PS97/68, PS97/72; Vorrath et al., 2020). AMS  $^{14}\text{C}$  dates obtained for nearby seafloor surface sediments in the vicinity of the South Shetland Islands and the Antarctic Sound revealed ages of 100 years and 142 years BP, respectively (Vorrath et al., 2019). As both uncorrected ages lie within the range of the modern marine reservoir effect (e.g. Gordon and Harkness, 1992), we consider these two dates still as recent. However, in an area that is significantly affected by rapid climate warming over the past decades and a regionally variable sea-ice coverage, the age uncertainties for at least  $^{14}\text{C}$  dated samples may easily lead to an over- or underestimation of biomarker-based sea-ice cover and ocean temperatures, respectively, which needs to be taken into account for comparisons with instrumental data. The utilization of (paleo-) model data may alleviate the lack of age control for each seafloor sediment sample to some extent. Nevertheless, we recommend that for a robust calibration of e.g., PIPSO<sub>25</sub> values against satellite-derived sea-ice concentrations only surface sediment samples with a modern age confirmed by  $^{210}\text{Pb}$ -dating are incorporated.

#### 4.5.2 Production and preservation of biomarkers

Biomarkers have the potential to reveal the former occurrence of their producers, which requires knowledge of the source organisms. While there is general consensus on Thaumarchaeota being the major source for iso-GDGTs (Fietz et al., 2020 and references therein) and diatoms synthesizing HBIs (Volkman, 2006), the main source of brassicasterol, which is not only found in diatoms but also in dinoflagellates and haptophytes (Volkman, 2006), remains unclear. Accordingly, the use of brassicasterol to determine the PIPSO<sub>25</sub> index may introduce uncertainties regarding the environmental information recorded by this phytoplankton biomarker. A further aspect concerns the different chemical structures of HBIs and sterols, which raises the risk of a selective degradation (see Belt, 2018 and Rontani et al., 2018; 2019 for detailed discussion) with potentially considerable effects on the PIPSO<sub>25</sub> index. Regarding the different areas investigated in our study, also spatially different microbial communities and varying depositional regimes, such as sedimentation rate, redox conditions and water depth, may

lead to different degradation patterns. This means that variations in the biomarker concentrations between different areas may not strictly reflect changes in the production of these compounds (driven by sea surface conditions) but may also relate to different degradation states. In particular, lower sedimentation rates and thus extended oxygen exposure times promote chemical alteration and degradation processes (Hedges et al., 1990; Schouten et al., 2013). However, it has been previously reported that the formation of mineral aggregates and fecal pellets often accelerates the transport of organic matter from the sea surface through the water column to the seafloor during the melting season, leading to a more rapid burial and hence better preservation of the organic compounds (Bauerfeind et al., 2005; Etourneau et al., 2019; Müller et al., 2011).

Another rather technical drawback concerning the use of the PIPSO<sub>25</sub> index occurs when the concentrations of the sea-ice proxy IPSO<sub>25</sub> and the phytoplankton marker are similarly low (due to unfavorable conditions for both ice algae and phytoplankton) or similarly high (due to a significant seasonal shift in sea-ice cover and/or stable ice edge conditions). This may lead to similar PIPSO<sub>25</sub> values, although the sea-ice conditions are fundamentally different from each other. This scenario is evident for five sampling sites in the Weddell Sea (PS111/13-2, /15-1, /16-3, /29-3, and /40-2; Fig. 4.3 b+c), where IPSO<sub>25</sub> and the HBI Z-triene concentrations are close to the detection limit and P<sub>Z</sub>IPSO<sub>25</sub> values are very low, suggesting a reduced sea-ice cover. Satellite and model data, however, show that these sample locations are influenced by heavy, nearly year-round sea-ice cover. We conclude that biomarker concentrations of both biomarkers at or close to the detection limit need to be treated with caution. Here, we assigned a maximum P<sub>Z</sub>IPSO<sub>25</sub> value of 1 to those samples, and we note that such a practice always needs to be clarified when applying the PIPSO<sub>25</sub> approach. Nonetheless, the coupling of IPSO<sub>25</sub> with a phytoplankton marker provides more reliable sea-ice reconstructions. Regarding all these ambiguities, we recommend not only to calculate the PIPSO<sub>25</sub> index, but also to carefully consider individual biomarker concentrations and, if possible, to utilize other sea-ice proxies, such as data from well-preserved diatom assemblages (Lamping et al., 2020; Vorrath et al., 2019; 2020). While the PIPSO<sub>25</sub> index is not yet a fully quantitative proxy for paleo sea-ice concentrations, several calibration iterations have been applied to the GDGT-paleothermometers (Fietz et al., 2020). As noted above, the observation of distinctly warm-biased TEX<sup>L</sup><sub>86</sub>-derived SOTs calls for further efforts

of regional calibration studies and/or investigations of archaic adaptation strategies at different water depths and under different nutrient and temperature conditions.

#### 4.5.3 The role of platelet ice for the production of IPSO<sub>25</sub>

The sympagic, tube-dwelling, diatom *B. adeliensis* is a common constituent of Antarctic sea ice and preferably flourishes in the relatively open channels of sub-ice platelet layers in near-shore locations covered by fast ice (Medlin, 1990; Riaux-Gobin and Poulin, 2004). Based on investigations of sea-ice samples from the Southern Ocean, Belt et al. (2016) detected this diatom species to be a source of IPSO<sub>25</sub>, which, according to its habitat, led to the assumption of the sea-ice proxy being a potential indicator for the presence of platelet ice. As stated above, *B. adeliensis* is not confined to platelet ice, but is also observed in basal sea ice and described as well adapted to changes in the texture of sea ice during ice melt (Riaux-Gobin et al., 2013). Platelet ice formation, however, plays an important role in sea-ice generation along some coastal regions of Antarctica (Hoppmann et al., 2015; 2020; Lange et al., 1989; Langhorne et al., 2015). In these regions, CDW and High Saline Shelf Water (HSSW) flow into sub-ice shelf cavities of ice shelves and cause basal melting and the discharge of cold and less saline water (Fig. 4.8; Hoppmann et al., 2020, Scambos et al., 2017). The surrounding water is cooled and freshened and is then transported towards the surface. Under the large Filchner-Ronne and Ross ice shelves the pressure relief can cause this water, called Ice Shelf Water (ISW), to be supercooled (Foldvik and Kvinge, 1974). The temperature of the supercooled ISW is typically below the in-situ freezing point, which eventually causes the formation of ice platelets that accumulate under landfast ice attached to adjacent ice shelves (Fig. 4.8; Holland et al., 2007; Hoppmann et al., 2015; 2020).

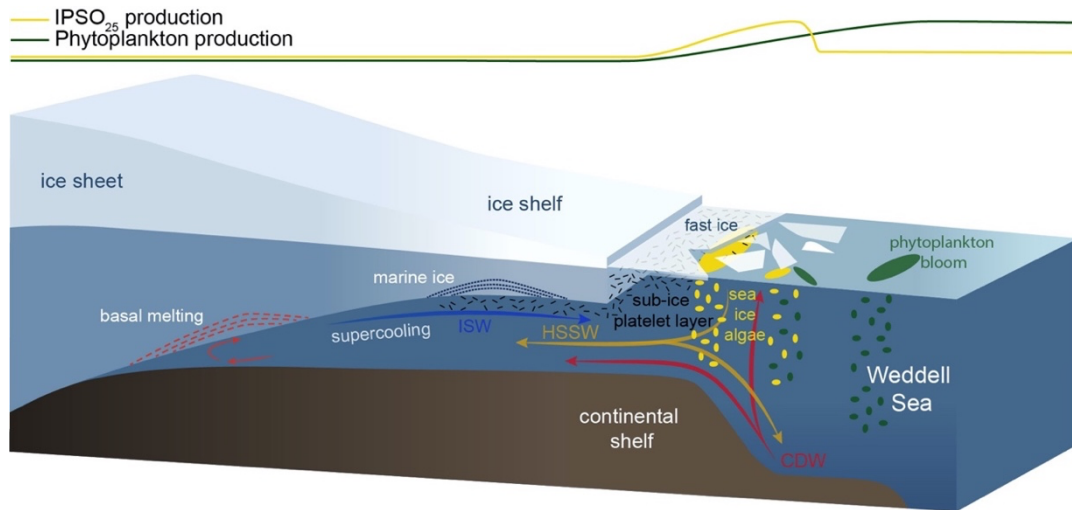


Fig. 4.8: Schematic illustration of the formation of platelet ice and the main production areas of sea ice algae producing IPSO<sub>25</sub> (yellow ellipses) and phytoplankton (green ellipses), also displayed by yellow and green curves at the top. CDW: Circumpolar Deep Water, HSSW: High Saline Shelf Water, ISW: Ice Shelf Water. Illustration modified from Scambos et al. (2017).

In an attempt to elucidate the relationship between IPSO<sub>25</sub> and platelet ice, we investigated our data in respect to locations of observed platelet ice formation. While the maximum IPSO<sub>25</sub> concentrations in front of the Filchner Ice Shelf could be directly related to the above-mentioned platelet ice formation in this area, the elevated IPSO<sub>25</sub> concentrations north of the Larsen C Ice Shelf at the EAP could be linked to several processes. According to Langhorne et al. (2015), sea-ice cores retrieved from that area did not incorporate platelet ice. The high IPSO<sub>25</sub> concentrations could hence be explained by either input from drift ice transported with the Weddell Gyre or by basal freeze-on. However, we note that our samples may reflect much longer time periods than the sea-ice samples investigated by Langhorne et al. (2015) and the lack of platelet ice in their investigated sea-ice cores does not rule out the former presence of platelet ice, which may be captured in our investigated sediment samples.

There are several previous studies on IPSO<sub>25</sub> that reported a close connection of the proxy with proximal, coastal locations and polynyas in the seasonal ice zone (i.e. Collins et al., 2013; Smik et al., 2016b). They do not, however, discuss the relation to adjacent ice shelves as possible “platelet ice factories”. We note that the core locations investigated by Smik et al. (2016b) are in the vicinity of the Moscow University Ice Shelf, where Langhorne et al. (2015) did not observe platelet ice within sea-ice cores. Hoppmann et al. (2020), however, report a sea-ice core from that area, which incorporates platelet ice. The different observations by Langhorne et al. (2015) and



Hoppmann et al. (2020) highlight the temporal variability in the occurrence of platelet ice in the cold water regime around the East Antarctic margin.

For the observed IPSO<sub>25</sub> minimum in the Amundsen Sea (Fig. 4.3 b; AS), which we tentatively relate to the extended and thick sea-ice coverage, the absence of platelet ice there is an alternative explanation. The Amundsen/Bellingshausen seas and WAP shelves are classified as “warm shelves” (Thompson et al., 2018), where the upwelling of warm CDW (Schmidtke et al., 2014) hinders the formation of ISW, which makes the presence of platelet ice under recent conditions highly unlikely (Hoppmann et al., 2020). This is also supported by Langhorne et al. (2015), who stated that platelet ice formation is not observed in areas where basal ice-shelf melting is considerable, such as on the West Antarctic continental shelf in the eastern Pacific sector of the Southern Ocean (Thompson et al., 2018). Accordingly, if the formation and accumulation of platelet ice – up to a certain degree – indicates sub-ice shelf melting on “cold shelves” (Hoppmann et al., 2015; Thompson et al., 2018), high IPSO<sub>25</sub> concentrations found in marine sediments may hence serve as indicator of past ISW formation and associated ice shelf dynamics. This is, however, probably only true up to a certain threshold, where platelet ice formation decreases or is hampered due to warm oceanic conditions causing too intense sub-ice shelf melting (Langhorne et al., 2015).

When using IPSO<sub>25</sub> as a sea-ice proxy in Antarctica, it is important to consider regional platelet ice formation processes, too, because these may affect the IPSO<sub>25</sub> budget. Determining thresholds associated with platelet ice formation is challenging. Therefore, further investigations, such as in-situ measurements of IPSO<sub>25</sub> concentrations in platelet ice or culture experiments in laboratories, are needed to better understand the connection between IPSO<sub>25</sub> and platelet ice formation (and basal ice-shelf melting).

#### 4.6 Conclusions

Biomarker analyses focusing on IPSO<sub>25</sub>, HBI-trienes, phytosterols and GDGTs in surface sediment samples from the Antarctic continental margin were investigated to depict recent sea-ice conditions and ocean temperatures in this climate sensitive region. Proxy-based reconstructions of these key variables were compared to (1) satellite sea-ice

data, (2) instrumental ocean temperature data, and (3) modelled sea-ice patterns and ocean temperatures. The semi-quantitative sea-ice index PIPSO<sub>25</sub>, combining the sea-ice proxy IPSO<sub>25</sub> with an open-water phytoplankton marker, yielded reasonably good correlations with satellite observations and numerical model results, while correlations with the sea-ice proxy IPSO<sub>25</sub> alone are rather low. Minimum concentrations of both biomarkers, used for the PIPSO<sub>25</sub> calculations, may lead to ambiguous interpretations and significant underestimations of sea-ice conditions. Therefore, different sea-ice measures should be considered when interpreting biomarker data.

Ocean temperature reconstructions based on the TEX<sup>L</sup><sub>86</sub>- and RI-OH'-paleothermometers show similar patterns, but different absolute temperatures. While TEX<sup>L</sup><sub>86</sub>-derived temperatures are significantly biased towards warm temperatures in Drake Passage, the RI-OH'-derived temperature range seems more realistic when compared to temperature data based on the WOA13 and modelled annual mean SOTs.

Further investigations of HBI- as well as GDGT-synthesis, transport, deposition and preservation within the sediments would help to guide the proxies' application. Further work on the taxonomy of the IPSO<sub>25</sub> producers, the composition of their habitat (basal sea ice, platelet ice, brine channels) and its connection to platelet ice formation via in-situ or laboratory measurements are required to better constrain the IPSO<sub>25</sub> potential as a robust sea-ice biomarker. The presumed relationship between IPSO<sub>25</sub> and platelet ice formation in connection to sub-ice shelf melting is supported by our data, showing high IPSO<sub>25</sub> concentrations in areas with known platelet ice formation and low IPSO<sub>25</sub> concentrations in areas without observed platelet ice formation. Accordingly, oceanic conditions and the intensity of sub-ice shelf melting need to be considered when using IPSO<sub>25</sub> (1) as an indirect indicator for sub-ice shelf melting processes and associated ice shelf dynamics and (2) for the application of the PIPSO<sub>25</sub> index to estimate sea-ice coverage.

## 4.7 Supplements

Table S4.1: Station list, TOC and biomarker data. Stations with \* are previously published data by Vorrath et al. (2019). PIPSO<sub>25</sub> indices for each sampling site were calculated using a concentration balance factor (c). PIPSO<sub>25</sub> values displayed in italics have been set to 1.

| Station Nr. | Long [°E] | Lat [°N] | Water<br>Depth [m] | TOC<br>[wt. %] | IPSO <sub>25</sub><br>[µg/g OC] | HBI Z-Triene<br>[µg/g OC] | HBI E-Triene<br>[µg/g OC] | Brassicasterol<br>[µg/g OC] | Dinosterol<br>[µg/g OC] |
|-------------|-----------|----------|--------------------|----------------|---------------------------------|---------------------------|---------------------------|-----------------------------|-------------------------|
| PS69/251-1  |           |          |                    |                |                                 |                           |                           |                             |                         |
| PS69/255-3  | -104,36   | -71,80   | 640                | 0,332          | 2,177                           | 0,490                     | 0,050                     |                             |                         |
| PS69/269-1  | -115,58   | -73,22   | 822                | 0,905          | 0,359                           | 0,036                     | 0                         |                             |                         |
| PS69/272-3  | -118,48   | -73,89   | 1529               | 0,302          | 0,038                           | 0                         | 0                         | 1,859                       | 2,736                   |
| PS69/275-2  | -117,55   | -73,89   | 1472               | 0,454          | 0,214                           | 0,031                     | 0                         | 5,014                       | 5,406                   |
| PS69/283-5  | -115,38   | -72,76   | 588                | 0,525          | 0,083                           | 0,016                     | 0,009                     | 120,480                     | 9,742                   |
| PS69/284-2  | -115,40   | -73,02   | 736                | 0,862          | 0,098                           | 0,006                     | 0,003                     | 171,151                     | 10,869                  |
| PS69/288-3  | -102,99   | -74,42   | 742                | 0,408          | 0,896                           | 0,018                     | 0,003                     | 6,957                       | 6,135                   |
| PS69/292-3  | -105,19   | -74,68   | 1113               | 0,355          | 0,435                           | 0                         | 0                         |                             |                         |
| PS69/297-1  | -103,67   | -74,08   | 460                | 0,425          | 3,327                           | 0,104                     | 0,014                     |                             |                         |
| PS69/299-1  | -103,65   | -73,44   | 685                | 0,446          | 0,590                           | 0,268                     | 0,032                     |                             |                         |
| PS69/302-3  | -105,65   | -71,13   | 544                | 0,165          | 1,267                           | 1,879                     | 0,207                     |                             |                         |
| PS104/012-4 | -101,62   | -74,68   | 358                | 0,224          | 0,081                           | 0                         | 0                         | 26,251                      | 1,950                   |
| PS104/014-2 | -102,59   | -74,55   | 600                | 0,594          | 2,066                           | 0,088                     | 0,031                     | 220,539                     | 20,604                  |
| PS104/017-2 | -104,75   | -74,36   | 1395               | 0,780          | 0,557                           | 0,028                     | 0,010                     | 43,853                      | 5,355                   |
| PS104/022-3 | -107,09   | -72,77   | 733                | 0,585          | 1,013                           | 0,055                     | 0,030                     | 187,134                     | 21,041                  |
| PS104/043-3 | -112,33   | -73,30   | 482                | 0,568          | 0,455                           | 0,028                     | 0,004                     | 107,429                     | 10,574                  |
| PS111/13-2  | -6,85     | -70,09   | 1775               | 0,333          | 0                               | 0,165                     | 0,318                     | 40,070                      | 9,186                   |
| PS111/15-1  | -15,78    | -71,67   | 1405               | 0,278          | 0                               | 0,067                     | 0,128                     | 24,126                      | 5,242                   |
| PS111/16-3  | -17,82    | -72,38   | 1418               | 0,244          | 0                               | 0,084                     | 0,085                     | 41,156                      | 10,205                  |
| PS111/27-1  | -29,08    | -75,95   | 425                | 0,177          | 1,122                           | 0,349                     | 0,171                     | 97,336                      | 6,208                   |
| PS111/29-3  | -27,68    | -75,97   | 411                | 0,112          | 0                               | 0,679                     | 0,413                     | 56,940                      | 6,826                   |
| PS111/40-2  | -54,24    | -76,00   | 513                | 0,453          | 0                               | 0,039                     | 0,029                     | 9,182                       | 2,018                   |
| PS111/42-1  | -53,36    | -76,14   | 493                | 0,382          | 13,414                          | 0,534                     | 0,082                     |                             |                         |
| PS111/47-2  | -60,00    | -74,98   | 660                | 0,504          | 2,530                           | 0,078                     | 0                         | 19,393                      | 4,875                   |
| PS111/53-3  | -54,12    | -76,03   | 497                | 0,461          | 6,404                           | 0,327                     | 0,101                     | 41,099                      | 10,552                  |
| PS111/60-3  | -45,41    | -77,02   | 332                | 0,181          | 4,321                           | 0,200                     | 0,070                     | 61,877                      | 12,996                  |
| PS111/70-2  | -33,65    | -76,11   | 794                | 0,517          | 21,346                          | 0,888                     | 0,158                     | 139,965                     | 8,628                   |
| PS111/80-3  | -35,43    | -76,64   | 932                | 0,420          | 8,322                           | 0,291                     | 0,091                     | 77,550                      | 9,054                   |
| PS111/98-3  | -40,45    | -77,80   | 928                | 0,390          | 15,092                          | 1,467                     | 0,249                     | 33,854                      | 11,943                  |
| PS111/114-3 | -33,93    | -76,38   | 839                | 0,340          | 7,092                           | 0,155                     | 0,068                     | 55,117                      | 5,890                   |
| PS111/131-2 | -36,94    | -74,61   | 387                | 0,076          | 73,873                          | 1,048                     | 0,170                     | 96,421                      | 11,811                  |
| PS111/139-2 | -25,28    | -74,82   | 663                | 0,250          | 0,508                           | 0,260                     | 0,054                     | 74,139                      | 5,370                   |
| PS118/5-3   | -57,75    | -64,98   | 428                | 0,611          | 16,319                          | 2,302                     | 0,556                     | 39,221                      | 10,294                  |
| PS118/8-4   | -55,90    | -63,98   | 414                | 0,826          | 17,736                          | 2,371                     | 0,554                     | 121,049                     | 25,368                  |
| PS118/10-3  | -55,98    | -64,00   | 414                | 0,861          | 13,538                          | 1,906                     | 0,537                     | 127,765                     | 27,221                  |
| PS118/12-2  | -55,74    | -63,81   | 455                | 0,220          | 12,587                          | 1,703                     | 0,626                     | 86,632                      | 22,980                  |
| PS118/24-2  | -51,43    | -62,26   | 3289               | 0,368          | 0,667                           | 0,102                     | 0,062                     | 17,097                      | 3,225                   |
| PS118/38-5  | -54,33    | -63,08   | 415                | 0,813          | 16,347                          | 1,626                     | 0,401                     | 84,665                      | 30,745                  |
| PS118/48-2  | -51,13    | -61,57   | 2908               | 0,218          | 0,591                           | 0,159                     | 0,093                     | 14,873                      | 4,294                   |
| PS118/62-3  | -46,56    | -60,93   | 329                | 0,571          | 5,356                           | 8,491                     | 1,595                     | 58,493                      | 18,327                  |
| PS118/75-1  | -49,65    | -60,85   | 2643               | 0,505          | 5,328                           | 1,124                     | 0,318                     | 27,708                      | 7,728                   |
| PS97/042-1* | -66,10    | -59,85   | 4172               | 0,254          | 0                               | 0,333                     | 0,152                     | 12,997                      | 0,425                   |
| PS97/044-1* | -66,03    | -60,62   | 1203               | 0,081          | 0                               | 1,080                     | 0                         | 143,688                     | 0                       |
| PS97/045-1* | -66,10    | -60,57   | 2292               | 0,118          | 0                               | 1,531                     | 0,386                     | 36,902                      | 3,172                   |
| PS97/046-6* | -65,36    | -60,00   | 2803               | 0,167          | 0                               | 1,359                     | 0,291                     | 214,634                     | 101,809                 |
| PS97/048-1* | -64,89    | -61,44   | 3455               | 0,223          | 0                               | 2,085                     | 0,375                     | 1859,609                    | 73,532                  |
| PS97/049-2* | -64,97    | -61,67   | 3752               | 0,250          | 0                               | 3,924                     | 0,851                     | 719,155                     | 178,446                 |
| PS97/052-3* | -64,30    | -62,51   | 2890               | 0,156          | 0                               | 0,679                     | 0                         | 26,554                      | 0,000                   |
| PS97/053-1* | -63,10    | -62,67   | 2021               | 0,333          | 0                               | 19,350                    | 5,948                     | 13,356                      | 332,868                 |
| PS97/054-2* | -61,35    | -63,24   | 1283               | 0,841          | 3,033                           | 2,675                     | 1,000                     | 337,686                     | 48,579                  |
| PS97/056-1* | -60,45    | -63,76   | 633                | 0,937          | 3,232                           | 0,752                     | 0,290                     | 268,190                     | 17,158                  |
| PS97/059-1* | -59,66    | -62,44   | 354                | 0,588          | 0,835                           | 2,523                     | 1,305                     | 3,386                       | 0,036                   |
| PS97/060-1* | -59,65    | -62,59   | 462                | 0,544          | 1,934                           | 12,937                    | 4,693                     | 5017,437                    | 1983,750                |
| PS97/061-1* | -59,80    | -62,56   | 467                | 0,522          | 1,018                           | 4,341                     | 1,870                     | 302,356                     | 119,512                 |
| PS97/062-1* | -59,86    | -62,57   | 477                | 0,435          | 0,907                           | 4,044                     | 1,787                     | 276,372                     | 88,272                  |
| PS97/065-2* | -59,36    | -62,49   | 480                | 0,592          | 2,416                           | 9,184                     | 4,549                     | 4788,292                    | 1587,309                |
| PS97/067-2* | -59,15    | -62,42   | 793                | 0,172          | 1,785                           | 4,038                     | 1,710                     | 406,567                     | 113,728                 |
| PS97/068-2* | -59,30    | -63,17   | 794                | 0,937          | 16,206                          | 4,558                     | 1,152                     | 2096,690                    | 653,977                 |
| PS97/069-1* | -58,55    | -62,59   | 1642               | 1,022          | 17,814                          | 6,115                     | 1,824                     | 2472,025                    | 774,345                 |
| PS97/072-2* | -56,07    | -62,01   | 1992               | 1,063          | 13,689                          | 4,997                     | 1,277                     | 192,625                     | 40,686                  |
| PS97/073-2* | -55,66    | -61,84   | 2624               | 0,729          | 10,369                          | 4,283                     | 1,451                     | 2388,458                    | 1180,752                |
| PS97/074-1* | -56,35    | -60,87   | 1831               | 0,168          | 0,371                           | 12,075                    | 3,409                     | 1539,629                    | 438,073                 |
| PS97/077-1* | -55,71    | -60,60   | 3587               | 0,430          | 2,267                           | 16,356                    | 4,874                     | 1647,616                    | 589,731                 |
| PS97/079-1* | -59,00    | -60,15   | 3539               | 0,342          | 0                               | 1,893                     | 0,510                     | 479,917                     | 154,400                 |
| PS97/080-2* | -59,64    | -59,68   | 3113               | 0,430          | 0                               | 12,021                    | 2,705                     | 4019,003                    | 1329,129                |
| PS97/083-1* | -60,57    | -58,00   | 3756               | 0,217          | 0                               | 18,256                    | 8,280                     | 686,502                     | 308,610                 |
| PS97/084-2* | -60,88    | -58,87   | 3617               | 0,334          | 0                               | 26,857                    | 13,871                    | 1245,652                    | 648,474                 |

| Station Nr. | P <sub>z</sub> IPSO <sub>25</sub><br>(c=1.847) | P <sub>i</sub> IPSO <sub>25</sub><br>(c=5.413) | P <sub>B</sub> IPSO <sub>25</sub><br>(c=0.009) | P <sub>b</sub> IPSO <sub>25</sub><br>(c=0.027) | TEX <sub>1-86</sub> -derived<br>SOT | RI-OHP-derived<br>SST | BIT-Index<br>(<0.3) |
|-------------|--|--|--|--|-------------------------------------|-----------------------|---------------------|
| PS69/251-1  |  |  |  |  | 2,222                               | 0,738                 | 0,044               |
| PS69/255-3  | 0,71   | 0,889  |  |  | 2,391                               | 1,635                 | 0,000               |
| PS69/269-1  | 0,84   | 1  |  |  | 0,410                               | -0,887                | 0,018               |
| PS69/272-3  | 1  | 1  | 0,691  | 0,339  | 0,468                               | -1,827                | 0,061               |
| PS69/275-2  | 0,79   | 1  | 0,825  | 0,595  | 2,125                               | -1,551                | 0,045               |
| PS69/283-5  | 0,73   | 0,642  | 0,071  | 0,241  | -2,020                              | -1,027                | 0,026               |
| PS69/284-2  | 0,90   | 0,852  | 0,060  | 0,252  | 1,970                               | -0,041                | 0,023               |
| PS69/288-3  | 0,96   | 0,983  | 0,934  | 0,845  | 2,135                               | -0,991                | 0,027               |
| PS69/292-3  | 1  | 1  |  |  |                                     |                       |                     |
| PS69/297-1  | 0,95   | 0,978  |  |  | -0,717                              | -0,344                | 0,025               |
| PS69/299-1  | 0,54   | 0,775  |  |  | 1,487                               | 1,069                 | 0,032               |
| PS69/302-3  | 0,27   | 0,531  |  |  | -0,339                              | -0,064                | 0,006               |
| PS104/012-4 | 1  | 1  | 0,254  | 0,607  |                                     | -2,618                | 0,040               |
| PS104/014-2 | 0,93   | 0,925  | 0,509  | 0,789  | -0,984                              | -0,219                | 0,005               |
| PS104/017-2 | 0,92   | 0,915  | 0,584  | 0,795  | 2,812                               | -0,459                | 0,047               |
| PS104/022-3 | 0,91   | 0,864  | 0,374  | 0,642  | 2,784                               | -0,666                | 0,000               |
| PS104/043-3 | 0,90   | 0,954  | 0,319  | 0,616  | -0,723                              | -0,917                | 0,026               |
| PS111/13-2  | <i>l</i>                                       | <i>l</i>                                       | <i>l</i>                                       | <i>l</i>                                       | 1,969                               | -0,279                | 0,006               |
| PS111/15-1  | <i>l</i>                                       | <i>l</i>                                       | <i>l</i>                                       | <i>l</i>                                       | 1,202                               | -0,142                | 0,006               |
| PS111/16-3  | <i>l</i>                                       | <i>l</i>                                       | <i>l</i>                                       | <i>l</i>                                       | 1,174                               | -1,271                | 0,010               |
| PS111/27-1  | 0,63   | 0,548  | 0,560  | 0,871  | 0,058                               | -1,048                | 0,009               |
| PS111/29-3  | <i>l</i>                                       | <i>l</i>                                       | <i>l</i>                                       | <i>l</i>                                       | -1,164                              | -2,025                | 0,007               |
| PS111/40-2  | <i>l</i>                                       | <i>l</i>                                       | <i>l</i>                                       | <i>l</i>                                       | -0,987                              | -1,696                | 0,041               |
| PS111/42-1  | 0,93   | 0,968  |  |  |                                     |                       |                     |
| PS111/47-2  | 0,95   | 1  | 0,935  | 0,951  | -0,114                              | -1,509                | 0,009               |
| PS111/53-3  | 0,91   | 0,921  | 0,945  | 0,958  | -0,697                              | -1,486                | 0,015               |
| PS111/60-3  | 0,92   | 0,919  | 0,885  | 0,925  | 0,105                               | -1,220                | 0,007               |
| PS111/70-2  | 0,93   | 0,962  | 0,944  | 0,989  | -1,785                              | -1,452                | 0,009               |
| PS111/80-3  | 0,94   | 0,944  | 0,922  | 0,972  | 0,326                               | -1,689                | 0,008               |
| PS111/98-3  | 0,85   | 0,918  | 0,980  | 0,979  | 0,945                               | -2,026                | 0,004               |
| PS111/114-3 | 0,96   | 0,950  | 0,934  | 0,978  | -0,957                              | -1,618                | 0,005               |
| PS111/131-2 | 0,97   | 0,988  | 0,988  | 0,996  | -1,710                              | -1,919                | 0,000               |
| PS111/139-2 | 0,51   | 0,636  | 0,431  | 0,779  | -2,384                              | -2,153                | 0,004               |
| PS118/5-3   | 0,79   | 0,844  | 0,979  | 0,983  | -2,036                              | -1,616                | 0,019               |
| PS118/8-4   | 0,80   | 0,855  | 0,942  | 0,963  | 0,372                               | -1,067                | 0,030               |
| PS118/10-3  | 0,79   | 0,823  | 0,921  | 0,949  | 2,611                               | -0,911                | 0,029               |
| PS118/12-2  | 0,80   | 0,788  | 0,941  | 0,953  | 4,374                               | -0,676                | 0,041               |
| PS118/24-2  | 0,78   | 0,667  | 0,812  | 0,885  | 0,967                               | -1,298                | 0,021               |
| PS118/38-5  | 0,84   | 0,883  | 0,955  | 0,952  | 0,896                               | -0,237                | 0,023               |
| PS118/48-2  | 0,67   | 0,540  | 0,815  | 0,837  | 2,367                               | -1,520                | 0,019               |
| PS118/62-3  | 0,25   | 0,383  | 0,910  | 0,916  | 1,455                               | -0,997                | 0,019               |
| PS118/75-1  | 0,72   | 0,756  | 0,955  | 0,962  | 2,606                               | -0,239                | 0,016               |
| PS97/042-1* | 0  | 0  | 0  | 0  | 8,755                               | 3,568                 | 0,024               |
| PS97/044-1* | 0  | 0  | 0  | 0  | 7,293                               | -2,618                | 0,009               |
| PS97/045-1* | 0  | 0  | 0  | 0  | 8,014                               | 4,152                 | 0,004               |
| PS97/046-6* | 0  | 0  | 0  | 0  | 7,671                               | 4,672                 | 0,007               |
| PS97/048-1* | 0  | 0  | 0  | 0  | 8,021                               | 3,474                 | 0,037               |
| PS97/049-2* | 0  | 0  | 0  | 0  | 6,590                               | 2,926                 | 0,016               |
| PS97/052-3* | 0  | 0  | 0  | 0  | 5,610                               | 2,830                 | 0,023               |
| PS97/053-1* | 0  | 0  | 0  | 0  | 3,223                               | 1,109                 | 0,023               |
| PS97/054-2* | 0,38   | 0,359  | 0,498  | 0,699  | 1,093                               | -1,416                | 0,005               |
| PS97/056-1* | 0,70   | 0,673  | 0,571  | 0,875  | 1,254                               | -1,512                | 0,007               |
| PS97/059-1* | 0,15   | 0,106  | 0,965  | 0,999  | 3,168                               | -0,381                | 0,016               |
| PS97/060-1* | 0,07   | 0,071  | 0,041  | 0,035  | 2,699                               | -0,899                | 0,012               |
| PS97/061-1* | 0,11   | 0,091  | 0,271  | 0,241  | 1,770                               | -1,014                | 0,016               |
| PS97/062-1* | 0,11   | 0,086  | 0,266  | 0,277  | 1,797                               | -0,976                | 0,017               |
| PS97/065-2* | 0,12   | 0,089  | 0,053  | 0,054  | 2,903                               | -0,954                | 0,014               |
| PS97/067-2* | 0,19   | 0,162  | 0,327  | 0,369  | 1,899                               | -1,033                | 0,014               |
| PS97/068-2* | 0,66   | 0,722  | 0,461  | 0,480  | 0,457                               | -0,918                | 0,014               |
| PS97/069-1* | 0,61   | 0,643  | 0,443  | 0,461  | 1,873                               | -1,650                | 0,004               |
| PS97/072-2* | 0,60   | 0,664  | 0,887  | 0,926  | 1,880                               | -1,657                | 0,004               |
| PS97/073-2* | 0,57   | 0,569  | 0,324  | 0,246  | 0,190                               | -1,580                | 0,007               |
| PS97/074-1* | 0,02   | 0,020  | 0,026  | 0,031  | 4,504                               | 0,937                 | 0,012               |
| PS97/077-1* | 0,07   | 0,079  | 0,132  | 0,125  | 3,583                               | 0,485                 | 0,007               |
| PS97/079-1* | 0  | 0  | 0  | 0  | 5,152                               | 3,300                 | 0,041               |
| PS97/080-2* | 0  | 0  | 0  | 0  | 7,874                               | 2,509                 | 0,023               |
| PS97/083-1* | 0  | 0  | 0  | 0  | 5,410                               | 1,395                 | 0,007               |
| PS97/084-2* | 0  | 0  | 0  | 0  | 6,754                               | 2,575                 | 0,007               |

Table S4.2: Modelled spring SIC [%] for 1951-2014 CE, 2ka BP, 4ka BP, 6ka BP and modelled annual mean SST and SOT [°C] based on AWIESM2.

| Station Nr. | Modelled Spring SIC 1951-2014 CE [%] | Modelled Spring SIC 2ka BP [%] | Modelled Spring SIC 4ka BP [%] | Modelled Spring SIC 6ka BP [%] | Modelled Annual mean SST [°C] | Modelled Annual mean SOT (410 m) [°C] |
|-------------|--------------------------------------|--------------------------------|--------------------------------|--------------------------------|-------------------------------|---------------------------------------|
| PS69/255-3  | 81                                   | 86                             | 85                             | 86                             | -1,120                        | 0,305                                 |
| PS69/269-1  | 87                                   | 90                             | 90                             | 93                             | -1,215                        | 0                                     |
| PS69/272-3  | 65                                   | 75                             | 75                             | 82                             | -1,028                        | 0                                     |
| PS69/275-2  | 64                                   | 75                             | 74                             | 82                             | -1,073                        | 0                                     |
| PS69/283-5  | 88                                   | 91                             | 90                             | 93                             | -1,153                        | 0,6875                                |
| PS69/284-2  | 88                                   | 91                             | 90                             | 93                             | -1,178                        | 0,535                                 |
| PS69/288-3  | 35                                   | 39                             | 37                             | 41                             | -0,620                        | 0                                     |
| PS69/292-3  | 69                                   | 72                             | 71                             | 71                             | -0,918                        | 0                                     |
| PS69/297-1  | 43                                   | 48                             | 45                             | 51                             | -0,733                        | 0                                     |
| PS69/299-1  | 32                                   | 36                             | 33                             | 36                             | -0,913                        | 0                                     |
| PS69/302-3  | 79                                   | 87                             | 87                             | 90                             | -0,960                        | 0,97                                  |
| PS104/012-4 | 32                                   | 35                             | 32                             | 36                             | -0,700                        | 0                                     |
| PS104/014-2 | 38                                   | 42                             | 40                             | 43                             | -0,675                        | 0                                     |
| PS104/017-2 | 60                                   | 66                             | 63                             | 66                             | -0,775                        | 0                                     |
| PS104/022-3 | 78                                   | 82                             | 81                             | 84                             | -1,185                        | 0,1825                                |
| PS104/043-3 | 87                                   | 91                             | 90                             | 93                             | -1,183                        | 0,2375                                |
| PS111/13-2  | 89                                   | 90                             | 90                             | 90                             | -0,770                        | -0,7125                               |
| PS111/15-1  | 82                                   | 85                             | 85                             | 87                             | -0,673                        | -0,5875                               |
| PS111/16-3  | 84                                   | 87                             | 87                             | 88                             | -0,618                        | -0,385                                |
| PS111/27-1  | 66                                   | 68                             | 68                             | 70                             | -0,828                        | 0                                     |
| PS111/29-3  | 46                                   | 50                             | 50                             | 53                             | -0,725                        | 0                                     |
| PS111/40-2  | 53                                   | 54                             | 54                             | 56                             | -1,458                        | 0                                     |
| PS111/42-1  | 68                                   | 68                             | 68                             | 69                             | -1,465                        | 0                                     |
| PS111/47-2  | 59                                   | 61                             | 62                             | 64                             | -1,408                        | -0,92                                 |
| PS111/53-3  | 53                                   | 54                             | 54                             | 56                             | -1,458                        | 0                                     |
| PS111/60-3  | 87                                   | 86                             | 85                             | 87                             | -1,543                        | 0                                     |
| PS111/70-2  | 89                                   | 89                             | 89                             | 90                             | -1,165                        | -1,5975                               |
| PS111/80-3  | 90                                   | 89                             | 89                             | 89                             | -1,263                        | -1,7                                  |
| PS111/98-3  | 89                                   | 87                             | 86                             | 88                             | -1,295                        | -1,7075                               |
| PS111/114-3 | 88                                   | 87                             | 88                             | 88                             | -1,073                        | -1,5175                               |
| PS111/131-2 | 88                                   | 88                             | 89                             | 90                             | -1,183                        | -1,385                                |
| PS111/139-2 | 22                                   | 26                             | 28                             | 30                             | -0,563                        | -1,3525                               |
| PS118/5-3   | 41                                   | 47                             | 51                             | 56                             | -0,743                        | 0                                     |
| PS118/8-4   | 34                                   | 43                             | 45                             | 49                             | -0,493                        | 0                                     |
| PS118/10-3  | 34                                   | 43                             | 45                             | 49                             | -0,493                        | 0                                     |
| PS118/12-2  | 33                                   | 42                             | 44                             | 49                             | -0,333                        | 0                                     |
| PS118/24-2  | 46                                   | 58                             | 62                             | 67                             | -0,320                        | 0,755                                 |
| PS118/38-5  | 41                                   | 54                             | 56                             | 62                             | -0,525                        | -0,3975                               |
| PS118/48-2  | 37                                   | 51                             | 55                             | 62                             | -0,188                        | 0,52                                  |
| PS118/62-3  | 32                                   | 50                             | 53                             | 65                             | 0,548                         | 1,2375                                |
| PS118/75-1  | 30                                   | 45                             | 49                             | 59                             | 0,273                         | 1,0625                                |
| PS97/042-1* | 0                                    | 1                              | 1                              | 3                              | 3,608                         | 2,74                                  |
| PS97/044-1* | 0                                    | 1                              | 2                              | 5                              | 3,300                         | 2,665                                 |
| PS97/045-1* | 0                                    | 1                              | 1                              | 4                              | 3,408                         | 2,685                                 |
| PS97/046-6* | 0                                    | 1                              | 2                              | 5                              | 2,968                         | 2,55                                  |
| PS97/048-1* | 2                                    | 9                              | 10                             | 17                             | 1,638                         | 1,98                                  |
| PS97/049-2* | 2                                    | 9                              | 10                             | 17                             | 1,638                         | 1,98                                  |
| PS97/052-3* | 5                                    | 18                             | 20                             | 36                             | 1,095                         | 0,6525                                |
| PS97/053-1* | 7                                    | 20                             | 24                             | 40                             | 0,855                         | 0,185                                 |
| PS97/054-2* | 25                                   | 44                             | 49                             | 64                             | 0,508                         | -0,335                                |
| PS97/056-1* | 46                                   | 55                             | 58                             | 63                             | 0,078                         | -0,175                                |
| PS97/059-1* | 26                                   | 44                             | 49                             | 61                             | 0,103                         | -0,7775                               |
| PS97/060-1* | 26                                   | 44                             | 49                             | 61                             | 0,103                         | -0,7775                               |
| PS97/061-1* | 29                                   | 47                             | 52                             | 63                             | 0,138                         | -0,71                                 |
| PS97/062-1* | 29                                   | 47                             | 52                             | 63                             | 0,138                         | -0,71                                 |
| PS97/065-2* | 26                                   | 44                             | 49                             | 61                             | 0,103                         | -0,7775                               |
| PS97/067-2* | 26                                   | 44                             | 49                             | 61                             | 0,103                         | -0,7775                               |
| PS97/068-2* | 42                                   | 54                             | 57                             | 65                             | -0,020                        | -0,86                                 |
| PS97/069-1* | 33                                   | 50                             | 55                             | 65                             | 0,005                         | -0,65                                 |
| PS97/072-2* | 25                                   | 41                             | 46                             | 57                             | -0,068                        | -0,4325                               |
| PS97/073-2* | 23                                   | 39                             | 44                             | 55                             | 0,098                         | -0,3525                               |
| PS97/074-1* | 7                                    | 17                             | 19                             | 33                             | 0,778                         | 0,5                                   |
| PS97/077-1* | 4                                    | 11                             | 12                             | 25                             | 1,503                         | 0,965                                 |
| PS97/079-1* | 1                                    | 5                              | 6                              | 12                             | 2,188                         | 1,6175                                |
| PS97/080-2* | 0                                    | 2                              | 3                              | 7                              | 2,400                         | 1,915                                 |
| PS97/083-1* | 0                                    | 0                              | 0                              | 0                              | 5,443                         | 3,64                                  |
| PS97/084-2* | 0                                    | 1                              | 1                              | 4                              | 3,168                         | 2,4025                                |

Table S4.3: Satellite-derived mean monthly sea ice concentrations for spring (SON), summer (DJF) and winter (JJA) including standard deviations. Data are averaged over the period from October 1978 to February of the individual expedition year; PS69 (2006), PS97 (2016), PS104 (2017), PS111 (2018), PS118 (2019). Downloaded from the National Snow and Ice Data Center, NSIDC; Cavalieri et al. (1996).

| Station Nr. | Satellite Winter SIC [%] | Satellite Winter SIC SD [%] | Satellite Spring SIC [%] | Satellite Spring SIC SD [%] | Satellite Summer SIC [%] | Satellite Summer SIC SD [%] |
|-------------|--------------------------|-----------------------------|--------------------------|-----------------------------|--------------------------|-----------------------------|
| PS69/255-3  | 78,92                    | 6,62                        | 82,67                    | 8,11                        | 67,76                    | 28,99                       |
| PS69/269-1  | 85,14                    | 6,15                        | 84,72                    | 10,93                       | 19,64                    | 25,03                       |
| PS69/272-3  | 81,61                    | 5,23                        | 82,92                    | 6,24                        | 31,90                    | 31,18                       |
| PS69/275-2  | 80,38                    | 4,95                        | 80,87                    | 7,95                        | 23,91                    | 28,80                       |
| PS69/283-5  | 83,98                    | 6,68                        | 86,97                    | 8,04                        | 35,27                    | 29,35                       |
| PS69/284-2  | 85,14                    | 6,15                        | 84,72                    | 10,93                       | 19,64                    | 25,03                       |
| PS69/288-3  | 84,25                    | 5,84                        | 79,54                    | 15,60                       | 39,53                    | 37,25                       |
| PS69/292-3  | 69,64                    | 3,50                        | 69,62                    | 5,41                        | 53,32                    | 24,08                       |
| PS69/297-1  | 86,54                    | 5,27                        | 82,82                    | 12,38                       | 39,01                    | 32,76                       |
| PS69/299-1  | 84,77                    | 4,96                        | 83,50                    | 10,69                       | 39,75                    | 31,30                       |
| PS69/302-3  | 78,53                    | 6,08                        | 82,11                    | 6,22                        | 63,65                    | 31,01                       |
| PS104/012-4 | 68,24                    | 8,46                        | 60,11                    | 21,90                       | 38,90                    | 38,08                       |
| PS104/014-2 | 78,89                    | 7,00                        | 70,54                    | 21,45                       | 36,09                    | 38,78                       |
| PS104/017-2 | 77,44                    | 4,74                        | 74,50                    | 10,42                       | 33,63                    | 30,52                       |
| PS104/022-3 | 82,07                    | 7,39                        | 85,24                    | 7,46                        | 74,75                    | 30,83                       |
| PS104/043-3 | 75,44                    | 9,00                        | 57,26                    | 22,16                       | 4,04                     | 9,48                        |
| PS111/13-2  | 73,86                    | 3,89                        | 70,85                    | 8,33                        | 34,37                    | 29,55                       |
| PS111/15-1  | 84,31                    | 4,54                        | 79,25                    | 9,38                        | 33,87                    | 28,93                       |
| PS111/16-3  | 84,89                    | 3,61                        | 79,84                    | 8,81                        | 26,49                    | 29,46                       |
| PS111/27-1  | 79,43                    | 2,77                        | 76,06                    | 5,52                        | 24,71                    | 26,65                       |
| PS111/29-3  | 78,20                    | 4,20                        | 73,00                    | 8,30                        | 21,96                    | 24,62                       |
| PS111/40-2  | 69,44                    | 4,28                        | 68,56                    | 5,77                        | 59,03                    | 18,00                       |
| PS111/42-1  | 75,78                    | 4,58                        | 75,10                    | 5,89                        | 62,45                    | 21,81                       |
| PS111/47-2  | 64,98                    | 5,90                        | 63,40                    | 8,22                        | 51,93                    | 23,52                       |
| PS111/53-3  | 69,44                    | 4,28                        | 68,56                    | 5,77                        | 59,03                    | 18,00                       |
| PS111/60-3  | 91,46                    | 4,53                        | 87,62                    | 7,71                        | 68,96                    | 23,21                       |
| PS111/70-2  | 94,80                    | 2,35                        | 93,69                    | 3,09                        | 60,07                    | 32,99                       |
| PS111/80-3  | 92,87                    | 3,23                        | 91,74                    | 3,75                        | 65,21                    | 31,29                       |
| PS111/98-3  | 85,85                    | 9,15                        | 85,34                    | 9,54                        | 77,83                    | 22,11                       |
| PS111/114-3 | 94,12                    | 2,60                        | 93,12                    | 3,23                        | 62,40                    | 31,90                       |
| PS111/131-2 | 96,07                    | 2,74                        | 93,95                    | 4,26                        | 74,37                    | 23,46                       |
| PS111/139-2 | 70,15                    | 4,80                        | 63,02                    | 8,55                        | 22,05                    | 20,29                       |
| PS118/5-3   | 93,42                    | 6,37                        | 86,42                    | 18,85                       | 72,37                    | 34,12                       |
| PS118/8-4   | 82,86                    | 11,67                       | 63,30                    | 24,28                       | 37,00                    | 32,60                       |
| PS118/10-3  | 82,86                    | 11,67                       | 63,30                    | 24,28                       | 37,00                    | 32,60                       |
| PS118/12-2  | 77,65                    | 12,41                       | 55,30                    | 25,71                       | 29,20                    | 30,76                       |
| PS118/24-2  | 78,22                    | 12,71                       | 51,26                    | 29,19                       | 18,82                    | 26,86                       |
| PS118/38-5  | 64,28                    | 13,78                       | 38,45                    | 23,52                       | 14,84                    | 21,07                       |
| PS118/48-2  | 71,51                    | 17,07                       | 41,67                    | 30,05                       | 12,64                    | 22,36                       |
| PS118/62-3  | 67,85                    | 19,52                       | 44,97                    | 33,03                       | 5,18                     | 13,78                       |
| PS118/75-1  | 57,79                    | 21,30                       | 28,66                    | 28,08                       | 6,09                     | 14,68                       |
| PS97/042-1* | 1,11                     | 4,94                        | 0,04                     | 0,18                        | 0,00                     | 0,00                        |
| PS97/044-1* | 3,57                     | 9,27                        | 0,88                     | 3,18                        | 0,02                     | 0,22                        |
| PS97/045-1* | 2,58                     | 7,71                        | 0,50                     | 2,04                        | 0,01                     | 0,07                        |
| PS97/046-6* | 2,77                     | 8,44                        | 0,28                     | 1,32                        | 0,00                     | 0,00                        |
| PS97/048-1* | 10,22                    | 17,98                       | 4,03                     | 8,37                        | 0,00                     | 0,00                        |
| PS97/049-2* | 12,83                    | 19,72                       | 6,39                     | 11,65                       | 0,00                     | 0,00                        |
| PS97/052-3* | 22,57                    | 24,72                       | 16,11                    | 21,33                       | 0,38                     | 2,87                        |
| PS97/053-1* | 20,09                    | 24,00                       | 19,26                    | 23,31                       | 0,27                     | 2,38                        |
| PS97/054-2* | 20,47                    | 20,86                       | 11,02                    | 15,35                       | 0,49                     | 0,85                        |
| PS97/056-1* | 25,83                    | 23,05                       | 10,81                    | 16,18                       | 4,79                     | 3,28                        |
| PS97/059-1* | 24,83                    | 20,28                       | 13,59                    | 16,11                       | 4,18                     | 2,24                        |
| PS97/060-1* | 30,02                    | 22,07                       | 12,50                    | 16,84                       | 1,86                     | 2,11                        |
| PS97/061-1* | 27,32                    | 21,31                       | 12,47                    | 16,16                       | 1,83                     | 2,03                        |
| PS97/062-1* | 27,32                    | 21,31                       | 12,47                    | 16,16                       | 1,83                     | 2,03                        |
| PS97/065-2* | 30,02                    | 22,07                       | 12,50                    | 16,84                       | 1,86                     | 2,11                        |
| PS97/067-2* | 31,83                    | 22,64                       | 12,11                    | 17,18                       | 0,82                     | 1,84                        |
| PS97/068-2* | 33,78                    | 23,07                       | 15,15                    | 19,20                       | 4,95                     | 3,40                        |
| PS97/069-1* | 40,52                    | 24,07                       | 14,40                    | 19,80                       | 0,41                     | 2,28                        |
| PS97/072-2* | 50,49                    | 24,76                       | 17,38                    | 22,55                       | 1,38                     | 5,25                        |
| PS97/073-2* | 50,22                    | 25,68                       | 17,58                    | 23,02                       | 1,74                     | 5,98                        |
| PS97/074-1* | 12,39                    | 19,12                       | 6,05                     | 13,40                       | 0,03                     | 0,14                        |
| PS97/077-1* | 11,56                    | 17,68                       | 5,36                     | 11,98                       | 0,04                     | 0,13                        |
| PS97/079-1* | 6,40                     | 15,31                       | 2,98                     | 8,73                        | 0,02                     | 0,26                        |

| Station Nr. | Satellite Winter SIC [%] | Satellite Winter SIC SD [%] | Satellite Spring SIC [%] | Satellite Spring SIC SD [%] | Satellite Summer SIC [%] | Satellite Summer SIC SD [%] |
|-------------|--------------------------|-----------------------------|--------------------------|-----------------------------|--------------------------|-----------------------------|
| PS97/080-2* | 5,03                     | 14,01                       | 1,99                     | 7,37                        | 0,01                     | 0,07                        |
| PS97/083-1* | 0,84                     | 4,21                        | 0,02                     | 0,23                        | 0,00                     | 0,00                        |
| PS97/084-2* | 2,17                     | 9,47                        | 0,38                     | 2,16                        | 0,00                     | 0,00                        |

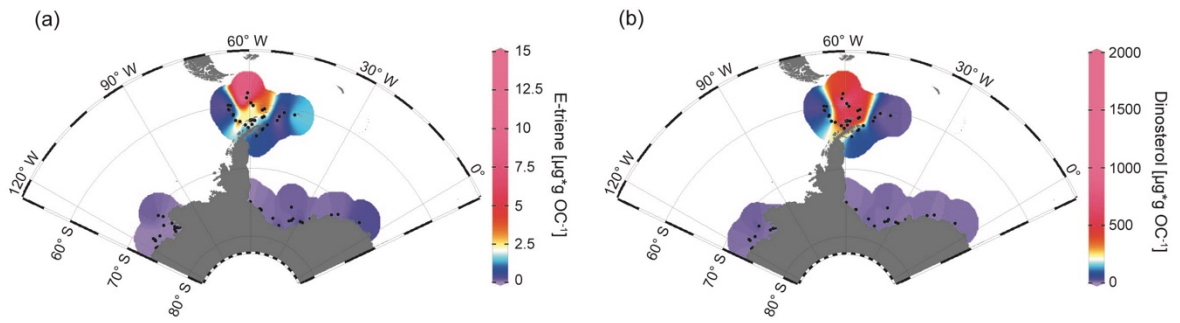


Fig. S4.1: Distribution of (a) HBI E-trienes [ $\mu\text{g} \cdot \text{g OC}^{-1}$ ] and (b) dinosterol [ $\mu\text{g} \cdot \text{g OC}^{-1}$ ] in surface sediment samples.

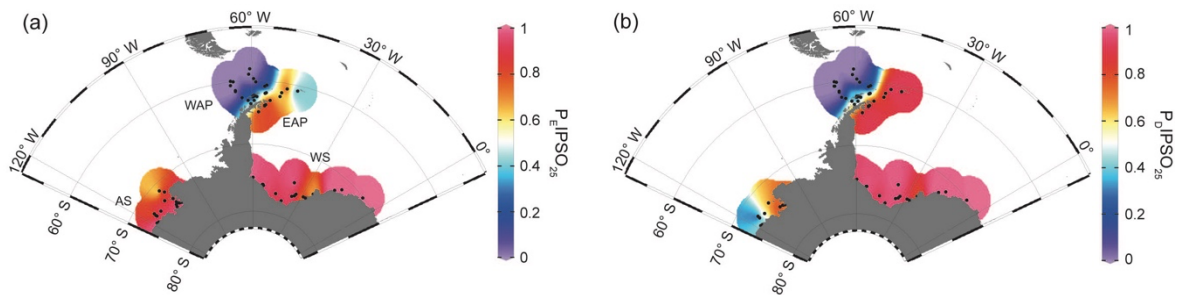


Fig. S4.2: Distribution of (a)  $P_E\text{IPSO}_{25}$  and (b)  $P_D\text{IPSO}_{25}$  in surface sediment samples.

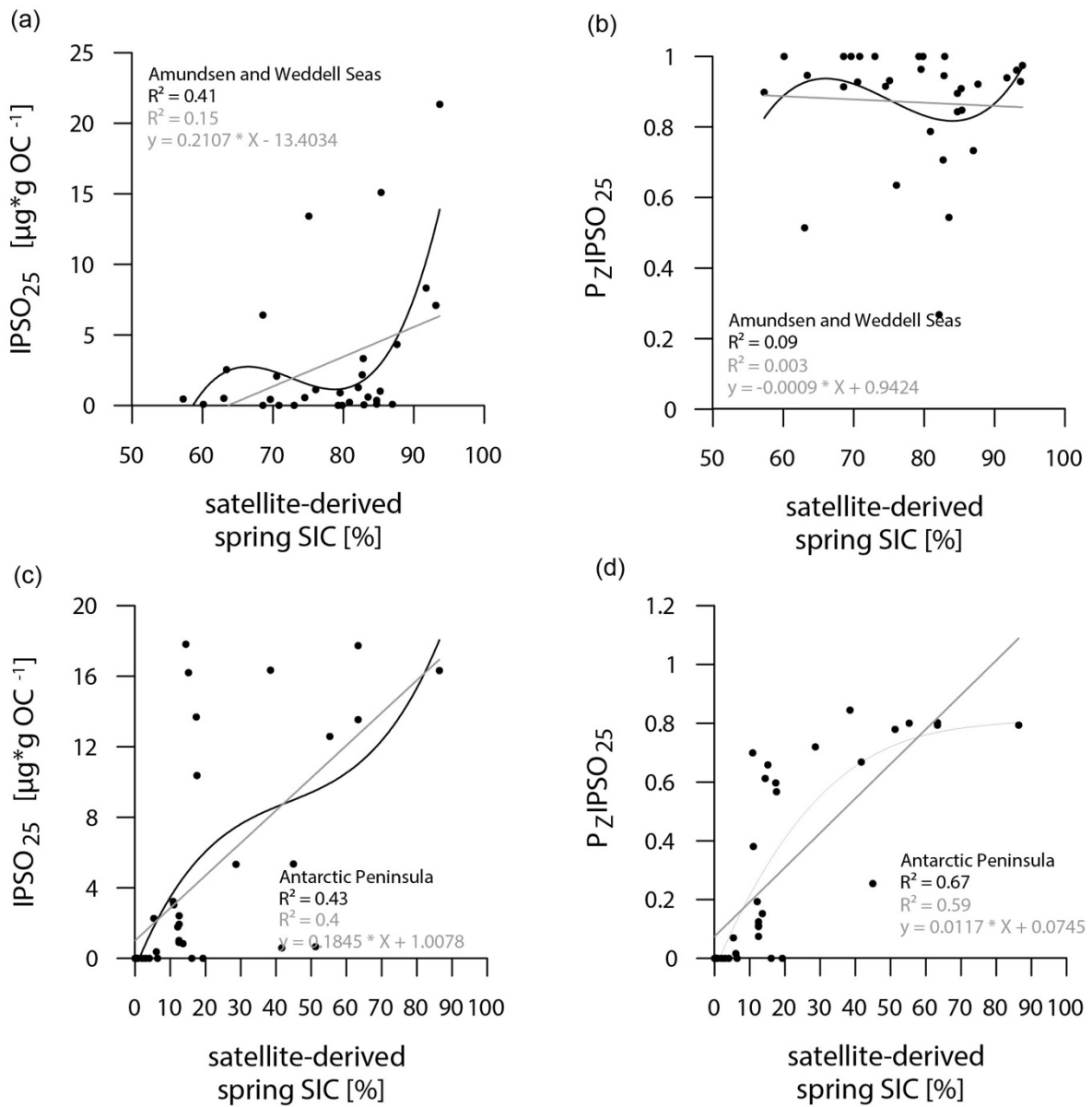


Fig. S4.3: Correlations of (a) IPSO<sub>25</sub> concentrations [ $\mu\text{g} \cdot \text{g OC}^{-1}$ ] vs. satellite-derived spring SIC [%] for the Amundsen and Weddell seas, (b) P<sub>Z</sub>IPSO<sub>25</sub> values vs. satellite-derived spring SIC [%] for the Amundsen and Weddell seas, (c) IPSO<sub>25</sub> concentrations [ $\mu\text{g} \cdot \text{g OC}^{-1}$ ] vs. satellite-derived spring SIC [%] for the Antarctic Peninsula (d) P<sub>Z</sub>IPSO<sub>25</sub> values vs. satellite-derived spring SIC [%] for the Antarctic Peninsula. Coefficients of determination ( $R^2$ ) are given for the respective regression lines.



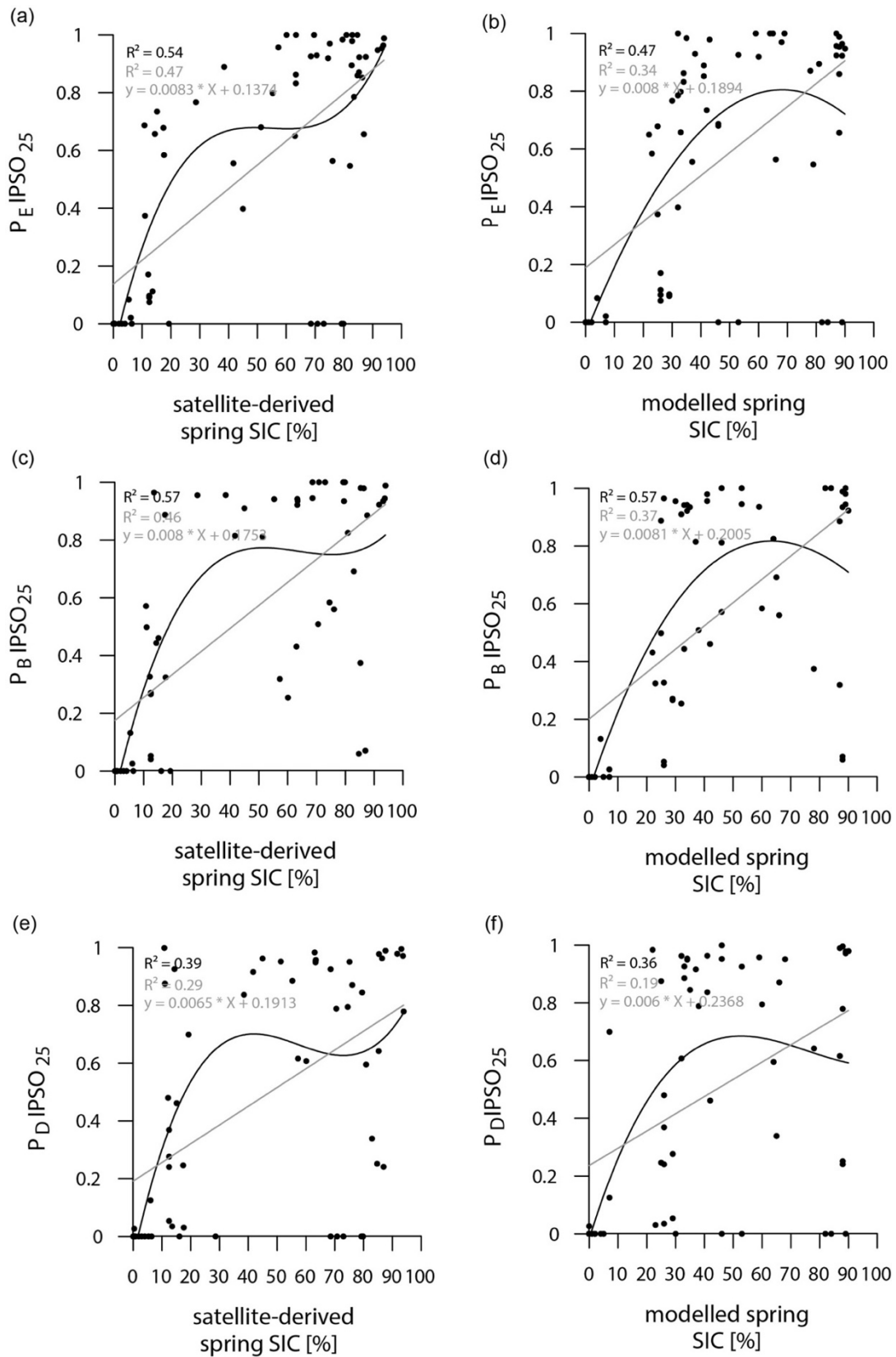


Fig. S4.4: Correlations of (a)  $P_E$ IPSO<sub>25</sub> values vs. satellite-derived spring SIC [%], (b)  $P_E$ IPSO<sub>25</sub> values vs. modelled spring SIC [%], (c)  $P_B$ IPSO<sub>25</sub> values vs. satellite-derived spring SIC [%], (d)  $P_B$ IPSO<sub>25</sub> values vs. modelled spring SIC [%], (e)  $P_D$ IPSO<sub>25</sub> values vs. satellite-derived spring SIC [%] and (f)  $P_D$ IPSO<sub>25</sub> values vs. modelled spring SIC [%]. Coefficients of determination ( $R^2$ ) are given for the respective regression lines.

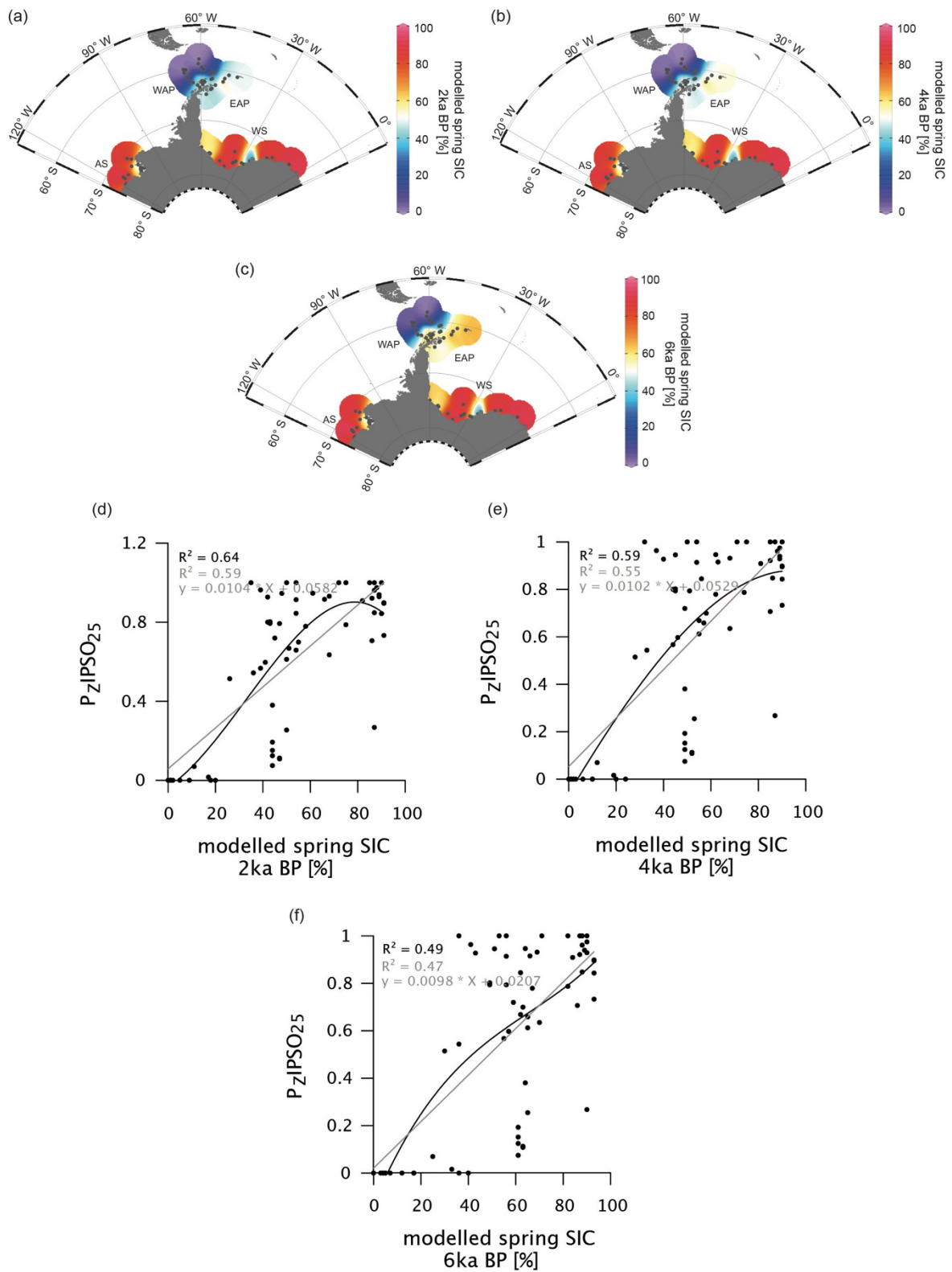


Fig. S4.5: Distribution of modelled spring SIC for (a) 2 ka BP, (b) 4 ka BP, (c) 6 ka BP in %. Correlations of (d) PzIPSO<sub>25</sub> values vs. modelled spring SIC 2 ka BP [%], (e) PzIPSO<sub>25</sub> values vs. modelled spring SIC 4 ka BP [%] and (f) PzIPSO<sub>25</sub> values vs. modelled spring SIC 6 ka BP [%]. Coefficients of determination ( $R^2$ ) are given for the respective regression lines.

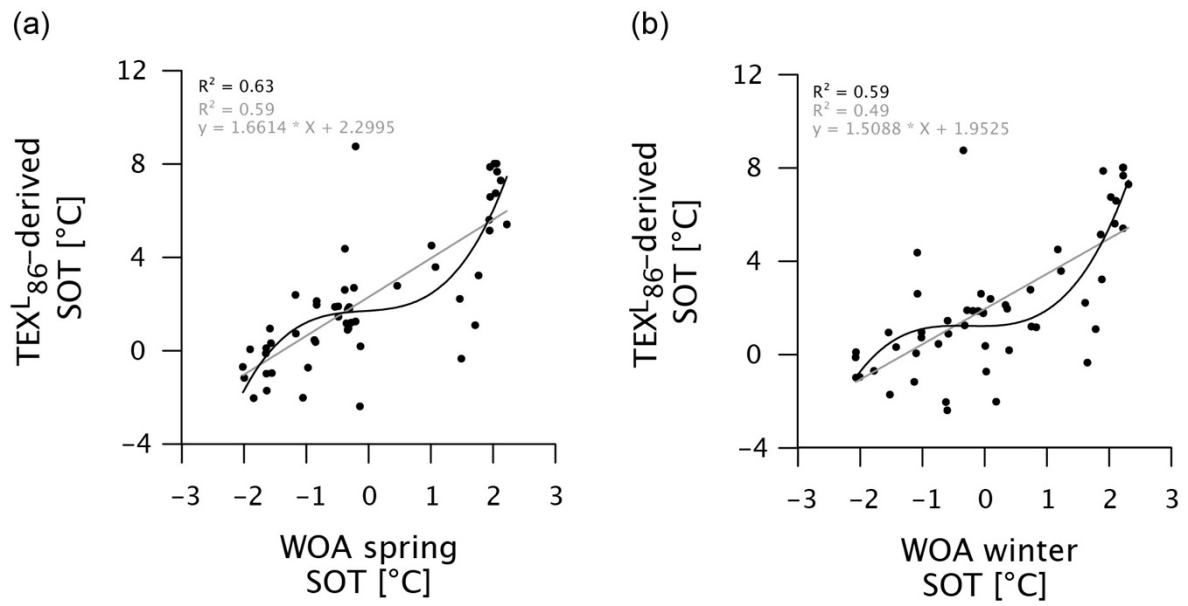


Fig. S4.6: Correlations of (a) TEX<sup>L</sup>-86-derived SOT vs. WOA spring SOT (410 m) and (b) TEX<sup>L</sup>-86-derived SOT vs. WOA winter SOT (410 m) in °C. Coefficients of determination ( $R^2$ ) are given for the respective regression lines.

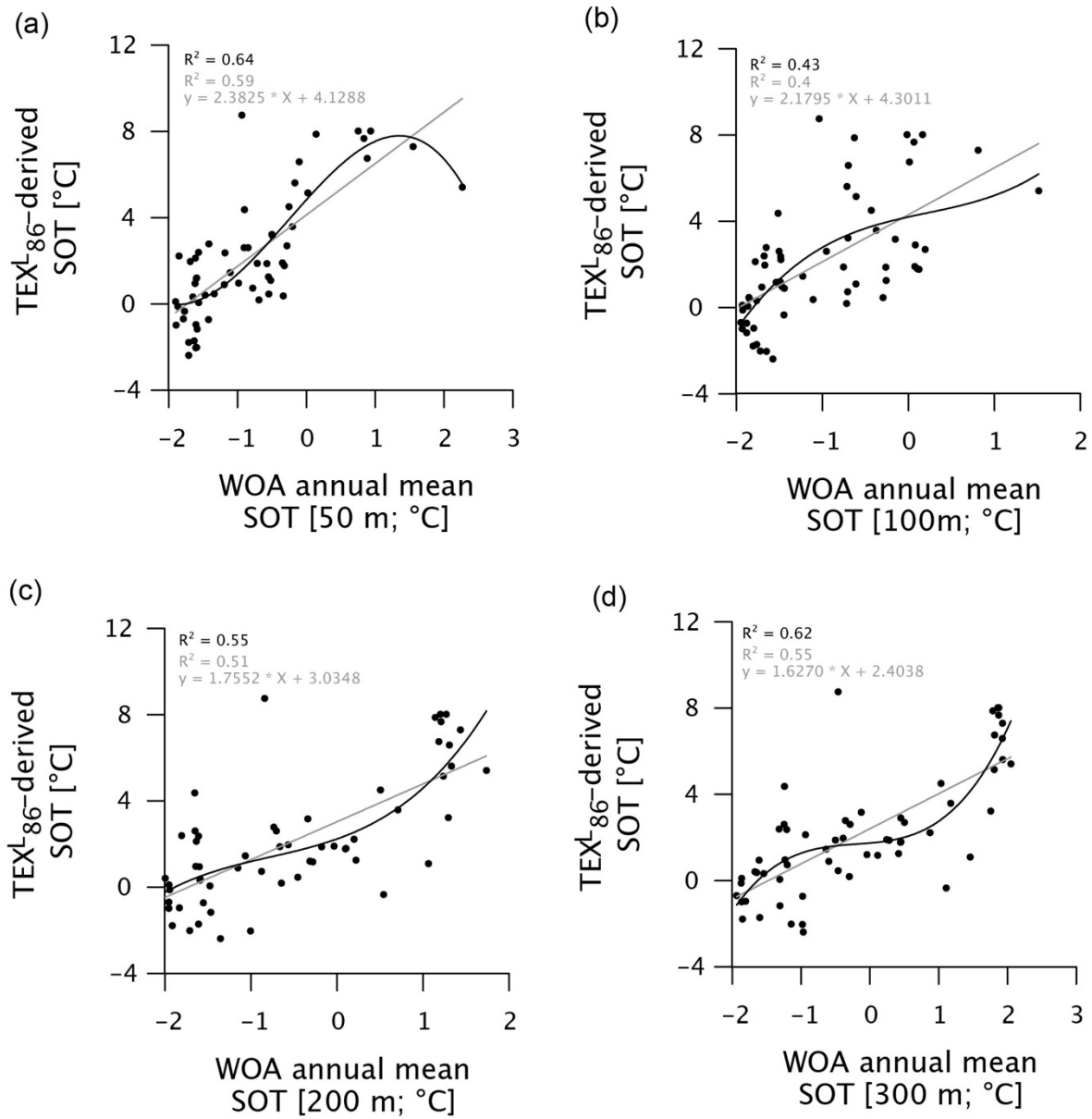


Fig. S4.7: Correlations of (a)  $\text{TEX}^{\text{I-86}}$ -derived SOT vs. WOA annual mean SOT (50 m), (b)  $\text{TEX}^{\text{I-86}}$ -derived SOT vs. WOA annual mean SOT (100 m), (c)  $\text{TEX}^{\text{I-86}}$ -derived SOT vs. WOA annual mean SOT (200 m) and (d)  $\text{TEX}^{\text{I-86}}$ -derived SOT vs. WOA annual mean SOT (300 m) in °C. Coefficients of determination ( $R^2$ ) are given for the respective regression lines.

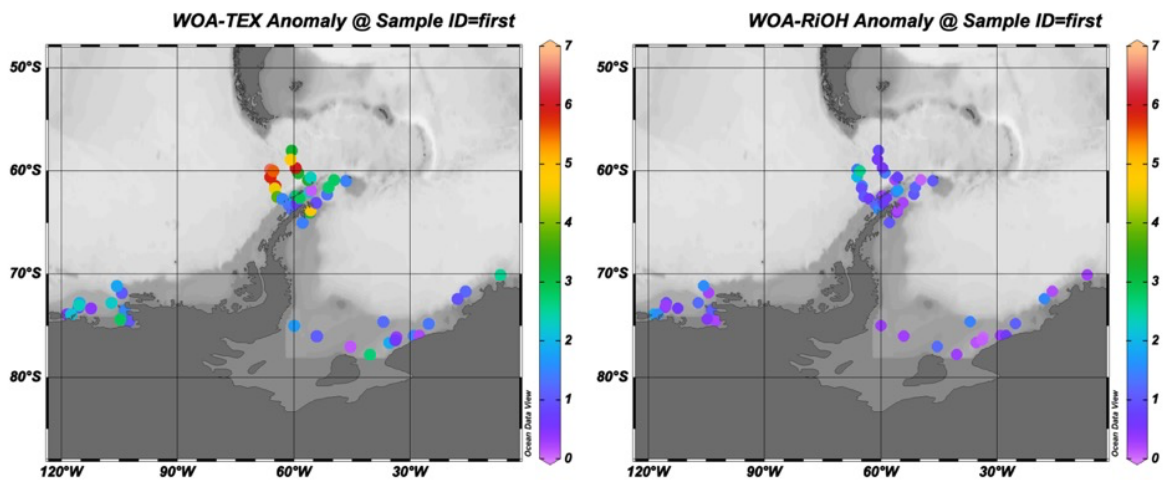


Fig. S4.8: Anomalies between (left) WOA annual mean SOT (410 m) and  $\text{TEX}^{\text{L}}_{86}$ -derived SOTs and (right) WOA annual mean SOT (410 m) and Ri-OH<sup>2</sup>-derived temperatures.

#### Data availability

Data sets related to this article can be found online on the *PANGAEA Data Publisher for Earth & Environmental Science*. (<https://doi.org/10.1594/PANGAEA.932265>; Lamping et al., 2021).

#### Acknowledgements

Denise Diekstall, Mandy Kuck and Jonas Haase are kindly acknowledged for laboratory support. We thank the captains, crews and science parties of RV *Polarstern* cruises PS69, PS97, PS104, PS111 and PS118. Specifically, Frank Niessen, Sabine Hanisch and Michael Schreck are thanked for their support during PS118. Simon Belt is acknowledged for providing the 7-HND internal standard for HBI quantification. AWI, MARUM – University of Bremen, the British Antarctic Survey and NERC UK-IODP are acknowledged for funding expedition PS104. Nele Lamping, Maria-Elena Vorrath and Juliane Müller were funded through the Helmholtz-Gemeinschaft. The two anonymous reviewers are thanked for their constructive and helpful comments, which led to a significant improvement in this paper.

## 5 Study No. 2: High-resolution reconstruction of early Holocene sea-ice and productivity fluctuations in the eastern Amundsen Sea Embayment: from a polynya to a sea-ice dominated setting

Nele Steinberg<sup>1</sup>, Juliane Müller<sup>1,2,3</sup>, Johann Philipp Klages<sup>1</sup>, Claus-Dieter Hillenbrand<sup>4</sup>

<sup>1</sup>Alfred-Wegener-Institut Helmholtz-Zentrum für Polar- und Meeresforschung, Am Alten Hafen 26, 27568, Bremerhaven, Germany

<sup>2</sup>Department of Geosciences, University of Bremen, Klagenfurter Straße, 28359 Bremen, Germany

<sup>3</sup>Marum - Center for Marine Environmental Sciences, Leobener Straße 8, 28359 Bremen, Germany

<sup>4</sup>British Antarctic Survey, High Cross, Madingley Road, Cambridge CB3 0ET, United Kingdom

In preparation for submission to a peer-reviewed scientific journal.

### Abstract

Until a few years ago, Antarctic sea ice has been considered a relatively stable feature of the Southern Ocean, exhibiting an overall increasing trend from 1979 to 2014 documented by means of satellite sea-ice observations. However, this trend seems to be reversed now and more recent sea-ice extent record-lows alarm scientists in the polar research community. Sea ice does not only play a critical role in the global climate system but is especially important for the stability of the West Antarctic Ice Sheet (WAIS), which is particularly prone to a possible future collapse. The Amundsen Sea has experienced a significant sea-ice loss during the last two decades leaving the WAIS even more vulnerable. Any observational data on past sea-ice conditions in this region are crucial for understanding its influence on ice-shelf and ice-sheet dynamics and the marine environment. Here, we present an early Holocene, high-resolution sediment record from the eastern Amundsen Sea Embayment, located immediately in front of the PIG. We analyzed specific biomarker lipids, such as IPSO<sub>25</sub> and highly branched isoprenoid (HBI) trienes, phytosterols as well as the organic carbon content and sedimentological parameters for reconstructing paleo sea-ice and primary productivity conditions and to infer ice-shelf dynamics in this sensitive area. This multi-proxy dataset reveals the environmental evolution from a polynya to a sea-ice dominated regime during the early

Holocene and a subsequent intensification of the ice coverage. We further discuss potential linkages between Circumpolar Deep Water (CDW) intrusions affecting and being affected by local sea-ice conditions.

## 5.1 Introduction

The Amundsen Sea Embayment (ASE) in western Antarctica is characterized by a relatively narrow continental shelf and an extended perennial sea-ice cover over large parts of its area (Arrigo & Van Dijken, 2003). At the same time, two distinct coastal polynyas, the Amundsen Sea Polynya (ASP) and the Pine Island Polynya (PIP) are situated adjacent to large floating ice shelves of glaciers draining into the Amundsen Sea (Fig. 5.1). The ASP and PIP are two to three times more productive polynyas than any other coastal polynya surrounding Antarctica, with concentrations of chlorophyll a (Chl a) exceeding  $7 \text{ mg m}^{-3}$  in the ASP and  $4 \text{ mg m}^{-3}$  in the PIP during spring (Arrigo & Van Dijken, 2003). This extraordinarily high abundance of phytoplankton makes them to crucial carbon sinks for atmospheric carbon dioxide (Arrigo et al., 2008) and to biologically rich environments, harboring upper trophic organisms such as penguins (Ballard et al., 2010). The glaciers, draining into the Amundsen Sea, such as Thwaites Glacier, Smith Glacier and Pine Island Glacier (PIG), are found to be extremely prone to ice loss, mostly triggered by considerable sub-ice shelf melting (Joughin et al., 2021; Pritchard et al., 2012). The loss of PIG alone would add more than a quarter to Antarctica's total contribution to sea-level rise (Rignot et al., 2019; Shepherd et al., 2018b). Over the past decades, especially the PIG has experienced a severe grounding line (GL) retreat (Favier et al., 2014; Joughin et al., 2010) which has now accelerated with a speedup of up to 12 % from late 2017 to September 2020 (Joughin et al., 2021). The upwelling of relatively warm CDW onto the Amundsen Sea shelf is considered the main driver of accelerated thinning of ice shelves, a rapid GL retreat and fast ice discharge (Joughin & Alley, 2011; 2021; Joughin et al., 2010; Rignot et al., 2014; Tinto & Bell, 2011). The thinning of floating ice shelves leads to accelerated flow speed of the grounded ice, since the ice shelves' function as a buffer is reduced. A stabilizing factor for these vulnerable ice shelves, however, is floating on the ocean's surface - sea ice. Sea ice does not only act as a protective buffer by shielding the destructive effects of ocean

swells on ice shelves (Massom et al., 2018), but during its formation, very dense brines are being released into the water column, building a barrier of denser waters. These brines hinder the inflow of relatively warm deep waters onto the shelf, consequently reducing basal melting of ice shelves in some regions (Hellmer et al., 2012). Further, sea ice is also considered as one of the most dynamic features on Earth's surface, thereby impacting various feedback mechanisms in the global climate system. Its substantial seasonal and interannual transitions affect atmospheric and oceanic processes (Thomas, 2017). Sea ice is a limiting element between the ocean and atmosphere, preventing heat, moisture and gas exchange (Bopp et al., 2003; Thomas, 2017) and influences the thermohaline circulation and primary productivity (Smith Jr, 1987). The high albedo of sea ice reflects most of the incoming solar radiation, thereby reducing the oceanic heat uptake (Hall, 2004; Massom et al., 2001).

Considering the enormous influence of sea ice on our climate system, it is of vital importance to collect as many data as possible, to gain a more detailed understanding of the short- and long-term variations of sea ice and its role in different regional and temporal contexts. With this knowledge, numerical sea-ice models can be tested and refined.

Over the last decades, proxy-based sea-ice reconstructions in the Southern Ocean were mainly based on the analyses of sea-ice associated fossil diatom assemblages preserved in marine sediments (Allen et al., 2011; Armand & Leventer, 2003; Crosta et al., 1998; Esper & Gersonde, 2014a; Gersonde & Zielinski, 2000; Leventer, 1998). A critical drawback of this method, however, is the dissolution effect on the silicified diatom shells, occurring either in the water column or within the sea floor sediments. A biased assemblage record may ultimately result in inaccurate sea-ice reconstructions (Leventer, 1998; Zielinski et al., 1998). During the past decade, specific organic geochemical lipids, HBIs, came into focus as an additional proxy for past Southern Ocean sea-ice reconstructions. The di-unsaturated HBI alkene  $C_{25:2}$  is synthesized by sea-ice algae and has already been used to distinguish between open marine and seasonally sea-ice covered settings (Barbara et al., 2013; Denis et al., 2010; Etourneau et al., 2013). This proxy is structurally closely related to the mono-unsaturated  $C_{25:1}$  HBI,  $IP_{25}$ , in the Arctic Ocean (Belt et al., 2018; Belt et al., 2007; Belt & Müller, 2013). Hence, the term  $IPSO_{25}$  (Ice Proxy of the Southern Ocean with 25 carbon atoms) was established (Belt



et al., 2016). Vorrath et al. (2019) introduced a combined approach, following the PIP<sub>25</sub> concept for the Arctic (Müller et al., 2011), by combining a phytoplankton-derived HBI triene and/or sterol with IPSO<sub>25</sub>, resulting in the sea-ice index PIPSO<sub>25</sub>. Several studies have evaluated and applied this newly developed proxy on different time scales and in different study areas in Antarctica and combined it with other micropaleontological, sedimentological and geochemical proxies, providing a thorough assessment of past sea-ice conditions (Barbara et al., 2016; Etourneau et al., 2013; Lamping et al., 2020; 2021; Sadatzki et al., 2023; Vorrath et al., 2019; 2020, 2023).

Here, we present a highly resolved biomarker record of gravity core PS104\_14-3 from the eastern ASE documenting the evolution of the sea-surface conditions in the direct vicinity of the PIG during the early Holocene. The sea-ice biomarker lipid IPSO<sub>25</sub> is applied alongside phytoplankton markers, such as HBI-trienes and phytosterols, and compared to sedimentological proxies, enabling us to determine the progression from polynya conditions proximal to the ice-shelve edge of the PIG to a sea-ice dominated setting after a phase of retreat of the PIG. We further comment on the influence of CDW on carbon sequestration in the Amundsen Sea sector and how sea ice, on the other hand, influences the inflow of CDW onto the shelf.

## 5.2 Regional setting

The continental shelf in the ASE is characterized by the upwelling of relatively warm CDW along deep glacially eroded troughs and into the sub-ice shelf cavities (Jacobs et al., 2011; Jenkins et al., 2016; Nakayama et al., 2013). CDW is considered the main driver of basal melting of ice shelves in this area, when reaching the ice shelves' GL (Hillenbrand et al., 2017; Jenkins et al., 2018; Shepherd et al., 2004). Further North, the Antarctic Circumpolar Current (ACC), which is the largest current system in the world (Meredith et al., 2011), flows in an eastward direction and its landward limit is marked by the Southern Boundary of the ACC (SBACC). This boundary divides the Perennial Sea Ice Zone in the south (where sea-ice cover persists throughout summer) from the Seasonal Sea Ice Zone in the north (which is affected only by winter sea ice; Orsi et al. (1995)). Further South, the Antarctic Slope Current flows westward along the continental shelf and is affected by perennial and seasonal (winter) sea-ice coverage (Mathiot et al.,

2011b). In the last two decades, sea ice extent in the ASE has been decreasing (Comiso et al., 2017; De Santis et al., 2017; Parkinson, 2019). Record-lows during the austral summers of 2017 and 2022, culminating in a new minimum of 1.77 million square kilometers on 19 February 2023, which is 36 % less than the average daily minimum sea-ice extent from 1979-2022 (Purich & Doddridge, 2023), however, alarm scientists of the polar research community.

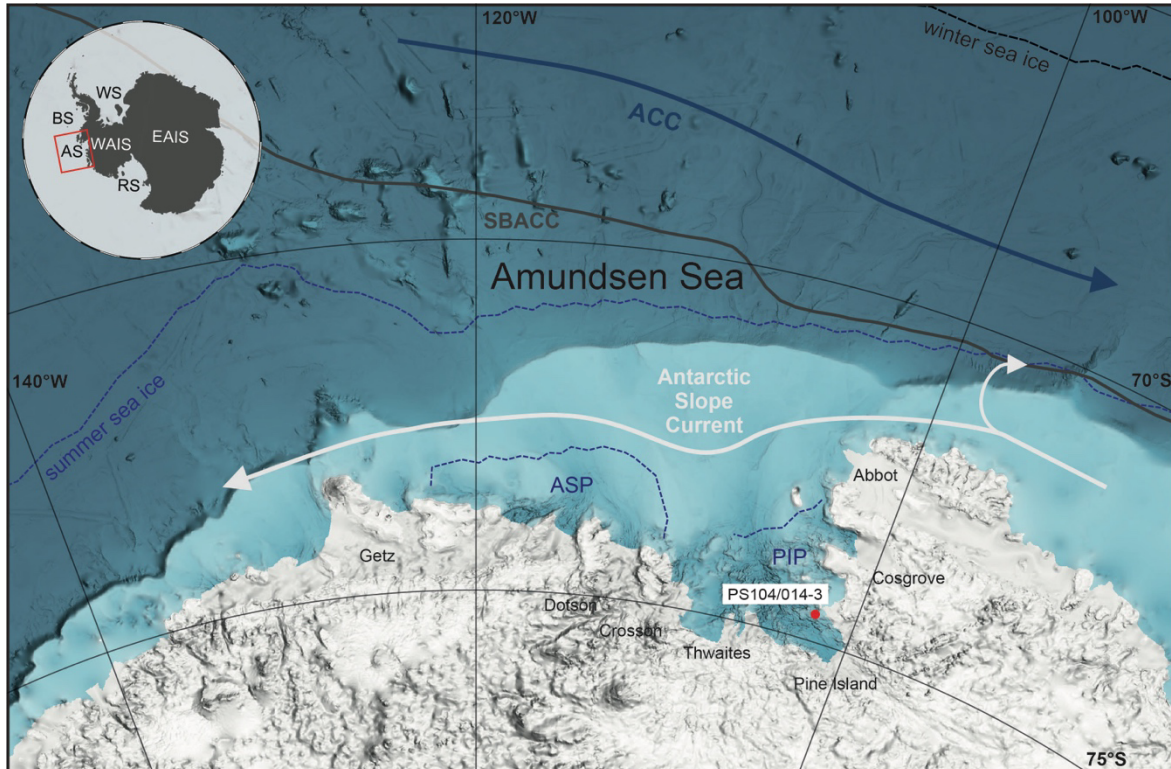


Fig. 5.1: Map of the Amundsen Sea Embayment (indicated by red rectangle in insert map). Red dot shows the location of gravity core PS104\_14-3 in Pine Island Bay. Winter sea-ice boundary is marked by black dashed line. Summer sea-ice boundaries and polynyas are marked by blue dashed lines (Fetterer et al., 2016). Blue arrow shows eastward flow direction of Antarctic Circumpolar current (ACC). Solid dark grey line marks the Southern Boundary of the ACC (SBACC). Antarctic Slope Current in westward direction is displayed as white arrows (Mathiot et al., 2011a; Orsi et al., 1995). Abbreviations: ASP: Amundsen Sea Polynya, PIP: Pine Island Polynya. Abbreviations Insert Map: EAIS: East Antarctic Ice Sheet, WAIS: West Antarctic Ice Sheet, WS: Weddell Sea, RS: Ross Sea, AS: Amundsen Sea, BS: Bellingshausen Sea. Insert Map shows grounded ice extent only. Background bathymetry derived from IBCSO (Dorschel et al., 2022).

Gravity core PS104\_14-3 is currently located within the PIP in the eastern ASE, in front of the PIG and thus ideally suited to track past changes in the occurrence and position of the polynya (Fig. 5.1). The open water area of the PIP from 1998-2014 was on average 19688 km<sup>2</sup> with 108 days of open water during spring and summer (Arrigo et al., 2015).

### 5.3 Material and methods

#### 5.3.1 Sediment samples and radiocarbon chronology

The herein investigated gravity core PS104\_14-3 (74.55°S, 102.59°W; 600 m water depth; recovery 8.24 m) was retrieved from the eastern Pine Island Bay during RV *Polarstern* cruise PS104 (ANT-XXXII/3) in 2017 (Gohl, 2017). Radiocarbon dating of benthic foraminifers revealed an early Holocene age of the sediments with very high sedimentation rates up to 1700 cm/ka (Table 5.1). The lack of age constraints at the sediment surface due to the absence and/or poor preservation of carbonates hampers the proper assessment of more recent (mid-late Holocene) environmental conditions. However, while we cannot rule out the possibility of the loss of the core top during coring operations, the distinct decrease in sedimentation rate to 0.03 cm/ka in the upper two meters of the gravity core, could indicate the deposition of these strata in a sediment starved sub-ice-shelf environment (Smith et al., 2019). The herein analyzed proxies are plotted versus depth with the ages being indicated (Figs. 5.2 + 5.4).

Table 5.1: Age model for core PS104\_14-3 based on radiocarbon dating of benthic foraminifera. Conventional and calibrated  $^{14}\text{C}$  ages are given. For the calibration, the Southern Ocean marine reservoir effect of  $1300 \pm 100$  years ( $\Delta R = 900 \pm 100$  years) was used. Reversed ages are marked in italics. Calibrated with Calib 14 (Stuiver & Reimer, 1993), using the Marine 20 calibration curve (Heaton et al., 2020; data input September 2020).

| Sample depth [cmbsf] | Lithology   | Lithological unit | Conventional $^{14}\text{C}$ age [ $^{14}\text{C}$ a BP] | Calibrated $^{14}\text{C}$ age [cal. $^{14}\text{C}$ a BP] | Sedimentation rate (cm/ka) |
|----------------------|---|-------------------|--|--|----------------------------|
| 203                  | bioturbated mud with dispersed sand and gravel    | III               | 7 767 $\pm$ 109  | 7 155  | 28                         |
| 231                  | laminated mud                                     | II                | 8 564 $\pm$ 102  | 7 938  | 36                         |
| 301                  | laminated mud                                     | II                | 8 680 $\pm$ 102  | 8 071  | 526                        |
| 413                  | <i>laminated mud</i>                              | <i>II</i>         | <i>8 898 <math>\pm</math> 100</i>                        | <i>8 285</i>   | <i>523</i>                 |
| 478.5                | <i>laminated mud</i>                              | <i>II</i>         | <i>8 878 <math>\pm</math> 94</i>                         | <i>8 266</i>   | <i>-3447</i>               |
| 549                  | laminated mud                                     | II                | 8 922 $\pm$ 106  | 8 306  | 1763                       |
| 609                  | laminated to stratified mud to gravelly sandy mud | I                 | 9 045 $\pm$ 109  | 8 658  | 170                        |
| 683                  | laminated to stratified mud to gravelly sandy mud | I                 | 9 304 $\pm$ 123  | 8 775  | 632                        |
| 719                  | laminated to stratified mud to gravelly sandy mud | I                 | 9 429 $\pm$ 117  | 8 938  | 221                        |
| 776                  | laminated to stratified mud to gravelly sandy mud | I                 | 9 592 $\pm$ 110  | 9 144  | 277                        |

#### 5.3.2 Bulk sediment and lipid biomarker analyses

The sediment samples taken from gravity core PS104\_14-3 were freeze-dried and homogenized by using an agate mortar. To prevent the degradation of the targeted molecular components, the samples were always kept in glass vials and stored at  $-20^\circ\text{C}$ . After removing the inorganic carbon with 500  $\mu\text{L}$  12 N hydrochloric acid, TOC contents were measured on 0.1 g of sediment. The measurements were carried out using a carbon-

sulfur analyser (CS 2000; Eltra). Before sample analysis and after every 10th sample (error  $\pm 0.02$  %), standards for calibration are routinely measured. Total carbon and nitrogen contents to determine the  $\text{CaCO}_3$  content and the  $C_{(\text{org})}/N_{(\text{tot})}$  ratio, respectively, were analyzed using an Elementar Vario EL III. Grain-size analyses were carried out on discrete sediment samples (every 5-10 cm), disaggregated by means of deionized  $\text{H}_2\text{O}$  and wet-sieved over  $63 \mu\text{m}$  and 2 mm mesh sizes. Mud ( $<63 \mu\text{m}$ ), sand ( $63 \mu\text{m}$ -2 mm) and gravel ( $>2 \text{mm}$ ) proportions were determined on a weight basis. Magnetic susceptibility and wet-bulk density were logged using a GEOTEK Multi Sensor Core Logger (MSCL).

The extraction of lipid biomarkers from the sediments (6 g per sample) was done via ultrasonication (3 x 15 min) using  $\text{DCM}:\text{MeOH}$  (3 x 6 mL; 2:1  $v/v$ ). For quantification of HBIs and sterols, the internal standards 7-HND (0.057  $\mu\text{g}$  per sample) and  $5\alpha$ -androstane-3-ol (1.04  $\mu\text{g}$  per sample) were added to each sample, respectively. By eluting the apolar (HBIs) and polar (sterols) fractions with 5 mL *n*-hexane and 5 mL  $\text{DCM}:\text{MeOH}$  1:1, respectively, the extract was fractionated using an open-column chromatography with  $\text{SiO}_2$  as stationary phase. The polar fraction was then split into two fractions (sterols and isoprenoidal glycerol dialkyl glycerol tetraethers (GDGTs)) for further processing. With 300  $\mu\text{L}$  BSTFA (for 2 hours at 60  $^\circ\text{C}$ ), the sterol fraction was silylated. Compound analyses of sterols and HBIs were carried out on an Agilent Technologies 7890B GC (fitted with a 30 m DB 1MS column; 0.25 mm diameter and 0.25  $\mu\text{m}$  film thickness) coupled to an Agilent Technologies 5977B MSD; with 70 eV constant ionization potential, ion source temperature of 230  $^\circ\text{C}$ ). The GC oven was set to 60  $^\circ\text{C}$  (for 3 min), 150  $^\circ\text{C}$  (rate: 15  $^\circ\text{C min}^{-1}$ ), 320  $^\circ\text{C}$  (rate: 10  $^\circ\text{C min}^{-1}$ ) and 320  $^\circ\text{C}$  (15 min isothermal) for the analysis of hydrocarbons and to 60  $^\circ\text{C}$  (for 2 min), 150  $^\circ\text{C}$  (rate: 15  $^\circ\text{C min}^{-1}$ ), 320  $^\circ\text{C}$  (rate: 3  $^\circ\text{C min}^{-1}$ ) and 320  $^\circ\text{C}$  (20 min isothermal) for the analysis of sterols. As carrier gas, helium was used. Sterol and HBI compounds were subsequently identified by their GC retention times and mass spectra (Belt, 2018; Belt et al., 2000; Boon et al., 1979). Quantification of lipids was done by comparing the individual gas chromatography mass spectrometry (GC-MS) peak area to the peak area of the respective internal standard and by normalizing the amount of extracted sediment.  $\text{IPSO}_{25}$  and HBI-trienes were quantified by their molecular ions ( $\text{IPSO}_{25}$ ,  $m/z$  348, and

HBI-trienes,  $m/z$  346) to the fragment ion  $m/z$  266 of the internal standard 7-HND (Belt, 2018). Quantification of sterols was done by relating the molecular ion of the individual sterol to the molecular ion  $m/z$  348 of the internal standard 5 $\alpha$ -androstan-3-ol. As recommended by Belt et al. (2014) and Fahl and Stein (2012), instrumental response factors for the target lipids were considered. To account for different depositional conditions, all biomarker concentrations were normalized to the TOC content of each sample.

Calculations of the phytoplankton IPSO<sub>25</sub> (PIPSO<sub>25</sub>) index are done by using the equation introduced by Vorrath et al. (2019):

$$\text{PIPSO}_{25} = \text{IPSO}_{25} / (\text{IPSO}_{25} + (\text{phytoplankton marker} \times c)), \quad (1)$$

with  $c$  ( $c = \text{mean IPSO}_{25} / \text{mean phytoplankton marker}$ ) as a concentration balance factor to account for high concentration offsets between IPSO<sub>25</sub> and the phytoplankton biomarker. Here, we determine that concentrations of dinosterol and HBI Z-triene (to calculate the PIPSO<sub>25</sub> index) below 0.15 ng/g OC and 0.1  $\mu\text{g/g}$  OC, respectively, classify the threshold denoting a maximum ice cover and hence allocate PIPSO<sub>25</sub> values of 1 to the corresponding samples (see Müller and Stein (2014) and Lamping et al. (2020) for further details).

## 5.4 Results

Based on sedimentological data of the gravity core PS104\_14-3, the sediments can be divided into three units (Unit I-III; Fig. 5.2), reflecting the paleoenvironmental changes in the study area. Unit I comprises laminated to stratified mud alternating with laminated to stratified gravelly sandy mud. Unit II is predominantly laminated mud, while Unit III is comprised of bioturbated mud with dispersed sand and gravel (ice rafted detritus (IRD); Fig. 5.3).

### 5.4.1 Lithological succession

In the lowermost part of the core (824-560 cmbsf; Unit I), the magnetic susceptibility has highest values, ranging from 1200-3500  $10^{-6}$  SI and is thus significantly higher than in the overlying units. Similarly, the WBD exhibits its highest values in this unit, ranging from 1.4-2 g/cm<sup>3</sup>. The CaCO<sub>3</sub> content reaches ca. 2 %, with distinct higher values (up

to 4 %) from ca. 690-670 cmbsf (which we define as a subunit). The C/N-ratio varies between 8-14 and decreases to 1 in the subunit. The TOC content in Unit I ranges between 0.1-0.2 %. Grain sizes in Unit I are coarsest, compared to the overlying units, with a gravel content of about 0-11.5 % (with one distinct peak at ca. 770 cm and 49.1 % gravel content), the sand content ranging between 2-73 % and mud concentrations varying from 16-97 %. The subunit can also be distinguished in the grain sizes, with very

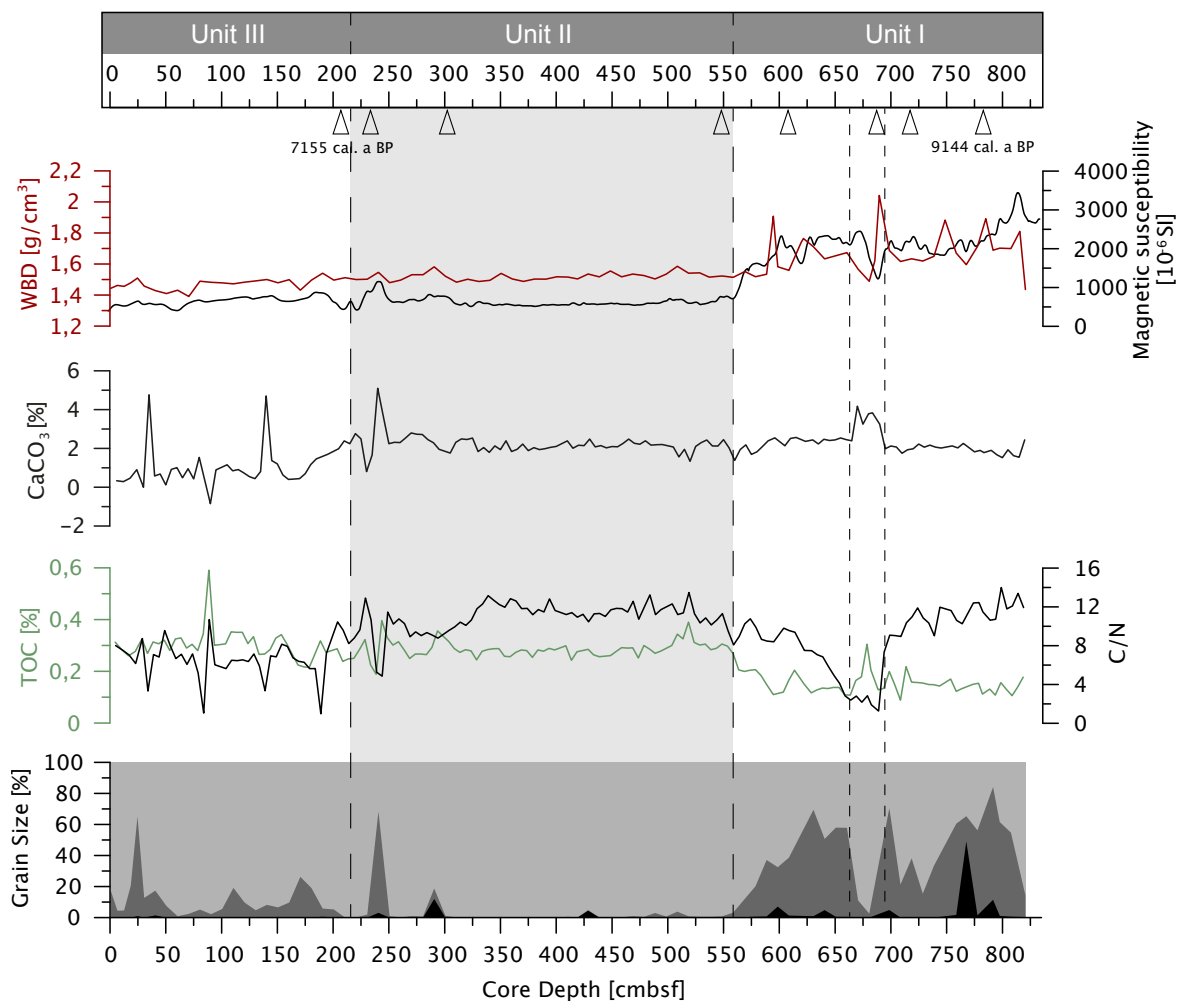


Fig. 5.2: Wet bulk density (WBD), magnetic susceptibility,  $\text{CaCO}_3$ , TOC, C/N ratio and contents of mud (0-63  $\mu\text{m}$ ; light grey infill), sand (63  $\mu\text{m}$ -2 mm; dark grey infill) and gravel (>2 mm; black infill) for gravity core PS104\_14-3. Youngest and oldest calibrated  $^{14}\text{C}$  ages are given in cal. a BP on the upper axis. For additional calibrated  $^{14}\text{C}$  ages throughout the core highlighted by triangles on the upper axis (except for age reversals), see Table 5.1. Core is divided into three units as indicated in the topmost bar: Unit I to Unit III.

high mud concentrations (up to 98 %) in this depth interval.

In the second unit, Unit II, from 560-215 cmbsf, the magnetic susceptibility is relatively low with values between 550-820  $10^{-6}$  SI. The WBD in this unit can also be described as consistent with values of around  $1.5 \text{ g/cm}^3$ . The  $\text{CaCO}_3$  content is similar

to the underlying Unit I, with values of around 2, but with a more variable content at the top of the unit (ca. 250-215 cmbsf). Here, the CaCO<sub>3</sub> content first reaches its maximum of about 5 % at ca. 242 cmbsf and a low of 0.8 % at 232 cmbsf. The C/N-ratio is relatively high, reaching values of around 12, and becoming more variable towards the top of the unit. The TOC content is generally higher than in the underlying unit and varies around 0.3 %. In Unit II, the sediments contain around 99 % mud. Two distinct peaks towards the top of the unit can however be determined. At around 280 cmbsf, the gravel and sand contents reach 12 and 6.7 %, respectively, while at around 240 cmbsf, the gravel and sand contents reach 3 and 65.2 %, respectively. In the uppermost Unit III (from 215-0 cmbsf), the magnetic susceptibility and WBD are similar to the underlying unit, with values ranging around 430-880 10<sup>-6</sup> SI and 1.5 g/cm<sup>3</sup>, respectively.

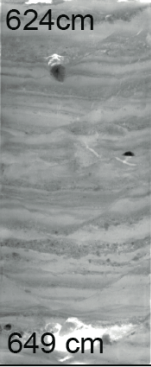
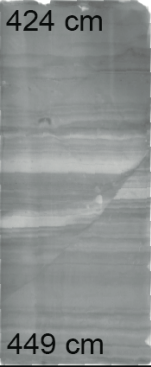
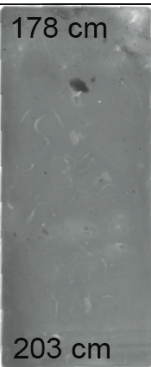
|                          | Exemplary x-ray   | Lithology  | Physical and chemical characteristics | Palaeo-environment  |
|--------------------------|---|--|---------------------------------------|---|
| Unit I<br>824-560 cmbsf  |    | laminated to stratified mud alternating with laminated to stratified gravelly sandy mud; IRD | MagSus > 2000 10 <sup>-6</sup> SI     | relative proximity to PIG's calving line; iceberg transport                           |
|                          |   |  | WBD 1.6-1.8 g/cm <sup>3</sup>         |   |
| Unit II<br>560-215 cmbsf |   | predominantly laminated mud  | MagSus < 1000 10 <sup>-6</sup> SI     | higher distance to PIG's calving line; suspension settling                            |
|                          |   |  | WBD 1.5-1.6 g/cm <sup>3</sup>         |   |
| Unit III<br>215-0 cmbsf  |  | bioturbated mud, with dispersed sand and gravel grains; IRD                                  | MagSus < 1000 10 <sup>-6</sup> SI     | higher distance to PIG's calving line; iceberg transport                              |
|                          |   |  | WBD 1.4-1.5 g/cm <sup>3</sup>         |   |
|                          |   |  | TOC < 0.2 %                           | winter/spring sea ice; polynya setting; possible CDW advection                        |
|                          |   |  | Phytosterols high                     |   |
|                          |   |  | PIPISO <sub>25</sub> low              |   |
|                          |   |  | TOC 0.2-0.3 %                         | heavy sea-ice cover; short summer sea-ice reductions; inflow of CDW possibly hindered |
|                          |   |  | Phytosterols decreasing               |   |
|                          |   |  | PIPISO <sub>25</sub> increasing       |   |
|                          |   |  | TOC ≥ 0.3 %                           | maximum sea-ice cover; inflow of CDW possibly hindered                                |
|                          |   |  | Phytosterols low                      |   |
|                          |   |  | PIPISO <sub>25</sub> high             |   |

Fig. 5.3: Exemplary x-rays for each Unit I-III with description of lithologies and paleoenvironments derived from proxy-data.

The content of CaCO<sub>3</sub> is more variable than in the underlying units, ranging between 0.1 and 4.7 %. A higher variability can also be noted in the C/N-ratio, which is generally lower than in the underlying unit and varies between 5-10. The TOC content is similar to the underlying unit, ranging around 0.3 %, but also shows a slightly higher variability. The grain size in Unit III is still dominated by mud (around 90 %), but the sand content is higher than in the underlying unit, with values of 0.1-64.2 %.



### 5.4.2 Biomarker data

In the lowermost unit, Unit I (from 824-560 cmbsf), concentrations of the sea-ice biomarker IPSO<sub>25</sub> are relatively low at the bottom and increasing throughout the unit, ranging between 0.5-10 µg/g OC (Fig. 5.4). The subunit from 690-670 cmbsf, can also

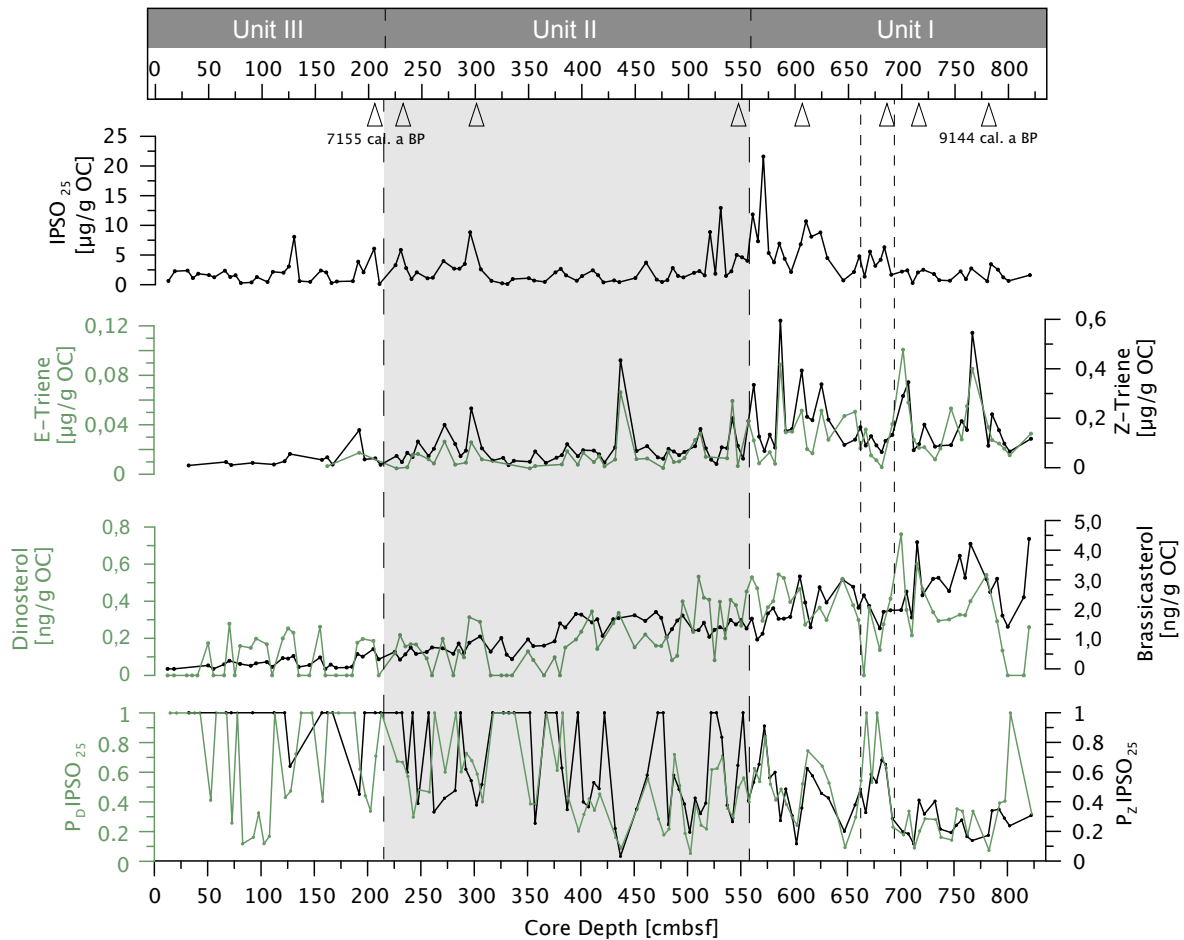


Fig. 5.4: IPSO<sub>25</sub>, E-triene, Z-triene, dinosterol, brassicasterol, P<sub>D</sub>IPSO<sub>25</sub> and P<sub>Z</sub>IPSO<sub>25</sub> for gravity core PS104\_14-3. Youngest and oldest calibrated <sup>14</sup>C ages are given in cal. a BP on the upper axis. For additional calibrated <sup>14</sup>C ages throughout the core highlighted by triangles on the upper axis (except for age reversals), see Table 5.1. Core is divided into three units as indicated in the topmost bar: Unit I to Unit III.

be observed in the biomarker data. Here, IPSO<sub>25</sub> concentrations are relatively higher than in the underlying samples. The overlying sediments, however, reveal an increase in IPSO<sub>25</sub> concentrations towards the top of Unit I. The phytoplankton biomarkers HBI Z-triene and E-triene are highly variable throughout Unit I and show highest concentrations, compared to the rest of the sediment core (0.1-0.5 µg/g OC and 0.006-0.1 µg/g OC, respectively). Interestingly, within the subunit from 690-670 cmbsf, concentrations of both phytoplankton biomarkers are at a minimum compared to the rest of the unit. Brassicasterol and dinosterol exhibit highest concentrations in Unit I,

with a slight decrease from bottom to top and values ranging between 1.0-4.0 ng/g OC and 0-0.776 ng/g OC, respectively. Both PIPSO<sub>25</sub> indices, derived from the sea-ice proxy IPSO<sub>25</sub> combined with dinosterol (P<sub>D</sub>IPSO<sub>25</sub>) and HBI Z-triene (P<sub>Z</sub>IPSO<sub>25</sub>), are relatively low. Below the subunit identified between 690-670 cmbsf, PIPSO<sub>25</sub> values are lowest and range between 0.1 and 0.4. Within the subunit, P<sub>D</sub>IPSO<sub>25</sub> and P<sub>Z</sub>IPSO<sub>25</sub> show a peak of up to 1 and 0.7, respectively. At the top of the unit, PIPSO<sub>25</sub> values are slightly increasing up to 0.9 and are highly variable.

Unit II (from 560-215 cmbsf) is characterized by relatively low IPSO<sub>25</sub> concentrations ranging around 2 µg/g OC, with a few distinct peaks reaching up to 8-12 µg/g OC. The phytoplankton derived HBI Z-triene and E-triene are lower concentrated than in the underlying unit, ranging around 0.05 µg/g OC and 0.01 µg/g OC, respectively. A few distinct peaks in both records with concentrations up to 0.4 µg/g OC (HBI Z-triene) and 0.06 µg/g OC (HBI E-triene). Brassicasterol and dinosterol show a continuously decreasing trend throughout Unit II. Concentrations of brassicasterol decrease from ca. 1.7 ng/g OC at the bottom to 0.5 ng/g OC at the top of the unit, while concentrations of dinosterol show a similar trend, with concentrations decreasing from ca. 0.4 ng/g OC to 0.1 ng/g OC. The PIPSO<sub>25</sub> values in Unit II are slightly increasing throughout the unit and are highly variable.

Unit III (from 215-0 cmbsf) is characterized by similar IPSO<sub>25</sub> concentrations than in the underlying Unit II, ranging around 2 µg/g OC, with a few distinct peaks reaching concentrations of up to 8 µg/g OC. The phytoplankton derived HBI Z-triene and E-triene concentrations are relatively low. While HBI Z-triene is slightly lower concentrated than in the underlying unit (ca. 0.03 µg/g OC). The HBI E-triene concentration, except for two samples from this unit, is below the detection limit and could hence not be determined. The two samples, however, have similar concentrations than the samples from the underlying unit, ranging around 0.01 µg/g OC. Concentrations of brassicasterol and dinosterol are lowest, varying between 0 and 0.6 ng/g OC and 0 and 0.3 ng/g OC. While P<sub>Z</sub>IPSO<sub>25</sub> is generally high, mostly with values of 1 and two distinct lows at around 0.4, P<sub>D</sub>IPSO<sub>25</sub> is highly variable, ranging between 0.1 and 1, whereas the overall trend is relatively higher than in the underlying units.

## 5.5 Paleoenvironmental reconstructions

### 5.5.1 Unit I – polynya dynamics

Based on the lithological data and the physical properties of the sediments, we propose that Unit I may have been deposited in relative proximity to the calving zone of the PIG between around 9144 and 8306 cal. a BP. Following the idealized sedimentary sequence deposited under a retreating ice shelf as suggested by Smith et al. (2019), a calving zone is characterized by IRD and rain-out processes. We hence propose that the gravelly sandy mud layers in Unit I could be the result of rain-out, while coarser gravel may have reached the core site through iceberg discharge or mini turbidites (Smith et al., 2019). At the same time, our organic geochemical biomarkers suggest a high primary productivity during the deposition of Unit I with successive intervals of favorable growing conditions for sterol and HBI-triene synthesizing organisms. We suggest that this may be a result of the recurring spring and summer opening of a polynya during that time interval. Hillenbrand et al. (2017) studied the chemical compositions of foraminifer shells and benthic foraminifer assemblages in marine sediment core PS75/160, very closely located to the herein investigated sediment core (Fig. 5.1). They conclude that an enhanced CDW upwelling until ca. 8164 cal. a BP has forced deglaciation in this area, which coincides with the time of deposition of Unit I of PS104\_14-3. An enhanced CDW upwelling during that time could be an explanation for the increased primary productivity indicated by our biomarkers, because these warm water masses could have promoted the formation of a polynya – similar to the modern PIP (Fig. 5.5).

An increase of IPSO<sub>25</sub> towards the top of Unit I indicates a transition from a polynya-dominated regime towards a more sea-ice dominated setting. This proposition is supported by overall increasing PIPSO<sub>25</sub> values, indicating a slight increase in sea-ice presence towards the top of Unit I. Interestingly, the relatively low TOC content seems to contradict the inference of a high primary productivity during the time of deposition but this may result from either an immediate consumption by organisms or, following Lee et al. (2017), the intrusion of CDW flushing particulate organic carbon out of the shelf. This may have prevented the sequestration of TOC.

Regarding the biomarker record, the environment prevailing during the deposition of the subunit, from 690-670 cmbsf (ca. 8700 cal. a BP), appears to be characterized by

higher sea-ice concentrations, which may relate to longer winter seasons and/or a limited time of the opening of the PIP.

### 5.5.2 Unit II – increased sea-ice cover

At around 8300 cal. a BP, the depositional environment at our core location changed. As documented by Smith et al. (2019), laminated muds, as present in Unit II, are indicative of a distal GL/sub-ice shelf depositional environment. When interpreting the lithology after Smith et al. (2019), one may assume that these strongly laminated and stratified muds were deposited as a suspension settling from sediment plumes at a

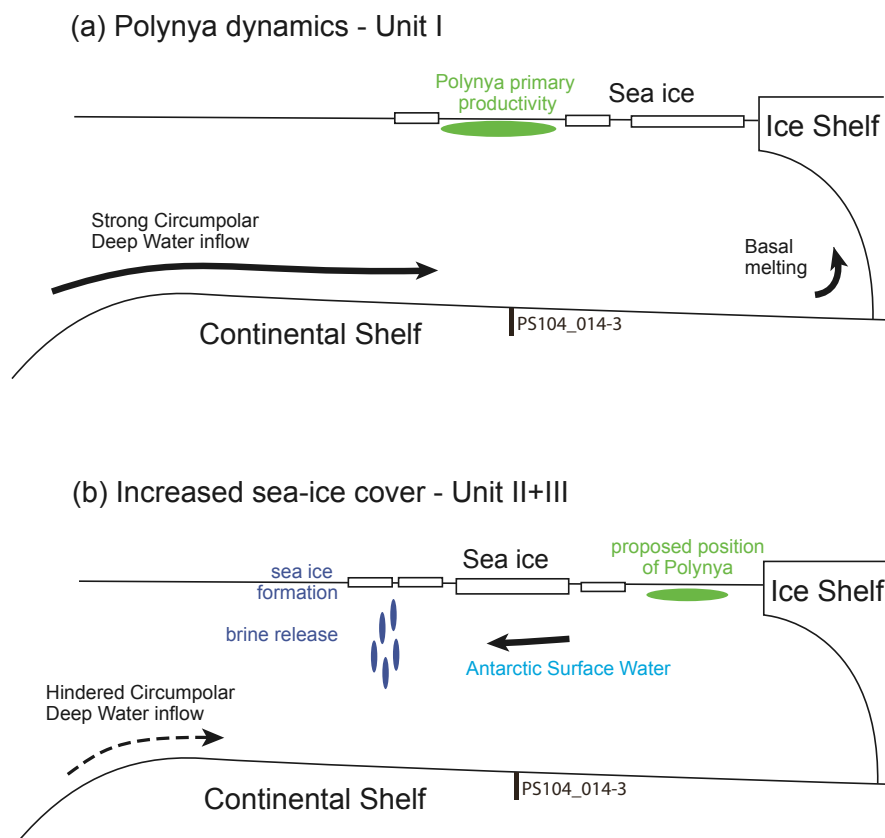


Fig. 5.5: Schematics of water circulation as proposed by Hillenbrand et al. (2017) and polynya position during the deposition of Unit I, II and III of PS104\_14-3 on the Amundsen Sea shelf: (a) limited presence of sea ice allows unhindered CDW inflow onto the shelf, promoting the formation of the PIP (b) high sea-ice formation releases brines that hinder the inflow of CDW onto the shelf. The PIP has shifted to a more southerly location and the formation of AASW increases. Adapted from Lee et al., 2017.

constantly high sedimentation rate. Our organic geochemical proxies, however, suggest the presence of a heavy sea-ice cover that increases throughout Unit II, limiting the light availability for IPSO<sub>25</sub> producing organisms. However, we propose short summer reductions of the heavy sea-ice cover permitting phytoplankton productivity, explaining the presence of HBI-trienes and sterols in the sediments of Unit II. The TOC content

of Unit II is slightly elevated relative to Unit I. With regard to the mechanism proposed by Lee et al. (2017), the elevated TOC content can be interpreted as a function of increased brine rejection due to heavy sea-ice formation, which leads to a hindered inflow of CDW and allows an increased vertical TOC export towards the seafloor. Based on the findings from the investigated sediment core PS75/160 from Hillenbrand et al. (2017), the CDW inflow has weakened from 7500 cal. a BP on, while the influence of Antarctic Surface Water (AASW) increased. The PIP may have changed its position towards a more southerly location (Fig. 5.5). Few peaks of gravel content may be indicative of recurring iceberg discharge during this period.

### 5.5.3 Unit III – maximum sea-ice cover

The sediments of Unit III were deposited after 7155 cal. a BP. The depositional environment is not significantly different to the one of Unit II. Further decreasing concentrations in phytoplankton biomarkers (HBI-trienes and sterols), support the assumption of a continuously growing sea-ice cover lasting throughout summer. Smaller peaks in dinosterol, however, may indicate short-term intervals of summer ice-free conditions, permitting episodic primary production. The increase in sand content suggests a higher iceberg transport possibly related to an ice-shelf re-advance and/or sea-ice rafting of coarser grains. Hillenbrand et al. (2017) relate the weaker inflow of CDW in the ASE since 7500 cal. a BP to a northward shift of the westerly wind belt and we note that such a relocation of the westerlies could also have promoted the expansion of sea ice in the study area. The associated release of dense brine could have further restricted the CDW advection thus re-enforcing the overall cooling. The lack of age constraints in this unit is problematic and may point to either a hiatus or a significantly reduced sedimentation rate at the core site during the mid-late Holocene. We note that, similarly to PS104\_14-3, also the upper intervals of the sediment cores PS75/214 and PS75/167 in front of the Thwaites and PIG, respectively, lack any <sup>14</sup>C dateable microfossils (Hillenbrand et al., 2013), which may infer a common mechanism such as perennial ice cover affecting larger parts of the ASE.

## 5.6 Conclusions

The sea-ice biomarker IPSO<sub>25</sub>, HBI-trienes and phytosterols were used to reconstruct sea surface changes in the eastern ASE during the early Holocene. For a semi-quantitative assessment of ice cover, we additionally applied the sea-ice index PIPSO<sub>25</sub> alongside sedimentological parameters and physical properties. Our high-resolution sediment record, located immediately in front of the PIG, revealed a transition from a polynya setting towards a sea-ice dominated setting.

The PIG and the sea-ice cover in the study area experienced a dynamic evolution with a potential presence of the PIP between around 9144 and 8306 cal. a BP, with a relative proximity to the ice shelf's calving front. Elevated primary productivity indicated by our biomarkers may be the result of an enhanced upwelling of CDW onto the shelf, promoting the formation of a polynya. Following this interval, the biomarker records reveal the presence of a heavy sea-ice cover, with limited light availability for IPSO<sub>25</sub> producing organisms but short-term summer reductions permitting phytoplankton productivity. Elevated TOC contents may result from an increased brine rejection which hinders the inflow of CDW, allowing a stronger vertical export of TOC. After 7155 cal. a BP, our biomarker record suggests a further growing sea-ice cover with higher iceberg discharge and weaker inflow of CDW, which may result from a relocation of the westerlies and potentially promotes sea-ice formation. The brine rejection during sea-ice formation possibly re-inforced an overall cooling by further restricting the CDW inflow.

Our study demonstrates that the application of the combined biomarker approach, such as the PIPSO<sub>25</sub> index, alongside other sea-ice measures, sedimentological parameters and physical properties of the sediments allow for a proper assessment of paleo sea surface environments on West Antarctic continental shelves. It is, however, of vital importance to further investigate HBI-synthesis, deposition and preservation within the sediments and the taxonomy of the IPSO<sub>25</sub> synthesizing organisms to specify the proxy's limitations and potential.

## 6 Study No. 3: Highly branched isoprenoids reveal onset of deglaciation followed by dynamic sea-ice conditions in the western Amundsen Sea, Antarctica

Nele Steinberg (Lamping)<sup>1</sup>, Juliane Müller<sup>1,2,3</sup>, Oliver Esper<sup>1</sup>, Claus-Dieter Hillenbrand<sup>4</sup>, James A. Smith<sup>4</sup>, Gerhard Kuhn<sup>1</sup>

<sup>1</sup>Alfred-Wegener-Institut Helmholtz-Zentrum für Polar- und Meeresforschung, Am Alten Hafen 26, 27568, Bremerhaven, Germany

<sup>2</sup>Department of Geosciences, University of Bremen, Klagenfurter Straße, 28359, Bremen, Germany

<sup>3</sup>Marum - Center for Marine Environmental Sciences, Leobener Straße 8, 28359, Bremen, Germany

<sup>4</sup>British Antarctic Survey, High Cross, Madingley Road, Cambridge, CB3 0ET, United Kingdom

Published in the journal “Quaternary Science Reviews” in January 2020.

### Abstract

The Amundsen Sea drainage sector of the West Antarctic Ice Sheet (WAIS) is widely regarded as a candidate for triggering potential WAIS collapse. The grounded ice sheet drains into the Amundsen Sea Embayment and is thereby buttressed by its fringing ice shelves, which have thinned at an alarming rate. Satellite-based observations additionally reveal a considerable long-term decrease in sea-ice cover in the Amundsen Sea over the last two decades although the long-term significance of this trend is unclear due to the short instrumental record since the 1970s. In this context, investigations of past sea-ice conditions are crucial for improving our understanding of the influence that sea-ice variability has on the adjacent marine environment as well as any role it plays in modulating ice shelf and ice sheet dynamics. In this study, we apply novel organic geochemical biomarker techniques to a marine sediment core from the western Amundsen Sea shelf in order to provide a valuable long-term perspective on sea-ice conditions and the retreat of the Getz Ice Shelf during the last deglaciation. We analysed a specific biomarker lipid called IPSO<sub>25</sub> alongside a phytoplankton biomarker and sedimentological parameters and additionally applied diatom transfer functions for reconstructing paleo sea-ice coverage. This multi-proxy data set reveals a dynamic behavior of the Getz Ice Shelf and sea-ice cover during the deglaciation following the

last ice age, with potential linkages to inter-hemispheric seesaw climate patterns. We further apply and evaluate the recently proposed PIPSO<sub>25</sub> approach for semi-quantitative sea-ice reconstructions and discuss potential limitations.

## 6.1 Introduction

Southern Ocean sea-ice cover is one of the most variable features on Earth's surface with extreme seasonal and often considerable interannual changes. Consequently, it plays a key role in the global climate system by influencing major atmospheric and oceanic processes (Thomas, 2017). Satellite-based observations of Antarctic sea ice reveal a positive overall trend in sea-ice extent from 1979 to 2014 (Comiso et al., 2017; De Santis et al., 2017; Parkinson and Cavalieri, 2012). Parkinson (2019) recently reported a reversal of this trend and note a decrease in Antarctic sea-ice extent since 2014, reaching record lows in 2017 and 2018. The positive overall trend, which is still displayed by the 40-y record (Parkinson, 2019), however, shows huge interannual variabilities and also large opposing regional trends. These regions include the Bellingshausen and Amundsen Seas, where a sustained decline in annual sea-ice cover has been observed since the 1970s, and the Weddell and Ross Seas, where the area of annual sea-ice cover has increased during the same time interval (Comiso et al., 2017; Parkinson and Cavalieri, 2012; Stammerjohn et al., 2012). Consequently, reconstructing regional (paleo) sea-ice conditions is also crucial for understanding and interpreting current climate evolution and for improving predictions of its future (De Santis et al., 2017; Shepherd et al., 2018a). Furthermore, sea-ice seasonality and sea-ice cover are poorly resolved in current climate models (Rosenblum and Eisenman, 2017) and proxy-based sea-ice reconstructions provide a tool with which to validate and improve these predictive models (Vaughan et al., 2013).

Sea ice triggers complex feedback mechanisms in the global climate system. It is a limiting factor for the gas, heat and moisture exchange between the ocean and atmosphere (Bopp et al., 2003; Thomas, 2017) and also affects primary productivity and the thermohaline circulation (Perrette et al., 2011; Smith and Nelson, 1986; Smith, 1987). The bright surface of sea ice is highly reflective (high albedo) inhibiting oceanic uptake of incoming solar radiation (Hall, 2004; Massom et al., 2001). During sea-ice formation, brines are released into the water column, building a barrier of denser waters that



preclude incursions of relatively warm deep waters from entering sub-ice shelf cavities, consequently minimising basal melt of ice shelves in some regions (e.g. Hellmer et al., 2012). Brines also make a major contribution to the formation of Antarctic Bottom Water (AABW; e.g. Nicholls et al., 2009). Furthermore, Massom et al. (2018) found that sea-ice presence in the vicinity of weakened or flooded ice shelves acts as a protective buffer by reducing the destructive effects of ocean swells.

In the Southern Ocean, proxy-based sea-ice reconstructions mainly rely on analyses of sea-ice associated diatom assemblages preserved in marine sediments to determine past positions of mean seasonal and perennial sea-ice extent and to infer relative shifts in the duration of the sea-ice/open water seasons (Allen et al., 2011; Crosta et al., 1998; Gersonde and Zielinski, 2000; Leventer et al., 1996; Leventer, 1998). Diatom-based transfer functions (TF) have allowed for quantitative reconstructions of sea-ice concentrations and SSTs (Armand et al., 2005; Benz et al., 2016; Crosta et al., 1998; Esper and Gersonde, 2014a; Gersonde et al., 2005; Zielinski et al., 1998), but the application of this TF approach can be limited due to dissolution effects of the thin silica frustules of diatoms within the water column or after deposition (e.g. Leventer, 1998; Zielinski et al., 1998). Highly branched isoprenoid (HBI) alkenes, organic geochemical lipids bio-synthesized by certain diatoms have recently been shown to provide an alternative and robust proxy to reconstruct past Antarctic sea ice (Barbara et al., 2010; Collins et al., 2013; Denis et al., 2010; Etourneau et al., 2013; Massé et al., 2011). The di-unsaturated HBI alkene C<sub>25:2</sub> has been measured in Southern Ocean sediments and recently found to be produced by the Southern Ocean sympagic tube-dwelling diatom *Berkeleya adeliensis*, which is commonly associated with land-fast ice and consolidated platelet ice (Belt et al., 2016; Riaux-Gobin and Poulin, 2004). Because of its structurally close relationship to the well-established mono-unsaturated C<sub>25:1</sub> HBI, IP<sub>25</sub>, in the Arctic Ocean (Belt et al., 2007; Belt and Müller, 2013; Belt, 2018), the term IPSO<sub>25</sub> (Ice Proxy for the Southern Ocean with 25 carbon atoms) was introduced (Belt et al., 2016). The Arctic sea-ice proxy IP<sub>25</sub> was proven a reliable proxy for sea-ice conditions and has since been combined with open-water phytoplankton biomarkers, such as brassicasterol, dinosterol (Volkman, 1986; Volkman et al., 1993) or HBI trienes (HBI III; Smik et al., 2016b), to obtain a more accurate picture of prevailing sea-ice conditions (Müller et al., 2009, 2011). The absence of IPSO<sub>25</sub> in the sediments can be the result of either

permanent open-ocean conditions or a floating ice canopy (either a perennial sea-ice cover or ice-shelf cover), which prevents light penetration needed for ice algae growth. In order to avoid misinterpretations, the so called PIP<sub>25</sub> index was established, with “P” representing an open-water phytoplankton biomarker (e.g. Belt and Müller, 2013; Müller et al., 2011; Xiao et al., 2015).

A common approach in Antarctic waters, so far, is the application of a ratio of IPSO<sub>25</sub> and an HBI triene (C<sub>25:3</sub>), which may reflect the relative contributions of sea-ice and open-water phytoplankton inputs of organic matter, respectively, to the seabed sediments (Barbara et al., 2010; Collins et al., 2013; Denis et al., 2010; Massé et al., 2011). Recently, Vorrath et al. (2019) proposed a new approach for more semi-quantitative reconstructions of sea ice in Antarctica, following the PIP<sub>25</sub> concept initially used in the Arctic. The so called PIPSO<sub>25</sub> index is, similar to PIP<sub>25</sub>, a combination of the sea-ice proxy IPSO<sub>25</sub> and an open-water phytoplankton biomarker. The results obtained from surface sediments from the Antarctic Peninsula are in general agreement with sea-ice distribution data derived from satellite data and diatom assemblages, and suggest that the PIPSO<sub>25</sub> index may serve as a suitable approach for sea-ice reconstructions in Antarctica (Vorrath et al., 2019).

Reconstructions of paleo sea-ice conditions in the Amundsen Sea are still sparse, yet knowledge about how the environment has changed is critical to better understand the current trend of declining sea ice (since the 1970s; Parkinson, 2019; Stammerjohn et al., 2015) in this climate sensitive area. Well-constrained proxy-records will lead to a more complete understanding of the long-term relationship between climate and sea-ice variability that will help to validate numerical model predictions of future scenarios of ice sheet dynamics and ocean-cryosphere interactions.

Here, we present the first biomarker-based paleo-record for the western Amundsen Sea Embayment (ASE) shelf documenting the retreat of the Getz Ice Shelf and the onset of sea-ice coverage since the last deglaciation. The application of the sea-ice biomarker lipid IPSO<sub>25</sub> alongside the phytoplankton marker dinosterol enables us to reconstruct how the sea-ice/ice shelf cover in the western ASE has changed and how these changes might be linked to inter-hemispheric bipolar seesaw climate patterns. We compare our environmental interpretations based on the results of the organic geochemical biomarker analyses with interpretations derived from investigations of sedimentological proxies

(Hillenbrand et al., 2010) and winter sea-ice (WSI) concentrations reconstructed from diatom TF on marine sediment core PS69/274-1.

## 6.2 Regional setting

North of the West Antarctic continental shelf of the Amundsen Sea, the Antarctic Circumpolar Current (ACC), the largest current system in the world (Meredith et al., 2011), flows in an eastward direction. Offshore from the ASE shelf, the Southern Boundary of the ACC (SBACC) marks the landward limit of the ACC and roughly divides the Seasonal Sea Ice Zone (affected by winter sea-ice cover) in the north from the perennial Sea Ice Zone in the south, where sea-ice cover persists throughout summer (Orsi et al., 1995). Waters on the continental shelf are characterized by the generally westward flowing Antarctic Slope Current (Mathiot et al., 2011) and are affected by seasonal (winter) and perennial sea-ice coverage (Fig. 6.1).

At present, perpendicular to the coast, relatively warm deep water, modified Circumpolar Deep Water (mCDW), is locally upwelling along deep glacially-carved troughs into the sub-ice shelf cavities of the continental shelf and up to the ice sheet grounding lines (e.g. Jacobs et al., 2011; Jenkins et al., 2010, 2018; Nakayama et al., 2013). The inflow of these relatively warm water masses is considered as a main driver for basal melting of ice shelves in the ASE (Hillenbrand et al., 2017; Jenkins et al., 2010, 2018; Shepherd et al., 2004; Thoma et al., 2008).

The inner shelf of the ASE is further characterized by the presence of two coastal polynyas, the Pine Island Polynya in Pine Island Bay and the Amundsen Sea Polynya (ASP) north of the Dotson and westernmost Getz ice shelves (Fig. 6.1; Alderkamp et al., 2012). Coastal polynyas play an important role in a number of physical and biological processes, such as sea-ice production, salt flux, water mass formation and elevated primary and secondary production, which is controlled by light availability at these high latitude environments (Arrigo and Van Dijken, 2003; Arrigo et al., 2015; Kern, 2009; Maqueda et al., 2004; Martin, 2001). The core analysed in this study is today located within the ASP (~27 000 km<sup>2</sup>), which is the most biologically productive polynya in Antarctica (Arrigo and Van Dijken, 2003; Arrigo et al., 2012; Kim et al., 2015, 2016; Lee et al., 2017; Yager et al., 2012). In the ASP region, the length of the sea-ice season has

declined by  $60 \pm 9$  days since 1979, which is attributed to the earlier opening of the ASP in the year by  $52 \pm 9$  days (Yager et al., 2012).

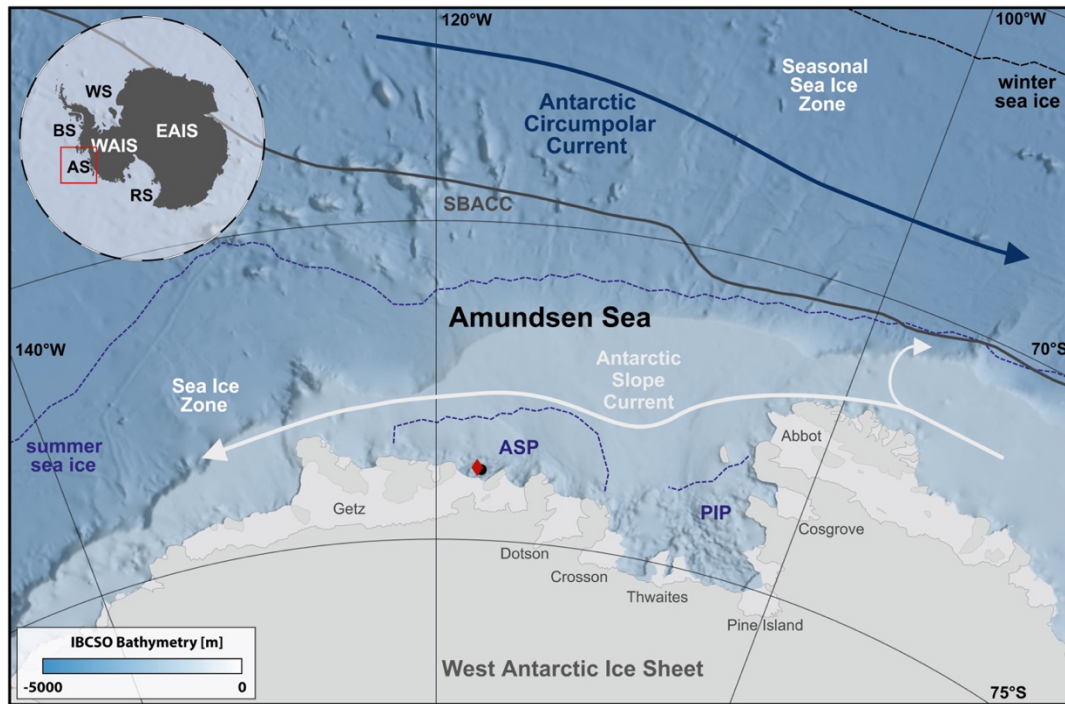


Fig. 6.1: Map of the Amundsen Sea (indicated by red box in insert map), showing the locations of marine sediment core PS69/274-1 (red diamond) and the nearby surface sediment sample from site PS69/275-2 (black dot). Summer sea-ice boundaries, polynyas and winter sea-ice boundaries are marked by dashed blue and black lines, respectively (Fetterer et al., 2016). Southern Boundary of the Antarctic Circumpolar Current (SBACC) is displayed as solid dark grey line and flow direction of the Antarctic Circumpolar Current (ACC) is indicated by the dark blue arrow. White arrows illustrate the flow direction of the Antarctic Slope Current (Mathiot et al., 2011; Orsi et al., 1995). Abbreviations: WAIS: West Antarctic Ice Sheet, EAIS: East Antarctic Ice Sheet, WS: Weddell Sea, BS: Bellingshausen Sea, AS: Amundsen Sea, RS: Ross Sea, ASP: Amundsen Sea Polynya, PIP: Pine Island Polynya. Background bathymetry derived from IBCSO data (Arndt et al., 2013). Insert map shows extent of grounded ice only (i.e., no ice shelves). (For interpretation of the references to color in this figure legend, the reader is referred to the Web version of this article.)

The mean seasonal sea-ice cover in the coastal area of the western ASE lasted on average 314 days per year during the period from 1979 to 2013, and annual sea-ice cover between 1993 and 2013 was on average two months shorter than between 1979 and 1992, associated with changes in spring sea-ice retreat (Stammerjohn et al., 2015). The trend in sea-ice area for the period from 1979 to 2014 in the Bellingshausen and Amundsen Seas was the only one that is negative around Antarctica, with an average decrease of  $-3.2 \% \pm 1.4 \% \text{ decade}^{-1}$  (Parkinson, 2019).

## 6.3 Material and methods

### 6.3.1 Material

Gravity core PS69/274-1 (73.85 °S, 117.78 °W; 1452 m water depth; recovery 4.51 m) and nearby giant box core PS69/275-2 (73.89 °S, 117.55 °W; 1472 m water depth), which provided an un- disturbed seafloor surface sediment sample, were collected offshore from the westernmost Getz Ice Shelf on the western ASE shelf (Fig. 6.1) during RV *Polarstern* cruise ANT-XXIII/4 in 2006 (PS69; Gohl, 2007). Sediment core PS69/274-1 was previously divided into three lithological units by Hillenbrand et al. (2010). Unit I (0-196 cm) was described as bioturbated and stratified mud and silty clay, Unit II (196-239 cm) as bioturbated and stratified diatomaceous ooze and diatomaceous mud. Unit III was split into two subunits with Unit IIIa (239-317 cm) comprising bioturbated mud, sandy mud and muddy sand (with diatoms) and Unit IIIb (317-451 cm) comprising strongly laminated to stratified mud, sandy mud and muddy sand barren of diatoms. In this study, we adopt the age model of core PS69/274-1 (Table 1) obtained by radiocarbon dating of the acid-insoluble organic fraction (AIO) of the sediments and constrained by relative paleomagnetic intensity (RPI) dating (Hillenbrand et al., 2010; Smith et al., 2011).

Table 6.1: Age model for core PS69/274-1 based on radiocarbon dating of the acid insoluble organic fraction (AIO) and published by Hillenbrand et al. (2010). Conventional  $^{14}\text{C}$  ages, local contamination offset (LCO) and calibrated  $^{14}\text{C}$  ages are given. For the calibration, the LCO corrected age and the Southern Ocean marine reservoir effect of  $1\,300 \pm 100$  years ( $\Delta R = 900 \pm 100$  years) (e.g., Berkman and Forman, 1996) were used. Unreliable ages are highlighted in italics.

| Sample depth [cmbsf] | Lithology         | Lithological unit | Conventional $^{14}\text{C}$ age [ $^{14}\text{C}$ a BP] | LCO [a]     | LCO corr. age [corr. $^{14}\text{C}$ a BP] | Age model [cal. a BP] |
|----------------------|-------------------|-------------------|--|-------------|--|-----------------------|
| 59.5-60.5            | Mud               | D                 | 7 740 $\pm$ 39   | 2650        | 5 090                                      | 4 272                 |
| 139.5-140.5          | Mud               | D                 | 14 199 $\pm$ 61  | 2650        | 11 549                                     | 11 968                |
| 231.5-232.5          | Diatomaceous ooze | C                 | 11 967 $\pm$ 49  | 0           | 11 967                                     | 12 681                |
| <i>311.5-312.5</i>   | <i>Mud</i>        | <i>B</i>          | <i>24 416 <math>\pm</math> 198</i>                       | <i>2650</i> | <i>21 766</i>                              | <i>24 534</i>         |

The oldest AIO  $^{14}\text{C}$  age obtained from a sample at 311.5e312.5 cmbsf (24 543 cal. a BP) is considered unreliable because of significant contamination with reworked fossil organic carbon (Hillenbrand et al., 2010), which is supported by observations that the proximity of the grounding line during sediment deposition in a proglacial setting leads to high inputs of reworked fossil carbon (Domack, 1992; Heroy and Anderson, 2007).

Due to the relative coarse resolution of the age model, the proxies are plotted versus depth and the age model is presented as age constraints on the depth-axis. However, data presented along an age-axis are presented in Supplementary Figs. S6.1 and S6.2.

### 6.3.2 Bulk sediment and biomarker analyses

The sediment samples (avg. of ca 13 g) were stored in glass vials at -20 °C before and after being freeze-dried and homogenized with a mortar. Prior to the grinding, the coarse fraction comprising coarse sand and gravel (>0.5 mm) was removed from the sediment by sieving and converted into weight percent. After the removal of inorganic carbon (carbonates, total inorganic carbon) with 500 ml 12 N hydrochloric acid, the analysis of TOC contents was conducted on 0.1 g of sediment and measured with a carbon-sulphur determinator (CS 2000; Eltra). Standards were measured for calibration before the sample analyses and after every tenth sample to ensure accuracy (error  $\pm$  0.02 %). The weight per- centages (wt %) of total carbon (TC) and nitrogen (TN) were ana- lysed using a CNS (Elementar Vario EL III) analyser. The percentage of carbonate was calculated from the difference between the amount of TC and organic carbon, using the following equation:  $\text{CaCO}_3$  (%) = (TC - TOC) x 8.333. The precision (relative standard deviation,  $1\sigma$ ) of the measurements was better than 4 % and accuracy better than 1 % relative. For biomarker analyses, ca 4 g of the freeze-dried and homogenized sediment was extracted using ultrasonication (3 x 15 min) and DCM:MeOH (3 x 6 ml; 2:1 *v/v*) as solvent. Prior to extraction, the internal standards 7-HND (20 ml/sample) and 5 $\alpha$ -androstane-3-ol (40 ml for surface sample PS69/275-2, 60 ml for PS69/274-1) were added for later quantification of HBIs and sterols, respectively. Fractionation of the extract was achieved by open- column chromatography, using SiO<sub>2</sub> as stationary phase. Elution of the HBIs and sterols was conducted with 5 ml n-hexane and 8 ml ethylacetate:n-hexane (20:80 *v/v*), respectively. Sterols were silylated with 300  $\mu$ l bis-silyl-trifluoroacetamide (BSTFA; 60 °C; 2 h). Compound identification was carried out using a GC (Agilent Technologies 7890B fitted with a 30 m DB 1MS column, 0.25 mm diameter and 0.25 mm film thickness) coupled to an MSD (Agilent Technologies 5977B, with 70 eV constant ionization potential, ion source temperature of 230 °C). For hydrocarbon analysis, the temperature program of the GC was set to: 60 °C (3 min), 150 °C (rate: 15 °C/ min), 320 °C (rate: 10 °C/min), 320 °C (15 min isothermal) and for

sterol analysis: 60 °C (2 min), 150 °C (rate: 15 °C/min), 320 °C (rate: 3 °C/min), 320 °C (20 min isothermal). Helium served as carrier gas. HBI and sterol compounds were identified based on their GC retention times and mass spectral characteristics (Belt et al., 2000; Belt, 2018; Boon et al., 1979). Quantification of each lipid was achieved by setting the integrated GC-MS peak area in relation to that of the respective internal standard and by normalizing the resulting ratios by means of an instrumental response factor obtained for the individual lipid (Belt et al., 2014; Fahl and Stein, 2012). For IPSO<sub>25</sub> quantification, the molecular ion ( $m/z$  348) was used in relation to the fragment ion  $m/z$  266 of the internal standard 7-HND (Belt, 2018). For sterol quantification, the molecular ion  $m/z$  500 for dinosterol (4,23,24 trimethyl-5 $\alpha$ -cholest-22 E-en-3 $\beta$ -ol) was compared to the fragment ion  $m/z$  348 of the internal standard 5 $\alpha$ -androstan-3-ol. The masses of IPSO<sub>25</sub> and dinosterol derived by the GC-MS were then converted to sedimentary concentrations using the mass of extracted sediment. Concentrations of IPSO<sub>25</sub> and dinosterol were corrected to the TOC contents of each sample.

Following Müller et al. (2011), we specified the PIPSO<sub>25</sub> index by using the subscript “D” as P<sub>D</sub>IPSO<sub>25</sub> which refers to the use of dinosterol as phytoplankton biomarker. The P<sub>D</sub>IPSO<sub>25</sub> index was calculated based on the following equation:

$$P_{D}IPSO_{25} = IPSO_{25} / (IPSO_{25} + (\text{dinosterol} \times c)) \quad (1)$$

with  $c$  being a concentration balance factor to account for significant concentration differences between IPSO<sub>25</sub> and dinosterol calculated as the ratio of mean IPSO<sub>25</sub> concentration to mean dinosterol concentration (Müller et al., 2011). Means and standard deviations of IPSO<sub>25</sub>, P<sub>D</sub>IPSO<sub>25</sub>, dinosterol and TOC for each unit and subunit can be found in Supplementary Table S6.1.

### 6.3.3 Diatom transfer function derived winter sea-ice concentrations

We reconstructed WSI concentrations with a TF developed by Esper and Gersonde (2014a), applying the Modern Analog Technique (MAT) (after Hutson, 1980). Statistical details, background of the method and its performance at different application levels in comparison with other estimation methods are presented in Esper and Gersonde (2014a). For this purpose, quantitative diatom slides were prepared following the standard techniques (Gersonde and Zielinski, 2000). For diatom counting, the methods of Schrader and Gersonde (1978) were applied using a Zeiss Axioplan 2 microscope at

1000x magnification. Diatoms were identified to species or species group level and, if possible, to forma or variety level. The taxonomy follows primarily Hasle and Syvertsen (1996), Zielinski and Gersonde (1997), and Armand and Zielinski (2001). Species and species groups used for sea-ice reconstructions exhibit close relationships to environmental variables (Zielinski and Gersonde, 1997; Armand et al., 2005; Crosta et al., 2005; Romero et al., 2005; Esper et al., 2010; Esper and Gersonde, 2014a, b). For estimating WSI concentrations we applied the TF MAT-D274/28/6an, comprising 274 reference samples from surface sediments in the western Indian, the Atlantic and the Pacific sectors of the Southern Ocean, with 28 diatom taxa and taxa groups, and an average of 6 analogs (Esper and Gersonde, 2014a). The WSI estimates refer to September sea-ice concentrations averaged over a time period from 1981 to 2010 at each surface sediment site (National Oceanic and Atmospheric Administration, NOAA; Reynolds et al., 2002, 2007). The reference data set is suitable for our approach as it uses a 1 deg. by 1 deg. grid, giving a higher resolution than previously used and results in root mean square errors of prediction (RMSEP) of 5.52 % (Esper and Gersonde, 2014a).

## 6.4 Results and discussion

### 6.4.1 Reconstruction of the paleoenvironment from proxies

Based on our organic geochemical records, content of coarse-grained terrigenous debris >0.5 mm (supplied either by icebergs or sea ice, or transported at the base of an ice shelf and at some distance from the grounding line), on the basis of C/N ratios, carbonate (CaCO<sub>3</sub>) as well as TOC content and TF (diatom) results in addition to previously published magnetic susceptibility, shear strength, biogenic opal, smectite/chlorite ratios (Sm/Chl ratios) in the clay fraction and grain size data (Hillenbrand et al., 2010; Smith et al., 2011), the sediments of core PS69/274-1 can be divided into four units (A-D), reflecting the paleoenvironmental changes in the western ASE since the last deglaciation (Figs. 6.2-6.4). These units do not correspond directly to the three main lithostratigraphic units defined by Hillenbrand et al. (2010) or the two facies units distinguished by Smith et al. (2011) because the biomarker data permit a more detailed reconstruction of the paleo-sea surface conditions and, for example, the identification of the first retreat of the floating ice canopy from the core site and the onset of favorable growth conditions



for biomarker synthesizing phytoplankton and sea-ice diatoms. The biomarker data are the main basis for the new definition of these units, which are now numbered chronologically from A to D (with Unit A being the oldest and Unit D being the youngest), which are then discussed and compared with the already published data by Hillenbrand et al. (2010) for reconstructing the paleoenvironmental changes in the western ASE (Fig. 6.3).

#### 6.4.1.1 Unit A: Floating ice canopy subsequent to grounding line retreat

In the lowermost unit of the core (Unit A; 451 to 317 cm below seafloor [cmbsf]), concentrations of the sea-ice biomarker lipid IPSO<sub>25</sub> and of the phytoplankton-derived biomarker dinosterol are below the detection limit (Fig. 6.2 c and b, respectively). Hence, the calculation of the P<sub>D</sub>IPSO<sub>25</sub> index is not possible. The absence of both biomarker proxies suggests that the environmental conditions were not favorable either for open-water phytoplankton nor for IPSO<sub>25</sub> producing sea-ice diatoms. In previous studies, the absence of sea ice and phytoplankton-derived biomarkers in marine sediments has been interpreted to relate to a very thick ice cover (Belt, 2018; Müller et al., 2009).

Such an ice cover would also explain the lack of diatom frustules in the corresponding sediments, which, together with the lack of bioturbation, was also attributed to ice-shelf or permanent sea-ice cover by Hillenbrand et al. (2010) (Fig. 6.3). Assuming that the core site was covered by a floating ice canopy during deposition of this unit we assigned a maximum P<sub>D</sub>IPSO<sub>25</sub> value of 1 to these samples to maintain the sea-ice scaling of the P<sub>D</sub>IPSO<sub>25</sub> results and aid visualization (displayed as triangles in Figs. 6.2 and 6.3).

TOC and biogenic opal contents in Unit A are extremely low, varying around 0.1 wt % and 1 wt %, respectively (Figs. 6.2 d and 6.3 c), with the low opal content either reflecting the rare presence of fragments of siliceous microfossils (i.e., too tiny for being identified under a microscope) or being an artefact caused by the partial leaching of clay minerals or volcanic glass (e.g. Müller and Schneider, 1993). These low TOC and opal values thus indicate a time interval of low or absent biological production. The unit is characterized by the highest magnetic susceptibility values measured on the core, varying between 300 and 500 x 10<sup>-5</sup> SI units (Fig. 6.3 f), which points to a high input of terrigenous detritus from a nearby grounding line (see Hillenbrand et al., 2010; Smith et al., 2011). Clay mineral data from neighboring gravity core PS69/ 275-1 (for site location,

see Fig. 6.1), reveal high chlorite contents in sediments deposited as subglacial till or proximal to the grounding line (Ehrmann et al., 2011). Therefore, the relatively low Sm/Chl ratio around 0.6 in Unit A sediments of core PS69/274-1 (Fig. 6.3 d; Smith et al., 2011) probably indicates sediment deposition not far away from the grounding line.

The grain size composition of Unit A is mainly dominated by mud (ca 80 wt %), but shows two distinct maxima in gravel and sand contents (<60 wt %) at 400 and 320 cmbsf (Smith et al., 2011), with coarse-grained debris >0.5 mm peaking at the same depths (<1.8 wt %; Fig. 6.3 h and g). Such maxima in gravel and sand contents can be interpreted as the result of two episodes, when either freely drifting icebergs transported ice-rafted detritus (IRD) to the core location or when the core site was located closer to the grounding line and affected by rain-out of debris from the base of an ice shelf. Hillenbrand et al. (2010) observed lamination and stratification in the corresponding core interval but also reported absence of diatoms. Based on the findings from the productivity proxies (TOC, biogenic opal and dinosterol contents), we conclude that Unit A was deposited under a floating ice canopy formed either by perennial sea-ice cover or part of the Getz Ice Shelf (Fig. 6.4; Unit A). The coarse-grained debris peaks together with the clay mineral data indicate a position of the core site not far away from the grounding line, suggesting that the site was most likely covered by an ice shelf. According to the oldest reliable AIO  $^{14}\text{C}$  age from 232 cmbsf depth, Unit A must have been deposited earlier than 12.7 cal. ka BP, with the RPI age model for core PS69/274-1 constraining its deposition to the time before 13 ka (Table 6.1; Hillenbrand et al., 2010). We therefore conclude that the deposition of Unit A took place during the last deglaciation, subsequent to grounded ice-retreat (Smith et al., 2011). Grounded ice-retreat from the inner Antarctic continental shelf during that time has also been reported for other areas. For example, a reconstruction by Milliken et al. (2009) reveals initial decoupling of the ice sheet from Maxwell Bay (South Shetland Island) at ca 14 cal. ka BP, whilst a study by Sjunneskog and Taylor (2002) on a diatom abundance record from Palmer Deep (inner shelf west of the Antarctic Peninsula) indicates that grounded ice-retreat there occurred at ca 13.2 ka BP. Minzoni et al. (2017) report grounding line retreat from Ferrero Bay (inner shelf of the eastern ASE) before ~11 cal. ka, which coincides with WAIS retreat from inner Pine Island Bay (Hillenbrand et al., 2013). Given the deposition of Unit A, under a floating ice canopy, not far away from the grounding line,

we assume that it was deposited at very high sedimentation rates, which are expected to be at least an order of magnitude higher than at more distal locations (Andrews, 1987; Domack and McClennen, 1996). Interestingly, Milliken et al. (2009) report extremely low sedimentation rates in a similar setting with sedimentation under a permanent floating ice canopy in Maxwell Bay, which highlights the need to consider geomorphological features and the relative distance to the grounding line of an ice shelf.

#### 6.4.1.2 Unit B: Dynamic ice front

In Unit B, from 317 to 239 cmbsf, concentrations of the sea-ice biomarker lipid IPSO<sub>25</sub> range from 4 to 8 mg\*g OC<sup>-1</sup> and are significantly higher than in the underlying Unit A, except for an interval around 275 cmbsf, where the lipid is absent (Fig. 6.2 c). Concentrations of the phytoplankton-derived biomarker dinosterol show a similar pattern; increased values of 200-400 mg\*g OC<sup>-1</sup> (Fig. 6.2 b) relative to Unit A, interrupted by its absence at ca 275 cmbsf. The P<sub>D</sub>IPSO<sub>25</sub> index varies between 0.4 and 0.8 (Fig. 6.2 a).

The overall higher concentrations of both biomarker proxies in sediments from Unit B, when compared to those in sediments of Unit A, suggest more favorable environmental conditions for phytoplankton and IPSO<sub>25</sub> producing sea-ice diatoms, which we interpret as a result of break-up or retreat of the Getz Ice Shelf and establishment of seasonally open marine conditions (Fig. 6.4; Unit B). Ice shelf break-up conditions would also explain the low but significant diatom frustule concentrations in Unit B (cf. Hillenbrand et al., 2010). This conclusion is supported by our diatom TF which indicates a WSI concentration of ca 90 % during the deposition of this unit (Fig. 6.3 a).

Also, TOC, CaCO<sub>3</sub> and biogenic opal contents in Unit B sediments range from 0.2 to 0.4 wt %, 1-3 wt % and 2 wt %, respectively, and thus are higher than in the underlying sediments (Figs. 6.2 and 6.3), indicating increased marine productivity. The magnetic susceptibility generally decreases upwards throughout the unit to 200-350 x 10<sup>-5</sup> SI units, suggesting a reduction in the supply of terrigenous detritus or increase in supply of biogenic material. A peak of 350 x 10<sup>-5</sup> SI units at ca 275 cmbsf interrupts the decreasing trend, pointing to a higher terrigenous input as it is evident from a coinciding distinct maximum in coarse-grained debris >0.5 mm (1.7 wt %; Fig. 6.3). The grain-size is

dominated by mud (>90 wt %) throughout Unit B (Fig. 6.3 h), pointing to a grounding line distal glacimarine depositional setting (Hillenbrand et al., 2010; Smith et al., 2011). According to the RPI age model, Unit B is older than 12.7 cal. ka. Importantly, our new biomarker record provides greater detail than previous sedimentological studies (Hillenbrand et al., 2010; Smith et al., 2011), by revealing the onset of seasonal open-marine productivity at 317 cmbsf. This is shown by the rapid increase of both biomarkers from 317 to ca 280 cmbsf and intermediate to high  $P_{DIPSO_{25}}$  values. Based on a new study on marine sediments from the Antarctic Peninsula (Vorrath et al., 2019), such changes can result from a transition from extensive sea-ice cover to marginal sea-ice/ice-edge conditions. A similar transition from a floating ice canopy to sea-ice dominated conditions from ca. 14.1-14.8 ka to 10.1 ka BP has also been reported by Milliken et al. (2009) for Maxwell Bay.

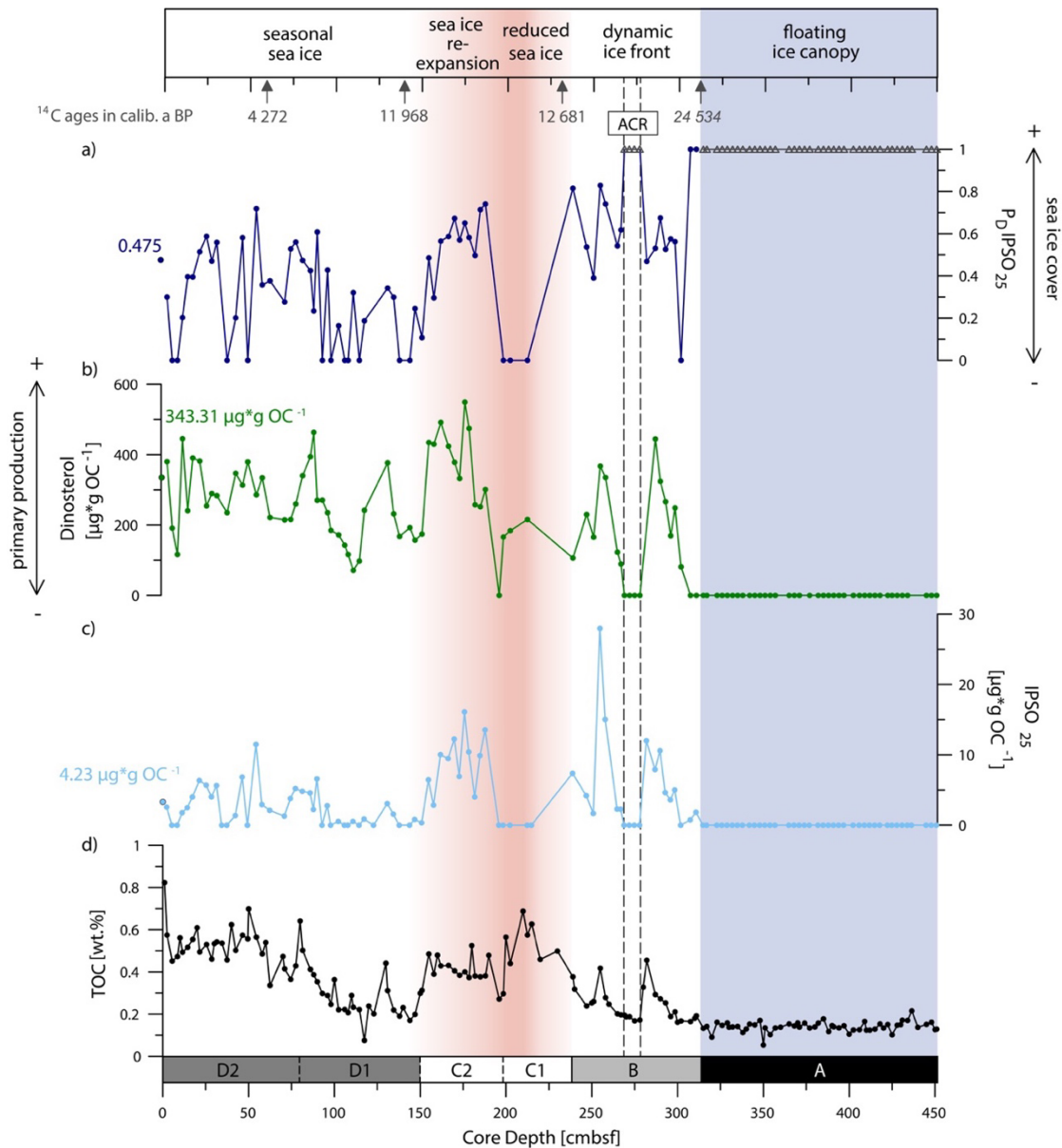


Fig. 6.2: Contents of  $P_D \text{IPSO}_{25}$  (a), dinosterol (b),  $\text{IPSO}_{25}$  (c) and TOC (d) in sediment core PS69/274-1. AMS  $^{14}\text{C}$  age constraints in calib. a before present (BP) in dark grey; unreliable age given in italics (Hillenbrand et al., 2010). Interval highlighted by dashed grey line marks the Antarctic Cold Reversal (ACR; Jouzel et al., 1995). Biomarker concentrations and calculated  $P_D \text{IPSO}_{25}$  value of the surface sample (box core PS69/275-2) indicated by dots with black circle and label in respective color. Triangles in  $P_D \text{IPSO}_{25}$ -curve: thick ice cover, maximum value of 1 assigned to these samples. Core is divided into four units as indicated in the lowermost and topmost bar: Unit A: floating ice canopy (blue shading), Unit B: dynamic ice front, Unit C: reduced sea ice/sea-ice re-expansion (red shading), Unit D: seasonal sea ice. (For interpretation of the references to color in this figure legend, the reader is referred to the Web version of this article.)

We attribute the lack of both biomarkers from 278 to 269 cmtbsf and the peak in magnetic susceptibility in this depth interval to a thick ice coverage, probably caused by an ice-shelf re-advance or the predominance of a perennial sea-ice cover and consequently also assign a maximum  $P_D \text{IPSO}_{25}$  value of 1 to these samples (displayed as triangles in Figs. 6.2 and 6.3). As Milliken et al. (2009) do not report (or resolve) such a

specific cooling interval in Maxwell Bay, we note that this suggested re-advance in ice-cover at our relatively more ice-shelf proximal core site may result from changes in local oceanic and/or atmospheric circulation patterns or a rapid ice-shelf surge.

However, taking account of the coarse resolution of the age model of core PS69/274-1, we contemplate that this hypothesized re-advance of the Getz Ice Shelf or development of perennial sea-ice cover tentatively may have been associated with the atmospheric cooling during the Antarctic Cold Reversal (ACR), which interrupted warming in Antarctica during the last deglaciation and lasted from 14.5 to 12.9 ka BP (Blunier et al., 1997; Blunier and Brook, 2001; Jouzel et al., 1995; WAIS Divide Project Members, 2013). The ACR coincided with the abrupt warming of the Bølling-Allerød interstadial in the North Atlantic and was characterized by Southern Ocean cooling and Antarctic sea ice reversing its deglacial retreat trend because of interhemispheric coupling mechanisms (Skinner et al., 2010). These opposing climate trends of the two hemispheres are proposed to be driven by oceanic and/or atmospheric processes and referred to as the bipolar seesaw (Anderson et al., 2009; Broecker, 1998; Pedro et al., 2011). Hitherto, the temporal and spatial extent of the ACR is mainly documented in Antarctic ice cores (e.g. Pedro et al., 2016), while only few marine records document re-advances of (sub-) Antarctic glaciers and elevated WSI concentrations during this time period (Bianchi and Gersonde, 2004; Graham et al., 2017; Xiao et al., 2016). Xiao et al. (2016), for example, compiled high resolution diatom composition records from the Antarctic Zone of Atlantic and Western Indian sectors of the Southern Ocean and determined the variability in summer sea surface temperatures and sea-ice conditions of the past 30 ka. They report a cooling observed in all investigated cores at 14-12 ka. Graham et al. (2017) used sea-floor geophysical data and marine sediment records off South Georgia and conclude on a cooling between 15.2 and 13.3 ka, both linking these cooling events to the ACR, revealing that this climate pattern extended up into the Atlantic sector of the Southern Ocean. Hence, locations more distal to the ice sheet (such as Southern Ocean pelagic records) seem to reflect atmospheric climate patterns rather than local trends, whilst locations in closer proximity to the ice shelf (such as our record), are much more likely influenced by, for example, a local or rapid ice-shelf surge.

Interestingly, in the sediments at ca 280 cmbsf, directly underlying the horizon of absence of both biomarkers, we observe a higher concentration of dinosterol as well as

relative maxima in the TOC and CaCO<sub>3</sub> contents and in the Sm/Chl ratios (Fig. 6.3 e and d). These peaks can be attributed to a short but significant warming period characterized by more open water conditions and higher productivity. Antarctic ice cores, such as the WAIS Divide Ice Core, and marine records from the Scotia Sea and the eastern Atlantic sector of the Southern Ocean (Xiao et al., 2016), also revealed a significant warming prior to the ACR during the Antarctic Isotope Maximum (AIM) 1 (Cuffey et al., 2016; WAIS Divide Project Members, 2013), which could have caused an increase in primary productivity reflected in higher dinosterol, TOC and CaCO<sub>3</sub> contents and of Sm/Chl ratios observed in core PS69/274-1 just shortly before the onset of the ACR. These elevated productivity proxies during AIM 1 argue against a perennial sea-ice or ice-shelf cover at the core site, though seasonal (winter/spring) sea ice must have occurred as it is indicated by the presence of IPSO<sub>25</sub> and diatom TF derived WSI concentrations of ca 90 %.

#### 6.4.1.3 Unit C: Reduced sea-ice cover followed by sea-ice re-expansion

Unit C in core PS69/274-1 (239-150 cmbsf) can be divided into two subunits (C1 and C2). Subunit C1 (239-196 cmbsf) comprises a diatomaceous ooze consisting of very well-preserved frustules of *Corethron pennatum*, which are considered open-water diatoms indicative of ice-free conditions (Maddison et al., 2005) and provided two AIO <sup>14</sup>C ages of 12.7 cal. ka BP, consistent with the RPI age constraints (Hillenbrand et al., 2010). The lower half of the subunit is not resolved by the biomarker data, while the upper half is characterized by the absence of the sea-ice biomarker IPSO<sub>25</sub> (Fig. 6.2 c). Concentrations of the phytoplankton-derived biomarker dinosterol vary slightly around a value of 180 mg\*g OC<sup>-1</sup>, also not resolving the lower half of the subunit (Fig. 6.2 b). The calculated sea-ice index P<sub>D</sub>IPSO<sub>25</sub> is 0, indicating the absence of spring sea-ice cover and predominantly open water conditions during spring and summer (Fig. 6.2 a; Belt, 2018; Müller et al., 2011). The relatively low dinosterol concentrations could be explained by unfavorable preservation conditions for organic compounds in the diatomaceous ooze, where an aggregation between fine-grained detritus and organic matter is severely restricted by the absence of silt and clay particles. Alternatively, either a limited nutrient supply in the open ocean could have reduced the productivity of dinosterol synthesizing phytoplankton species or exceptionally high sedimentation rates could have led to a

dilution of the biomarker signal (i.e. dinosterol) within the sediment (Belt, 2018; Lizotte, 2001). Sea-ice concentrations derived from diatom TF show a similar trend within subunit C1 and point towards a reduced WSI cover, even though the WSI concentration still ranges from 65 to 80 % (Fig. 6.3 a). The alleged discrepancy in the reconstructed sea surface conditions, under which subunit C1 was deposited, can be attributed to the different seasons represented by the two sea-ice proxies: While the sea-ice index  $P_{DI}PSO_{25}$  indicates a reduced sea-ice cover during spring and summer, the diatom TF derived WSI concentration reveals reduced but still existing sea-ice cover during the winter months (Fig. 6.3 a). With values between 0.4 and 0.6 wt %, 3 wt % and 40 wt %, respectively, the TOC,  $CaCO_3$  and biogenic opal contents in subunit C1 are even higher than in underlying Unit B (Fig. 6.3). Taking into account that the opal content determined for the sediments of subunit C1 is most likely underestimated because the leaching method applied for its measurement (Hillenbrand et al., 2010) is better suited for quantifying low opal contents (Müller and Schneider, 1993), the productivity proxies indicate high primary productivity, consistent with reduced sea-ice cover during spring and summer inferred from the biomarker data. The magnetic susceptibility values show an absolute minimum of  $<10 \times 10^{-5}$  SI units (Fig. 6.3 f), pointing to a very low content of terrigenous components and highlighting the biogenic composition of this subunit. The diatom TF derived WSI data, the biogenic opal and the magnetic susceptibility do, unlike the biomarker record, resolve the lower half of the subunit, suggesting the onset of reduced sea ice during spring and summer at around 12.7 cal. ka BP (239 cmbfs). A similar observation was made by Sjunneskog and Taylor (2002), whose diatom abundance record from Palmer Deep suggests that open water primary productivity commenced at 12.8 ka BP. The grain size distribution shows no significant change, unlike the phase of ice shelf break-up/retreat recorded in Unit B.

Based on these findings we conclude that during deposition of subunit C1 spring and summer sea-ice cover reached its minimum (Fig. 6.4; Unit C) promoting a higher diatom productivity and the deposition of the diatomaceous ooze. We tentatively suggest that the drastic decrease in spring/summer sea-ice coverage was linked to Antarctic warming that coincided with the onset of the Younger Dryas stadial in the Northern Hemisphere from 12.9-11.7 ka BP (centered at 12.85 ka BP; e.g. Denton et al., 2010). As already noted for the ACR, the environmental conditions at core site PS69/274-1 may have been



subject to local oceanic and atmospheric controls rather than to global teleconnections and attempts to relate these observations to interhemispheric feedback mechanisms certainly require more data from the Amundsen Sea and robust chronologies. However, the assignment of this minimum sea-ice/high productivity interval with the Younger Dryas is supported by AIO  $^{14}\text{C}$  dates obtained from the diatomaceous ooze in subunit C1 and in other cores recovered offshore from the westernmost Getz Ice Shelf (Hillenbrand et al., 2010, Figs. 6.2 and 6.3).

The reliability of these ages is considered high for three reasons: (1) AIO  $^{14}\text{C}$  ages obtained from sediments with very high biogenic contents, such as the very pure diatomaceous ooze of subunit C1, provide reliable dates because of high contents of fresh organic matter (e.g., Andrews et al., 1999); (2) the marine setting distal from the ice sheet grounding line implies that it is less affected by contamination with reworked fossil organic matter (Hillenbrand et al., 2010); and (3) confirmation by the RPI age model (Hillenbrand et al., 2010).

In subunit C2 from 196 to 150 cmbsf, concentrations of  $\text{IPSO}_{25}$  range from 6 to 16  $\text{mg}\cdot\text{g OC}^{-1}$  and are significantly higher than in the underlying subunit C1. The phytoplankton-derived biomarker dinosterol also shows significantly higher concentrations of 300-600  $\text{mg}\cdot\text{g OC}^{-1}$ , relative to the underlying subunit. The calculated sea-ice index  $\text{P}_{\text{D}}\text{IPSO}_{25}$  values around 0.7 resemble those in Unit B, which was deposited during the post-LGM break-up/ retreat of the Getz Ice Shelf (Fig. 6.2 a). Rising  $\text{IPSO}_{25}$  concentrations point to a re-expansion of spring sea-ice cover, while the strong increase and high concentrations in dinosterol point to either ice-free summer sea surface conditions or sustained ice-edge phytoplankton blooms. Primary production in marginal ice zones (MIZ) can exceed that of the permanently open ocean (Belt, 2018; Lizotte, 2001) and would explain the maximum concentration of dinosterol in subunit C2. Since diatom derived TF reconstructions for this subunit indicate a WSI concentration of 90 %, we assume that sea ice prevailed also during spring (promoting  $\text{IPSO}_{25}$  synthesis) but retreated in summer (permitting phytoplankton growth). TOC concentrations vary

around an average value of 0.4 wt %, whilst magnetic susceptibility values are also relatively constant (mean value of  $150 \times 10^{-5}$  SI units; Fig. 6.3 e and f).

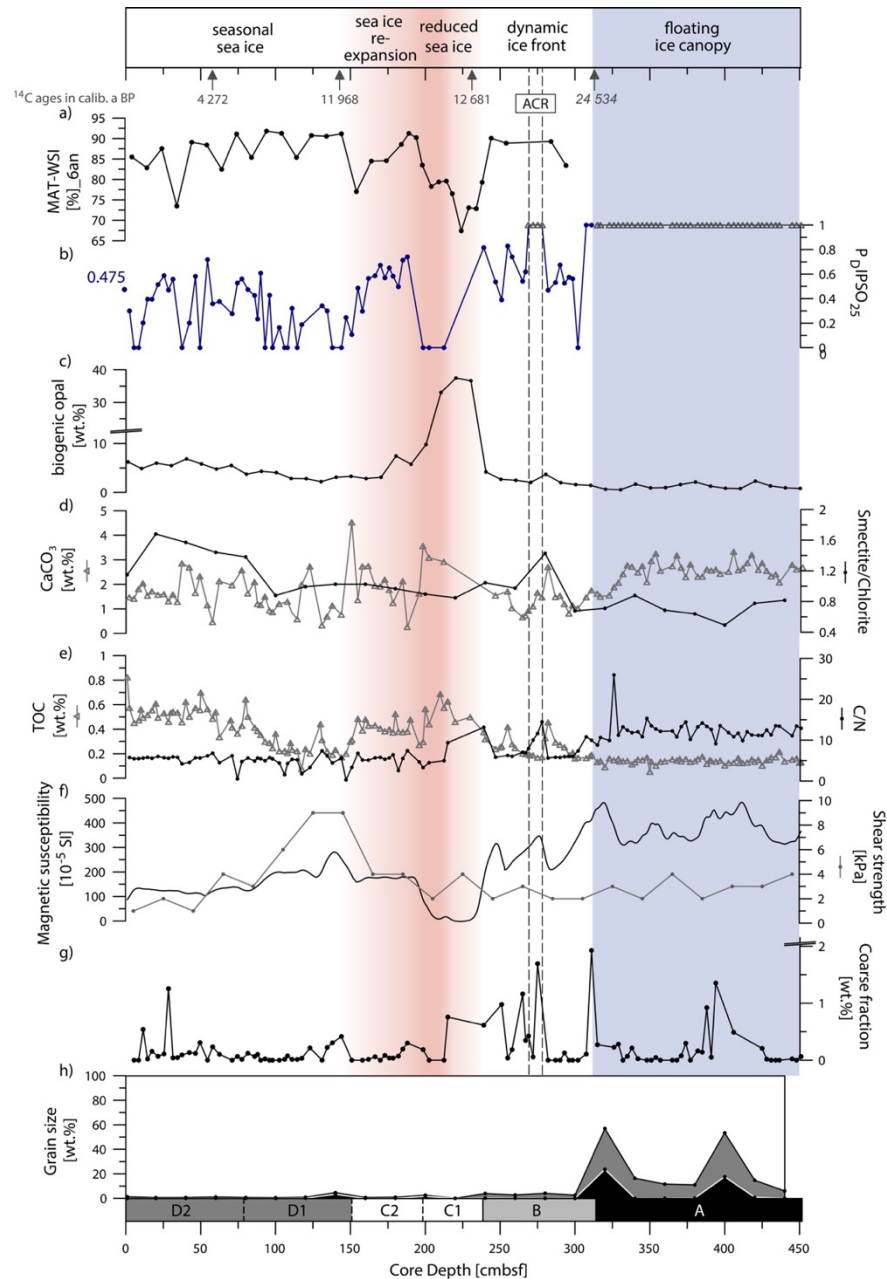


Fig. 6.3: Winter sea-ice concentrations based on diatom transfer functions (a),  $P_D$ IPSO<sub>25</sub> (b), biogenic opal (c), CaCO<sub>3</sub> and smectite/chlorite ratio (d), TOC and C/N ratio (e), magnetic susceptibility and shear strength (f), content of coarse-grained terrigenous debris (>0.5 mm; determined on distinct biomarker samples prior grinding; g) and contents of mud (0–63 mm; white infill), sand (63 mm–2 mm; grey infill) and gravel (>2 mm; black infill; h) for sediment core PS69/274-1. AMS <sup>14</sup>C age constraints in calib. a BP in dark grey; unreliable age given in italics (Hillenbrand et al., 2010). Interval highlighted by dashed grey line marks the Antarctic Cold Reversal (ACR; Jouzel et al., 1995). Calculated  $P_D$ IPSO<sub>25</sub> value of the surface sample (multi-core PS69/275-2) indicated by blue dot with black circle and label in respective color. Triangles in  $P_D$ IPSO<sub>25</sub>-curve: thick ice cover, maximum value of 1 assigned to these samples. Core is divided into four units as indicated in the lowermost and topmost bar: Unit A: floating ice canopy (blue shading), Unit B: dynamic ice front, Unit C: reduced sea ice/sea-ice re-expansion (red shading), Unit D: seasonal sea ice, as indicated in Fig. 6.2. (For interpretation of the references to color in this figure legend, the reader is referred to the Web version of this article.)

Likewise, there is no significant change in grain sizes in comparison to that of subunit C1, with mainly silt and clay being deposited (Fig. 6.3 h).

Based on these findings we conclude that subunit C2 reflects a time of sea-ice re-expansion during spring, which allowed for a high production of IPSO<sub>25</sub>. We suggest that this interval of sea-ice re-expansion coincided with the end of the Younger Dryas stadial in the Northern Hemisphere, which is roughly consistent with the AIO <sup>14</sup>C date of 11 989 cal. a BP (Hillenbrand et al., 2010, Figs. 6.2 and 6.3).

#### 6.4.1.4 Unit D: Seasonal sea-ice cover environment

The uppermost Unit D (150-0 cmbsf) spans the time after ca 12 ka BP (Hillenbrand et al., 2010) and is marked by highly variable biomarker concentrations. It can be divided into two subunits (D1 and D2).

In subunit D1 (150-80 cmbsf) concentrations of the sea-ice biomarker IPSO<sub>25</sub> are characterized by low values of ca 1 mg\*g OC<sup>-1</sup> (Fig. 6.2 c), while concentrations of the phytoplankton-derived biomarker dinosterol are more variable (100-400 mg\*g OC<sup>-1</sup>; Fig. 6.2 b). The generally low P<sub>D</sub>IPSO<sub>25</sub> values of 0-0.4 suggest a reduced sea-ice cover during deposition of subunit D1 (Fig. 6.2 a). In contrast, the diatom derived TF reconstructions indicate maximum WSI concentrations of ca 92 % (Fig. 6.3 a). These contrasting reconstructions highlight the potential limitations of the P<sub>D</sub>IPSO<sub>25</sub> proxy, which are discussed in more detail in chapter 6.5. At 140 cmbsf core depth, a minimum observed in both biomarker proxies coincides with a TOC minimum and elevated magnetic susceptibility values and gravel content (Fig. 6.3). The high values in magnetic susceptibility are in this case likely due to less dilution from biogenic material rather than increased terrigenous flux associated with IRD input or advance of the grounding line. Shear strength data in core PS69/274-1 show a significant increase from 3 to 9 kPa in subunit D1 (Fig. 6.3 f), which is also observed in other cores offshore from the westernmost Getz Ice Shelf (Hillenbrand et al., 2010; Smith et al., 2011) and possibly results from the slightly coarse-grained composition of this sediment interval as it is evident from the elevated gravel contents.

The upper subunit D2 (80-0 cmbsf) shows highly variable concentrations of the sea-ice biomarker IPSO<sub>25</sub> ranging between 0 and 12 mg\*g OC<sup>-1</sup> (Fig. 6.2 c), while intermediate concentrations of the phytoplankton-derived biomarker dinosterol vary

from 200 to 500 mg\*g OC<sup>-1</sup> (Fig. 6.2 b). The sea-ice index P<sub>D</sub>IPSO<sub>25</sub> fluctuates between 0 and 0.7 (Fig. 6.2 a), indicating highly variable sea-ice conditions. Diatom-based TF reveals WSI concentrations between 73 and 90 % (Fig. 6.3 a). TOC contents reach highest concentrations in the record (0.8 wt %; Fig. 6.3 e), indicating relatively high productivity during this time interval, which is also supported by the increase in biogenic opal concentration throughout subunit D2 with values from 2 to 7 wt % (Fig. 6.3 c). Magnetic susceptibility values slightly decrease upwards throughout the subunit from ca 200 to 120 x 10<sup>-5</sup> SI units, while the grain size remains unchanged with almost 100 % mud content (Fig. 6.3 f and h). The decreasing magnetic susceptibility values may refer to a reduced input of siliciclastic material resulting in lower sedimentation rates, which in turn may have led to a relative enrichment in biogenic material.

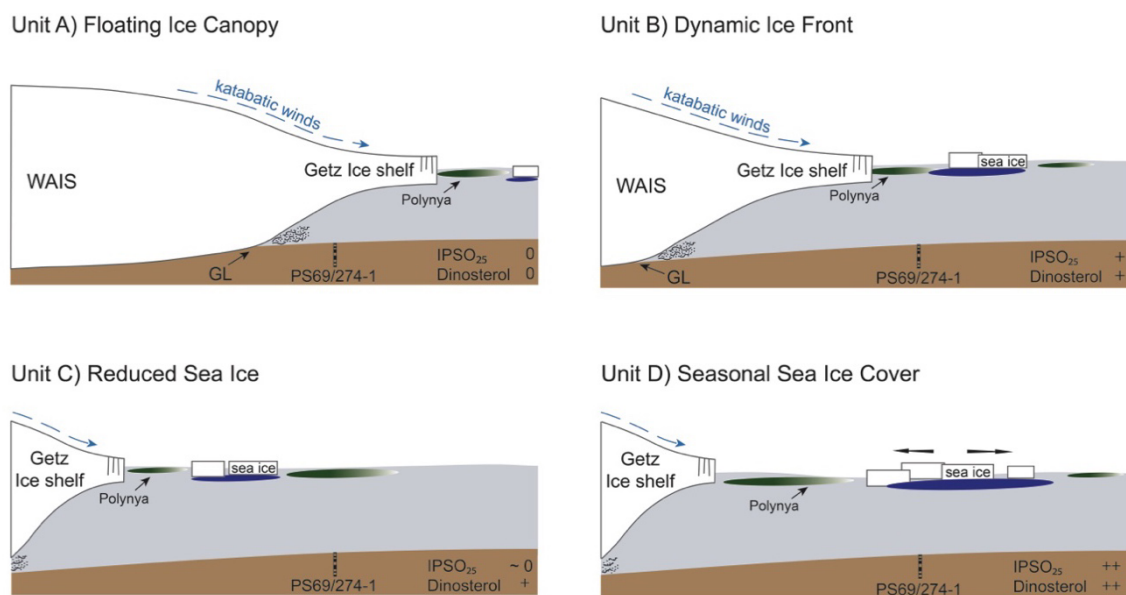


Fig. 6.4: Schematic cross-section showing the core location of sediment core PS69/274-1, illustrating the four general phases (Unit A-D) of sea-ice cover evolution and the retreat of the Getz Ice Shelf. Note that reconstruction refers to spring/summer sea-ice conditions. Production areas of IPSO<sub>25</sub> are shown in blue, phytoplankton dinosterol in green and input of coarse-grained debris >0.5 mm at grounding line (GL); WAIS: West Antarctic Ice Sheet. (For interpretation of the references to color in this figure legend, the reader is referred to the Web version of this article.)

Concentrations of the coarse grains >0.5 mm are relatively constant throughout Unit D, with a few distinct peaks up to 1.2 wt % in subunit D2 (Fig. 6.3 g; 26 cmbsf, 12.5 cmbsf). Based on these findings, we assume that Unit D in core PS69/274-1 was deposited in a seasonally open marine (i.e. only sea-ice covered during winter and spring) setting similar to today, while the overall co-occurrence and the in-phase changes of both biomarkers are potentially attributable to the establishment of the ASP (Fig. 6.4; Unit D)

favoring both IPSO<sub>25</sub> producing sea-ice diatom productivity as well as ice-edge phytoplankton blooms (cf. Belt, 2018). In this regard, we refer to Campagne et al. (2015) who reveal that each calving event of the Mertz Glacier Tongue (East Antarctica) since the last 250 years results in elevated abundances of IPSO<sub>25</sub> followed by a slow decrease of the sea-ice proxy and a concomitant increase of open-water proxies. Campagne et al. (2015) and Nihashi and Ohshima (2015) both conclude that local, rather than regional/global dynamics, such as the calving and regrowth of glacier tongues or landfast sea ice, play an important role in the formation and variability of polynya conditions and the resulting sedimentary biomarker/proxy records. Constraining polynya dynamics, however, is very challenging, since it is still debated, for example, whether the high productivity within the ASP is really archived in the underlying sediments (Kim et al., 2016) or not (Lee et al., 2017). Hence, it is important to make this subject a focus of future research. The limited availability of Holocene age constraints for core PS69/274-1 impedes direct comparisons with other marine records, from e.g. the Antarctic Peninsula, documenting warming and cooling periods such as the Mid Holocene Climatic Optimum or the Neoglacial (e.g. Heroy et al., 2008; Milliken et al., 2009; Sjunneskog and Taylor, 2002). However, we note that also the overall trends in IPSO<sub>25</sub>, dinosterol and TOC in Unit D do not exhibit significant similarity with records from the Antarctic Peninsula and hence tentatively suggest that the environment at the core site was controlled by local, potentially ASP, conditions.

#### 6.5 Applicability of the combined open-water phytoplankton biomarker and IPSO<sub>25</sub> approach

The PIPSO<sub>25</sub> approach combines information on ocean surface conditions derived from sea-ice algae and open-water phytoplankton. In this respect, it has the potential to be a powerful semi-quantitative tool for reconstructing sea-ice cover during the past. However, it is apparent that this novel proxy also has its limitations that need to be considered in order to establish robust interpretations. Most open-water phytoplankton biomarkers have multiple source organisms and are not specific to certain environments. Although dinoflagellates are the major source of the herein used open-water phytoplankton dinosterol, it is not unique to these organisms and is also found in

diatoms (Volkman et al., 1993; Volkman, 2006). Despite the different sources of dinosterol, it can still be considered a useful proxy for open water environments, since it has not yet been found in any other organisms of sympagic origin (Belt et al., 2018). Furthermore, selective degradation of IPSO<sub>25</sub> and phytoplankton biomarkers likely influences the ratio between their source and sedimentary environments (Rontani et al., 2019a, b). More in-situ studies investigating the transport and preservation of HBIs and sterols under varying oceanographic conditions (including different sedimentation rates) are needed to address these aspects.

Despite the need for further investigations to overcome these specific knowledge gaps, the combined approach of PIPSO<sub>25</sub> can help circumvent misleading interpretations, such as over-/underestimations of sea-ice cover on the basis of high/low IPSO<sub>25</sub> concentrations in the sediments. It is, however, important to carefully interpret the PIPSO<sub>25</sub> index when, for instance, fluctuations of IPSO<sub>25</sub> and the phytoplankton biomarker are in-phase. On the basis of work in the Arctic, Müller et al. (2011) demonstrated that coevally high (for marginal ice zone conditions) or low (for a perennial sea-ice cover) concentrations of both biomarkers can lead to similar PIP<sub>25</sub> values, despite the very different sea-ice conditions. The same principle also applies to the PIPSO<sub>25</sub> index, suggesting the need to interpret these data alongside other proxies.

Unit D1 (150-80 cmbsf) in core PS69/274-1, for instance, is characterized by intervals of very low concentrations of both biomarkers, which usually reflects unfavorable environmental conditions for sea ice diatoms as well as for phytoplankton. In general, these unfavorable environmental conditions are related to a very thick, perennial (sea) ice cover limiting light availability required for photosynthesis. The calculated low P<sub>D</sub>IPSO<sub>25</sub> values for this interval, however, point to a reduced sea-ice cover. This severe underestimation of sea-ice cover is revealed by the contrasting very high WSI concentrations (up to 90 %) derived from diatom TF. This scenario of a more extensive sea-ice cover than inferred from the P<sub>D</sub>IPSO<sub>25</sub> index is additionally supported by relatively low TOC concentrations and high magnetic susceptibility values. It is therefore important to carefully interpret the PIPSO<sub>25</sub> index not only in combination with other biomarker records but also alongside other proxy records, such as diatom TF data and sedimentological parameters.

## 6.6 Summary and conclusions

Changes in ice shelf/sea-ice cover in the western ASE since the post-LGM deglaciation have been reconstructed using the sea-ice proxy IPSO<sub>25</sub> and the phytoplankton-derived biomarker dinosterol. For a semi-quantitative reconstruction of ice cover, the phytoplankton-IPSO<sub>25</sub> index (P<sub>D</sub>IPSO<sub>25</sub>) was applied and compared to both WSI concentrations derived from diatom TF reconstructions and environmental constraints deduced from sedimentological data.

The Getz Ice Shelf and sea-ice cover in the study area show a dynamic behavior since the last deglaciation with a first break-up or retreat of the ice shelf and the establishment of a dynamic ice front just before 13 cal. ka BP. During the break-up/retreat phase, the biomarker proxy records tentatively suggest either a brief re-advance of the ice shelf or the temporary establishment of a perennial sea-ice cover, which could be linked to atmospheric cooling during the Antarctic Cold Reversal. Following this episode, the biomarker records reveal a phase with significantly reduced sea-ice cover during spring and summer around 12.7 cal. ka BP, which was characterized by deposition of a relatively pure diatomaceous ooze. This phase may be linked to a warming in Antarctica, which potentially coincided with the onset of the Younger Dryas stadial in the Northern Hemisphere, and may thus document interhemispheric climate coupling via the bipolar seesaw. After the predominantly open marine phase, a re-expansion of spring sea ice occurred in the western ASE and was followed by highly variable sea-ice conditions throughout the Holocene.

Our study demonstrates that pairing IPSO<sub>25</sub> and a phytoplankton biomarker has the potential to provide a valuable proxy for the assessment of past sea-ice environments in Antarctica. However, to obtain robust paleoenvironmental information, we recommend that the biomarker lipids are applied alongside other proxies, including diatom TF and TOC data and sedimentological parameters.

## 6.7 Supplements

Table S6.1: Mean and  $\pm$  standard deviations for each unit of sediment core PS69/274-1 (Cruise: ANT-XXIII/4; Station: PS69/274-1; Lon [dE]: -117,7757; Lat [dN]: -73,855; Water Depth: 1452 m).

| Unit | IPSO <sub>25</sub> | Dinosterol            | P <sub>D</sub> IPSO <sub>25</sub> | TOC               |
|------|--------------------|-----------------------|-----------------------------------|-------------------|
| A    | 0.000 $\pm$ 0.000  | 0.000 $\pm$ 0.000     | 1.000 $\pm$ 0.000                 | 0.145 $\pm$ 0.021 |
| B    | 5.355 $\pm$ 6.886  | 190.662 $\pm$ 211.790 | 0.690 $\pm$ 0.268                 | 0.244 $\pm$ 0.085 |
| C1   | 0.000 $\pm$ 0.000  | 199.772 $\pm$ 22.494  | 0.000 $\pm$ 0.000                 | 0.547 $\pm$ 0.096 |
| C2   | 6.001 $\pm$ 5.232  | 333.131 $\pm$ 151.671 | 0.497 $\pm$ 0.228                 | 0.380 $\pm$ 0.056 |
| D1   | 2.807 $\pm$ 2.833  | 248.654 $\pm$ 129.380 | 0.207 $\pm$ 0.199                 | 0.261 $\pm$ 0.099 |
| D2   | 3.217 $\pm$ 2.932  | 288.911 $\pm$ 82.068  | 0.351 $\pm$ 0.224                 | 0.491 $\pm$ 0.066 |

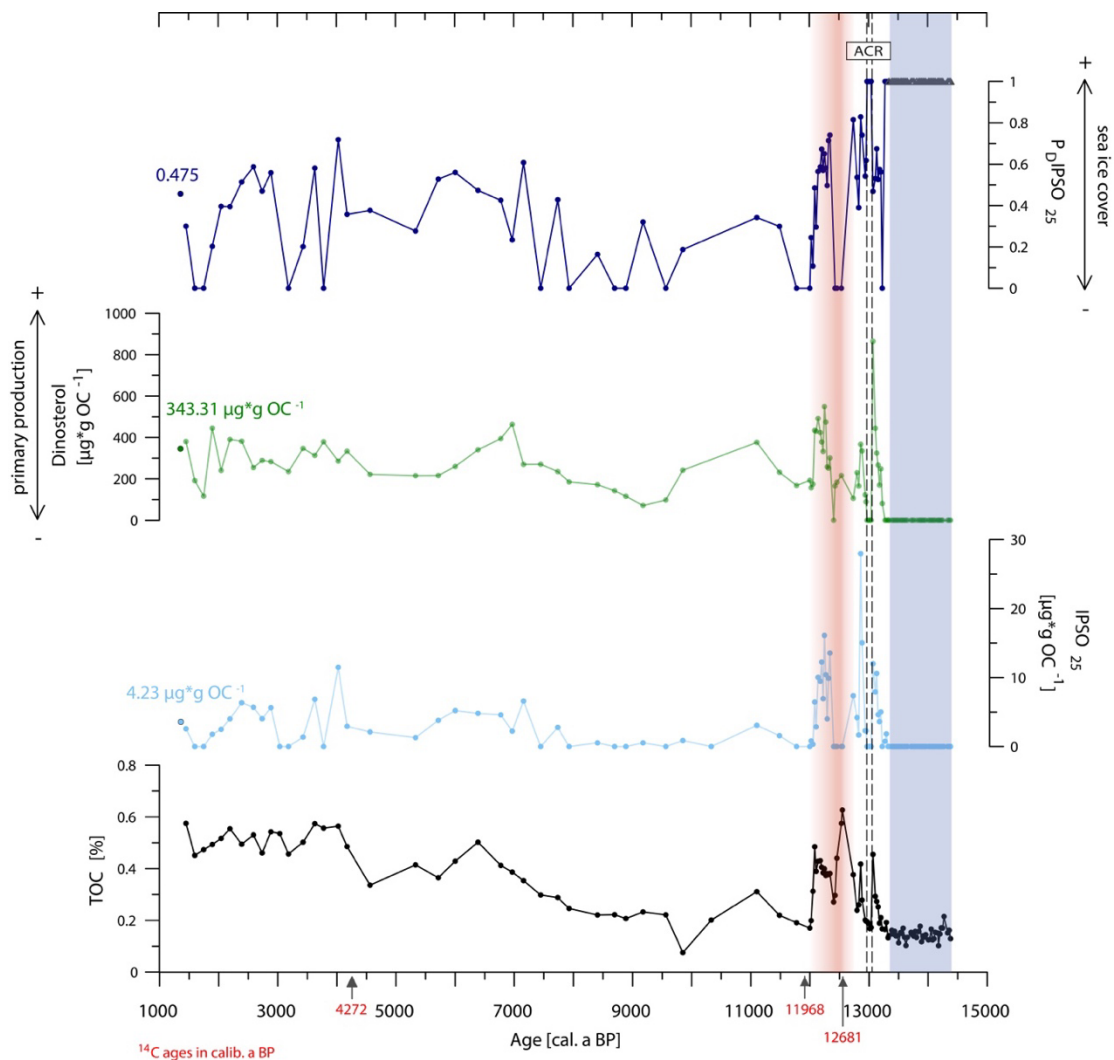


Fig. S6.1: Contents of P<sub>D</sub>IPSO<sub>25</sub>, dinosterol, IPSO<sub>25</sub> and TOC in sediment core PS69/274-1 plotted versus age. AMS <sup>14</sup>C age constraints in calib. a before present (BP) in red; unreliable age at 311.5-312.5 cmbsf was neglected for calculation of the age model. Interval highlighted by dashed grey line marks the Antarctic Cold Reversal (ACR; Jouzel et al., 1995). Biomarker concentrations and calculated P<sub>D</sub>IPSO<sub>25</sub> value of the surface sample (box core PS69/275-2) indicated by dots with black circle and label in respective color. Triangles in P<sub>D</sub>IPSO<sub>25</sub> curve: thick ice cover, maximum value of 1 assigned to these samples. Blue and red shading indicate the different units.



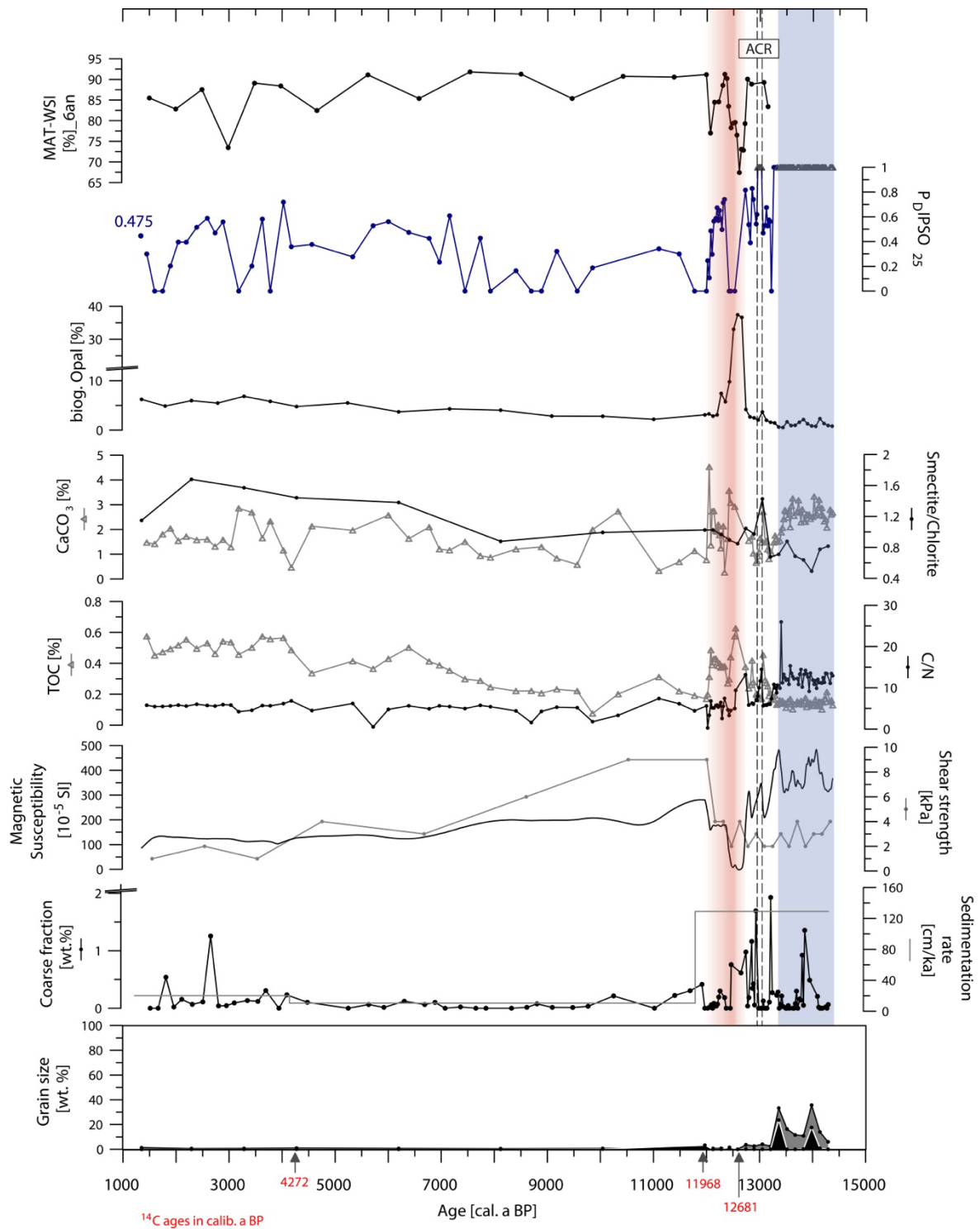


Fig. S6.2: Winter sea-ice concentrations based on diatom transfer functions,  $P_{DIPSO_{25}}$ , biogenic opal,  $CaCO_3$  and smectite/chlorite-ratio, TOC and C/N ratio, magnetic susceptibility and shear strength, content of coarse-grained terrigenous debris ( $>0.5$  mm; determined on distinct biomarker samples prior grinding), sedimentation rate [in cm/ka] and contents of mud (0-63  $\mu$ m; white infill), sand (63  $\mu$ m-2 mm; grey infill) and gravel ( $> 2$ mm; black infill) for sediment core PS69/274-1 plotted versus age. AMS  $^{14}C$  age constraints in calib. a BP in red; unreliable age at 311.5-312.5 cmtsf was neglected for calculation of the age model. Sedimentation rate earlier than the oldest age constrain is expected to have remained unchanged. Interval highlighted by dashed grey line marks the Antarctic Cold Reversal (ACR; Jouzel et al., 1995). Calculated  $P_{DIPSO_{25}}$  value of the surface sample (multi-core PS69/275-2) indicated by blue dot with black circle and label in respective color. Triangles in  $P_{DIPSO_{25}}$ -curve: thick ice cover, maximum value of 1 assigned to these samples. Blue and red shading indicate the different units.

## 6.8 Corrigendum to “Highly branched isoprenoids reveal onset of deglaciation followed by dynamic sea-ice conditions in the western Amundsen Sea, Antarctica” [Quat. Sci. Rev. 228 (2020) 106103]

After publication of the article, the authors noticed a mistake in the concentration calculations of the two biomarker lipids IPSO<sub>25</sub> and dinosterol. The volume of the internal standards 7-HND and 5 $\alpha$ -androstan-3-ol had incorrectly been calculated twice. Hence, the absolute concentrations of IPSO<sub>25</sub> are erroneously higher by factor 20 and the concentrations of dinosterol are erroneously higher by factor 60. The calculated P<sub>D</sub>IPSO<sub>25</sub> index is not affected by these changes. The changes have no impact on the scientific results and reasoning presented in the paper.

### *In 4.1.2. Unit B: Dynamic ice front*

The value for IPSO<sub>25</sub> was reported as 4-8 mg\*g OC<sup>-1</sup>, but should now be corrected to 0.2-0.4 mg\*g OC<sup>-1</sup>.

The value for dinosterol was reported as 200-400 mg\*g OC<sup>-1</sup>, but should now be corrected to ca 2-7 mg\*g OC<sup>-1</sup>.

### *In 4.1.3. Unit C: Reduced sea-ice cover followed by sea-ice re-expansion*

In subunit C1, the value for dinosterol was reported as 180 mg\*g OC<sup>-1</sup>, but should be corrected to 3 mg\*g OC<sup>-1</sup>.

In subunit C2, the value for IPSO<sub>25</sub> was reported as 6-16 mg\*g OC<sup>-1</sup>, but should be corrected to 0.3-0.8 mg\*g OC<sup>-1</sup>.

In subunit C2, the value for dinosterol was reported as 300-600 mg\*g OC<sup>-1</sup>, but should be corrected to 5-10 mg\*g OC<sup>-1</sup>.

### *In 4.1.4. Unit D: Seasonal sea-ice cover environment*

In subunit D1, the value for IPSO<sub>25</sub> was reported as ca 1 mg\*g OC<sup>-1</sup>, but should be corrected to ca 0.05 mg\*g OC<sup>-1</sup>.

In subunit D1, the value for dinosterol was reported as 100-400 mg\*g OC<sup>-1</sup>, but should be corrected to ca 1-7 mg\*g OC<sup>-1</sup>. In subunit D2, the value for IPSO<sub>25</sub> was reported as 0-12 mg\*g OC<sup>-1</sup>, but should be corrected to 0-0.2 mg\*g OC<sup>-1</sup>.

In subunit D2, the value for dinosterol was reported as 200-500 mg\*g OC<sup>-1</sup>, but should be corrected to ca 3-8 mg\*g OC<sup>-1</sup>.

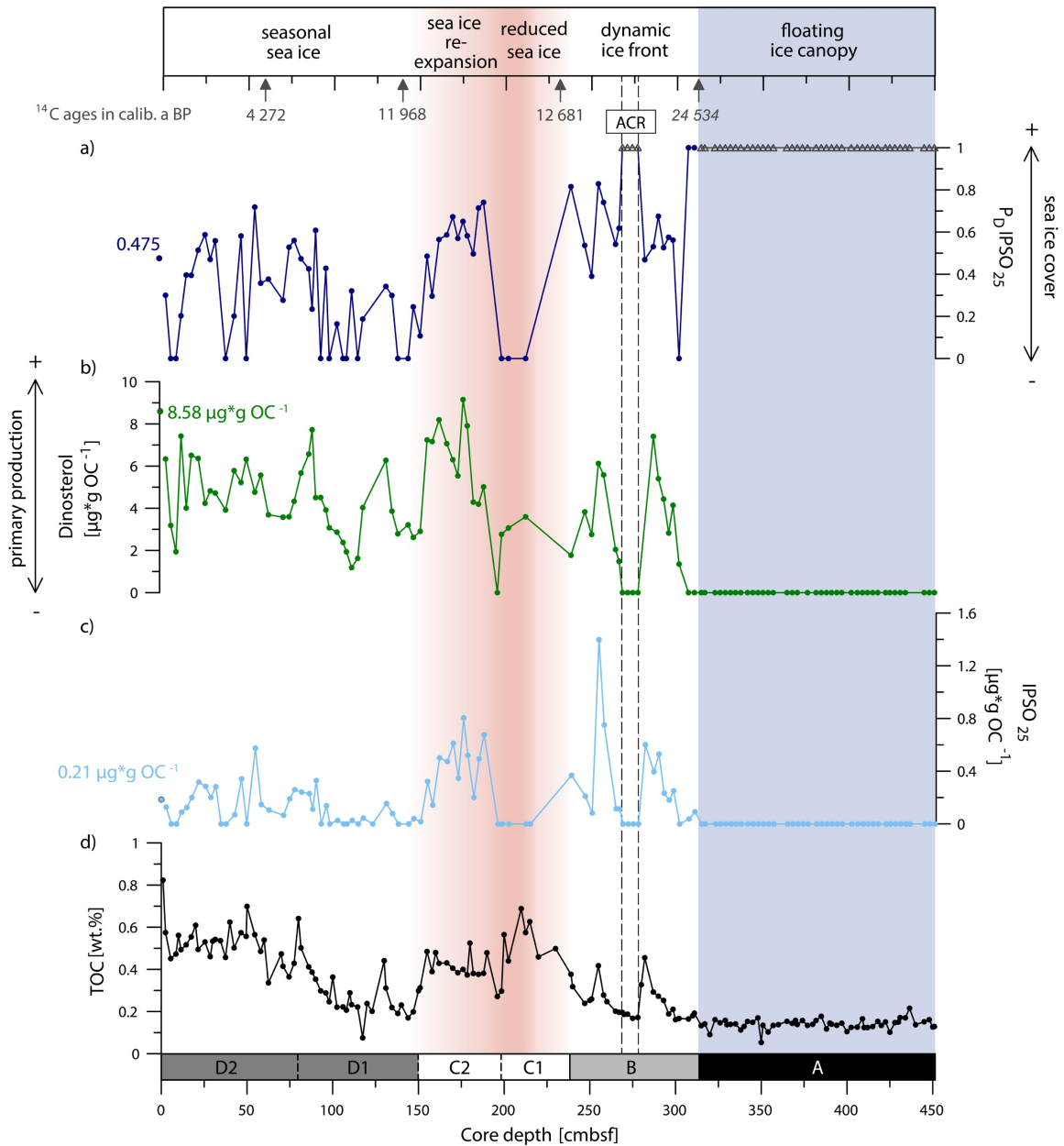


Fig. 6.2: Contents of  $P_D$ IPSO<sub>25</sub> (a), dinosterol (b), IPSO<sub>25</sub> (c) and TOC (d) in sediment core PS69/274-1. AMS <sup>14</sup>C age constraints in calib. a before present (BP) in dark grey; unreliable age given in italics (Hillenbrand et al., 2010). Interval highlighted by dashed grey line marks the Antarctic Cold Reversal (ACR; Jouzel et al., 1995). Biomarker concentrations and calculated  $P_D$ IPSO<sub>25</sub> value of the surface sample (box core PS69/275-2) indicated by dots with black circle and label in respective color. Triangles in  $P_D$ IPSO<sub>25</sub>-curve: thick ice cover, maximum value of 1 assigned to these samples. Core is divided into four units as indicated in the lowermost and topmost bar: Unit A: floating ice canopy (blue shading), Unit B: dynamic ice front, Unit C: reduced sea ice/sea-ice re-expansion (red shading), Unit D: seasonal sea ice. (For interpretation of the references to color in this figure legend, the reader is referred to the Web version of this article).

### Data availability

Datasets related to this article can be found online on *PANGAEA Data Publisher for Earth & Environmental Science* (doi:10.1594/PANGAEA.904263).

## Acknowledgements

Denise Diekstall, Maximilian Mues, Robert Grosser and Mandy Kuck are kindly acknowledged for laboratory support. We thank the captain, crew and science party of RV *Polarstern* cruise PS69. Simon Belt is acknowledged for providing the 7-HND internal standard for HBI quantification. N.L. and J.M. were funded through the Helmholtz Research Grant VH-NG-1101. J.A.S. and C.D.H. were funded by NERC grant NE/M013081/1. G.K. was funded through the research program PACES II: Polar Regions and Coasts in the changing EarthSystem.

## 7 Conclusions and outlook

### Conclusions

This thesis provides a thorough evaluation of the applicability of the sea-ice biomarker proxy IPSO<sub>25</sub> as well as the combinatory approach PIPSO<sub>25</sub> (the combination of IPSO<sub>25</sub> with an open-water phytoplankton biomarker) and their potential to serve as reliable indicators for recent and past sea-ice conditions in the Southern Ocean.

Analyses on IPSO<sub>25</sub>, HBI-trienes, phytosterols and GDGTs performed on surface sediments from the Antarctic Peninsula, the Amundsen and Weddell Seas, revealed their suitability as proxies for recent sea-ice conditions and ocean temperatures, as shown in chapter 4 of this thesis. Correlations of proxy-based sea-ice reconstructions based on the PIPSO<sub>25</sub> index with satellite sea-ice data and modelled sea-ice data provided good results, while reconstructions of ocean temperatures based on the RI-OH' paleothermometer revealed a better agreement with instrumental and model data than the TEX<sup>L</sup><sub>86</sub> paleothermometer. Furthermore, the data collected within this study support the presumed relationship between IPSO<sub>25</sub> and platelet ice formation. This study thus helped confirming not only the reliability of the biomarker sea-ice proxy IPSO<sub>25</sub> and its semi-quantitative approach PIPSO<sub>25</sub>, but also to further specify its spatial use.

The specific application of IPSO<sub>25</sub> on paleo sediment records enabled a first reconstruction of sea surface conditions in the eastern and western Amundsen Sea based on biomarker records.

In chapter 5 of this thesis, the PIPSO<sub>25</sub> index was used in a multi-proxy approach on a high-resolution sediment core located in the direct vicinity of the PIG in the eastern Amundsen Sea. By means of the PIPSO<sub>25</sub> index alongside phytoplankton markers, sedimentological parameters and physical properties, the transition from a polynya setting relatively close to the calving front towards a sea-ice dominated setting during the early Holocene was reconstructed. These findings were brought into context with a changing influence of CDW in the region.

Further, a sediment record from the western Amundsen Sea was tested for IPSO<sub>25</sub> and phytoplankton markers and interpreted in a multi-proxy approach as described in chapter 6. Based on the PIPSO<sub>25</sub> index in comparison with winter sea-ice concentrations derived from diatom TF alongside sedimentological parameters, changes in ice

shelf/sea-ice cover since the last deglaciation were revealed. The biomarker records show that after a first break-up of the Getz Ice Shelf (just before 13 cal. ka BP), a heavy ice cover dominated, followed by a phase of reduced sea ice (at around 12.7 cal. ka BP) allowing primary productivity until a re-expansion of sea ice occurred with highly variable sea-ice conditions throughout the Holocene.

The findings collected throughout this thesis motivate to further collect biomarker data along the West Antarctic continental shelves to specify the use of IPSO<sub>25</sub> as a (paleo) sea-ice indicator for the Southern Ocean since the results collected within this thesis revealed its potential as such.

## Outlook

Compared to the sea-ice proxy IP<sub>25</sub> in the Arctic, the sea-ice proxy for the Southern Ocean IPSO<sub>25</sub> is significantly less studied. The biomarker records presented in this study hence contribute to the knowledge about the application of IPSO<sub>25</sub> for paleo sea-ice reconstructions and add, as the first biomarker records, to the understanding about the evolution of ice shelf and sea-ice conditions in the eastern and western Amundsen Sea, i.e. the evolution of the PIG and the Getz Ice Shelf since the post-LGM deglaciation.

Still, there are many unknowns in the equation. A first step to fill these gaps of knowledge for future IPSO<sub>25</sub> studies would be an expansion of surface sediment studies from different areas of the Southern Ocean to further refine the applicability of the proxy, gather information about the source organisms (by analyzing diatom assemblages within sediment or sea-ice samples) and their habitat as well as degradation effects during transport (by using sediment traps) and after deposition within the sediments. Further, acquiring more paleo-records of IPSO<sub>25</sub> would add to the collection of biomarker-based sea-ice reconstructions for the Southern Ocean and thereby extending the temporal and spatial range of the sea-ice proxy. The West Antarctic continental shelves are surely of special interest, since the most pronounced negative sea-ice trends are observed in these climate sensitive regions. More sea-ice reconstructions here would not only yield more detailed information on the evolution of sea ice in the past, but also contribute to the understanding of the different feedback mechanisms concerning sea ice – its effect on the albedo, ice sheet stability, oceanographic and atmospheric processes. The more

detailed data from the past are collected, the better the modern climate models are able to predict future scenarios in a warming world.

Apart from the West Antarctic continental shelves, however, a look into the other, (so far) more stable part of Antarctica, the East Antarctic continental shelves occurs rather interesting. Here, even less studies have been conducted so far, but it would surely provide useful information on the spatial applicability of IPSO<sub>25</sub>.

To date, most Southern Ocean sea-ice reconstructions based on marine sediments are inferred from diatom assemblages which provide useful insights into winter sea-ice distributions. But this only applies if sediment preservation allows it, since the fragile diatom frustules are prone to dissolution effects (especially proximal to ice shelves). Hence, comparison studies on different sea-ice proxies would be of special value, since other sea-ice proxies, such as HBIs (i.e., IPSO<sub>25</sub>) would complement sea-ice reconstructions derived from diatom assemblages. IPSO<sub>25</sub> yields a high potential to reconstruct sea-ice conditions proximal to ice shelves and may hence give valuable information on sea-ice and ice shelf interactions.

Even though it is still in its infancy, another promising tool for comparison studies has just emerged, that exploits the genetic biodiversity preserved in marine sediments, sedimentary ancient DNA. With this approach, the ancient DNA of specific sea-ice organisms (mainly microbial eukaryotes, directly linked to sea ice or specific sea-ice organisms) preserved in marine sediments are used as paleo sea-ice indicators. This proxy may have the potential to close not only the temporal but also the spatial gap currently existing in sea-ice reconstructions, since ancient DNA has already been identified in geological records back to ca. 100 ka ago and related to changing sea-ice conditions and also been recovered from deep-ocean sediments.

By using the advantages of each of the existing sea-ice proxies, a broader view (spatially and temporal) on past sea-ice conditions may be achieved and the collected observational data are of special value for improving model simulations for the future perspective of sea ice in our warming world.

## 8 References

- Abernathy, R.P., Cerovecki, I., Holland, P.R., Newsom, E., Mazloff, M., Talley, L.D., 2016. Water-mass transformation by sea ice in the upper branch of the Southern Ocean overturning. *Nature Geoscience* 9, 596-601.
- Adusumilli, S., Fricker, H., Medley, B., Padman, L., Siegfried, M., 2020. Interannual variations in meltwater input to the Southern Ocean from Antarctic ice shelves. *Nature Geoscience* 13, 1-5.
- Alderkamp, A.-C., Mills, M.M., van Dijken, G.L., Laan, P., Thuróczy, C.-E., Gerringa, L.J., de Baar, H.J., Payne, C.D., Visser, R.J., Buma, A.G., 2012. Iron from melting glaciers fuels phytoplankton blooms in the Amundsen Sea (Southern Ocean): Phytoplankton characteristics and productivity. *Deep Sea Research Part II: Topical Studies in Oceanography* 71, 32-48.
- Allen, C.S., Pike, J., Pudsey, C.J., 2011. Last glacial–interglacial sea-ice cover in the SW Atlantic and its potential role in global deglaciation. *Quaternary Science Reviews* 30, 2446-2458.
- Alonso-Sáez, L., Andersson, A., Heinrich, F., Bertilsson, S., 2011. High archaeal diversity in Antarctic circumpolar deep waters. *Environmental microbiology reports* 3, 689-697.
- Anderson, P.S., 1993. Evidence for an Antarctic winter coastal polynya. *Antarctic science* 5, 221-226.
- Anderson, R., Ali, S., Bradtmiller, L., Nielsen, S., Fleisher, M., Anderson, B., Burckle, L., 2009. Wind-driven upwelling in the Southern Ocean and the deglacial rise in atmospheric CO<sub>2</sub>. *Science* 323, 1443-1448.
- Andrews, J.T., 1987. Late Quaternary marine sediment accumulation in fiord-shelf-deep-sea transects, Baffin Island to Baffin Bay. *Quaternary Science Reviews* 6, 231-243.
- Andrews, J.T., Domack, E.W., Cunningham, W.L., Leventer, A., Licht, K.J., Jull, A.T., DeMaster, D.J., Jennings, A.E., 1999. Problems and possible solutions concerning radiocarbon dating of surface marine sediments, Ross Sea, Antarctica. *Quaternary Research* 52, 206-216.
- Armand, L., Zielinski, U., 2001. Diatom species of the genus *Rhizosolenia* from Southern Ocean sediments: distribution and taxonomic notes. *Diatom Research* 16, 259-294.
- Armand, L.K., Leventer, A., 2003. Palaeo sea ice distribution–reconstruction and palaeoclimatic significance. *Sea ice—an introduction to its physics, biology, chemistry, and geology*, 333-372.
- Armand, L.K., Crosta, X., Romero, O., Pichon, J.-J., 2005. The biogeography of major diatom taxa in Southern Ocean sediments: 1. Sea ice related species. *Palaeogeography, Palaeoclimatology, Palaeoecology* 223, 93-126.
- Armand, L., Ferry, A., and Leventer, A., 2017. Advances in palaeo sea-ice estimation, in: *Sea Ice Edition 3*, edited by: Thomas, D., Wiley-Blackwell, Oxford, UK, Ch. 26., 600–629.
- Arndt, J.E., Schenke, H.W., Jakobsson, M., Nitsche, F.O., Buys, G., Goleby, B., Rebesco, M., Bohoyo, F., Hong, J., Black, J., Greku, R., Udintsev, G., Barrios, F., Reynoso-Peralta, W., Taisei, M., Wigley, R., 2013. The International Bathymetric Chart of the Southern Ocean (IBCSO) Version 1.0—A new bathymetric compilation covering circum-Antarctic waters. *Geophysical Research Letters* 40, 3111-3117.
- Arrigo, K.R., 2017. Sea ice as a habitat for primary producers. *Sea ice*, 352-369.



- Arrigo, K.R., Thomas, D.N., 2004. Large scale importance of sea ice biology in the Southern Ocean. *Antarctic Science* 16, 471-486.
- Arrigo, K.R., van Dijken, G., Long, M., 2008. Coastal Southern Ocean: A strong anthropogenic CO<sub>2</sub> sink. *Geophysical Research Letters* 35.
- Arrigo, K.R., Van Dijken, G.L., 2003. Phytoplankton dynamics within 37 Antarctic coastal polynya systems. *Journal of Geophysical Research: Oceans* 108.
- Arrigo, K.R., van Dijken, G.L., Strong, A.L., 2015. Environmental controls of marine productivity hot spots around Antarctica. *Journal of Geophysical Research: Oceans* 120, 5545-5565.
- Arrigo, K.R., Worthen, D.L., Lizotte, M.P., Dixon, P., Dieckmann, G., 1997. Primary production in Antarctic sea ice. *Science* 276, 394-397.
- Ballard, G., Toniolo, V., Ainley, D.G., Parkinson, C.L., Arrigo, K.R., Trathan, P.N., 2010. Responding to climate change: Adélie penguins confront astronomical and ocean boundaries. *Ecology* 91, 2056-2069.
- Barbara, L., Crosta, X., Leventer, A., Schmidt, S., Etourneau, J., Domack, E., Massé, G., 2016. Environmental responses of the Northeast Antarctic Peninsula to the Holocene climate variability. *Paleoceanography* 31, 131-147.
- Barbara, L., Crosta, X., Massé, G., Ther, O., 2010. Deglacial environments in eastern Prydz Bay, East Antarctica. *Quaternary Science Reviews* 29, 2731-2740.
- Barbara, L., Crosta, X., Schmidt, S., Massé, G., 2013. Diatoms and biomarkers evidence for major changes in sea ice conditions prior the instrumental period in Antarctic Peninsula. *Quaternary Science Reviews* 79, 99-110.
- Belt, S.T., 2018. Source-specific biomarkers as proxies for Arctic and Antarctic sea ice. *Organic Geochemistry*.
- Belt, S.T., Allard, W.G., Massé, G., Robert, J.-M., Rowland, S.J., 2000. Highly branched isoprenoids (HBIs): identification of the most common and abundant sedimentary isomers. *Geochimica et Cosmochimica Acta* 64, 3839-3851.
- Belt, S.T., Brown, T.A., Ampel, L., Cabedo-Sanz, P., Fahl, K., Kocis, J.J., Masse, G., Navarro-Rodriguez, A., Ruan, J., Xu, Y., 2014. An inter-laboratory investigation of the Arctic sea ice biomarker proxy IP<sub>25</sub> in marine sediments: key outcomes and recommendations. *Clim. Past* 10, 155-166.
- Belt, S.T., Brown, T.A., Smik, L., Assmy, P., Mundy, C., 2018. Sterol identification in floating Arctic sea ice algal aggregates and the Antarctic sea ice diatom *Berkeleleya adeliensis*. *Organic geochemistry* 118, 1-3.
- Belt, S.T., Brown, T.A., Smik, L., Tatarek, A., Wiktor, J., Stowasser, G., Assmy, P., Allen, C.S., Husum, K., 2017. Identification of C<sub>25</sub> highly branched isoprenoid (HBI) alkenes in diatoms of the genus *Rhizosolenia* in polar and sub-polar marine phytoplankton. *Organic Geochemistry* 110, 65-72.
- Belt, S.T., Cabedo-Sanz, P., Smik, L., Navarro-Rodriguez, A., Berben, S.M.P., Knies, J., Husum, K., 2015. Identification of paleo Arctic winter sea ice limits and the marginal ice zone: Optimised biomarker-based reconstructions of late Quaternary Arctic sea ice. *Earth and Planetary Science Letters* 431, 127-139.
- Belt, S.T., Massé, G., Rowland, S.J., Poulin, M., Michel, C., LeBlanc, B., 2007. A novel chemical fossil of palaeo sea ice: IP<sub>25</sub>. *Organic Geochemistry* 38, 16-27.

- Belt, S.T., Massé, G., Vare, L.L., Rowland, S.J., Poulin, M., Sicre, M.-A., Sampei, M., Fortier, L., 2008. Distinctive  $^{13}\text{C}$  isotopic signature distinguishes a novel sea ice biomarker in Arctic sediments and sediment traps. *Marine Chemistry* 112, 158-167.
- Belt, S.T., Müller, J., 2013. The Arctic sea ice biomarker IP<sub>25</sub>: a review of current understanding, recommendations for future research and applications in palaeo sea ice reconstructions. *Quaternary Science Reviews* 79, 9-25.
- Belt, S.T., Smik, L., Brown, T.A., Kim, J.H., Rowland, S.J., Allen, C.S., Gal, J.K., Shin, K.H., Lee, J.I., Taylor, K.W.R., 2016. Source identification and distribution reveals the potential of the geochemical Antarctic sea ice proxy IPSO<sub>25</sub>. *Nature Communications* 7, 12655.
- Benz, V., Esper, O., Gersonde, R., Lamy, F., Tiedemann, R., 2016. Last Glacial Maximum sea surface temperature and sea-ice extent in the Pacific sector of the Southern Ocean. *Quaternary Science Reviews* 146, 216-237.
- Berger, A., 1978. Long-term variations of daily insolation and Quaternary climatic changes. *Journal of the atmospheric sciences* 35, 2362-2367.
- Berkman, P.A., Forman, S.L., 1996. Pre-bomb radiocarbon and the reservoir correction for calcareous marine species in the Southern Ocean. *Geophysical Research Letters* 23, 363-366.
- Blunier, T., Brook, E.J., 2001. Timing of millennial-scale climate change in Antarctica and Greenland during the last glacial period. *Science* 291, 109-112.
- Blunier, T., Schwander, J., Stauffer, B., Stocker, T., Dällenbach, A., Indermühle, A., Tschumi, J., Chappellaz, J., Raynaud, D., Barnola, J.M., 1997. Timing of the Antarctic Cold Reversal and the atmospheric CO<sub>2</sub> increase with respect to the Younger Dryas event. *Geophysical Research Letters* 24, 2683-2686.
- Boon, J.J., Rijpstra, W.I.C., de Lange, F., De Leeuw, J., Yoshioka, M., Shimizu, Y., 1979. Black Sea sterol—a molecular fossil for dinoflagellate blooms. *Nature* 277, 125.
- Bopp, L., Kohfeld, K.E., Le Quéré, C., Aumont, O., 2003. Dust impact on marine biota and atmospheric CO<sub>2</sub> during glacial periods. *Paleoceanography* 18.
- Broecker, W.S., 1998. Paleocean circulation during the last deglaciation: a bipolar seesaw? *Paleoceanography* 13, 119-121.
- Brown, T., 2011. Production and preservation of the Arctic sea ice diatom biomarker IP<sub>25</sub>. University of Plymouth.
- Brown, T.A., Belt, S.T., Tatarek, A., Mundy, C., 2014. Source identification of the Arctic sea ice proxy IP<sub>25</sub>. *Nature Communications* 5, 4197.
- Campagne, P., Crosta, X., Houssais, M.-N., Swingedouw, D., Schmidt, S., Martin, A., Devred, E., Capo, S., Marieu, V., Closset, I., 2015. Glacial ice and atmospheric forcing on the Mertz Glacier Polynya over the past 250 years. *Nature communications* 6, 6642.
- Cavalieri, D., Parkinson, C., Gloersen, P., Zwally, H., 1996. Sea ice concentrations from Nimbus-7 SMMR and DMSP SSM/I passive microwave data. National Snow and Ice Data Center, Boulder, Colorado, USA.
- Collares, L.L., Mata, M.M., Kerr, R., Arigony-Neto, J., Barbat, M.M., 2018. Iceberg drift and ocean circulation in the northwestern Weddell Sea, Antarctica. *Deep Sea Research Part II: Topical Studies in Oceanography* 149, 10-24.

- Colleoni, F., De Santis, L., Siddoway, C.S., Bergamasco, A., Golledge, N.R., Lohmann, G., Passchier, S., Siegert, M.J., 2018. Spatio-temporal variability of processes across Antarctic ice-bed–ocean interfaces. *Nature communications* 9, 2289.
- Collins, L.G., Allen, C.S., Pike, J., Hodgson, D.A., Weckström, K., Massé, G., 2013b. Evaluating highly branched isoprenoid (HBI) biomarkers as a novel Antarctic sea-ice proxy in deep ocean glacial age sediments. *Quaternary Science Reviews* 79, 87-98.
- Collins, M., R. Knutti, J. Arblaster, J.-L. Dufresne, T. Fichet, P. Friedlingstein, X. Gao, W.J. Gutowski, T. Johns, G. Krinner, M. Shongwe, C. Tebaldi, A.J. Weaver and M. Wehner, 2013a. Long-term Climate Change: Projections, Commitments and Irreversibility. In: *Climate Change 2013: The Physical Science Basis. Contribution of Working Group I to the Fifth Assessment Report of the Intergovernmental Panel on Climate Change* [Stocker, T.F., D. Qin, G.-K. Plattner, M. Tignor, S.K. Allen, J. Boschung, A. Nauels, Y. Xia, V. Bex and P.M. Midgley (eds.)]. Cambridge University Press, Cambridge, United Kingdom and New York, NY, USA.
- Comiso, J.C., Gersten, R.A., Stock, L.V., Turner, J., Perez, G.J., Cho, K., 2017. Positive Trend in the Antarctic Sea Ice Cover and Associated Changes in Surface Temperature. *Journal of Climate* 30, 2251-2267.
- Cook, A.J., Holland, P., Meredith, M., Murray, T., Luckman, A., Vaughan, D.G., 2016. Ocean forcing of glacier retreat in the western Antarctic Peninsula. *Science* 353, 283-286.
- Crosta, X., Kohfeld, K.E., Bostock, H.C., Chadwick, M., Du Vivier, A., Esper, O., Etourneau, J., Jones, J., Leventer, A., Müller, J., 2022. Antarctic sea ice over the past 130 000 years—Part 1: a review of what proxy records tell us. *Clim. Past.* 18, 1729-1756.
- Crosta, X., Pichon, J.J., Burckle, L., 1998. Application of modern analog technique to marine Antarctic diatoms: Reconstruction of maximum sea-ice extent at the Last Glacial Maximum. *Paleoceanography and Paleoclimatology* 13, 284-297.
- Crosta, X., Romero, O., Armand, L.K., Pichon, J.-J., 2005. The biogeography of major diatom taxa in Southern Ocean sediments: 2. Open ocean related species. *Palaeogeography, Palaeoclimatology, Palaeoecology* 223, 66-92.
- Cuffey, K.M., Clow, G.D., Steig, E.J., Buizert, C., Fudge, T., Koutnik, M., Waddington, E.D., Alley, R.B., Severinghaus, J.P., 2016. Deglacial temperature history of West Antarctica. *Proceedings of the National Academy of Sciences* 113, 14249-14254.
- Cunningham, S., Alderson, S., King, B., Brandon, M., 2003. Transport and variability of the Antarctic circumpolar current in drake passage. *Journal of Geophysical Research: Oceans* 108.
- Curry, J.A., Schramm, J.L., Ebert, E.E., 1995. Sea ice-albedo climate feedback mechanism. *Journal of Climate* 8, 240-247.
- Danilov, S., Sidorenko, D., Wang, Q., Jung, T., 2017. The Finite-volumE Sea ice–Ocean Model (FESOM2). *Geosci. Model Dev.* 10, 765-789.
- Darby, D.A., Bischof, J.F., 2004. A Holocene record of changing Arctic Ocean ice drift analogous to the effects of the Arctic Oscillation. *Paleoceanography* 19.
- De Jong, J., Schoemann, V., Lannuzel, D., Croot, P., de Baar, H., Tison, J.L., 2012. Natural iron fertilization of the Atlantic sector of the Southern Ocean by continental shelf sources of the Antarctic Peninsula. *Journal of Geophysical Research: Biogeosciences* 117.

- De Santis, A., Maier, E., Gomez, R., Gonzalez, I., 2017. Antarctica, 1979-2016 sea ice extent: total versus regional trends, anomalies, and correlation with climatological variables. *Int. J. Remote Sens.* 38, 7566-7584.
- DeConto, R.M., Pollard, D., 2016. Contribution of Antarctica to past and future sea-level rise. *Nature* 531, 591-597.
- Delille, B., Vancoppenolle, M., Geilfus, N.-X., Tilbrook, B., Lannuzel, D., Schoemann, V., Becquevort, S., Carnat, G., Delille, D., Lancelot, C., Chou, L., Dieckmann, G.S., Tison, J.-L., 2014. Southern Ocean CO<sub>2</sub> sink: The contribution of the sea ice. *Journal of Geophysical Research: Oceans* 119, 6340-6355.
- Denis, D., Crosta, X., Barbara, L., Massé, G., Renssen, H., Ther, O., Giraudeau, J., 2010. Sea ice and wind variability during the Holocene in East Antarctica: insight on middle–high latitude coupling. *Quaternary Science Reviews* 29, 3709-3719.
- Denton, G.H., Anderson, R.F., Toggweiler, J., Edwards, R., Schaefer, J., Putnam, A., 2010. The last glacial termination. *Science* 328, 1652-1656.
- Dieckmann, G.S., Hellmer, H.H., 2009. The Importance of Sea Ice: An Overview, *Sea Ice*, pp. 1-22.
- Domack, E., 1992. Modern carbon-<sup>14</sup>ages and reservoir corrections for the Antarctic Peninsula and Gerlache Strait area. *Antarctic Journal of the United States* 27, 63-64.
- Domack, E.W., McClennen, C.E., 1996. Accumulation of glacial marine sediments in fjords of the Antarctic Peninsula and their use as late Holocene paleoenvironmental indicators. *Foundations for ecological research west of the Antarctic Peninsula* 70, 135-154.
- Dorschel, B., 2019. The Expedition PS118 of the Research Vessel POLARSTERN to the Weddell Sea in 2019. *Berichte zur Polar-und Meeresforschung= Reports on polar and marine research* 735.
- Dorschel, B., Hehemann, L., Viquerat, S., Warnke, F., Dreutter, S., Tenberge, Y.S., Accettella, D., An, L., Barrios, F., Bazhenova, E., Black, J., Bohoyo, F., Davey, C., De Santis, L., Dotti, C.E., Fremand, A.C., Fretwell, P.T., Gales, J.A., Gao, J., Gasperini, L., Greenbaum, J.S., Jencks, J.H., Hogan, K., Hong, J.K., Jakobsson, M., Jensen, L., Kool, J., Larin, S., Larter, R.D., Leitchenkov, G., Loubrieu, B., Mackay, K., Mayer, L., Millan, R., Morlighem, M., Navidad, F., Nitsche, F.O., Nogi, Y., Pertuisot, C., Post, A.L., Pritchard, H.D., Purser, A., Rebesco, M., Rignot, E., Roberts, J.L., Rovere, M., Ryzhov, I., Sauli, C., Schmitt, T., Silvano, A., Smith, J., Snaith, H., Tate, A.J., Tinto, K., Vandenbossche, P., Weatherall, P., Wintersteller, P., Yang, C., Zhang, T., Arndt, J.E., 2022. The International Bathymetric Chart of the Southern Ocean Version 2. *Scientific Data* 9, 275.
- Doty, M.S., Oguri, M., 1956. The island mass effect. *ICES Journal of Marine Science* 22, 33-37.
- Eayrs, C., Faller, D., Holland, D.M., 2020. Mechanisms driving the asymmetric seasonal cycle of Antarctic Sea Ice in the CESM Large Ensemble. *Annals of Glaciology* 61, 171-180.
- Eayrs, C., Li, X., Raphael, M.N., Holland, D.M., 2021. Rapid decline in Antarctic sea ice in recent years hints at future change. *Nature Geoscience* 14, 460-464.
- Ehrmann, W., Hillenbrand, C.-D., Smith, J.A., Graham, A.G., Kuhn, G., Larter, R.D., 2011. Provenance changes between recent and glacial-time sediments in the Amundsen Sea embayment, West Antarctica: clay mineral assemblage evidence. *Antarctic Science* 23, 471-486.

- Esper, O., Gersonde, R., 2014a. New tools for the reconstruction of Pleistocene Antarctic sea ice. *Palaeogeography, Palaeoclimatology, Palaeoecology* 399, 260-283.
- Esper, O., Gersonde, R., 2014b. Quaternary surface water temperature estimations: New diatom transfer functions for the Southern Ocean. *Palaeogeography, Palaeoclimatology, Palaeoecology* 414, 1-19.
- Esper, O., Gersonde, R., Kadagies, N., 2010. Diatom distribution in southeastern Pacific surface sediments and their relationship to modern environmental variables. *Palaeogeography, Palaeoclimatology, Palaeoecology* 287, 1-27.
- Etourneau, J., Collins, L.G., Willmott, V., Kim, J.-H., Barbara, L., Leventer, A., Schouten, S., Damsté, J.S., Bianchini, A., Klein, V., 2013. Holocene climate variations in the western Antarctic Peninsula: evidence for sea ice extent predominantly controlled by changes in insolation and ENSO variability. *Clim. Past.* 9, 1431-1446.
- Etourneau, J., Sgubin, G., Crosta, X., Swingedouw, D., Willmott, V., Barbara, L., Houssais, M.-N., Schouten, S., Damsté, J.S.S., Goosse, H., 2019. Ocean temperature impact on ice shelf extent in the eastern Antarctic Peninsula. *Nature Communications* 10, 1-8.
- Fahl, K., Stein, R., 2012. Modern seasonal variability and deglacial/Holocene change of central Arctic Ocean sea-ice cover: new insights from biomarker proxy records. *Earth and Planetary Science Letters* 351, 123-133.
- Falkowski, P.G., Barber, R.T., Smetacek, V., 1998. Biogeochemical controls and feedbacks on ocean primary production. *science* 281, 200-206.
- Favier, L., Durand, G., Cornford, S.L., Gudmundsson, G.H., Gagliardini, O., Gillet-Chaulet, F., Zwinger, T., Payne, A., Le Brocq, A.M., 2014. Retreat of Pine Island Glacier controlled by marine ice-sheet instability. *Nature Climate Change* 4, 117-121.
- Fetterer, F., Knowles, K., Meier, W., Savoie, M., and Windnagel, A. K., 2016. Updated Daily, Sea Ice Index, Version 2. [Median Sea Ice Extent 1981–2010], NSIDC: National Snow and Ice Data Center [data set], Boulder, Colorado USA, <https://doi.org/10.7265/N5736NV7> (last access: 24 July 2017).
- Fietz, S., Ho, S., Hugué, C., 2020. Archaeal Membrane Lipid-Based Paleothermometry for Applications in Polar Oceans. *Oceanography* 33.
- Fietz, S., Hugué, C., Rueda, G., Hambach, B., Rosell-Melé, A., 2013. Hydroxylated isoprenoidal GDGTs in the Nordic Seas. *Marine Chemistry* 152, 1-10.
- Foldvik, A., Kvinge, T., 1974. Conditional instability of sea water at the freezing point, *Deep Sea Research and Oceanographic Abstracts*. Elsevier, pp. 169-174.
- Frölicher, T.L., Sarmiento, J.L., Paynter, D.J., Dunne, J.P., Krasting, J.P., Winton, M., 2015. Dominance of the Southern Ocean in Anthropogenic Carbon and Heat Uptake in CMIP5 Models. *Journal of Climate* 28, 862-886.
- Gersonde, R., Crosta, X., Abelmann, A., Armand, L., 2005. Sea-surface temperature and sea ice distribution of the Southern Ocean at the EPILOG Last Glacial Maximum—a circum-Antarctic view based on siliceous microfossil records. *Quaternary science reviews* 24, 869-896.
- Gersonde, R., Zielinski, U., 2000. The reconstruction of late Quaternary Antarctic sea-ice distribution—the use of diatoms as a proxy for sea-ice. *Palaeogeography, Palaeoclimatology, Palaeoecology* 162, 263-286.

- Gohl, K., 2007. The expedition ANTARKTIS-XXIII/4 of the research vessel Polarstern in 2006. *Berichte zur Polar-und Meeresforschung (Reports on Polar and Marine Research)* 557.
- Gohl, K., 2017. The Expedition PS104 of the Research Vessel POLARSTERN to the Amundsen Sea in 2017. *Berichte zur Polar-und Meeresforschung= Reports on polar and marine research* 712.
- Gordon, A.L., 1981. Seasonality of Southern Ocean sea ice. *Journal of Geophysical Research: Oceans* 86, 4193-4197.
- Gordon, J.E., Harkness, D.D., 1992. Magnitude and geographic variation of the radiocarbon content in Antarctic marine life: implications for reservoir corrections in radiocarbon dating. *Quaternary Science Reviews* 11, 697-708.
- Graham, A.G.C., Kuhn, G., Meisel, O., Hillenbrand, C.-D., Hodgson, D.A., Ehrmann, W., Wacker, L., Wintersteller, P., dos Santos Ferreira, C., Römer, M., White, D., Bohrmann, G., 2017. Major advance of South Georgia glaciers during the Antarctic Cold Reversal following extensive sub-Antarctic glaciation. *Nature Communications* 8, 14798.
- Hall, A., 2004. The role of surface albedo feedback in climate. *Journal of Climate* 17, 1550-1568.
- Hanke, K., Lund-Hansen, L.C., Lamare, M.L., Højlund Pedersen, S., King, M.D., Andersen, P., Sorrell, B.K., 2018. Extreme low light requirement for algae growth underneath sea ice: A case study from Station Nord, NE Greenland. *Journal of Geophysical Research: Oceans* 123, 985-1000.
- Hanna, E., Navarro, F.J., Pattyn, F., Domingues, C.M., Fettweis, X., Ivins, E.R., Nicholls, R.J., Ritz, C., Smith, B., Tulaczyk, S., 2013. Ice-sheet mass balance and climate change. *Nature* 498, 51-59.
- Harms, S., Fahrbach, E., Strass, V.H., 2001. Sea ice transports in the Weddell Sea. *Journal of Geophysical Research: Oceans* 106, 9057-9073.
- Hasle, G.R., Syvertsen, E.E., 1996. *Identifying Marine Diatoms and Dinoflagellates*. Academic Press Limited, London.
- Heaton, T.J., Köhler, P., Butzin, M., Bard, E., Reimer, R.W., Austin, W.E., Ramsey, C.B., Grootes, P.M., Hughen, K.A., Kromer, B., 2020. Marine20—the marine radiocarbon age calibration curve (0–55,000 cal BP). *Radiocarbon* 62, 779-820.
- Hellmer, H.H., Kauker, F., Timmermann, R., Determann, J., Rae, J., 2012. Twenty-first-century warming of a large Antarctic ice-shelf cavity by a redirected coastal current. *Nature* 485, 225.
- Hellmer, H.H., Rhein, M., Heinemann, G., Abalichin, J., Abouchami, W., Baars, O., Cubasch, U., Dethloff, K., Ebner, L., Fahrbach, E., 2016. Meteorology and oceanography of the Atlantic sector of the Southern Ocean—a review of German achievements from the last decade. *Ocean Dynamics* 66, 1379-1413.
- Heroy, D.C., Anderson, J.B., 2007. Radiocarbon constraints on Antarctic Peninsula ice sheet retreat following the Last Glacial Maximum (LGM). *Quaternary Science Reviews* 26, 3286-3297.
- Heroy, D.C., Sjunneskog, C., Anderson, J.B., 2008. Holocene climate change in the Bransfield Basin, Antarctic Peninsula: evidence from sediment and diatom analysis. *Antarctic Science* 20, 69-87.

- Hillenbrand, C.-D., Kuhn, G., Smith, J.A., Gohl, K., Graham, A.G., Larter, R.D., Klages, J.P., Downey, R., Moreton, S.G., Forwick, M., 2013. Grounding-line retreat of the west Antarctic ice sheet from inner Pine Island Bay. *Geology* 41, 35-38.
- Hillenbrand, C.-D., Smith, J.A., Hodell, D.A., Greaves, M., Poole, C.R., Kender, S., Williams, M., Andersen, T.J., Jernas, P.E., Elderfield, H., 2017. West Antarctic Ice Sheet retreat driven by Holocene warm water incursions. *Nature* 547, 43.
- Hillenbrand, C.D., Smith, J.A., Kuhn, G., Esper, O., Gersonde, R., Larter, R.D., Maher, B., Moreton, S.G., Shimmield, T.M., Korte, M., 2010. Age assignment of a diatomaceous ooze deposited in the western Amundsen Sea Embayment after the Last Glacial Maximum. *Journal of Quaternary Science* 25, 280-295.
- Hobbs, W.R., Bindoff, N.L., Raphael, M.N., 2015. New perspectives on observed and simulated Antarctic sea ice extent trends using optimal fingerprinting techniques. *Journal of Climate* 28, 1543-1560.
- Hobbs, W.R., Massom, R., Stammerjohn, S., Reid, P., Williams, G., Meier, W., 2016. A review of recent changes in Southern Ocean sea ice, their drivers and forcings. *Global and Planetary Change* 143, 228-250.
- Holland, P.R., Feltham, D.L., Jenkins, A., 2007. Ice shelf water plume flow beneath Filchner-Ronne Ice Shelf, Antarctica. *Journal of Geophysical Research: Oceans* 112.
- Hopmans, E.C., Weijers, J.W., Schefuß, E., Herfort, L., Damsté, J.S.S., Schouten, S., 2004. A novel proxy for terrestrial organic matter in sediments based on branched and isoprenoid tetraether lipids. *Earth and Planetary Science Letters* 224, 107-116.
- Hoppmann, M., Nicolaus, M., Paul, S., Hunkeler, P.A., Heinemann, G., Willmes, S., Timmermann, R., Boebel, O., Schmidt, T., Kühnel, M., 2015. Ice platelets below Weddell Sea landfast sea ice. *Annals of Glaciology* 56, 175-190.
- Hoppmann, M., Richter, M.E., Smith, I.J., Jendersie, S., Langhorne, P.J., Thomas, D.N., Dieckmann, G.S., 2020. Platelet ice, the Southern Ocean's hidden ice: a review. *Annals of Glaciology*, 1-28.
- Huguet, C., de Lange, G.J., Gustafsson, Ö., Middelburg, J.J., Damsté, J.S.S., Schouten, S., 2008. Selective preservation of soil organic matter in oxidized marine sediments (Madeira Abyssal Plain). *Geochimica et Cosmochimica Acta* 72, 6061-6068.
- Huguet, C., Fietz, S., Rosell-Melé, A., Daura, X., Costenaro, L., 2017. Molecular dynamics simulation study of the effect of glycerol dialkyl glycerol tetraether hydroxylation on membrane thermostability. *Biochimica et Biophysica Acta (BBA)-Biomembranes* 1859, 966-974.
- Hutson, W.H., 1980. The Agulhas Current during the Late Pleistocene: Analysis of modern faunal analogs. *Science* 207, 64-66.
- Iacono, M.J., Delamere, J.S., Mlawer, E.J., Shephard, M.W., Clough, S.A., Collins, W.D., 2008. Radiative forcing by long-lived greenhouse gases: Calculations with the AER radiative transfer models. *Journal of Geophysical Research: Atmospheres* 113.
- Intergovernmental Panel on Climate Change, 2023. *Climate Change 2021 – The Physical Science Basis: Working Group I Contribution to the Sixth Assessment Report of the Intergovernmental Panel on Climate Change*. Cambridge University Press, Cambridge.
- Jacobs, S.S., Jenkins, A., Giulivi, C.F., Dutrieux, P., 2011. Stronger ocean circulation and increased melting under Pine Island Glacier ice shelf. *Nature Geoscience* 4, 519.

- Jenkins, A., Dutrieux, P., Jacobs, S., Steig, E.J., Gudmundsson, G.H., Smith, J., Heywood, K.J., 2016. Decadal ocean forcing and Antarctic ice sheet response: Lessons from the Amundsen Sea. *Oceanography* 29, 106-117.
- Jenkins, A., Dutrieux, P., Jacobs, S.S., McPhail, S.D., Perrett, J.R., Webb, A.T., White, D., 2010. Observations beneath Pine Island Glacier in West Antarctica and implications for its retreat. *Nature Geoscience* 3, 468.
- Jenkins, A., Jacobs, S., 2008. Circulation and melting beneath George VI ice shelf, Antarctica. *Journal of Geophysical Research: Oceans* 113.
- Jenkins, A., Shoosmith, D., Dutrieux, P., Jacobs, S., Kim, T.W., Lee, S.H., Ha, H.K., Stammerjohn, S., 2018. West Antarctic Ice Sheet retreat in the Amundsen Sea driven by decadal oceanic variability. *Nature Geoscience* 11, 733-738.
- Johns, L., Wraige, E., Belt, S., Lewis, C., Massé, G., Robert, J.-M., Rowland, S., 1999. Identification of a C 25 highly branched isoprenoid (HBI) diene in Antarctic sediments, Antarctic sea-ice diatoms and cultured diatoms. *Organic Geochemistry* 30, 1471-1475.
- Jones, J.M., Gille, S.T., Goosse, H., Abram, N.J., Canziani, P.O., Charman, D.J., Clem, K.R., Crosta, X., De Lavergne, C., Eisenman, I., 2016. Assessing recent trends in high-latitude Southern Hemisphere surface climate. *Nature Climate Change* 6, 917-926.
- Joughin, I., Alley, R.B., 2011. Stability of the West Antarctic ice sheet in a warming world. *Nature Geoscience* 4, 506.
- Joughin, I., Shapero, D., Dutrieux, P., Smith, B., 2021. Ocean-induced melt volume directly paces ice loss from Pine Island Glacier. *Science Advances* 7, eabi5738.
- Joughin, I., Smith, B.E., Holland, D.M., 2010. Sensitivity of 21st century sea level to ocean-induced thinning of Pine Island Glacier, Antarctica. *Geophysical Research Letters* 37.
- Jouzel, J., Vaikmae, R., Petit, J., Martin, M., Duclos, Y., Stievenard, M., Lorius, C., Toots, M., Mélières, M., Burckle, L., 1995. The two-step shape and timing of the last deglaciation in Antarctica. *Climate Dynamics* 11, 151-161.
- Kalanetra, K.M., Bano, N., Hollibaugh, J.T., 2009. Ammonia-oxidizing Archaea in the Arctic Ocean and Antarctic coastal waters. *Environmental Microbiology* 11, 2434-2445.
- Kern, S., 2009. Wintertime Antarctic coastal polynya area: 1992–2008. *Geophysical Research Letters* 36.
- Key, J.R., Wang, X., Stoeve, J.C., Fowler, C., 2001. Estimating the cloudy-sky albedo of sea ice and snow from space. *Journal of Geophysical Research: Atmospheres* 106, 12489-12497.
- Khazendar, A., Rignot, E., Schroeder, D.M., Seroussi, H., Schodlok, M.P., Scheuchl, B., Mouginot, J., Sutterley, T.C., Velicogna, I., 2016. Rapid submarine ice melting in the grounding zones of ice shelves in West Antarctica. *Nature communications* 7, 1-8.
- Kim, J.-H., Crosta, X., Willmott, V., Renssen, H., Bonnin, J., Helmke, P., Schouten, S., Sinninghe Damsté, J.S., 2012. Holocene subsurface temperature variability in the eastern Antarctic continental margin. *Geophysical Research Letters* 39.
- Kim, J.-H., Schouten, S., Hopmans, E.C., Donner, B., Damsté, J.S.S., 2008. Global sediment core-top calibration of the TEX<sub>86</sub> paleothermometer in the ocean. *Geochimica et Cosmochimica Acta* 72, 1154-1173.
- Kim, J.-H., Van der Meer, J., Schouten, S., Helmke, P., Willmott, V., Sangiorgi, F., Koç, N., Hopmans, E.C., Damsté, J.S.S., 2010. New indices and calibrations derived from the



- distribution of crenarchaeal isoprenoid tetraether lipids: Implications for past sea surface temperature reconstructions. *Geochimica et Cosmochimica Acta* 74, 4639-4654.
- Kim, M., Hwang, J., Kim, H.J., Kim, D., Yang, E.J., Ducklow, H.W., La Hyoung, S., Lee, S.H., Park, J., Lee, S., 2015. Sinking particle flux in the sea ice zone of the Amundsen shelf, Antarctica. *Deep Sea Research Part I: Oceanographic Research Papers* 101, 110-117.
- Kim, M., Hwang, J., Lee, S.H., Kim, H.J., Kim, D., Yang, E.J., Lee, S., 2016. Sedimentation of particulate organic carbon on the Amundsen Shelf, Antarctica. *Deep Sea Research Part II: Topical Studies in Oceanography* 123, 135-144.
- Kim, Y.S., Orsi, A.H., 2014. On the variability of Antarctic Circumpolar Current fronts inferred from 1992–2011 altimetry. *Journal of Physical Oceanography* 44, 3054-3071.
- Klinck, J.M., Hofmann, E.E., Beardsley, R.C., Salihoglu, B., Howard, S., 2004. Water-mass properties and circulation on the west Antarctic Peninsula Continental Shelf in Austral Fall and Winter 2001. *Deep Sea Research Part II: Topical Studies in Oceanography* 51, 1925-1946.
- Köhler, P., Nehrbass-Ahles, C., Schmitt, J., Stocker, T.F., Fischer, H., 2017. A 156 kyr smoothed history of the atmospheric greenhouse gases CO<sub>2</sub>, CH<sub>4</sub>, and N<sub>2</sub>O and their radiative forcing. *Earth Syst. Sci. Data* 9, 363-387.
- Kremer, A., 2018. The variability of sea ice in the Fram Strait throughout glacial-interglacial transitions of the Late Quaternary (MIS 11 to MIS 1), Die Variabilität von Meereis in der Framstraße während der Glazial-Interglazial-Zyklen des Spätquartärs (MIS 11 bis MIS 1). Universität Bremen Fachbereich 05: Geowissenschaften (FB 05).
- Lamping, N., Müller, J., Esper, O., Hillenbrand, C.-D., Smith, J.A., Kuhn, G., 2020. Highly branched isoprenoids reveal onset of deglaciation followed by dynamic sea-ice conditions in the western Amundsen Sea, Antarctica. *Quaternary Science Reviews* 228, 106103.
- Lamping, N., Müller, J., Hefter, J., Mollenhauer, G., Haas, C., Shi, X., Vorrath, M.-E., Lohmann, G., Hillenbrand, C.-D., 2021. Evaluation of lipid biomarkers as proxies for sea ice and ocean temperatures along the Antarctic continental margin. *Clim. Past* 17, 2305-2326.
- Lange, M., Ackley, S., Wadhams, P., Dieckmann, G., Eicken, H., 1989. Development of sea ice in the Weddell Sea. *Annals of Glaciology* 12, 92-96.
- Langhorne, P., Hughes, K., Gough, A., Smith, I., Williams, M., Robinson, N., Stevens, C., Rack, W., Price, D., Leonard, G., 2015. Observed platelet ice distributions in Antarctic sea ice: An index for ocean-ice shelf heat flux. *Geophysical Research Letters* 42, 5442-5451.
- Lee, S., Hwang, J., Ducklow, H.W., Hahm, D., Lee, S.H., Kim, D., Hyun, J.H., Park, J., Ha, H.K., Kim, T.W., 2017. Evidence of minimal carbon sequestration in the productive Amundsen Sea polynya. *Geophysical Research Letters* 44, 7892-7899.
- Leventer, A., 1998. The fate of Antarctic “sea ice diatoms” and their use as paleoenvironmental indicators. *Antarctic sea ice. Biological processes, interactions and variability*, 121-137.
- Leventer, A., Domack, E.W., Ishman, S.E., Brachfeld, S., McClennen, C.E., Manley, P., 1996. Productivity cycles of 200–300 years in the Antarctic Peninsula region: understanding linkages among the sun, atmosphere, oceans, sea ice, and biota. *Geological Society of America Bulletin* 108, 1626-1644.
- Liu, R., Han, Z., Zhao, J., Zhang, H., Li, D., Ren, J., Pan, J., Zhang, H., 2020. Distribution and source of glycerol dialkyl glycerol tetraethers (GDGTs) and the applicability of GDGT-

- based temperature proxies in surface sediments of Prydz Bay, East Antarctica. *Polar Research*.
- Liu, X.L., Summons, R.E., Hinrichs, K.U., 2012. Extending the known range of glycerol ether lipids in the environment: structural assignments based on tandem mass spectral fragmentation patterns. *Rapid Communications in Mass Spectrometry* 26, 2295-2302.
- Lizotte, M.P., 2001. The contributions of sea ice algae to Antarctic marine primary production. *American Zoologist* 41, 57-73.
- Locarnini, R.A., Mishonov, A.V., Antonov, J.I., Boyer, T.P., Garcia, H.E., Baranova, O.K., Zweng, M.M., Paver, C.R., Reagan, J.R., Johnson, D.R., 2013. World ocean atlas 2013. Volume 1, Temperature. NOAA Atlas NESDIS 73, 40 pp.
- Lohmann, G., Butzin, M., Eissner, N., Shi, X., Stepanek, C., 2020. Abrupt climate and weather changes across time scales. *Paleoceanography and Paleoclimatology* 35, e2019PA003782.
- López-García, P., Rodríguez-Valera, F., Pedrós-Alió, C., Moreira, D., 2001. Unexpected diversity of small eukaryotes in deep-sea Antarctic plankton. *Nature* 409, 603-607.
- Lorenz, S.J., Lohmann, G., 2004. Acceleration technique for Milankovitch type forcing in a coupled atmosphere-ocean circulation model: method and application for the Holocene. *Climate Dynamics* 23, 727-743.
- Lott, F., 1999. Alleviation of stationary biases in a GCM through a mountain drag parameterization scheme and a simple representation of mountain lift forces. *Monthly weather review* 127, 788-801.
- Loveland, T.R., Reed, B.C., Brown, J.F., Ohlen, D.O., Zhu, Z., Yang, L., Merchant, J.W., 2000. Development of a global land cover characteristics database and IGBP DISCover from 1 km AVHRR data. *Int. J. Remote Sens.* 21, 1303-1330.
- Lü, X., Liu, X.-L., Elling, F.J., Yang, H., Xie, S., Song, J., Li, X., Yuan, H., Li, N., Hinrichs, K.-U., 2015. Hydroxylated isoprenoid GDGTs in Chinese coastal seas and their potential as a paleotemperature proxy for mid-to-low latitude marginal seas. *Organic Geochemistry* 89-90, 31-43.
- Lythe, M.B., Vaughan, D.G., 2001. BEDMAP: A new ice thickness and subglacial topographic model of Antarctica. *Journal of Geophysical Research: Solid Earth* 106, 11335-11351.
- Maddison, E.J., Pike, J., Leventer, A., Domack, E.W., 2005. Deglacial seasonal and sub-seasonal diatom record from Palmer Deep, Antarctica. *Journal of Quaternary Science: Published for the Quaternary Research Association* 20, 435-446.
- Maqueda, M.M., Willmott, A.J., Biggs, N.R.T., 2004. Polynya Dynamics: a Review of Observations and Modeling. *Reviews of Geophysics* 42.
- Martin, S., 2001. Polynyas, in: Steele, J.H. (Ed.), *Encyclopedia of Ocean Sciences* (Second Edition). Academic Press, Oxford, pp. 540-545.
- Massé, G., Belt, S.T., Crosta, X., Schmidt, S., Snape, I., Thomas, D.N., Rowland, S.J., 2011. Highly branched isoprenoids as proxies for variable sea ice conditions in the Southern Ocean. *Antarctic Science* 23, 487-498.
- Massom, R., Reid, P., Stammerjohn, S., Raymond, B., Fraser, A., Ushio, S., 2013. Change and variability in East Antarctic sea ice seasonality, 1979/80–2009/10. *PLoS One* 8, e64756.
- Massom, R.A., Eicken, H., Hass, C., Jeffries, M.O., Drinkwater, M.R., Sturm, M., Worby, A.P., Wu, X., Lytle, V.I., Ushio, S., 2001. Snow on Antarctic sea ice. *Reviews of Geophysics* 39, 413-445.

- Massom, R.A., Scambos, T.A., Bennetts, L.G., Reid, P., Squire, V.A., Stammerjohn, S.E., 2018. Antarctic ice shelf disintegration triggered by sea ice loss and ocean swell. *Nature* 558, 383.
- Mathiot, P., Goosse, H., Fichefet, T., Barnier, B., Gallée, H., 2011. Modelling the seasonal variability of the Antarctic Slope Current. *Ocean Science* 7, 455-470.
- Medlin, L., 1990. *Berkeleya* spp. from Antarctic waters, including *Berkeleya adeliensis*, sp. nov., a new tube dwelling diatom from the undersurface of sea-ice. *Beihefte zur Nova Hedwigia* 100, 77-89.
- Meredith, M.P., Woodworth, P.L., Chereskin, T.K., Marshall, D.P., Allison, L.C., Bigg, G.R., Donohue, K., Heywood, K.J., Hughes, C.W., Hibbert, A., 2011. Sustained monitoring of the Southern Ocean at Drake Passage: Past achievements and future priorities. *Reviews of Geophysics* 49.
- Meyers, P.A., 1997. Organic geochemical proxies of paleoceanographic, paleolimnologic, and paleoclimatic processes. *Organic geochemistry* 27, 213-250.
- Milliken, K., Anderson, J., Wellner, J., Bohaty, S., Manley, P., 2009. High-resolution Holocene climate record from Maxwell Bay, South Shetland Islands, Antarctica. *Geology* 37, 1711-1725.
- Minzoni, R.T., Majewski, W., Anderson, J.B., Yokoyama, Y., Fernandez, R., Jakobsson, M., 2017. Oceanographic influences on the stability of the Cosgrove Ice Shelf, Antarctica. *The Holocene* 27, 1645-1658.
- Moore, J.K., Abbott, M.R., 2002. Surface chlorophyll concentrations in relation to the Antarctic Polar Front: seasonal and spatial patterns from satellite observations. *Journal of Marine Systems* 37, 69-86.
- Müller, J., Massé, G., Stein, R., Belt, S.T., 2009. Variability of sea-ice conditions in the Fram Strait over the past 30,000 years. *Nature Geoscience* 2, 772-776.
- Müller, J., Stein, R., 2014. High-resolution record of late glacial and deglacial sea ice changes in Fram Strait corroborates ice-ocean interactions during abrupt climate shifts. *Earth and Planetary Science Letters* 403, 446-455.
- Müller, J., Wagner, A., Fahl, K., Stein, R., Prange, M., Lohmann, G., 2011. Towards quantitative sea ice reconstructions in the northern North Atlantic: A combined biomarker and numerical modelling approach. *Earth and Planetary Science Letters* 306, 137-148.
- Müller, P.J., Schneider, R., 1993. An automated leaching method for the determination of opal in sediments and particulate matter. *Deep Sea Research Part I: Oceanographic Research Papers* 40, 425-444.
- Nakayama, Y., Menemenlis, D., Zhang, H., Schodlok, M., Rignot, E., 2018. Origin of Circumpolar Deep Water intruding onto the Amundsen and Bellingshausen Sea continental shelves. *Nature communications* 9, 3403.
- Nakayama, Y., Schröder, M., Hellmer, H.H., 2013. From circumpolar deep water to the glacial meltwater plume on the eastern Amundsen Shelf. *Deep Sea Research Part I: Oceanographic Research Papers* 77, 50-62.
- Nicholls, K.W., Østerhus, S., Makinson, K., Gammelsrød, T., Fahrbach, E., 2009. Ice-ocean processes over the continental shelf of the southern Weddell Sea, Antarctica: A review. *Reviews of Geophysics* 47.

- Nichols, P.D., Palmisano, A.C., Volkman, J.K., Smith, G.A., White, D.C., 1988. Occurrence of an isoprenoid C<sub>25</sub> di-unsaturated alkene and high neutral lipid content in Antarctic sea-ice diatom communities 1. *Journal of Phycology* 24, 90-96.
- Nielsdóttir, M.C., Bibby, T.S., Moore, C.M., Hinz, D.J., Sanders, R., Whitehouse, M., Korb, R., Achterberg, E.P., 2012. Seasonal and spatial dynamics of iron availability in the Scotia Sea. *Marine Chemistry* 130, 62-72.
- Nihashi, S., Ohshima, K.I., 2015. Circumpolar mapping of Antarctic coastal polynyas and landfast sea ice: Relationship and variability. *Journal of climate* 28, 3650-3670.
- Nolting, R., De Baar, H., Van Bennekom, A., Masson, A., 1991. Cadmium, copper and iron in the Scotia Sea, Weddell Sea and Weddell/Scotia confluence (Antarctica). *Marine Chemistry* 35, 219-243.
- Orsi, A.H., Johnson, G.C., Bullister, J.L., 1999. Circulation, mixing, and production of Antarctic Bottom Water. *Progress in Oceanography* 43, 55-109.
- Orsi, A.H., Whitworth III, T., Nowlin Jr, W.D., 1995. On the meridional extent and fronts of the Antarctic Circumpolar Current. *Deep Sea Research Part I: Oceanographic Research Papers* 42, 641-673.
- Otto-Bliesner, B.L., Brady, E.C., Zhao, A., Brierley, C.M., Axford, Y.L., Capron, E., Govin, A., Hoffman, J.S., Isaacs, E., Kageyama, M., 2021. Large-scale features of Last Interglacial climate: results from evaluating the lig127k simulations for the Coupled Model Intercomparison Project (CMIP6)-Paleoclimate Modeling Intercomparison Project (PMIP4). *Clim. Past.* 17, 63-94.
- Otto-Bliesner, B.L., Braconnot, P., Harrison, S.P., Lunt, D.J., Abe-Ouchi, A., Albani, S., Bartlein, P.J., Capron, E., Carlson, A.E., Dutton, A., 2017. The PMIP4 contribution to CMIP6—Part 2: Two interglacials, scientific objective and experimental design for Holocene and Last Interglacial simulations. *Geoscientific Model Development* 10, 3979-4003.
- Park, E., Hefter, J., Fischer, G., Iversen, M.H., Ramondenc, S., Nöthig, E.-M., Mollenhauer, G., 2019. Seasonality of archaeal lipid flux and GDGT-based thermometry in sinking particles of high-latitude oceans: Fram Strait (79° N) and Antarctic Polar Front (50° S). *Biogeosciences* 16, 2247-2268.
- Parkinson, C.L., 2019. A 40-y record reveals gradual Antarctic sea ice increases followed by decreases at rates far exceeding the rates seen in the Arctic. *Proceedings of the National Academy of Sciences* 116, 14414-14423.
- Parkinson, C.L., Cavalieri, D.J., 2012. Antarctic sea ice variability and trends, 1979-2010.
- Paul, S., Willmes, S., Heinemann, G., 2015. Long-term coastal-polynya dynamics in the southern Weddell Sea from MODIS thermal-infrared imagery. *The Cryosphere* 9, 2027-2041.
- Pedro, J.B., Bostock, H.C., Bitz, C.M., He, F., Vandergoes, M.J., Steig, E.J., Chase, B.M., Krause, C.E., Rasmussen, S.O., Markle, B.R., 2016. The spatial extent and dynamics of the Antarctic Cold Reversal. *Nature Geoscience* 9, 51.
- Pedro, J.B., Van Ommen, T., Rasmussen, S., Morgan, V.I., Chappellaz, J., Moy, A.D., Masson-Delmotte, V., Delmotte, M., 2011. The last deglaciation: timing the bipolar seesaw. *Clim. Past.* 7, 671-683.
- Perrette, M., Yool, A., Quartly, G.D., Popova, E.E., 2011. Near-ubiquity of ice-edge blooms in the Arctic. *Biogeosciences* 8, 515-524.

- Pritchard, H., Ligtenberg, S., Fricker, H., Vaughan, D., Van den Broeke, M., Padman, L., 2012. Antarctic ice-sheet loss driven by basal melting of ice shelves. *Nature* 484, 502-505.
- Purich, A., Doddridge, E.W., 2023. Record low Antarctic sea ice coverage indicates a new sea ice state. *Communications Earth & Environment* 4, 314.
- Raddatz, T., Reick, C., Knorr, W., Kattge, J., Roeckner, E., Schnur, R., Schnitzler, K.-G., Wetzel, P., Jungclaus, J., 2007. Will the tropical land biosphere dominate the climate–carbon cycle feedback during the twenty-first century? *Climate dynamics* 29, 565-574.
- Rantanen, M., Karpechko, A.Y., Lipponen, A., Nordling, K., Hyvärinen, O., Ruosteenoja, K., Vihma, T., Laaksonen, A., 2022. The Arctic has warmed nearly four times faster than the globe since 1979. *Communications Earth & Environment* 3, 168.
- Raphael, M.N., Handcock, M.S., 2022. A new record minimum for Antarctic sea ice. *Nature Reviews Earth & Environment* 3, 215-216.
- Reynolds, R.W., Rayner, N.A., Smith, T.M., Stokes, D.C., Wang, W., 2002. An Improved In Situ and Satellite SST Analysis for Climate. *Journal of Climate* 15, 1609-1625.
- Reynolds, R.W., Smith, T.M., Liu, C., Chelton, D.B., Casey, K.S., Schlax, M.G., 2007. Daily High-Resolution-Blended Analyses for Sea Surface Temperature. *Journal of Climate* 20, 5473-5496.
- Riaux-Gobin, C., Dieckmann, G.S., Poulin, M., Neveux, J., Labrune, C., Vétion, G., 2013. Environmental conditions, particle flux and sympagic microalgal succession in spring before the sea-ice break-up in Adélie Land, East Antarctica. *Polar Research* 32, 19675.
- Riaux-Gobin, C., Poulin, M., 2004. Possible symbiosis of *Berkeleya adeliensis* Medlin, *Synedropsis fragilis* (Manguin) Hasle et al. and *Nitzschia lecontei* Van Heurck (Bacillariophyta) associated with land-fast ice in Adélie Land, Antarctica. *Diatom Research* 19, 265-274.
- Rignot, E., Mouginot, J., Morlighem, M., Seroussi, H., Scheuchl, B., 2014. Widespread, rapid grounding line retreat of Pine Island, Thwaites, Smith, and Kohler glaciers, West Antarctica, from 1992 to 2011. *Geophysical Research Letters* 41, 3502-3509.
- Rignot, E., Mouginot, J., Scheuchl, B., Van Den Broeke, M., Van Wessel, M.J., Morlighem, M., 2019. Four decades of Antarctic Ice Sheet mass balance from 1979–2017. *Proceedings of the National Academy of Sciences* 116, 1095-1103.
- Rintoul, S., Hughes, C., Olbers, D., 2001. The Antarctic circumpolar current system, In: *Ocean Circulation and Climate*/G. Siedler, J. Church and J. Gould, eds. New York: Academic Press. p., pp. 271-302.
- Roeckner, E., Dümenil, L., Kirk, E., Lunkeit, F., Ponater, M., Rockel, B., Sausen, R., Schlese, U., 1989. The Hamburg version of the ECMWF model (ECHAM). Research activities in atmospheric and oceanic modelling. *CAS/JSC Working Group on Numerical Experimentation* 13, 7.1-7.4.
- Romero, O.E., Armand, L.K., Crosta, X., Pichon, J.J., 2005. The biogeography of major diatom taxa in Southern Ocean surface sediments: 3. Tropical/Subtropical species. *Palaeogeography, Palaeoclimatology, Palaeoecology* 223, 49-65.
- Rontani, J.-F., Smik, L., Belt, S.T., Vaultier, F., Armbrrecht, L., Leventer, A., Armand, L.K., 2019a. Abiotic degradation of highly branched isoprenoid alkenes and other lipids in the water column off East Antarctica. *Marine Chemistry* 210, 34-47.

- Rontani, J.-F., Smik, L., Belt, S.T., 2019b. Autoxidation of the sea ice biomarker proxy IPSO<sub>25</sub> in the near-surface oxic layers of Arctic and Antarctic sediments. *Organic geochemistry* 129, 63-76.
- Rosenblum, E., Eisenman, I., 2017. Sea Ice Trends in Climate Models Only Accurate in Runs with Biased Global Warming. *Journal of Climate* 30, 6265-6278.
- Rowland, S., Allard, W., Belt, S., Massé, G., Robert, J.-M., Blackburn, S., Frampton, D., Revill, A., Volkman, J., 2001. Factors influencing the distributions of polyunsaturated terpenoids in the diatom, *Rhizosolenia setigera*. *Phytochemistry* 58, 717-728.
- Rowland, S., Robson, J., 1990. The widespread occurrence of highly branched acyclic C<sub>20</sub>, C<sub>25</sub> and C<sub>30</sub> hydrocarbons in recent sediments and biota—a review. *Marine Environmental Research* 30, 191-216.
- Sadatzki, H., Opdyke, B., Menviel, L., Leventer, A., Hope, J.M., Brocks, J.J., Fallon, S., Post, A.L., O'Brien, P.E., Grant, K., 2023. Early sea ice decline off East Antarctica at the last glacial–interglacial climate transition. *Science Advances* 9, eadh9513.
- Sangrà, P., Gordo, C., Hernández-Arencibia, M., Marrero-Díaz, A., Rodríguez-Santana, A., Stegner, A., Martínez-Marrero, A., Pelegrí, J.L., Pichon, T., 2011. The Bransfield current system. *Deep Sea Research Part I: Oceanographic Research Papers* 58, 390-402.
- Scambos, T.A., Bell, R.E., Alley, R.B., Anandakrishnan, S., Bromwich, D., Brunt, K., Christianson, K., Creyts, T., Das, S., DeConto, R., 2017. How much, how fast?: A science review and outlook for research on the instability of Antarctica's Thwaites Glacier in the 21st century. *Global and Planetary Change* 153, 16-34.
- Schemm, S., 2018. Regional trends in weather systems help explain Antarctic sea ice trends. *Geophysical Research Letters* 45, 7165-7175.
- Schmidt, K., Brown, T.A., Belt, S.T., Ireland, L.C., Taylor, K.W., Thorpe, S.E., Ward, P., Atkinson, A., 2018. Do pelagic grazers benefit from sea ice? Insights from the Antarctic sea ice proxy IPSO<sub>25</sub>.
- Schmidtko, S., Heywood, K.J., Thompson, A.F., Aoki, S., 2014. Multidecadal warming of Antarctic waters. *Science* 346, 1227-1231.
- Schofield, O., Brown, M., Kohut, J., Nardelli, S., Saba, G., Waite, N., Ducklow, H., 2018. Changes in the upper ocean mixed layer and phytoplankton productivity along the West Antarctic Peninsula. *Philosophical Transactions of the Royal Society A: Mathematical, Physical and Engineering Sciences* 376, 20170173.
- Schouten, S., Hopmans, E.C., Schefuß, E., Sinninghe Damsté, J.S., 2002. Distributional variations in marine crenarchaeotal membrane lipids: a new tool for reconstructing ancient sea water temperatures? *Earth and Planetary Science Letters* 204, 265-274.
- Schouten, S., Hopmans, E.C., Sinninghe Damsté, J.S., 2013. The organic geochemistry of glycerol dialkyl glycerol tetraether lipids: A review. *Organic Geochemistry* 54, 19-61.
- Schrader, H., Gersonde, R., 1978. Diatoms and silicoflagellates. In: Zachariasse, W.J., Riedel, W.R., Sanfilippo, A., Schmidt, R.R., Brolsma, M.J., Schrader, H.J., Gersonde, R., Drooger, M.M., Broekman, J.A. (Eds.), *Micropaleontological Methods and Techniques - An Exercise on an Eight Meter Section of the Lower Pliocene of Capo Rossello, Sicily*. *Utrecht Micropaleontol. Bull.* 17, 129-176.

- Schröder, M., 2018. The Expedition PS111 of the Research POLARSTERN to the southern Weddell Sea in 2018. *Berichte zur Polar-und Meeresforschung= Reports on polar and marine research* 718.
- Shepherd, A., Fricker, H.A., Farrell, S.L., 2018a. Trends and connections across the Antarctic cryosphere. *Nature* 558, 223.
- Shepherd, A., Ivins, E., Rignot, E., Smith, B., van den Broeke, M., Velicogna, I., Whitehouse, P., Briggs, K., Joughin, I., Krinner, G., Nowicki, S., Payne, T., Scambos, T., Schlegel, N., A, G., Agosta, C., Ahlström, A., Babonis, G., Barletta, V., Blazquez, A., Bonin, J., Csatho, B., Cullather, R., Felikson, D., Fettweis, X., Forsberg, R., Gallee, H., Gardner, A., Gilbert, L., Groh, A., Gunter, B., Hanna, E., Harig, C., Helm, V., Horvath, A., Horvath, M., Khan, S., Kjeldsen, K.K., Konrad, H., Langen, P., Lecavalier, B., Loomis, B., Luthcke, S., McMillan, M., Melini, D., Mernild, S., Mohajerani, Y., Moore, P., Mougnot, J., Moyano, G., Muir, A., Nagler, T., Nield, G., Nilsson, J., Noel, B., Ootosaka, I., Pattle, M.E., Peltier, W.R., Pie, N., Rietbroek, R., Rott, H., Sandberg-Sørensen, L., Sasgen, I., Save, H., Scheuchl, B., Schrama, E., Schröder, L., Seo, K.-W., Simonsen, S., Slater, T., Spada, G., Sutterley, T., Talpe, M., Tarasov, L., van de Berg, W.J., van der Wal, W., van Wessem, M., Vishwakarma, B.D., Wiese, D., Wouters, B., The, I.t., 2018b. Mass balance of the Antarctic Ice Sheet from 1992 to 2017. *Nature* 558, 219-222.
- Shepherd, A., Wingham, D., Rignot, E., 2004. Warm ocean is eroding West Antarctic ice sheet. *Geophysical Research Letters* 31.
- Sidorenko, D., Goessling, H., Koldunov, N., Scholz, P., Danilov, S., Barbi, D., Cabos, W., Gurses, O., Harig, S., Hinrichs, C., 2019. Evaluation of FESOM2.0 coupled to ECHAM6. 3: Preindustrial and HighResMIP simulations. *Journal of Advances in Modeling Earth Systems* 11, 3794-3815.
- Sjunneskog, C., Taylor, F., 2002. Postglacial marine diatom record of the Palmer deep, Antarctic Peninsula (ODP Leg 178, Site 1098) 1. Total diatom abundance. *Paleoceanography* 17, PAL 4-1-PAL 4-8.
- Skinner, L.C., Fallon, S., Waelbroeck, C., Michel, E., Barker, S., 2010. Ventilation of the Deep Southern Ocean and Deglacial CO<sub>2</sub> rise. *Science* 328, 1147-1151.
- Smik, L., Belt, S.T., Lieser, J.L., Armand, L.K., Leventer, A., 2016b. Distributions of highly branched isoprenoid alkenes and other algal lipids in surface waters from East Antarctica: further insights for biomarker-based paleo sea-ice reconstruction. *Organic Geochemistry* 95, 71-80.
- Smik, L., Cabedo-Sanz, P., Belt, S.T., 2016a. Semi-quantitative estimates of paleo Arctic sea ice concentration based on source-specific highly branched isoprenoid alkenes: a further development of the PIP<sub>25</sub> index. *Organic geochemistry* 92, 63-69.
- Smith, A.C., Leng, M.J., Swann, G.E., Barker, P.A., Mackay, A.W., Ryves, D.B., Sloane, H.J., Chenery, S.R., Hems, M., 2016. An experiment to assess the effects of diatom dissolution on oxygen isotope ratios. *Rapid Communications in Mass Spectrometry* 30, 293-300.
- Smith, J.A., Andersen, T., Shortt, M., Gaffney, A., Truffer, M., Stanton, T.P., Bindshadler, R., Dutrieux, P., Jenkins, A., Hillenbrand, C.-D., 2017. Sub-ice-shelf sediments record history of twentieth-century retreat of Pine Island Glacier. *Nature* 541, 77-80.
- Smith, J.A., Graham, A.G., Post, A.L., Hillenbrand, C.-D., Bart, P.J., Powell, R.D., 2019. The marine geological imprint of Antarctic ice shelves. *Nature Communications* 10, 5635.

- Smith, J.A., Hillenbrand, C.-D., Kuhn, G., Klages, J.P., Graham, A.G.C., Larter, R.D., Ehrmann, W., Moreton, S.G., Wiers, S., Frederichs, T., 2014. New constraints on the timing of West Antarctic Ice Sheet retreat in the eastern Amundsen Sea since the Last Glacial Maximum. *Global and Planetary Change* 122, 224-237.
- Smith, J.A., Hillenbrand, C.-D., Kuhn, G., Larter, R.D., Graham, A.G., Ehrmann, W., Moreton, S.G., Forwick, M., 2011. Deglacial history of the West Antarctic Ice Sheet in the western Amundsen Sea embayment. *Quaternary Science Reviews* 30, 488-505.
- Smith Jr, W.O., 1987. Phytoplankton dynamics in marginal ice zones. *Oceanogr. Mar. Biol* 25, 11-38.
- Smith, W.O., Nelson, D.M., 1986. Importance of ice edge phytoplankton production in the Southern Ocean. *BioScience* 36, 251-257.
- Spencer-Jones, C.L., McClymont, E.L., Bale, N.J., Hopmans, E.C., Schouten, S., Müller, J., Abrahamsen, E.P., Allen, C., Bickert, T., Hillenbrand, C.-D., 2021. Archaeal intact polar lipids in polar waters: a comparison between the Amundsen and Scotia seas. *Biogeosciences* 18, 3485-3504.
- Spreen, G., Kaleschke, L., Heygster, G., 2008. Sea ice remote sensing using AMSR-E 89-GHz channels. *Journal of Geophysical Research: Oceans* 113.
- St. John, K., 2008. Cenozoic ice-rafting history of the central Arctic Ocean: Terrigenous sands on the Lomonosov Ridge. *Paleoceanography*, 23(1): PA1S05.
- Stammerjohn, S., Maksym, T., Massom, R., Lowry, K., Arrigo, K., Yuan, X., Raphael, M., Randall-Goodwin, E., Sherrell, R., Yager, P., 2015. Seasonal sea ice changes in the Amundsen Sea, Antarctica, over the period of 1979–2014. *Elem Sci Anth* 3.
- Stammerjohn, S., Massom, R., Rind, D., Martinson, D., 2012. Regions of rapid sea ice change: An inter-hemispheric seasonal comparison. *Geophysical Research Letters* 39.
- Stein, R., 2019. The late Mesozoic-Cenozoic Arctic Ocean climate and sea ice history: A challenge for past and future scientific ocean drilling. *Paleoceanography and Paleoclimatology* 34, 1851-1894.
- Stevens, B., Giorgetta, M., Esch, M., Mauritsen, T., Crueger, T., Rast, S., Salzmann, M., Schmidt, H., Bader, J., Block, K., 2013. Atmospheric component of the MPI-M Earth system model: ECHAM6. *Journal of Advances in Modeling Earth Systems* 5, 146-172.
- Stocker, T.F., Qin, D., Plattner, G.-K., Tignor, M., Allen, S.K., Boschung, J., Nauels, A., Xia, Y., Bex, V., Midgley, P.M., 2013. The physical science basis. Contribution of working group I to the fifth assessment report of the intergovernmental panel on climate change. *Computational Geometry* 18, 95-123.
- Stuiver, M. and Reimer, P.J., 1993. Extended  $^{14}\text{C}$  data base and revised CALIB 3.0  $^{14}\text{C}$  age calibration program, *Radiocarbon* 35: 215-230.
- Thoma, M., Jenkins, A., Holland, D., Jacobs, S., 2008. Modelling circumpolar deep water intrusions on the Amundsen Sea continental shelf, Antarctica. *Geophysical Research Letters* 35.
- Thomas, D.N., 2017. *Sea ice*. John Wiley & Sons.
- Thompson, A.F., Heywood, K.J., Thorpe, S.E., Renner, A.H., Trasviña, A., 2009. Surface circulation at the tip of the Antarctic Peninsula from drifters. *Journal of Physical Oceanography* 39, 3-26.



- Thompson, A.F., Stewart, A.L., Spence, P., Heywood, K.J., 2018. The Antarctic Slope Current in a changing climate. *Reviews of Geophysics* 56, 741-770.
- Tinto, K., Bell, R., 2011. Progressive unpinning of Thwaites Glacier from newly identified offshore ridge: Constraints from aerogravity. *Geophysical Research Letters* 38.
- Turner, J., Comiso, J., 2017. Solve Antarctica's sea-ice puzzle. *Nature* 547, 275-277.
- Turner, J., Marshall, G.J., Clem, K., Colwell, S., Phillips, T., Lu, H., 2020. Antarctic temperature variability and change from station data. *International Journal of Climatology* 40, 2986-3007.
- Turner, J., Orr, A., Gudmundsson, G.H., Jenkins, A., Bingham, R.G., Hillenbrand, C.-D., Bracegirdle, T.J., 2017. Atmosphere-ocean-ice interactions in the Amundsen Sea Embayment, West Antarctica. *Reviews of Geophysics* 55, 235-276.
- Valcke, S., 2013. The OASIS3 coupler: A European climate modelling community software. *Geoscientific Model Development* 6, 373.
- Varma, D., Hopmans, E.C., van Kemenade, Z.R., Kusch, S., Berg, S., Bale, N.J., Sangiorgi, F., Reichart, G.-J., Damsté, J.S.S., Schouten, S., 2023. Evaluating isoprenoidal hydroxylated GDGT-based temperature proxies in surface sediments from the global ocean. *Geochimica et Cosmochimica Acta*.
- Vaughan, D.G., 2008. West Antarctic Ice Sheet collapse—the fall and rise of a paradigm. *Climatic Change* 91, 65-79.
- Vaughan, D.G., Comiso, J.C., Allison, I., Carrasco, J., Kaser, G., Kwok, R., Mote, P., Murray, T., Paul, F., Ren, J., Rignot, E., Solomina, O., Steffen, K., Zhang, T., 2013. Observations: Cryosphere, in: Stocker, T.F., Qin, D., Plattner, G.-K., Tignor, M., Allen, S.K., Boschung, J., Nauels, A., Xia, Y., Bex, V., Midgley, P.M. (Eds.), *Climate Change 2013: The Physical Science Basis. Contribution of Working Group I to the Fifth Assessment Report of the Intergovernmental Panel on Climate Change*. Cambridge University Press, Cambridge, United Kingdom and New York, NY, USA, pp. 317–382.
- Vaughan, D.G., Marshall, G.J., Connolley, W.M., Parkinson, C., Mulvaney, R., Hodgson, D.A., King, J.C., Pudsey, C.J., Turner, J., 2003. Recent rapid regional climate warming on the Antarctic Peninsula. *Climatic change* 60, 243-274.
- Vernet, M., Geibert, W., Hoppema, M., Brown, P.J., Haas, C., Hellmer, H., Jokat, W., Jullion, L., Mazloff, M., Bakker, D., 2019. The Weddell Gyre, Southern Ocean: present knowledge and future challenges. *Reviews of Geophysics* 57, 623-708.
- Volkman, J.K., 1986. A review of sterol markers for marine and terrigenous organic matter. *Organic Geochemistry* 9, 83-99.
- Volkman, J.K., 2006. Lipid markers for marine organic matter, *Marine organic matter: Biomarkers, isotopes and DNA*. Springer, pp. 27-70.
- Volkman, J.K., Barrett, S.M., Blackburn, S.I., Mansour, M.P., Sikes, E.L., Gelin, F., 1998. Microalgal biomarkers: a review of recent research developments. *Organic Geochemistry* 29, 1163-1179.
- Volkman, J.K., Barrett, S.M., Dunstan, G.A., Jeffrey, S.W., 1993. Geochemical significance of the occurrence of dinosterol and other 4-methyl sterols in a marine diatom. *Organic Geochemistry* 20, 7-15.
- Vorrath, M.-E., Müller, J., Cárdenas, P., Opel, T., Mieruch, S., Esper, O., Lembke-Jene, L., Etourneau, J., Vieth-Hillebrand, A., Lahajnar, N., 2023. Deglacial and Holocene sea-ice and

- climate dynamics in the Bransfield Strait, northern Antarctic Peninsula. *Clim. Past.* 19, 1061-1079.
- Vorrath, M.-E., Müller, J., Esper, O., Mollenhauer, G., Haas, C., Schefuß, E., Fahl, K., 2019. Highly branched isoprenoids for Southern Ocean sea ice reconstructions: a pilot study from the Western Antarctic Peninsula. *Biogeosciences* 16, 2961-2981.
- Vorrath, M.-E., Müller, J., Rebolledo, L., Cárdenas, P., Shi, X., Esper, O., Opel, T., Geibert, W., Muñoz, P., Haas, C., 2020. Sea ice dynamics in the Bransfield Strait, Antarctic Peninsula, during the past 240 years: a multi-proxy intercomparison study. *Clim. Past.* 16, 2459-2483.
- Wadhams, P., 2000. Ice in the ocean.
- WAIS Divide Project Members; Fudge, T.J., Steig, E.J., Markle, B.R., Schoenemann, S.W., Ding, Q., Taylor, K.C., McConnell, J.R., Brook, E.J., Sowers, T., White, J.W.C., Alley, R.B., Cheng, H., Clow, G.D., Cole-Dai, J., Conway, H., Cuffey, K.M., Edwards, J.S., Lawrence Edwards, R., Edwards, R., Fegyveresi, J.M., Ferris, D., Fitzpatrick, J.J., Johnson, J., Hargreaves, G., Lee, J.E., Maselli, O.J., Mason, W., McGwire, K.C., Mitchell, L.E., Mortensen, N., Neff, P., Orsi, A.J., Popp, T.J., Schauer, A.J., Severinghaus, J.P., Sigl, M., Spencer, M.K., Vaughn, B.H., Voigt, D.E., Waddington, E.D., Wang, X., Wong, G.J., 2013. Onset of deglacial warming in West Antarctica driven by local orbital forcing. *Nature* 500, 440.
- Whitworth III, T., 1988. The Antarctic circumpolar current. *Oceanus* 31, 53-58.
- Xiao, W., Esper, O., Gersonde, R., 2016. Last Glacial-Holocene climate variability in the Atlantic sector of the Southern Ocean. *Quaternary Science Reviews* 135, 115-137.
- Xiao, X., Fahl, K., Müller, J., Stein, R., 2015. Sea-ice distribution in the modern Arctic Ocean: Biomarker records from trans-Arctic Ocean surface sediments. *Geochimica et Cosmochimica Acta* 155, 16-29.
- Yager, P.L., Sherrell, R.M., Stammerjohn, S.E., Alderkamp, A.-C., Schofield, O., Abrahamsen, E.P., Arrigo, K.R., Bertilsson, S., Garay, D.L., Guerrero, R., 2012. ASPIRE: the Amundsen Sea Polynya international research expedition. *Oceanography* 25, 40-53.
- Zamelczyk, K., Rasmussen, T.L., Husum, K., Hafliðason, H., de Vernal, A., Ravna, E.K., Hald, M., Hillaire-Marcel, C., 2012. Paleoceanographic changes and calcium carbonate dissolution in the central Fram Strait during the last 20 ka. *Quaternary Research* 78, 405-416.
- Zhang, C., Li, S., 2023. Causes of the record-low Antarctic sea-ice in austral summer 2022. *Atmospheric and Oceanic Science Letters*, 100353.
- Zhou, C., Zhang, T., Zheng, L., 2019. The characteristics of surface albedo change trends over the Antarctic sea ice region during recent decades. *Remote Sensing* 11, 821.
- Zielinski, U., Gersonde, R., 1997. Diatom distribution in Southern Ocean surface sediments (Atlantic sector): implications for paleoenvironmental reconstructions. *Palaeogeography, Palaeoclimatology, Palaeoecology* 129, 213-250.
- Zielinski, U., Gersonde, R., Sieger, R., Fütterer, D., 1998. Quaternary surface water temperature estimations: Calibration of a diatom transfer function for the Southern Ocean. *Paleoceanography and Paleoclimatology* 13, 365-383.
- Zwally, H.J., 1983. Antarctic sea ice, 1973-1976: Satellite passive-microwave observations. Scientific and Technical Information Branch, National Aeronautics and Space.